

NATIONAL & INTERNATIONAL SCIENTIFIC EVENTS

21st International Conference on Discrete Geometry for Computer Imagery

Venue: ESIEE Paris, Université Paris-Est
Location: Paris, France

Begins: March 25, 2019
Ends: March 29, 2019

6th International Conference on Food Digestion (Granada 2019)

Venue: Granada Exhibition & Conference Centre
Location: Granada, Spain

Begins: April 2, 2019
Ends: April 4, 2019

4th International Congress on 3D Printing (Additive Manufacturing) Technologies and Digital Industry 2019

Venue: Porto Bello Hotel Resort & Spa
Location: Antalya, Turkey

Begins: April 11, 2019
Ends: April 14, 2019

8th International Conference on Nanotechnology & Materials Science

Venue: Hotel Casa Amsterdam
Location: Amsterdam, The Netherlands

Begins: April 24, 2019
Ends: April 26, 2019

17th International Conference on Chemistry and the Environment

Venue: Aristotle University KEDEA Building
Location: Aristotle University KEDEA Building, Thessaloniki, Greece

Begins: June 18, 2019
Ends: June 20, 2019

8th International Symposium on Delivery of Functionality in Complex Food Systems

Venue: Sheraton Porto Hotel Conference Centre
Location: Porto, Portugal

Begins: July 7, 2019
Ends: July 10, 2019

22nd International Conference on General Relativity and Gravitation

Venue: Valencia Conference Centre
Location: Valencia, Spain

Begins: July 7, 2019
Ends: July 12, 2019

47th IUPAC World Chemistry Congress

Venue: Palais des Congrès Paris
Location: Paris, France

Begins: July 7, 2019
Ends: July 12, 2019

10th Triennial Congress of the International Society for Theoretical Chemical Physics

Venue: Clarion Hotel The Edge
Location: Tromsø, Norway

Begins: July 11, 2019
Ends: July 17, 2019

10th International Conference on Nanotechnology: Fundamentals and Applications (ICNFA'19)

Venue: Will be announced.
Location: Lisbon, Portugal

Begins: August 18, 2019
Ends: August 20, 2019

6th Drug Discovery & Therapy World Congress 2019

Venue: Sheraton Boston Hotel, Boston, MA
Location: Boston, USA

Begins: September 3, 2019
Ends: September 5, 2019

3rd World Congress on Electroporation and Pulsed Electric Fields

Venue: Pierre Baudin Congress Centre (Centre de Congrès)
Location: Toulouse, France

Begins: September 3, 2019
Ends: September 6, 2019



Abstracted & Indexed in:

TR Dizin Mühendislik ve Temel Bilimler Veri Tabanı | CrossRef | Google Scholar | MIP Database | StuartxChange | ResearchBib | Scientific Indexing Services (SIS)

HITTIT

HITTIT

JOURNAL OF SCIENCE & ENGINEERING

HJSE Official Journal of Hitit University Volume 5, Issue 4, 2018 www.hjse.hitit.edu.tr

HJSE Official Journal of Hitit University Volume 5, Issue 4, 2018 www.hjse.hitit.edu.tr

HJSE Official Journal of Hitit University Volume 5, Issue 4, 2018 www.hjse.hitit.edu.tr

HJSE Official Journal of Hitit University Volume 5, Issue 4, 2018 www.hjse.hitit.edu.tr

Volume 5, Issue 4, 2018

www.hjse.hitit.edu.tr

On Information Geometrical Structures

249-257

Fatma Muazzez Şimşir

The main motivation for this expository survey article is the lack of compact material that mainly address to mathematical audience because of the interdisciplinary content.

$$\mathcal{X} = \{x_0, x_1, \dots, x_n\}$$

$$\Xi = \left\{ \left[\xi^1, \xi^2, \dots, \xi^n \right] \mid \xi^i > 0 \forall i, \sum_{i=1}^n \xi^i < 1 \right\}$$

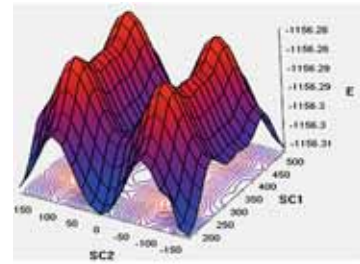
$$p(x, \xi) = \begin{cases} \xi^i & 1 \leq i \leq n \\ 1 - \sum_{i=1}^n \xi^i & i = 0 \end{cases}$$

Synthesis, Structural Characterization and Theoretical Investigations of New Azo-Azomethine Compounds Bearing Acryloyl Moiety

259-269

Sevil Özkınalı, M. Serdar Çavuş and Büşra Sakin

In this study the new azo-azomethine dyes has been synthesized containing acryloyl groups and the compounds were characterized by Uv-Vis, IR and NMR spectroscopy.



Review of Chromatography Methods for Purification of Paraoxonase Enzyme

271-274

Başak Gökçe

In this paper, several different purification and characterization methods of multi functional Enzyme paraoxonase 1(EC.3.3.8.1) was reviewed.

Table 1: Purification of paraoxonase 1 (EC.3.3.8.1) from human plasma

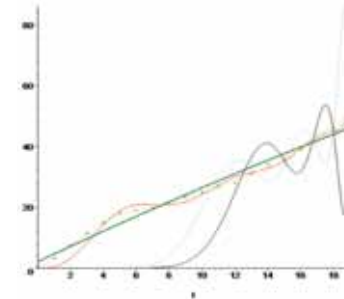
Step	Method	Yield (%)	Specific Activity (U/mg)	Purity (%)
1	Ammonium sulfate precipitation	85	1.2	15
2	DEAE ion exchange chromatography	75	2.5	30
3	Hydrophobic interaction chromatography	65	4.5	45
4	Size exclusion chromatography	55	6.5	60
5	Affinity chromatography	45	12.5	75
6	Final purification	35	25.0	90

Series Expansions and Polynomial Approximations of Monomolecular Growth Model for Some Populations of Eucalyptus camaldulensis Dehn. From Eastern Mediterranean Forest Research Manager

275-284

Mehmet Korkmaz and Erdal Unluyol

In this study the series expansions of only one of the growth models were presented to investigate the series expansions.



Combinations of Interleukin-10 Gene Promoter Polymorphisms with -1082A, -819T, -592A Minor Allele are Associated with Sinonasal Polyposis

285-292

Sibel Ozdas

The IL-10 -1082, -819, and -592 SNPs and their genotypic combinations in SP patients and controls to investigate the role of IL-10 in pathogenesis of SP have been studied in this study.

IL-10-1082 (G>A)

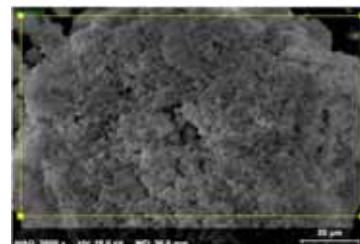
IL-10-819 (C>T)	GG		GA		AA	
	CC	CT	CC	CT	CC	CT
CC	49.0	78.0	24.0	9.0		
CT	17.0	3.0	3.0	7.0	1.0	1.0
TT	3.0	3.0	3.0	1.0	1.0	0.0

Development of Bismuth Telluride Nanostructure Pellet for Thermoelectric Applications

293-299

Hayati Mamur and M.R.A. Bhuiyan

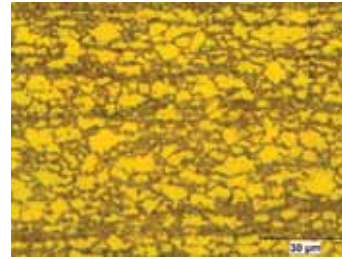
In this paper, a simple chemical method was tried to develop the Bi₂Te₃ nanostructure pellet for thermoelectric applications.



Strain Hardening Behavior Characterization of Dual Phase Steels 301-306

Kemal Davut, Caner Şimşir and Barış Çetin

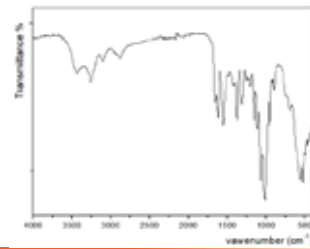
The aim of this study is to evaluate the strain hardening behavior of DP800 steels, obtained from different vendors and thus having different compositions and microstructures.



Kinetic and Equilibrium Studies of Adsorption of Reactive Red 120 on Chitin 307-311

Murat Torun, Y. Doruk Aracagök and Mahmut Kabalak

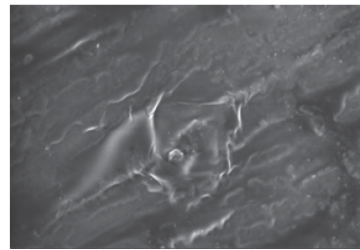
In this study, effect of chitin is followed for adsorption of reactive red 120 textile dye from water at different conditions such as pH, initial concentration of dye, ionic strength, initial concentration of chitin, effect of temperature, effect of contact time was studied.



The Effects of Olive Pomace Ash on The Color Change of The Composite Material and Its Mechanical Properties 313-316

Soner Celen, Sencer Süreyya Karabeyoğlu, Türkan Aktas and Aylin Akyildiz

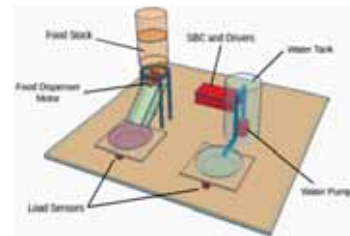
The purpose of this study is to convert olive pomace ash (prina ash), which is the remaining pulp after the pressing of olives, to a plastic material.



Low-cost IoT Design and Implementation of a Remote Food and Water Control System for Pet Owners 317-320

Ugur Baran Asaner and Armagan Elibol

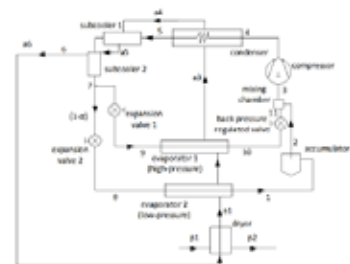
The main purpose of this paper is to state and detail an instance of low-cost IoT by designing a remote food and water control system for pet owners. The whole system consists of three subsystems; the performing unit, server, and mobile application.



Energetic And Exergetic Investigations of an Integrated Heat Pump System for Drying Applications 321-337

Canan Acar

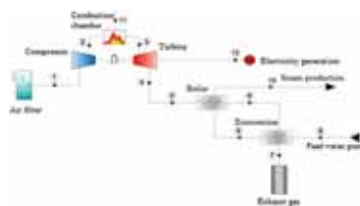
The main aim of this study is to conduct energetic and exergetic investigations of a dual stage heat pump for drying applications in order to evaluate the performance of the overall system.



Exergy Destruction Analysis of a Gas Turbine Power Plant 339-346

Ali Kilicarslan and Mehmet Kiris

In this study, the effect of the environment air temperature on the exergy destructions and exergetic efficiencies of the elements of the gas turbine cycle such as the compressor, combustion chamber, turbine, boiler and economizer were carried out from plant operating in the city of Corum, Turkey.



Journal Name : HITTITE JOURNAL OF SCIENCE AND ENGINEERING
Year : 2018
Managing Editor : Prof. Dr. Ali KILIÇARSLAN
Managing Office : Hitit University Faculty of Engineering
Managing Office Tel : +90 364 227 45 33 / 12 36
Publication Language : English
Publication Type : Peer Reviewed, Open Access, International Journal
Delivery Format : 4 times a year (quarterly)
Print ISSN : 2149-2123
Online ISSN : 2148-4171
Publisher Address : Hitit Üniversitesi Kuzey Kampüsü Çevre Yolu Bulvarı
19030 Çorum / TÜRKİYE
Publisher Tel : +90 364 227 45 33/1236



This new issue of Hittite Journal of Science and Engineering contains twelve manuscripts from the disciplines of chemistry, mathematics, chemical engineering, electrical and electronics engineering, mechanical engineering. These manuscripts were first screened by Section Editors using plagiarism prevention software and then reviewed and corrected according to the reviewer's comments. I would like to express my gratitude to all our authors and contributing reviewers of this issue.

I would like to thank to the President of Hitit University, Dr. Reha Metin Alkan, for his constant interest in HJSE and also to the Associate Editors of

HJSE, namely Dr. Dursun Ali Kose and Dr. Oncu Akyildiz, as well as our Production Editors Dr. Kazim Kose, Dr. Hülya Çakmak, Mustafa Reşit Haboğlu, Erhan Çetin, Harun Emre Kiran and Ömer Faruk Tozlu for their invaluable efforts in making of the journal.

It's my pleasure to invite the researchers and scientists from all branches of science and engineering to join us by sending their best papers for publication in Hittite Journal of Science and Engineering.

Dr. Ali Kiliçarslan

Editor-in-Chief



On Information Geometrical Structures

Fatma Muazzez Şimşir

Hitit University, Department of Mathematics, Çorum, TURKEY

ABSTRACT

Information geometry is a modern differential geometric approach to statistics, in particular theory of information. The main motivation for this expository survey article is the lack of compact material that mainly address to mathematical audience because of the interdisciplinary content. Information geometry simply described as applying the techniques of differential geometry to statistical models, represented as manifolds of probability distributions. This can be done either done by putting the concept of divergences on the center or the Fisher metric. This paper is motivated from the latter approach.

Keywords:

Information geometry; Dual affine connections; Statistical distributions

Article History:

Received: 2017/10/06

Accepted: 2017/11/18

Online: 2018/12/31

Correspondence to: Fatma Muazzez Şimşir Hitit University, Department of Mathematics, Ulukavak Mahallesi, 19040, Çorum, Turkey
E-mail: fmuaazzezsimisir@hitit.edu.tr
Phone: +90 364 2277000-1663

INTRODUCTION

Probability distributions are the basic tools of statistics and statistical inference. One of the main problems of mathematical statistics is finding a measure to distinguish one probability distribution from another. Moreover, in statistical inference a probability distribution is chosen from a set of candidates. This immediately brings up the question of what would happen if a neighbor distribution is selected. One way to answer such questions is to introduce a notion of "distance" between probability distributions.

Information theory originated in 1940's by Shannon, [25]. The earliest ideas of combining statistics and differential geometry goes back 1945's to Rao and Jeffreys [12, 23] who used independently Fisher information as a Riemannian metric. However, it was by Efron that the role of differential geometry started to play an important role in statistics. He defined the statistical curvature for one-parameter statistical models in 1975, [11]. However, in Efron's work tools of differential geometry was not used elaborately. The first step to use elegant differential geometry in the context of statistics was by Dawid, [10]. By using the notion of statistical curvature, he defined e -connection (exponential connection) on the space of positive probability distributions. Moreover, he also showed that on this space different connections may be defined. The (0) -connection (Levi Civita) and (m) -connection (mixture connection) of the Fisher metric were the examples. Since the space of positive probability distributions is infinite dimensional, it is not easy

to see this space as a manifold. Amari [2] in 1980's used tools of modern differential geometry and developed a systematic method to investigate informational theoretical concepts by taking projection of Efron's model into finite dimensional models. He and Nagaoka considered (e) -connection and (m) -connection as a pair of dual connections which will later be on the center of information geometry, [4]. Actually, Chentsov [7] had already been defined (α) -connections from a different viewpoint, however, the article was in Russian and their relationship with statistical estimation was omitted in the article. Hence, his contributions are not well-known among statisticians. The standard references to get familiar with information geometry are [1, 2, 3, 4, 8, 14, 19, and 26].

Throughout this paper the close relationship between statistical models and differential geometry, in particular affine differential geometry is emphasized. Most of the times, different schools of geometry prefer to use different terminology for the same concepts which cause confusion for those that are not much familiar with the field. Therefore, such cases are highlighted and nuances is also tried to be explained, as well.

STATISTICAL MODELS

The probability distributions on a set will be represented as follows: If \mathcal{X} is a discrete set (with finite or

countably infinite cardinality), then a probability distribution on χ is a function $P: \chi \rightarrow \mathbb{R}$ which satisfies.

$$p(x) \geq 0, \quad \forall x \in \chi \quad \text{and} \quad \sum_{x \in \chi} p(x) = 1 \quad (2.1)$$

If $\chi = \mathbb{R}^n$ then it is a function $P: \chi \rightarrow \mathbb{R}$ which satisfies

$$p(x) \geq 0, \quad \forall x \in \chi \quad \text{and} \quad \int p(x) dx = 1. \quad (2.2)$$

Consider a family S of probability distributions on χ . Suppose that each element of S , a probability distribution, may be parametrized using an n real-valued variables $[\xi^1, \dots, \xi^n]$ so that

$$S = \{ p_\xi = p(x; \xi) \mid \xi = [\xi^1, \dots, \xi^n] \in \Xi \}$$

where Ξ is a subset of \mathbb{R}^n and the mapping $\xi \rightarrow p_\xi$ is injective. Such S is called an n -dimensional statistical model, a parametric model, or simply a model on χ . Assumptions that we made on statistical models are:

- We may freely differentiate with respect to the parameters. Assume that Ξ is an open subset of \mathbb{R}^n and $\forall x \in \Xi$ the function $\xi \rightarrow \mathbb{R}$ is C^∞ .

- The order of integration and the differentiation may freely be rearranged. For instance,

$$\int \partial_i p(x; \xi) dx = \partial_i \int p(x; \xi) dx = \partial_i 1 = 0.$$

where $\partial_i = \frac{\partial}{\partial \xi^i}$.

- The model S is a subset of

$$P(\chi) = \{ p: \chi \rightarrow \mathbb{R} \mid p(x) > 0, \forall x \in \chi \text{ and } \int p(x) dx = 1 \}.$$

Some Examples of Statistical Models

- Normal Distribution

$$\chi = \mathbb{R}, \quad n = 2, \quad \xi = [\mu, \sigma], \quad \Xi = \{ [\mu, \sigma] \mid \mu \in \mathbb{R}, \sigma \in \mathbb{R}^+ \}$$

$$p(x, \xi) = \frac{1}{\sqrt{2\pi\sigma}} \exp\left\{-\frac{(x-\mu)^2}{2\sigma^2}\right\}$$

- Multivariate Normal Distribution

$$\chi = \mathbb{R}^k, \quad n = k + \frac{k(k+1)}{2}, \quad \xi = [\mu, \Sigma]$$

$$\Xi = \{ [\mu, \Sigma] \mid \mu \in \mathbb{R}^k, \Sigma \in \mathbb{R}^{k \times k} : \text{positive definite} \}$$

$$p(x; \xi) = (2\pi)^{-n/2} (\det \Sigma)^{-1/2} \exp\{-(x-\mu)' \Sigma^{-1} (x-\mu)\}$$

- Poisson Distribution

$$\chi = \{0, 1, 2, \dots\}, \quad n = 1, \quad \Xi = \{ \xi \mid \xi > 0 \}$$

$$p(x; \xi) = e^{-\xi} \frac{\xi^x}{x!}$$

$P(X)$ for finite χ

$$\chi = \{x_0, x_1, \dots, x_n\}$$

$$\Xi = \left\{ [\xi^1, \xi^2, \dots, \xi^n] \mid \xi^i > 0 \forall i, \sum_{i=1}^n \xi^i < 1 \right\}$$

$$p(x; \xi) = \begin{cases} \xi^i & 1 \leq i \leq n \\ 1 - \sum_{i=1}^n \xi^i & i = 0 \end{cases}$$

KAHLER AFFINE MANIFOLDS, STATISTICAL MANIFOLDS AND DUALY FLAT STRUCTURES

An affine manifold is a differential manifold whose coordinate changes are affine transformations which immediately give rise to existence of a torsion-free connection with vanishing curvature. Note that affine transformations are made up of a linear transformation followed by a translation. Since an affine manifold is a differentiable manifold with affine charts one may define a two tensor $g_{ij} = \frac{\partial^2 F}{\partial x^i \partial x^j} dx^i \otimes dx^j$ where φ is a strictly convex function. Thus, g is symmetric and positive definite. Hence, it is a Riemannian metric on M which will be called a Kahler affine metric. Note that the coefficients of the metric tensor g is invariant under affine transformations, [15, 16]. Such structures are first introduced by Cheng and Yau, [6]. Kahler affine metrics are called Hessian metrics by Japanese school due to the fact that g_{ij} is the Hessian of a convex local potential F , [26].

An affine manifold equipped with a Kahler affine metric is called a Kahler affine manifold. One may recover dually flat connections from this structure. Conversely, given mutually flat connections one may obtain local potential functions. The flat affine connection D and its dual D^* are called dually flat connections with respect to the Kahler affine metric g . In other words, for all vector fields X, Y on M , $Xg(Y, Z) = g(D_X Y, Z) + g(Y, D_X^* Z)$. On the other hand, a statistical manifold is simply a Riemannian manifold (M, g) together with two torsion free connections ∇ and ∇^* that satisfies a duality relation with respect to the Riemannian metric. Two torsion free connections ∇ and ∇^* are called dual to each other with respect to a Riemannian metric g if

for all vector fields X, Y, Z on M , $Xg(Y, Z) = g(\nabla_X Y, Z) + g(Y, \nabla_X^* Z)$. If $\nabla = \nabla^*$ the geometry reduces to the Riemannian one. One may refer to the works of Lauritzen, Kurose and Noguchi [19, 17, 22] for a detailed study of statistical manifolds. There is a close relationship between the statistical manifolds and Kahler affine manifolds. It can be seen from definitions that every Kahler affine manifold is a statistical manifold. However, not all statistical manifolds are Kahler affine. Consider \mathbb{R}^n with its standard affine coordinate system $\{x_1, \dots, x_n\}$ and let D be the canonical flat affine connection, i.e., $D_{\frac{\partial}{\partial x^i}} \frac{\partial}{\partial x^j} = 0$. Let $\Omega \subset \mathbb{R}^n$ be a domain and let φ be a strictly convex function on Ω . With the Kahler affine metric $g = \frac{\partial^2 \varphi}{\partial x^i \partial x^j} dx^i dx^j$, the triple (Ω, D, g) is a Kahler affine manifold. This triple is a flat statistical manifold. Conversely a flat statistical manifold is locally isometric to the Kahler affine manifold (Ω, D, g) .

The α -Connection

Let M be a Kahler affine manifold for $-1 \leq \alpha \leq 1$ the α -Connection is defined by

$$\Gamma_{ijk}^{(\alpha)} = \Gamma_{ijk}^{(0)} - \frac{\alpha}{2} \partial_i \partial_j \partial_k \varphi \quad (3.1)$$

where the Levi-Civita connection of g is denoted by $\Gamma_{ijk}^{(0)}$ and

$$\Gamma_{ijk}^{(0)} = \left\langle \nabla_{\frac{\partial}{\partial x^i}} \frac{\partial}{\partial x^j}, \frac{\partial}{\partial x^k} \right\rangle. \quad (3.2)$$

From (3.1) and (3.2)

$$\Gamma_{ijk}^{(0)} = \frac{1}{2} \partial_i \partial_j \partial_k \varphi, \quad (3.3)$$

and

$$\Gamma_{ijk}^{(\alpha)} = \frac{1}{2} (1 - \alpha) \partial_i \partial_j \partial_k \varphi. \quad (3.4)$$

Since 3.4 is symmetric with respect to i and j , $\nabla^{(\alpha)}$ is torsion free. Moreover,

$\Gamma_{ijk}^{(\alpha)} + \Gamma_{ijk}^{(-\alpha)} = 2\Gamma_{ijk}^{(0)}$, $\nabla^{(\alpha)}$ and $\nabla^{(-\alpha)}$ is dual to each other with respect to g . In other words, for all vector fields X, Y, Z

$$Zg(X, Y) = g(\nabla_Z^{(\alpha)} X, Y) + g(X, \nabla_Z^{(-\alpha)} Y). \quad (3.5)$$

Since $\Gamma_{ijk}^{(1)} = 0$, $\nabla^{(1)}$ defines a flat structure and x -coordinates are an affine coordinate system for $\nabla^{(1)}$. Therefore, the connection $\nabla^{(-1)}$ is dual to the connection $\nabla^{(1)}$ and its Christoffel symbols in x -coordinates is of the form

$$\Gamma_{ijk}^{(-1)} = \partial_i \partial_j \partial_k \varphi.$$

The dual affine coordinate θ is

$$\theta_j = \partial_j \varphi, \quad (3.6)$$

and so also

$$g_{ij} = \partial_i \theta_j. \quad (3.7)$$

The corresponding local potential function can be calculated by a Legendre transform

$$\phi(\theta) = \max_x (x^i \theta_i - \varphi(x)), \quad \varphi(x) + \phi(\theta) - x \cdot \xi = 0, \quad (3.8)$$

and

$$x^i = \partial^i \phi(\theta), \quad g^{ij} = \frac{\partial x^i}{\partial \theta_j} = \partial^i \partial^j \phi(\theta). \quad (3.9)$$

Therefore, a Kahler affine metric together with the flat affine connection yields a dual structure. Such structures constitutes the foundations of the information geometry. Conversely, from such a dually flat structure, the local potential functions or the Kahler affine structure can be obtained. Let $D = \nabla^{(1)}$ and $D^* = \nabla^{(-1)}$ be dually flat connections and let $\{x^1, \dots, x^n\}$ be the affine coordinates that is obtained from the flat connection D .

Hence, the vector fields $\partial_i = \frac{\partial}{\partial x^i}$ are parallel. We define ∂^j

$$g(\partial_i, \partial^j) = \delta_i^j = \begin{cases} 1 & i = j \\ 0 & i \neq j \end{cases}$$

and for every vector field X

$$Xg(\partial_i, \partial^j) = g(D_X \partial_i, \partial^j) + g(\partial_i, D_X^* \partial^j).$$

∂_i is parallel for D so is ∂^j for D^* . Since D^* is torsion free, $[\partial^j, \partial^k] = 0$ for all j, k . Hence, the affine coordinates θ_j where $\partial^j = \frac{\partial}{\partial \theta_j}$ is obtained.

Note that, when passing from x -coordinates to θ -coordinates ∂_i transforms contravariantly, whereas ∂^j transforms covariantly. The transformation rule between x and θ coordinates is given by $\partial^j = (\partial^j x^i) \partial_i$ and $\partial_i = (\partial_i \theta_j) \partial^j$. In the following sequel the metric tensor g in x and θ -coordinates will be calculated. Since $g_{ij} = g(\partial_i, \partial_j)$, $g^{ij} = g(\partial^i, \partial^j)$ and $g(\partial_i, \partial^j) = \delta_i^j$

$$g_{ij} = \frac{\partial \theta_j}{\partial x^i}$$

$$g^{ij} = \frac{\partial x^i}{\partial \theta_j}$$

We would like to find the local potential functions $\varphi(x)$ and $\phi(\theta)$ that satisfy $\theta_i = \partial_i \varphi(x)$, $x^i = \partial^i \phi(\theta)$. The first equation can be solved locally if $\partial_i \theta_j = \partial_j \theta_i$ using the fact that the metric tensor g is symmetric. Hence, $g_{ij} = \partial_i \partial_j \varphi$ and φ strictly convex function. $\phi := x^i \theta_i - \varphi$ is defined from the duality to get

$\partial^i \phi = x^i + \frac{\partial x^j}{\partial \theta_i} \theta_j - \frac{\partial x^j}{\partial \theta_i} \frac{\partial}{\partial x^j} \varphi = x^i$. Since φ and ϕ are strictly convex functions, they relate to each other by a Legendre transform

$$\phi(\theta) = \max_x (x^i \theta_i - \varphi(x)) \tag{3.10}$$

$$\varphi(x) = \max_\theta (x^i \theta_i - \phi(\theta)). \tag{3.11}$$

Moreover, Christoffel symbols of the metric g^{ij} in x -coordinates are

$$\Gamma^{ijk} = -\Gamma_{ijk} = -\frac{1}{2} \partial_i \partial_j \partial_k \varphi, \tag{3.12}$$

$$\Gamma^{(\alpha)ijk} = \Gamma^{ijk} - \frac{\alpha}{2} \partial_i \partial_j \partial_k \varphi = -\Gamma_{ijk}^{(-\alpha)}. \tag{3.13}$$

Consequently, $\Gamma^{(1)} = -\Gamma^{(-1)}$. Hence, $-\Gamma^{(-1)} = 0$ in θ -coordinates.

GEOMETRY OF STATISTICAL MODELS

In particular, why differential geometry is useful for statistics? A statistical model is a set of probability distributions to which we believe that the true distribution belongs. It is a subset of all possible probability distributions. One often uses a statistical model to carry out statistical inference, assuming that the true distribution is in the model. However, the true distribution may not be in the model but only close to it. Therefore, in order to evaluate statistical inference procedures, it is important to know what part the statistical model occupies in the entire set of probability distributions and what shape the statistical model has in the entire set of models. Hence, it is expected that a fundamental role is played in statistics by the geometric quantities such as the distance or divergence of two probability distributions, the flatness or the curvature of the statistical model. Statistical inference may be carried out more and more precisely as the number of observations increases so that one could construct a universal asymptotic theory of the statistical inference in the regular case. Since the estimated probability distribution lies very close to the true distribution in this case, it is sufficient when evaluating statistical procedures to take account of only local structure of the model in a small neighborhood of the true or estimated distribution. Thus, one can locally linearize the model at the true or estimated distribution even if the model is curved in the entire set.

Let $S = \{p_\xi \mid \xi \in \Xi\}$ be an n -dimensional statistical model. Given a point ξ , the Fisher Information Matrix of at ξ is an $n \times n$ matrix $[g_{ij}(\xi)]$ is defined by

$$g_{ij}(\xi) = E_\xi \left[\partial_i l_\xi \partial_j l_\xi \right] = \int \partial_i l_\xi \partial_j l_\xi p_\xi dx \tag{4.1}$$

where $l_\xi = l(x; \xi) = \log p(x; \xi)$ and is called log likelihood in statistics. Although there are some models in which the above integral diverges, we assume that g_{ij} is finite for all i, j and that $g_{ij} : \Xi \rightarrow \mathbb{R}$ is C^∞ . Note that one can write g_{ij} as:

$$g_{ij}(\xi) = -E_\xi \left[\partial_i \partial_j l_\xi \right]. \tag{4.2}$$

Another important representation is

$$g_{ij}(\xi) = 4 \int \sqrt{p(x; \xi)} \sqrt{p(x; \xi)} dx. \tag{4.3}$$

In finite case, it becomes

$$\Sigma_{k=1}^n \frac{1}{p_k} \frac{\partial p_k}{\partial \xi^i} \frac{\partial p_k}{\partial \xi^j}. \tag{4.4}$$

which is the Shashahani metric in mathematical biology, [13, 14]. This is simply the metric obtained on the simplex Σ^{n-1} when identifying it with the spherical sector S_+^{n-1} via the map $p = q^2$, $q \in S_+^{n-1}$. If the second derivatives vanish, i.e., if $p(x; \xi)$ is linear in ξ then

$$\Sigma_{k=1}^n \frac{1}{p_k} \frac{\partial p_k}{\partial \xi^i} \frac{\partial p_k}{\partial \xi^j} p_k = \frac{\partial^2}{\partial \xi^i \partial \xi^j} \Sigma_{k=1}^n p_k \log p_k$$

where $\Sigma_{k=1}^n p_k \log p_k$ is the entropy. As will be discussed later, negative of the entropy is a potential for the metric. The Fisher metric then induces a metric on any smooth family of probability measures on Ξ . Families of the form

$$p(x; \theta) = \exp(\gamma(x) + \sum_{i=1}^n f_i(x) \theta^i - \varphi(\theta))$$

where $\theta = (\theta^1, \dots, \theta^n)$ is an n -dimensional parameter and $\gamma(x)$ and $f_1(x), \dots, f_n(x)$ are functions on Ω are called exponential families. Of course the family is defined only for those θ for which $\int \exp(\gamma(x) + \sum f_i(x) \theta^i) dx < \infty$.

Fisher Metric Calculations For Some Distributions

Example 1 The normal distribution

The normal distribution $\frac{1}{\sqrt{2\pi\sigma}} \exp(-\frac{(x-\mu)^2}{2\sigma^2})$ on \mathbb{R} with parameters μ and σ can easily be written in this form by putting,

$$\gamma(x) = 0, \quad f_1(x) = x, \quad f_2(x) = x^2, \quad \theta^1 = \frac{\mu}{\sigma^2}, \quad \theta^2 = -\frac{1}{2\sigma^2}$$

$$\varphi(\theta) = \frac{\mu^2}{2\sigma^2} + \log \sqrt{2\pi\sigma} = -\frac{(\theta^1)^2}{4\theta^2} + \frac{1}{2} \log(-\frac{\pi}{\theta^2}).$$

For an exponential family, we have

$$\frac{\partial}{\partial \theta^i} \log p(x; \theta) = f_i(x) - \frac{\partial}{\partial \theta^i} \varphi(\theta)$$

$$\frac{\partial^2}{\partial \theta^i \partial \theta^j} \log p(x; \theta) = -\frac{\partial^2}{\partial \theta^i \partial \theta^j} \varphi(\theta)$$

This expression no longer depends on x , but only on the parameter θ . Therefore, the Fisher metric on such a family is given by

$$g_{ij}(p) = -E_p \left(\frac{\partial^2}{\partial \theta^i \partial \theta^j} \log p(x; \theta) \right) =$$

$$\int \frac{\partial^2}{\partial \theta^i \partial \theta^j} p(x; \theta) dx = \frac{\partial^2}{\partial \theta^i \partial \theta^j} \varphi(\theta)$$

For the normal distribution, we compute the metric in terms of θ^1 and θ^2 , using $\frac{\partial^2}{\partial \theta^i \partial \theta^j} \varphi(\theta)$ and transform the result to the variables μ and σ to obtain

$$g \left(\frac{\partial}{\partial \mu}, \frac{\partial}{\partial \mu} \right) = \frac{1}{\sigma^2} g \left(\frac{\partial}{\partial \mu}, \frac{\partial}{\partial \sigma} \right) = 0$$

$$g \left(\frac{\partial}{\partial \sigma}, \frac{\partial}{\partial \sigma} \right) = \frac{2}{\sigma^2}.$$

As the Fisher metric invariant under diffeomorphism of $\Omega = \mathbb{R}$, and since $x \rightarrow x - \mu$ is such a diffeomorphism, it suffices to perform the computation at $\mu = 0$. The metric computed there, however, up to a simple scaling is the hyperbolic metric of the half plane

$$H := \{(\mu, \sigma); \mu \in \mathbb{R}, \sigma > 0\}.$$

Therefore, the Fisher metric on the family of normal distributions is the hyperbolic metric. To summarize, the Fisher metric is constructed as the natural Riemannian metric on a projective space over a linear space. In the finite case, this projective space is simply a spherical sector. In particular, this metric is the standard metric on the sphere, and it therefore has sectional curvature $\kappa = 1$. This fact is valid for the general case, as well. As a consequence, the Fisher metric is not Euclidean.

These type of calculations can be carried out faster and with less pain without a coordinate change by using the properties of the expected value function. The expected value function for the discrete and continuous models are defined as follows:

- $E[x] = \sum_{x \in X} x f(x)$, discrete model.
- $E[x] = \int_{-\infty}^{\infty} x f(x) dx$, continuous model, where $f(x)$ represents the related probability density function.

Let X, X_1, X_2, \dots, X_n be real valued random variables with a common mean μ and a_1, a_2, \dots, a_n, c be arbitrary constants. In this case, some useful properties of the expected value function is listed below:

1. $E[c] = c$,
2. $E[\sum_{i=1}^n a_i X_i] = \sum_{i=1}^n a_i E[X_i]$, Linearity.
3. $E[X_i] = \mu$ for all $i = 1, \dots, n$ and $Y = \sum_{i=1}^n X_i$ then $E[Y] = n\mu$.
4. $E[X_i X_j] = E[X_i] E[X_j]$ if X_i and X_j
5. $E[X - \mu] = E[X] - \mu = \mu - \mu = 0$ since $E[X] = \mu$.

Moreover, the n^{th} moment $E(X^n)$ and n^{th} central moment $E[(X - \mu)^n]$ provides simplicity to the calculations. Since $E[x - \mu] = 0$ and the 3rd central moment $E[(x - \mu)^3] = 0$

$$g_{11}(\xi) - E_{\xi}[\partial_1 \partial_1 I_{\xi}] = \int \frac{1}{\sigma^2} \frac{1}{\sqrt{2\pi\sigma}} \exp\left(-\frac{1}{2} \frac{(x - \mu)^2}{\sigma^2}\right) dx$$

let $\frac{x - \mu}{\sigma} = t$ and use the Gaussian integral $\int_{-\infty}^{\infty} \exp(-x^2) dx = \sqrt{\pi}$ to get $g_{11}(\xi) = \frac{1}{\sigma^2}$.

Similarly,

$$g_{12}(\xi) = E[\partial_1 I_{\xi} \partial_2 I_{\xi}] = E\left[-\frac{(x - \mu)}{\sigma^3} + \frac{(x - \mu)^3}{\sigma^5}\right] =$$

$$-\frac{1}{\sigma^3} E[(x - \mu)] + \frac{1}{\sigma^5} E[(x - \mu)^3] = 0.$$

As a Riemannian metric Fisher information metric is symmetric hence $g_{21}(\xi) = 0$.

One may compute $g_{22}(\xi)$ from the definition of variance $E[(x - \mu)^2] = \sigma^2$

$$g_{22}(\xi) = E[\partial_2 I_{\xi} \partial_2 I_{\xi}] = -E[\partial_2^2 I_{\xi}]$$

$$= -E\left[\frac{1}{\sigma^2} - \frac{3(x - \mu)^2}{\sigma^4}\right] = \frac{3}{\sigma^4} E[(x - \mu)^2] - \frac{1}{\sigma^2} =$$

$$\frac{3}{\sigma^2} - \frac{1}{\sigma^2} = \frac{2}{\sigma^2}$$

Example 2 Multivariate normal distribution

In the following sequel the sample space will be \mathbb{R}^n in its standard vector coordinates $\{x^i\}_{1 \leq i \leq n}$. Let $\mu \in \mathbb{R}$ be a mean vector and $\Sigma = [\sigma_{ij}]$ be an $n \times n$ symmetric, positive definite covariance matrix. Hence, the multivariate Gaussian distribution in mean and covariance parameters can be written as

$$p(x; \mu; \Sigma) = (2\pi)^{-n/2} \exp\left(-\frac{1}{2} (x - \mu)^T \Sigma^{-1} (x - \mu)\right)$$

For the multivariate Gaussian distribution, compo-

nents of the Fisher information matrix is as follows:

$$I_{(\mu, \Sigma)} = (\partial_i \mu)^T \Sigma^{-1} (\partial_j \mu) + \frac{1}{2} \text{Tr}(\Sigma^{-1} (\partial_i \Sigma) \Sigma^{-1} (\partial_j \Sigma))$$

Since the parameter space of multivariate Gaussian Distribution is $n + \frac{n(n+1)}{2}$ dimensional with the Fisher metric it becomes a $n + \frac{n(n+1)}{2}$ dimensional Riemannian manifold. On the other hand, we can express the same distribution in its natural or in other words exponential parameters. In this case the probability density function and the Fisher metric can be expressed in terms of a potential function ϕ . One can rewrite the distribution in exponential or in other words natural coordinates defining

$$\theta = \Sigma^{-1} \mu$$

$$\Theta = -\frac{1}{2} \Sigma^{-1}$$

Representing \mathcal{G} as $\mathcal{G} = (\theta; \Theta)$ we may write our probability density function in \mathcal{G} coordinates as

$$p(x; \mathcal{G}) = \exp(\theta^T x + x^T \Theta x - \phi(\mathcal{G}))$$

$$\text{where } \phi(\mathcal{G}) = \frac{1}{2} \left(n \log 2\pi - \frac{1}{2} \theta^T \Theta^{-1} \theta - \log(-2)^n |\Theta| \right)$$

The detailed computations for the components of the Fisher metric in different coordinates can be found in [28] and [20].

Example 3 Poisson distribution

$$\mathcal{X} = \{0, 1, 2, \dots\}, n = 1, \Xi = \{\xi \mid \xi > 0\}$$

$$p(x, \xi) = \exp(-\xi) \frac{\xi^x}{x!}$$

Since $n = 1$ coefficients of the Fisher metric is represented by 1x1 matrix.

$$\log p(x; \xi) = -\xi + x \log(\xi) - \log(x!)$$

$$\frac{\partial \log p(x; \xi)}{\partial \xi} = -1 + \frac{x}{\xi}$$

$$G(\xi) = E\left[\left(\frac{\partial}{\partial \xi} \log p(x; \xi)\right)^2\right] = -E\left[\frac{\partial^2}{\partial \xi^2} \log p(x; \xi)\right] = -E_\xi\left[\frac{-x}{\xi^2}\right] = \frac{1}{\xi^2} E[x]$$

where

$$E[x] = \sum_{x=0}^{\infty} x \exp(-\xi) \frac{\xi^x}{x!} = \sum_{x=1}^{\infty} x \exp(-\xi) \frac{\xi^x}{x!} = \sum_{x=1}^{\infty} \frac{\xi^{x-1}}{(x-1)!} \xi \exp(-\xi)$$

Since $\sum_{x=1}^{\infty} \frac{\xi^{x-1}}{(x-1)!} = \exp(\xi)$, $E[x] = \xi$. Therefore, the coef-

ficients of the Fisher metric is $G(\xi) = \frac{1}{\xi}$.

Example 4 $P(\mathcal{X})$ for finite \mathcal{X}

$$\mathcal{X} = \{x_0, x_1, \dots, x_n\}$$

$$\Xi = \{[\xi^1, \dots, \xi^n] \mid \xi^i > 0, \forall i, \sum_{i=1}^n \xi^i < 1\}$$

Then,

$$p(x_i; \xi) = \begin{cases} \xi^i & 1 \leq i \leq n \\ 1 - \sum_{i=1}^n \xi^i & i = 0 \end{cases}$$

By using similar computations, one can show that the coefficients of the Fisher metric for finite discrete distribution is the $n \times n$ matrix

$$\begin{bmatrix} \frac{1}{1 - \sum_{i=1}^n \xi^i} + \frac{1}{\xi^1} & \cdot & \cdot & \frac{1}{1 - \sum_{i=1}^n \xi^i} \\ \cdot & \frac{1}{1 - \sum_{i=1}^n \xi^i} + \frac{1}{\xi^2} & \cdot & \cdot \\ \cdot & \cdot & \cdot & \cdot \\ \frac{1}{1 - \sum_{i=1}^n \xi^i} & \cdot & \cdot & \frac{1}{1 - \sum_{i=1}^n \xi^i} + \frac{1}{\xi^n} \end{bmatrix}$$

Connections

$p(x; \xi)$ be a n -dimensional smooth family of probability density functions depending on the parameter ξ . The components of the Fisher metric is of the following form:

$$g_{ij}(\xi) = E_\xi\left[\left(\frac{\partial}{\partial \xi^i} \log p(\cdot; \xi)\right) \left(\frac{\partial}{\partial \xi^j} \log p(\cdot; \xi)\right)\right] \quad (4.5)$$

$$= \int \frac{\partial}{\partial \xi^i} \log p(x; \xi) \frac{\partial}{\partial \xi^j} \log p(x; \xi) p(x; \xi) \quad (4.6)$$

The Levi-Civita connection of the Fisher metric can be computed from the following formula:

$$\Gamma_{ij}^k = \frac{1}{2} g^{kl} (g_{il,j} + g_{jl,i} - g_{ij,l}) \quad (4.7)$$

and note that $\Gamma_{ijk} = g_{il} \Gamma_{jk}^l$ where

$$\Gamma_{ijk}^{(0)} = E_\xi\left(\frac{\partial^2}{\partial \xi^i \partial \xi^j} \log p + \frac{1}{2} \frac{\partial}{\partial \xi^k} \log p + \frac{1}{2} \frac{\partial}{\partial \xi^i} \log p \frac{\partial}{\partial \xi^j} \log p \frac{\partial}{\partial \xi^k} \log p\right) \quad (4.8)$$

yields the Levi-Civita connection $\nabla^{(0)}$ for the Fisher metric. More generally, a family of connections depending on a parameter $\alpha \in \mathbb{R}$ can be defined as follows

$$\Gamma_{ijk}^{(\alpha)} = E_\xi\left[\left(\frac{\partial^2}{\partial \xi^i \partial \xi^j} \log p + \frac{1-\alpha}{2} \frac{\partial}{\partial \xi^k} \log p + \frac{1}{2} \frac{\partial}{\partial \xi^i} \log p \frac{\partial}{\partial \xi^j} \log p \frac{\partial}{\partial \xi^k} \log p\right)\right]$$

$$\Gamma_{ijk}^{(\alpha)} = \Gamma_{ijk}^{(0)} - \frac{\alpha}{2} E_p \left[\frac{\partial}{\partial \xi^i} \log p \frac{\partial}{\partial \xi^j} \log p \frac{\partial}{\partial \xi^k} \log p \right] \quad (4.9)$$

In particular, since this expression is symmetric in indices i and j , all the connections $\nabla^{(\alpha)}$ are torsion-free and

$$\Gamma_{ijk}^{(\alpha)} + \Gamma_{ijk}^{(-\alpha)} = \Gamma_{ijk}^{(0)}$$

Therefore, the connections $\nabla^{(\alpha)}$ and $\nabla^{(-\alpha)}$ are dual to each other.

Example 5 The exponential family

$$p(x; \theta) = \exp(\gamma(x) + f_i(x)\theta^i - \varphi(\theta))$$

$\Gamma_{ijk}^{(1)} = 0$ is obtained by substituting $\alpha = 1$ in equation 4.9. Thus, θ yields an affine coordinate system for the connection $\nabla^{(1)}$. This flat affine connection is called the exponential connection and abbreviated as e-connection.

Example 6 The mixture family

$$p(x; \eta) = c(x) + \sum_{i=1}^d g^i(x)\eta_i$$

is an affine family of probability density functions. A simple computation yields $\Gamma_{ijk}^{(-1)} = 0$. In other words, η is an affine coordinate system for the connection $\nabla^{(-1)}$ so called the mixture or m-connection. One can find local potential functions of the Fisher metric in x and n -coordinates as in section 3.1. It is important to note that $\nabla^{(-1)}$ is not flat in n -coordinates. Therefore, two flat affine connections $\nabla^{(1)}$ and $\nabla^{(-1)}$ that are dual to each other with respect to the Fisher metric is obtained. To summarize, the space of probability measures can be viewed as a linear space in two different manners:

On one hand, as in the finite case, it can be represented as a simplex in a vector space. Thus, any probability measure can be represented as a convex linear combination of certain extremal measures which is called the mixture representation.

On the other hand, space of probability measures can be represented as the exponential image of a linear tangent space which gives the so-called the exponential representation.

As it is discussed throughout the sections 3 and 4, these two structures are dual to each other, in the sense that each of them is the underlying affine structure for some connection, and the two corresponding connections are dual with respect to the Fisher metric. Of course, neither of these connections can be the Levi-Civita connection of the Fisher metric as the latter does not have vanishing curvature, [14]. Note that these results are valid locally for the global beha-

viour one may refer to [5].

CURVATURE COMPUTATIONS AND SECOND ORDER ESTIMATION

As it is mentioned in sections 3 and 4, dually flat structures are defined through the affine structure by mutually dual flat affine connections, namely the exponential and the mixture connections. Since these connections are not Levi-Civita connection of the Fisher metric unless the underlying statistical manifold or distribution is flat Riemannian. The dually flat structure allows to define dual parallel transports, dual potential functions and geodesics by means of which alternative Taylor approximations of a function can be defined. On the other hand, probability distributions can be considered as Riemannian manifolds equipped with the Fisher information metric. Thus, curvatures of the induced geometry may be computed and used for the purposes of inference. Both perspective has advantages and disadvantages.

On an Kahler affine manifold, the differential D_γ of the difference tensor $\nabla - D$, where ∇ is the Levi-Civita connection of the Kahler affine metric, is called the affine(Hessian) curvature tensor and denoted by Q . Unlike the Riemannian curvature tensor on a Kahler affine manifold, affine curvature reflects the affine structure since its defined through the flat affine connection. Affine curvature tensor is of type (1, 3) and in local affine coordinates its components are of the form

$$Q_{jk}^i = \frac{\partial \gamma_{jl}^i}{\partial x^k}, \quad (5.1)$$

[26, 27]. One can easily observe that for the Kahler affine metric

$$g_{ij} = \frac{\partial^2 \varphi}{\partial x^i \partial x^j}$$

$$Q_{ijkl} = \frac{1}{2} \frac{\partial^4 \varphi}{\partial x^i \partial x^j \partial x^k \partial x^l} - \frac{1}{2} g^{rs} \frac{\partial^3 \varphi}{\partial x^i \partial x^k \partial x^r} \frac{\partial^3 \varphi}{\partial x^j \partial x^l \partial x^s} \quad (5.2)$$

and its relation between Riemannian curvature tensor is given by

$$2R_{ijkl} = Q_{ijkl} - Q_{jikl} \quad (5.3)$$

where the components of the Riemannian curvature tensor is given by

$$R_{ijkl} = \frac{1}{4} g^{mn} \left(\frac{\partial^3 \varphi}{\partial x^m \partial x^l \partial x^i} \frac{\partial^3 \varphi}{\partial x^n \partial x^k \partial x^j} - \frac{\partial^3 \varphi}{\partial x^m \partial x^n \partial x^i} \frac{\partial^3 \varphi}{\partial x^j \partial x^k \partial x^l} \right) \quad (5.4)$$

It is remarkable that the Riemannian curvature of a Kahler affine metric depends only on the derivatives of the potential function to order at most three, whereas one wo-

uld expect fourth derivatives of it to appear. Duistermaat gives some explanation for this phenomenon [9]. This property of the Fisher information metric allows us to avoid prolix Riemannian curvature computations in case of multivariate Gaussian distributions. On contrary to Riemannian curvature, affine curvature does not have this property which make its computation lengthy. Similarly, one may define affine scalar curvature in local coordinates taking metric trace of the affine Ricci curvature tensor $Q_{ij} = Q_{ikj}^k$ as follows:

$$Q_{scal} = g^{ij}Q_{ij} \quad (5.5)$$

The concept of sectional curvature can also be carried to Kahler affine manifolds, [8, 26]. In this case, constant affine (Hessian) sectional Kahler affine manifolds can be constructed. There is a relationship between constant affine sectional Kahler affine manifolds and Riemannian manifolds of constant sectional curvature. If a Kahlerian manifold (M, g) is of constant affine sectional curvature c then (M, g) as a Riemannian manifold has constant sectional curvature $-\frac{c}{4}$.

Example 7 Curvature computations for normal (univariate Gaussian) distribution

Consider the normal distribution $p(x; \mu, \sigma) = \frac{1}{\sqrt{2\pi}\sigma} \exp\{-\frac{(x-\mu)^2}{2\sigma^2}\}$ with mean μ and variance σ . In this case, Ricci tensor is of the form

$$R_{ij} = \begin{bmatrix} -\frac{1}{2\sigma^2} & 0 \\ 0 & -\frac{1}{\sigma^2} \end{bmatrix} \quad (5.6)$$

Being the metric trace of Ricci curvature scalar curvature of the normal distribution is equal to -1. On the other hand, normal distribution in its natural coordinates is an exponential family with the coordinates $\theta^1 = \frac{1}{2\sigma^2}$ and $\theta^2 = \frac{\mu}{\sigma^2}$ where $\Theta = [\theta^1, \theta^2]$. For $\theta \in \Theta = \{[\theta^1, \theta^2] | \theta^1 \in \mathbb{R}^+, \theta^2 \in \mathbb{R}\}$ normal distribution in its natural coordinates is of the form

$$p(x; \theta^1, \theta^2) = \exp(\gamma_1(x)\theta^1 + \gamma_2(x)\theta^2 - \varphi(\Theta))$$

where $\gamma_1(x) = -x^2$, $\gamma_2(x) = x$, $\varphi(\theta) = \frac{(\theta^2)^2}{4\theta^1} + \frac{1}{2} \log\left(\frac{\pi}{\theta^1}\right)$.

Then, the components of the Fisher metric and that of its inverse are as follows:

$$[g_{ij}(\theta)] = \begin{bmatrix} \frac{(\theta^2)^2}{2(\theta^1)^3} + \frac{1}{2(\theta^1)^2} & \frac{-\theta^2}{2(\theta^1)^2} \\ \frac{-\theta^2}{2(\theta^1)^2} & \frac{1}{2\theta^1} \end{bmatrix}, \quad (5.7)$$

$$[g^{-1}(\theta)] = \begin{bmatrix} 2(\theta^1)^2 & 2\theta^1\theta^2 \\ 2\theta^1\theta^2 & 2\theta^1 + 2(\theta^2)^2 \end{bmatrix}. \quad (5.8)$$

Therefore,

$$R_{ij}(\theta) = \begin{bmatrix} -\frac{\theta^1 + (\theta^2)^2}{4(\theta^1)^3} & \frac{\theta^1 + \theta^1\theta^2 + (\theta^2)^2}{4(\theta^1)^3} \\ \frac{\theta^1 + \theta^1\theta^2 + (\theta^2)^2}{4(\theta^1)^3} & \frac{1}{4\theta^1} \end{bmatrix} \quad (5.9)$$

is the Ricci tensor of the normal distribution in its natural coordinates and hence the scalar curvature is

$$R = \frac{\theta^1\theta^2 + \theta^1(\theta^2)^2 + (\theta^2)^3}{(\theta^1)^2} \quad (5.10)$$

The Riemannian curvature can be extended to α -connections. In section 3.1, α -connections are defined by 3.1 as

$$\Gamma_{ijk}^{(\alpha)} = \Gamma_{ijk}^{(0)} - \frac{\alpha}{2} \partial_i \partial_j \partial_k \varphi.$$

Then, α -curvature tensor can be calculated from

$$R_{jkm}^{(\alpha)i} = \Gamma_{jm,k}^{(\alpha)i} - \Gamma_{jk,m}^{(\alpha)i} + \Gamma_{nk}^{(\alpha)i} - \Gamma_{jm}^{(\alpha)n} - \Gamma_{nm}^{(\alpha)i} - \Gamma_{jk}^{(\alpha)n}. \quad (5.11)$$

Note that original Riemannian curvature tensor is obtained for $\alpha=0$. Dual affine connections corresponds to the cases $\alpha=1$ and $\alpha=-1$, respectively.

For the normal distribution, only independent non-zero component of the α -curvature tensor is given by

$$R_{1212}^{(\alpha)} = \frac{1-\alpha^2}{\sigma^4} \quad (5.12)$$

Furthermore, only non-zero component of the α -Ricci tensor is

$$Ric_{11}^{(\alpha)} = \frac{\alpha^2 - 1}{2\sigma^2} \quad (5.13)$$

Note that more computations on different families of probability distributions one may refer to [1] and [24].

ACKNOWLEDGEMENTS

The author expresses her deep gratitude to TÜBİTAK (Turkish Scientific and Technological Research Council) since this work is supported under the project number 113F296 entitled as "Harmonic maps, affine manifolds and their applications to information geometry". The author is also grateful to Hitit University for the partial support by Hitit BAP: FEF01.13.006, "Afin Manifoldların Geometrisi".

References

1. K. Arwini, C. T. J. Dodson, *Information Geometry: Near Rank-domness and Near Independence*, Lecture Notes in Mathematics, 1953, Springer, 2008.
2. S. Amari, *Differential Geometrical Methods in Statistics*, Springer Lecture Notes in Statistics 28, Springer-Verlag, Berlin, 1985.
3. S. Amari, *Information Geometry and Its Applications*, Applied Mathematical Sciences, 194, Springer, 2016.
4. S. Amari, H. Nagaoka, *Methods of information geometry*, Transl.Math. Monogr. 191, AMS & Oxford Univ. Press, 2000.
5. N.Ay, W.Tuschmann, *Dually flat manifolds and global information geometry*, Open Sys.& Information Dyn.9, 195-200, 2002.
6. S.Y.Cheng, S.T.Yau, *The real Monge-Ampere equation and affine flat structures*, in: S.S.Chern, W.T.Wu (eds.), *Differential geometry and differential equations*, Proc. Beijing Symp.1980, pp.339- 370, 1982.
7. N.N.Chentsov, *Statistical decision rules and optimal inferences*, AMS, 1982 (Translation of the Russian version, Nauka, Moscow, 1972).
8. O. Calin, C. Udriste, *Geometric Modelling in Probability and Statistics*, Springer,2014.
9. J. Duistermaat, *Hessian Riemannian Structures*, Assian Jour. Math, 5, 79-91, 2001.
10. A. P. Dawid, *Invited discussion of Defining the statistical problem (with applications to second-order efficiency*, Ann. Statist., 3, 1231-1234, 1975.
11. B. Efron, *Defining the Curvature of a Statistical Problem (with applications to second order efficiency)*, Ann. Statist., 3, 1189-1242, 1975.
12. H. Jeffreys, *An invariant form for the prior probability in estimation problems*, Proceedings of Royal Society of London, Series A, Mathematical and Physical Sciences, 186, 453-461, 1946.
13. J. Hofbauer, K. Sigmund, *Evolutionary games and population dynamics*, Cambridge Univ Press, 1998.
14. J.Jost, *Information geometry*, Lecture Notes.
15. J. Jost, F. M. Şimsir, *Affine harmonic maps*, Analysis, 29, 185-197, 2009.
16. J. Jost, F. M. Şimsir, *Nondivergence harmonic maps, Harmonic maps and differential geometry*, Contemp. Math., 542, 231-238, 2011.
17. T. Kurose, *Dual connections and affine geometry*, Mathematische Zeitschrift, 203, pp. 115-121, 1990.
18. R. E. Kass, P.W. Vos, *Geometrical Foundations of Asymptotic Inference*, Wiley Series in Probability and Statistics, New York, 1997.
19. S.L. Lauritzen, *Statistical manifolds*, in: *Differential Geometry in Statistical Inference*, Institute of Mathematical Statistics Lecture Notes, 10, pp. 163-218, Berkeley 1987.
20. L. Malago, G. Pistone, *Information geometry of the Gaussian Distribution in view of stochastic optimization*, in: FOGA'15 Proceedings of the 2015 ACM Conference on Foundations of Genetic Algorithms XIII, 150-162, Wales 2015.
21. M. K. Murray, J. W. Rice, *Differential Geometry and Statistics*, Chapman Hall,1993.
22. M. Noguchi, *Geometry of Statistical Manifolds, Differential Geometry and its Applications 2*, pp. 197-222, 1992.
23. C. R. Rao, *Information and accuracy attainable in the estimation of statistical parameters*, Bulletin of the Calcutta Mathematical Society , 37, 81-91, 1945.
24. Y. Sato, K. Sugawa and M. Kawaguchi, *The geometrical structure of parameter space of the two dimensional normal distribution*, Division of Information Engineering, Hokkaido Univ., Sapporo, Japan, 1977.
25. C. E. Shannon, *A mathematical theory of communication*, Bell. Syst. Tech. J., 27, 379-423 and 623-656, 1948.
26. H. Shima, *The Geometry of Hessian Structures*, World Scientific, 2007.
27. H. Shima, *Hessian manifolds of constant Hessian sectional curvature*, J. Math. Soc. Japan, 47(4), 735-753, 1994.
28. L. T. Skovgaard, *Riemannian geometry of the multivariate normal model*, Scandinavian Journal of Statistics, 11(4), pp. 211-223, 1984.

Synthesis, Structural Characterization And Theoretical Investigations of New Azo-Azomethine Compounds Bearing Acryloyl Moiety

Sevil Özkınalı¹  M. Serdar Çavuş², Büşra Sakin¹

¹ Hitit University, Department of Chemistry, Çorum, Turkey

² Kastamonu University, Biomedical Engineering Department, Kastamonu, Turkey

ABSTRACT

In this study six new azo-azomethine dyes containing acryloyl group, 4-[[[4-(4'-methyl phenyl azo) phenyl] imino] methyl] phenyl-2-propenoat, 4-[[[4-(4'-hydroxy phenyl-azo) phenyl] imino] methyl] phenyl-2-propenoat, 4-[[[4-(phenyl azo) phenyl] imino] methyl]- phenyl-2-propenoat, 4-[[[4-(4'-chloro phenyl azo) phenyl] imino] methyl] phenyl-2-propenoat, 4-[[[4-(4'-nitro phenyl azo) phenyl] imino] methyl] phenyl-2-propenoat were synthesized. The acryloyl derivatives of the azo-azomethine dyes were prepared with metallic sodium and acryloyl chloride in 1:1 Molar ratio and characterized using elemental analysis, IR, UV-Vis, ¹H-NMR and ¹³C-NMR spectroscopy. The molecular geometry was also optimized using density functional theory (DFT/B3LYP) method with the 6-311G(2d,2p) and cc-pvtz basis sets in ground state. From the optimized geometry of the compounds, vibrational frequencies, UV-Vis, molecular electrostatic potential distribution and frontier molecular orbitals were performed using same method and basis sets, and the results were compared with the experimental data.

Keywords:

Azo-Azomethine, Schiff bases, Imine group, DFT, Acryloyl chloride

Article History:

Received: 2017/11/15

Accepted: 2017/11/27

Online: 2017/12/22

Correspondence to: Sevil Özkınalı

Hitit University, Department of Chemistry,
Çorum, Turkey

Tel: +90 (364) 226-7000 / 1636

Fax: +90 (364) 227-7005

E-Mail: sevilozkinali@hitit.edu.tr

INTRODUCTION

Azo dyes which are characterized by the presence of the azo chromophore [-N=N-] have attracted much attention not only for their easy preparation and lower cost but also for their wide application in industry as textile dyeing [1-3], coloring of plastic and polymers [1,4], colorimetric indicators [5-6], high-technology applications [3,7], cosmetics [8] and photostorage units [4,9]. In addition azo dyes and its derivatives exhibit photoactive properties with potential application as lasers [9], organic solar cells [10], organic NLO materials [6] and liquid crystals [9].

Azomethines, generally known as Schiff bases, are one of the most widely used organic compounds in various areas including photoluminescence materials [11], organic light emitting diodes [11], polymer stabilisers [12] and dyes and pigments [12]. Schiff bases also show a variety of the biological activities containing anti-fungal [12, 13], anti-bacterial [14], anti-malarial [14], anti-proliferative [12,14] and anti-viral [14] properties.

With the advancement in technology, one of the most important scientific problems is how to correlate between chemical and physical properties of the compound [2,15]. The density functional theory (DFT) method is widely used for structural determination of organic compounds, determining the mechanisms of chemical reactions, calculation of the ground state geometries and prediction of spectroscopic data such as UV-Vis, IR and NMR peaks [2,16].

In this study we have synthesized new azo-azomethine dyes containing acryloyl groups and the compounds were characterized by Uv-Vis, IR and NMR spectroscopy. Also in this research we report the results of DFT calculations to investigate UV-Vis absorption spectrum and FT-IR regions as well as HOMO-LUMO orbital energies, electrostatic potential (ESP) maps, chemical hardness and electronegativity of the compounds. Theoretical UV-Vis calculations were carried out in EtOH (polar protic), CH₂Cl₂ (apolar aprotic) and DMF (polar aprotic) phases in accordance with the

experiments and the solvent effect was also investigated.

Experimental Process

All reagents were analytical grade and purchased from commercial suppliers (Merck and Aldrich). All melting points were determined using Melting point apparatus (Stuart Melting Point 30) without any corrections. Ultra-Visible (UV-Vis) spectra were taken in CH_2Cl_2 (apolar aprotic), EtOH (polar protic) and DMF (polar aprotic) in the range of 600-190 nm using a quartz glass cell with a path length of 10 mm at room temperature. Infrared spectra's were obtained using ATR in the range of 4000-650 cm^{-1} Class 1 Laser product FTIR (Thermo Scientific, US) FT-IR spectrophotometer. NMR spectrums were recorded on a Bruker ^1H -NMR 400 MHz/ ^{13}C -NMR 100 MHz spectrometer in a d_6 -DMSO solvent with a internal standart TMS.

Theoretical Processes

Kohn-Sham density functional theory (DFT) [17-18] was used in the quantum-chemical calculations. Geometric restrictions were not placed on the optimization processes. Molecular structures of the compounds were optimized by using Becke3-Lee-Yang-Parr hybrid functional (B3LYP) with 6-311++g(2d,2p) and cc-pvtz basis set. Furthermore, mentioned methods were used to obtain ground state energies, molecular conformations, UV-Vis and IR spectra of the compounds. Time-dependent DFT (TDDFT) were employed to calculate vertical excitation energies. The Self-Consistent Reaction Field (SCRF) method and the Conductor-Polarizable Continuum Model (CPCM) were used for the geometry optimizations of compounds in different solvent environments such as EtOH, CH_2Cl_2 and DMF phases. IR calculations were also carried out in gas phase.

The highest occupied molecular orbital (HOMO) and lowest unoccupied molecular orbital (LUMO) energies were calculated with the titled methods and basis sets. Furthermore, molecular electrostatic potential (MEP) surfaces were also obtained. FMO energy eigenvalues were used to calculate the chemical hardness (η) and electronegativity (χ) of the compounds. All calculations were performed using the GAUSSIAN 09 software package program [19].

Initial conformations to be used for optimization calculations of the compounds were obtained by dihedral-scanning of unsubstituted compound 4 with a step size of 18° for a total of 400 steps (Figure 1), by using M06/3-21g method in order to predict the minimum energy conformations of the compounds.

6-311++g(2d,2p) and cc-pvtz basis sets used in the calculations gave very consistent results. As seen from Table 1, the functional groups CH_3 , OH, Cl and NO_2 have a great influence in determining the minimum molecular energy of the optimized compounds. The molecular energies of the compounds decreased as the electronegativity of the substituents increases. The minimum molecular energy of compound 4, which does not contain any substituent, was calculated to be around -1163 au, and of NO_2 substituted compound 6 was -1368 au with the lowest molecular energy. The dipole moments of the compounds 5 and 6 bearing higher electronegative substituent were calculated to be significantly higher than those of the other compounds because the higher electronegative substitue groups, attracting electron density on themselves, made the molecule more polarized. Substituent NO_2 greatly affected the HOMO and LUMO energies (Table 1 and Figure 2), and also increased the electronegativity of the compound while decreased the chemical hardness. The chemical hardness

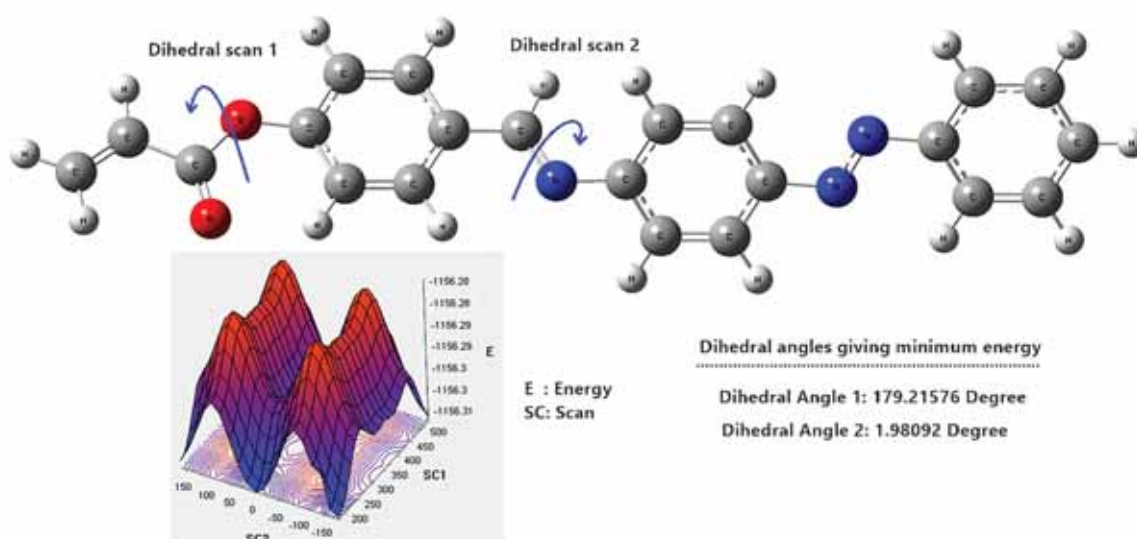
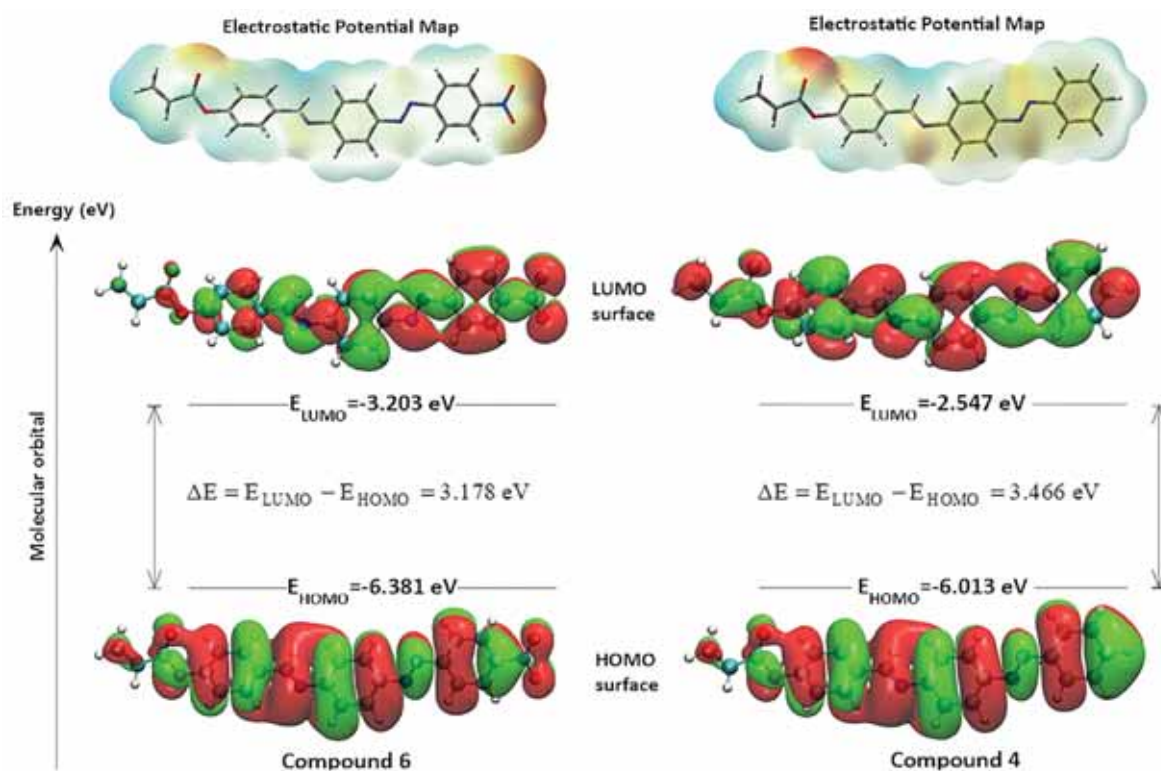


Figure 1. Dihedral scanning of unsubstituted compound 4.

Table 1. Theoretical calculations: Electronic and chemical parameters

Comp.	Method	E (au)	(eV)	(eV)	(eV)	(eV)	(eV)	m (Debye)
2	6-311++g(2d,2p)	-1202.895	-5.968	-2.544	3.424	1.712	4.256	2.762
3		-1238.817	-5.857	-2.523	3.333	1.667	4.190	2.474
4		-1163.565	-6.074	-2.624	3.449	1.725	4.349	2.893
5		-1623.190	-6.138	-2.755	3.383	1.691	4.447	4.958
6		-1368.135	-6.459	-3.330	3.129	1.565	4.895	9.926
2		cc-pvtz	-1202.959	-5.911	-2.470	3.441	1.721	4.190
3	-1238.882		-5.782	-2.435	3.346	1.673	4.109	2.3077
4	-1163.628		-6.013	-2.547	3.466	1.733	4.280	2.8431
5	-1623.259		-6.075	-2.675	3.399	1.700	4.375	4.9028
6	-1368.206		-6.381	-3.203	3.178	1.589	4.792	9.5686

E : Energy, χ : Chemical Hardness, Electronegativity, m : Dipole moment

**Figure 2.** HOMO-LUMO energy gap and ESP maps of compound 4 and 6.

of unsubstituted compound **4** was also calculated to be the highest (1.725 eV by 6-311++g(2d,2p) and 1.733 eV by cc-pvtz basis sets).

General procedure for the synthesis of azo-azomethine dyes

Azo-Azomethine compounds containing acryloyl group were synthesized by a two step procedure as shown in Figure 3. In the first step sodium salts of the azo-azomethine were synthesized by using metallic sodium in 1:1 molar ratio at room temperature for 24 h [9-11]. In the second step novel acryloyl derivatives of azo-azomethine compounds were synthesized using acryloyl

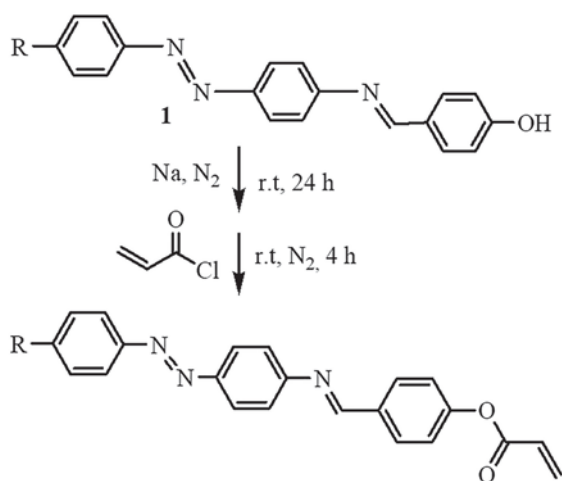
chloride under an inert atmosphere by our previous methods [20-24].

Synthesis of Azo-Azomethine Compounds, 1

Azo-azomethine derivatives (**1**) were synthesized by the coupling reaction with *E*-4-((phenylimino)methyl)phenol [25,26] and diazonium salts as described in the literature method [8,9,22,26].

Synthesized of 4-[[[4-[4'-methyl]phenylazo]phenyl]imino]methyl]phenyl-2-propenoate, 2

A solution of 4-[[[4-[(4-methylphenyl)azo]phenyl]imino]methyl]-Phenol (1.0 g; 3.04 mmol) and metallic sodium



R = -CH₃ (2); -OH (3); -H (4); -Cl (5); -NO₂ (6)

Figure 3. Synthetic route of azo-azomethine compounds bearing an acryloyl group.

(69 mg; 3.04 mmol) in dry THF (40 mL) was stirred at room temperature under N₂ atmosphere for 24 h. Then acryloyl chloride (0.245 mL; 3.04 mmol) was added to this solution at room temperature and stirred for 4 h under N₂ atmosphere. Dark red product was evaporated and purified with THF/water. Yield: %43 mp: Oily product IR (cm⁻¹): ν=3053 (C-H arom.), 2972, 2883 (aliph. C-H), 1749 (>C=O), 1671 (-C=C-), 1594 (-CH=N-), 1540, 1411 (-N=N-), 1249, 1045 (-C-O). ¹H-NMR (d₆-DMSO, ppm): δ= 1.23 (s, H1), 7.98 (m, H4), 7.95 (s, H6), 7.88 (m, H3), 7.78 (m, H7), 7.40 (m, H5), 7.05 (m, H2), 6.68 (m, H8), 6.33 (d, J=17.3 Hz, H11), 5.80 (d, J=10.9 Hz, H9), 5.72 (m, H10) ¹³C NMR (101 MHz, d₆-DMSO, ppm) δ 21.3 (C1), 141.7 (C2), 130.4 (C3), 123.9 (C4), 148.0 (C5), 150.5 (C6), 124.1 (C7), 122.8 (C8), 150.8 (C9), 162.8 (C10), 129.8 (C11), 129.06 (C12), 120.1 (C13), 162.8 (C14), 164.1 (C15), 129.4 (C16), 132.3 (C17). Elemental Analysis calc. (%) for C₂₃H₁₉N₃O₂: C 74.78, H 5.18, N 11.37; found: C 74.23, H 5.09, N 10.87

1.4 Synthesis of 4-[[[4-[4'-hydroxyphenyl-azo]phenyl]imino]methyl]phenyl-2-propenoat, 3

This compound was prepared with a method similar to that described in Section 1.3. Yield: %52 mp: oily product, IR (cm⁻¹): ν=3584-3180 (br, O-H), 3046 (C-H arom.), 2921, 2875 (Aliph. C-H), 1749 (>C=O), 1662 (-C=C-), 1572 (-CH=N-), 1513, 1442 (-N=N-), 1284, 1163 cm⁻¹ (-C-O). ¹H-NMR (d₆-DMSO, ppm): δ= 9.71 (s, H1), 8.13 (s, H6), 7.89 (s, H4), 7.89 (m, H3), 7.69 (m, H7), 7.69 (m, H5), 6.94 (m, H2), 6.94 (m, H8), 6.51 (m, H11), 5.97 (m, H9), 5.44 (m, H10) ¹³C NMR (101 MHz, d₆-DMSO, ppm) δ 163.1 (C2), 112.3 (C3), 128.3 (C4), 148.5 (C5), 149.0 (C6), 128.3 (C7), 116.3 (C8), 152.0 (C9), 164.4 (C10), 130.0 (C11), 132.3 (C12), 128.5 (C13), 160.4 (C14), 164.4 (C15), 129.1 (C16), 132.1 (C17). Elemental Analysis calc. (%) for C₂₂H₁₇N₃O₃: C 71.15, H 4.61, N 11.31; found: C 70.96, H 4.35, N 10.54

Synthesis of 4-[[[4-(phenylazo)phenyl]imino]methyl]-phenyl-2-propenoat, 4

This compound was prepared with a method similar to that described in Section 1.3. Yield: %56 mp: oily product, IR (cm⁻¹): ν=3134 (C-H arom.), 2924 cm⁻¹, 2850 (Aliph. C-H), 1740 (>C=O), 1668 (-C=C-), 1598 (-CH=N-), 1541, 1411 (-N=N-), 1248 (-C-O). ¹H-NMR (d₆-DMSO, ppm): δ= 7.92 (s, H6), 7.92 (s, H4), 7.92 (s, H3), 7.86 (d, J=7.87 Hz, H7), 7.59 (m, H1), 7.59 (m, H5), 7.59 (m, H2), 7.59 (m, H8), 6.48 (dd, J=6.50 Hz, H11), 6.35 (d, J=6.33 Hz, H9), 5.84 (d, J=5.83 Hz, H10) ¹³C NMR (101 MHz, d₆-DMSO, ppm) δ 131.6 (C2), 129.9 (C3), 122.8 (C4), 152.5 (C5), 142.6 (C6), 124.2 (C7), 119.7 (C8), 149.0 (C9), 163.9 (C10), 128.1 (C11), 132.1 (C12), 119.7 (C13), 163.9 (C14), 163.9 (C15), 127.5 (C16), 131.5 (C17). Elemental Analysis calc. (%) for C₂₂H₁₇N₃O₂: C 74.35, H 4.82, N 11.82; found: C 73.67, H 4.54, N 10.96

Synthesis of 4-[[[4-[4'-chlorophenylazo]phenyl]imino]methyl]phenyl-2-propenoat, 5

This compound was prepared with a method similar to that described in Section 1.3. Yield: %47 mp: oily product IR (cm⁻¹): ν= 3132 (C-H arom.), 2965, 2933 (Aliph. C-H), 1705 (>C=O), 1672 (-C=C-), 1594 (-CH=N-), 1537, 1407 (-N=N-), 1250, 1088 (-C-O), 830 (-C-Cl). ¹H-NMR (d₆-DMSO, ppm): δ= 7.95 (s, H6), 7.87 (m, H4), 7.87 (m, H3), 7.60 (m, H7), 7.60 (m, H5), 7.32 (m, H2), 7.32 (m, H8), 6.55 (m, H11), 6.32 (m, H9), 5.83 (m, H10). ¹³C NMR (101 MHz, d₆-DMSO, ppm) δ 138.4 (C2), 129.3 (C3), 124.5 (C4), 150.8 (C5), 142.8 (C6), 124.3 (C7), 119.6 (C8), 148.1 (C9), 162.7 (C10), 132.0 (C11), 129.9 (C12), 122.8 (C13), 152.4 (C14), 164.0 (C15), 128.1 (C16), 135.9 (C17). Elemental Analysis calc. (%) for C₂₂H₁₆ClN₃O₂: C 67.78, H 4.14, N 10.78; found: C 67.42, H 4.01, N 10.23

Synthesis of 4-[[[4-[4'-nitrophenylazo]phenyl]imino]methyl]phenyl-2-propenoat, 6

This compound was prepared with a method similar to that described in Section 1.3. Yield: %62 mp: oily product IR (cm⁻¹): ν=3071 (C-H arom.), 2968, 2921 (Aliph. C-H), 1702 (>C=O), 1595 (-C=C-), 1504 (-CH=N-), 1548, 1407 (-N=N-), 1173, 1016 (-C-O), 1504, 1323 (-NO₂). ¹H-NMR (d₆-DMSO, ppm): δ= 8.31 (s, H6), 8.22 (m, H2), 7.84 (m, H4), 7.84 (m, H3), 7.52 (m, H7), 7.48 (m, H5), 7.28 (m, H8), 6.71 (m, H11), 6.71 (m, H9), 6.60 (m, H10). ¹³C NMR (101 MHz, d₆-DMSO, ppm) δ 154.8 (C2), 122.1 (C3), 125.5 (C4), 156.4 (C5), 143.5 (C6), 126.8 (C7), 119.1 (C8), 149.1 (C9), 162.8 (C10), 129.26 (C11), 129.9 (C12), 112.8 (C13), 156.9 (C14), 170.4 (C15), 129.3 (C16), 136.2 (C17) Elemental Analysis calc. (%) for C₂₂H₁₆N₄O₄: C 66.00, H 4.03, N 13.99; found: C 65.86, H 3.94, N 13.38

RESULTS AND DISCUSSION

The UV-Vis spectrum of the compounds were recorded

in EtOH, CH₂Cl₂, DMF, pH=2 and pH=12 (in DMF) at the range of 190-600 nm. The UV-Vis spectra of the compounds 2-6 in all solvents, two bands were deduced at 297-342 nm and 355-510 nm which are attributed to $\pi \rightarrow \pi^*$ and $n \rightarrow \pi^*$ transitions respectively as seen in the Table 2. The UV-Vis spectra of the compound 4 are given in Figure 4. In EtOH the introduction of electron-withdrawing substituents (-NO₂, -Cl) into the phenyl ring (compound 5 and 6) has caused a bathochromic shift compared with the compound 2 and 3 having electron-donating groups (-CH₃ and -OH). In addition, bathochromic shift in λ_{\max} of all compounds in DMF (polar aprotic) and pH=12 (in DMF) were observed compared with EtOH (polar protic) and CH₂Cl₂ (apolar aprotic) due to the increasing of the polarity of the solvent.

In EtOH and CH₂Cl₂ the UV-Vis spectrum of the compounds 2-6 display two peaks at 355-396 nm and 380-431 nm as a shoulder peak and 343-380 nm and 442 nm as a shoulder peak which were attributed to $\pi \rightarrow \pi^*$ and $n \rightarrow \pi^*$ transitions, respectively. Furthermore, the calculated value of maximum wavelenghts in EtOH are 350- 469 nm (according to 6-311++g(2d,2p) basis set) and 343-457 nm (according to cc-pvtz basis set) and in CH₂Cl₂ 349-469 nm (according to 6-311++g(2d,2p) basis set) and 343-458 nm (according to cc-pvtz basis set). In DMF $\pi \rightarrow \pi^*$ and $n \rightarrow \pi^*$ transitions were observed at 327-383 nm and 359-467 nm experimentally whereas the theoretical value is calculated

as 351-472 nm (according to 6-311++g(2d,2p) basis set) and 343-459 nm (according to cc-pvtz basis set). The theoretical λ_{\max} of all compounds are given in Table 3.

The theoretical and experimental IR spectral data are given in Table 4. The aromatic =C-H stretching peaks appear in the range of 3000-3100 cm⁻¹ [2,26,27]. The aromatic =C-H stretching peaks were observed at 3046- 3134 cm⁻¹ which are in good agreement with the calculated frequencies such as 3148-3201 cm⁻¹ (according to cc-pvtz basis set) and 3154-3199 cm⁻¹ (according to 6-311++g(2d,2p) basis set). The >C=O stretching peaks of the compounds were assigned at 1702-1749 cm⁻¹ and the corresponding theoretical value is 1799-1802 cm⁻¹ (according to cc-pvtz basis set) and 1788-1790 cm⁻¹ (according to 6-311++g(2d,2p) basis set). This peak indicated the presence of acryloyl group. The -OH stretching peak of the compounds 3 were observed at 3584-3180 cm⁻¹ as a broad peak in agreement with the literature [6,22,26] and the theoretical value which appeared in the range of 3812 cm⁻¹ (according to cc-pvtz basis set) and 3832 cm⁻¹ (according to 6-311++g(2d,2p) basis set). The characteristic stretching peaks of the azo group -N=N- are observed in the range of 1400-1550 cm⁻¹ as a medium band in the literature [2,4,26,27]. In our study -N=N- stretching peaks of the compounds (2-6) are observed at 1407-1442 cm⁻¹ and 1513 -1548 cm⁻¹ experimentally and calculated as 1496-1547cm⁻¹ (according to cc-pvtz basis set) and 1478-1543 cm⁻¹ (according to 6-311++g(2d,2p) basis set).

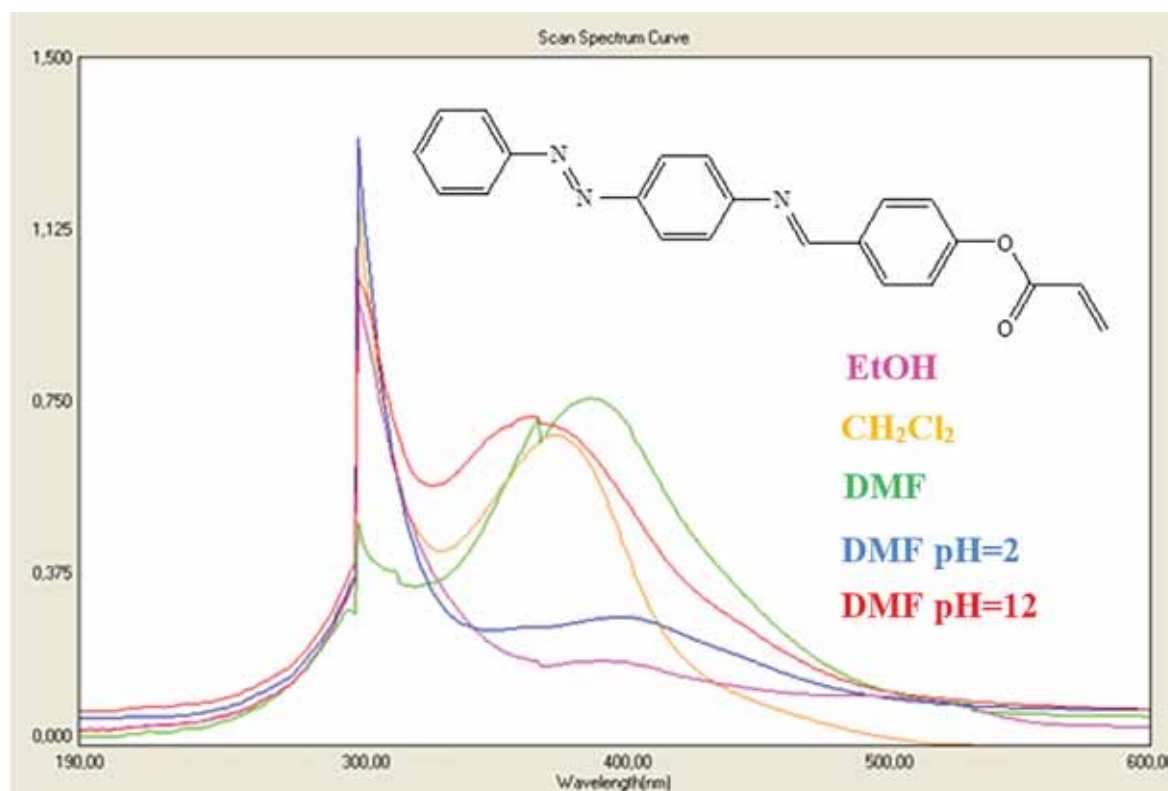


Figure 4. UV-Vis spectrum of the compound 4

Table 2. UV-Vis data of the compounds

Compound	λ max. EtOH	Log ϵ (l/mol.cm)	λ max CH ₂ Cl ₂	Log ϵ (l/mol.cm)	λ max DMF	Log ϵ (l/mol.cm)	λ max DMF (pH=2)	Log ϵ (l/mol.cm)	λ max DMF (pH= 12)	Log ϵ (l/mol.cm)
2	355	3.94	380	3.89	372	3.98	297	3.96	360	3.58
	380°	3.92	442°	3.49	430°	3.76	390°	3.59	510°	3.09
	431°	3.51					445°	3.46		
3	352	3.74	365	3.14	352	3.71	354	3.73	342	3.74
					396	3.44			460°	3.03
4	382	3.86	362	3.55	382	3.86	358	3.67	376	3.54
					467	3.26	437°	3.25		
5	374	3.88	343	3.67	327	3.73	372	3.08	383	3.69
					359	3.81			414°	3.56
6	396	3.68	367	3.39	383	3.41	368	3.54	356	3.43
					398	3.28	405°	3.21	408	3.27
									498	3.17

Table 3. Theoretical UV-Vis data of the compounds 2-6 (nm)

Comp	B3LYP					
	6-311++g(2d,2p)			cc-pvtz		
	CH ₂ Cl ₂	DMF	Ethanol	CH ₂ Cl ₂	DMF	Ethanol
2	417.48	418.13	416.30	414.37	414.67	412.99
3	426.13	426.85	424.87	423.46	423.53	421.67
4	412.55	413.12	411.31	410.06	409.50	407.84
5	420.53	421.00	419.16	411.81	411.23	409.59
6	469.07	472.55	469.99	458.20	459.18	457.49
	349.40	351.30	350.67	343.74	343.48	343.47

Experimentally the imine >C=N- stretching peak was observed at 1504-1598 cm⁻¹. The calculated values for the same peak were 1687-1688 cm⁻¹ (according to cc-pvtz basis set) and 1680-1681 cm⁻¹ (according to 6-311++g(2d,2p) basis set). The bands at 2968-2850 cm⁻¹ corresponds to the asymmetric and symmetric C-H stretching bands due to the imine and acryloyl group whereas theoretical calculations predicts these peaks at 3005-3009 cm⁻¹ (according to cc-pvtz basis set) and 3014-3017 cm⁻¹ (according to 6-311++g(2d,2p) basis set). The bands observed at 1672-1595 cm⁻¹ are assigned to the >C=C< stretching peaks which are in good agreement with the calculated peaks such as 1543-1651 cm⁻¹ (according to cc-pvtz basis set) and 1542-1645 cm⁻¹ (according to 6-311++g(2d,2p) basis set). NO₂ stretching peaks in the compound **6** are observed at 1504 cm⁻¹ and 1323 cm⁻¹ (Figure 6) as a strong band and calculated at 1582 cm⁻¹ and 1367 cm⁻¹ (according to cc-pvtz basis set) and 1561 cm⁻¹ and 1360 cm⁻¹ (according to 6-311++g(2d,2p) basis set). The correlation coefficient between experimental and theoretical values was calculated around R = 0.99 (Table 4), and the linear regression curve was given at Figure 5.

The ¹H-NMR and ¹³C-NMR spectra of compounds are obtained in d₆-DMSO and TMS was used as an internal

standard. The obtained data are given in Table 5 and Table 6, respectively. Theoretical data are in good agreement with the data given in Table 5. The imine protons were observed in the range of 7.92-8.31 ppm as a singlet peak. The aromatic protons of all compounds (**2-6**) were observed at 8.22-6.68 ppm as multiplet peaks. In the ¹H-NMR spectra of the compound **6** H₂ protons are most deshielded due to the nitro group compared with compound **2** and **3**. The ¹H-NMR spectra of compound **4** (Figure 7) consist of aromatic and vinyl protons which appear in the range of multiplet peaks 7.59-7.92 ppm and doublet peaks in the range of 5.84-6.35 ppm and double-doublet at 6.48 ppm. Compared with the other compounds (**2,3,5,6**) these peaks are shifted to high and low fields due to the substituted groups. These results are in agreement with the calculated values.

¹³C-NMR spectra of the compounds consist of seventeen carbon atoms which is given in Table 6. Aromatic and vinyl carbon atoms are appear in the same region. Carbonyl carbon atoms of the acryloyl group are observed in the range of 163.9 -170.4 ppm in accordance with the literature [13,22]. The ¹³C-NMR spectra of compound **4** (Figure 8) aromatic and vinyl carbon atoms were detected at 119.7-163.9 ppm in accordance with the literature. [13,22]

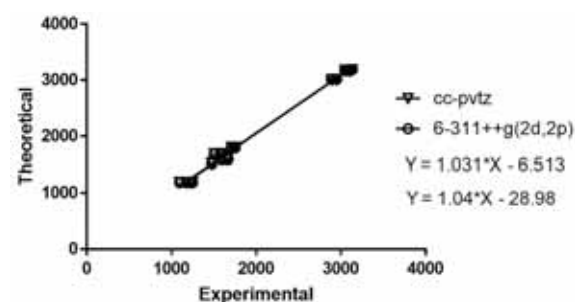
**Figure 5.** Linear regression analysis of experimental and theoretical IR data.

Table 4. Experimental and theoretical IR spectral data of compounds

Comp.	ν_{C-H} Arom	ν_{C-H} Aliph	$\nu_{C=O}$	$\nu_{C=C}$	$\nu_{C=N}$	$\nu_{N=N}$	ν_{Ar-O}	Other functional groups
2	3053	2972 2883	1749	1671	1594	1540 1411	1249 1045	2921-2883 (-CH ₃)
3	3046	2921 2875	1749	1662	1572	1513 1442	1284 1163	3584-3180 (-OH)
4	3134	2924 2850	1740	1668	1598	1541 1411	1248	-
5	3112	2965 2933	1705	1672	1594	1537 1407	1250 1088	830 (-C-Cl)
6	3071	2968 2921	1702	1595	1504	1548 1407	1173 1016	1504 (-NO ₂) 1323
Experimental								
2	3165.08 3156.82	3005.98	1802.13	1651-1601	1688.44	1547.70 1505.87	1228.84 1152.53	3103-3024 (-CH ₃)
3	3201.65 3148.76	3008.44	1799.37	1650-1601	1687.41	1547.33 1502.80	1228.32 1154.79	3812 (-OH)
4	3195.81 3186.18 3175.05	3008.64	1800.02	1647-1600	1687.90	1544.96 1505.99	1228.76 1153.21	-
5	3175.48 3149.08	3008.46	1800.13	1648-1601	1687.81	1546.51 1504.18	1229.01 1153.61	784 (-C-Cl)
6	3178.12 3168.98	3009.71	1800.97	1648-1543	1688.24	1533.93 1496.82	1230.77 1149.75	1582 (-NO ₂) 1367
B ₃ lyp/cc-pvtz								
2	3169.96 3161.54	3014.21	1790.40	1645-1597	1681.54	1543.29 1489.97	1223.23 1148.17	3109-3031 (-CH ₃)
3	3180.11 3154.68	3016.14	1788.75	1644-1597	1680.82	1543.17 1496.77	1222.99 1149.42	3832 (-OH)
4	3199.53 3190.01 3179.17	3016.30	1789.38	1642-1543	1681.45	1534.54 1478.73	1223.48 1148.58	-
5	3179.47 3173.55	3016.19	1789.59	1643-1542	1681.35	1537.58 1497.38	1223.77 1148.22	780 (-C-Cl)
6	3181.94 3173.79	3017.61	1790.54	1642-1542	1681.68	1529.27 1489.82	1225.53 1145.04	1561 (-NO ₂) 1360
B ₃ lyp/6-311g++(2d,2p)								
R	0.9941 obtained from Experimental versus cc-pvtz, 0.9938 obtained from Experimental versus 6-311++g(2d,2p)							

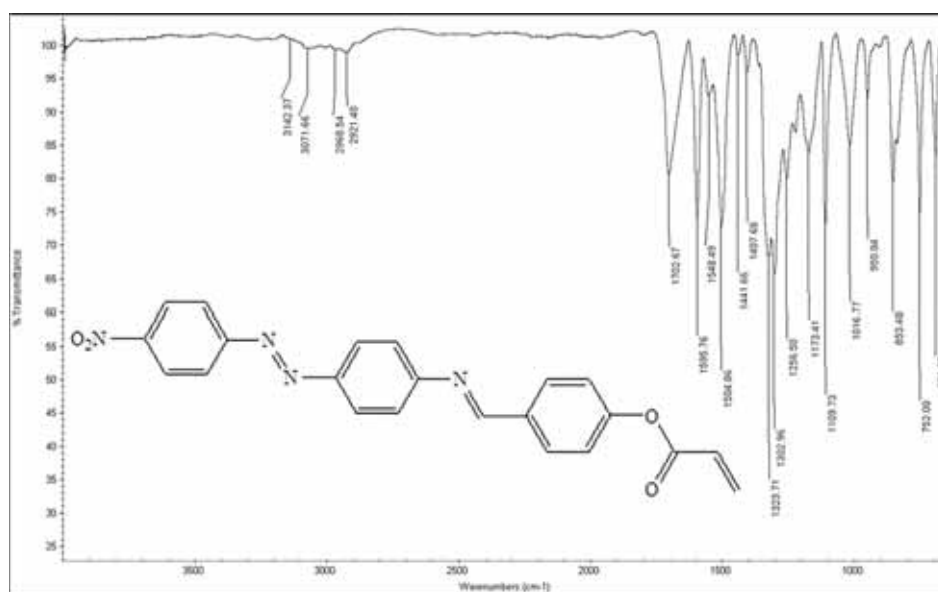
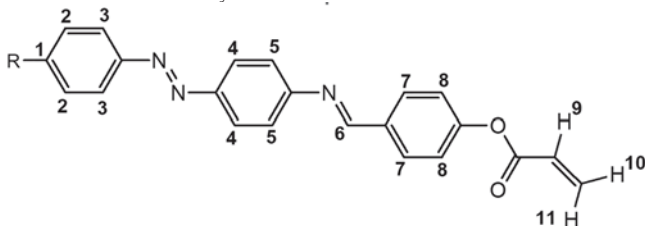


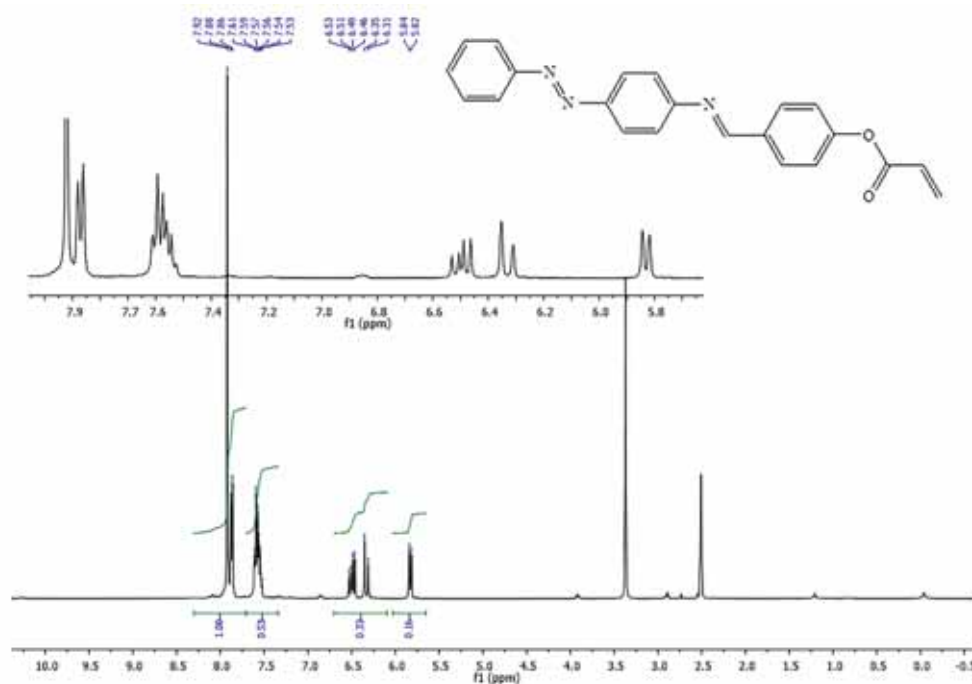
Figure 6. IR spectrum of the compound 6

Table 5. ¹H-NMR data of the compounds

$R = CH_3 (2), -OH (3), -H (4), -Cl (5), NO_2 (6)$



Comp.	H1	H2	H3	H4	H5	H6	H7	H8	H9	H10	H11
2	1.23	7.05	7.88	7.98	7.40	7.95	7.78	6.68	5.80	5.72	6.33
3	9.71	6.94	7.89	7.89	7.69	8.13	7.69	6.94	5.97	5.44	6.51
4	7.59	7.59	7.92	7.92	7.59	7.92	7.86	7.59	6.35	5.84	6.48
5	-	7.32	7.87	7.87	7.60	7.95	7.60	7.32	6.32	5.83	6.55
6	-	8.22	7.84	7.84	7.48	8.31	7.52	7.28	6.71	6.60	6.71
2	2,71	7.94	8.45	8.58	7.67	8.99	8.25	7.66	6.95	6.64	7.24
3	5.55	7.27	8.45	8.53	7.94	9.01	8.22	7.66	6.94	6.63	7.24
4	8.04	8.01	8.51	8.64	7.98	9.02	8.25	7.66	6.94	6.64	7.23
5	-	7.62	8.55	8.61	7.97	9.01	8.25	7.66	6.94	6.64	7.23
6	-	8.95	8.56	8.75	8.00	9.00	8.26	7.68	6.94	6.64	7.24

**Figure 7.** ¹H-NMR spectrum of the compound 4

C5, C6, C9 and C14 carbon atoms were deshielded to low-field compared with the other aromatic carbon atoms due to the electronegativity effect of nitrogen and oxygen atoms.

CONCLUSION

In this study novel azo-azomethine dyes bearing an acryloyl moiety have been successfully synthesized through a reaction between azo-azomethine dyes and acryloyl chloride in 1:1 M ratio at room temperature.

The characterisation of these compounds were made by IR, UV-Vis, ¹H-NMR and ¹³C-NMR spectroscopic techniques.

After esterification of azo-azomethine dyes in IR spectrum of acryloyl derivatives the -OH stretching peaks were disappeared. Also in ¹H-NMR spectra of compounds (2-6) evidence of vinyl protons at 5.44-7.24 ppm and in ¹³C-NMR spectra the evidence of

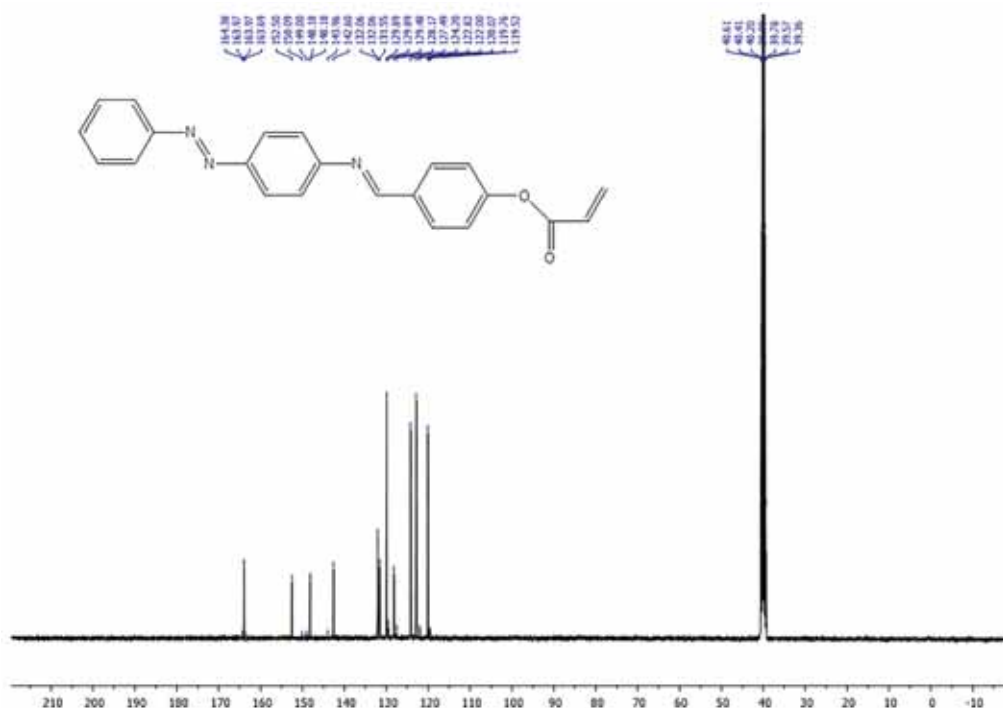


Figure 8. ^{13}C -NMR spectrum of the compound 4

Table 6. ^{13}C -NMR data of the compounds

	$R = \text{CH}_3$ (7), $-\text{OH}$ (8), $-\text{H}$ (9), $-\text{Cl}$ (10), NO_2 (11)				
	R	Substituted Phenyl	Azo Phenyl	Imine Phenyl	Acryloyl Group
	C_1	C_2, C_3, C_4, C_5	C_6, C_7, C_8, C_9	$C_{10}, C_{11}, C_{12}, C_{13}, C_{14}$	C_{15}, C_{16}, C_{17}
2	21.3	141.7 (C2), 130.4 (C3), 123.9 (C4), 148.0 (C5)	150.5 (C6), 124.1 (C7), 122.8 (C8), 150.8 (C9)	162.8 (C10), 129.8 (C11), 129.06 (C12), 120.1 (C13), 162.8 (C14)	164.1 (C15), 129.4 (C16), 132.3 (C17)
3	-	163.1 (C2), 112.3 (C3), 128.3 (C4), 148.5 (C5)	149.0 (C6), 128.3 (C7), 116.3 (C8), 152.0 (C9)	164.4 (C10), 130.0 (C11), 132.3 (C12), 128.5 (C13), 160.4 (C14)	164.4 (C15), 129.1 (C16), 132.1 (C17)
4	-	131.6 (C2), 129.9 (C3), 122.8 (C4), 152.5 (C5)	142.6 (C6), 124.2 (C7), 119.7 (C8), 149.0 (C9)	163.9 (C10), 128.1 (C11), 132.1 (C12), 119.7 (C13), 163.9 (C14)	163.9 (C15), 127.5 (C16), 131.5 (C17)
5	-	138.4 (C2), 129.3 (C3), 124.5 (C4), 150.8 (C5)	142.8 (C6), 124.3 (C7), 119.6 (C8), 148.1 (C9)	162.7 (C10), 132.0 (C11), 129.9 (C12), 122.8 (C13), 152.4 (C14)	164.0 (C15), 128.1 (C16), 135.9 (C17)
6	-	154.8 (C2), 122.1 (C3), 125.5 (C4), 156.4 (C5)	143.5 (C6), 126.8 (C7), 119.1 (C8), 149.1 (C9)	162.8 (C10), 129.26 (C11), 129.9 (C12), 112.8 (C13), 156.9 (C14)	170.4 (C15), 129.3 (C16), 136.2 (C17)

$>\text{C}=\text{O}$ peaks at 163.9-170.4 ppm demonstrated that of the acryloyl group are bonded to azo-azomethine dyes. Good agreement was observed between theoretical

calculations and experimental results. The results of UV-Vis calculations using the cc-PVTz basis set were observed at lower wavelengths than those of 6-311++g(2d,2p) basis

set. In the IR calculations, 6-311++g(2d,2p) basis set calculated the aromatic and aliphatic -C-H vibrations at higher frequencies while >C=O, -C=C-, >C=N-, -N=N- and Ar-O peaks at lower frequencies. The cc-pvtz basis set calculated the oscillation frequencies of the -NO₂ and -Cl substitute groups higher, while the -O-H vibration was lower. It can be said that the cc-pvtz basis set, in general, gave higher frequency in the calculation of the vibration frequencies of the double bounded structures. Furthermore, in calculations performed with 6-311++g(2d,2p), the ΔE was found to be lower, but the molecular energy, electronegativity and dipole moment were calculated to be larger. The correlation between the experimental data and theoretical calculations showed that the cc-pvtz basis set was more compatible with the experimental results.

To best of our knowledge, this report is the first example to compare theoretical and experimental spectroscopic results of new azo-azomethine dyes bearing acryloyl group. These compounds also have potential applications in textile industry and also may show anti-microbial properties.

REFERENCES

- Deshmukh MS, Sekar N. A combined experimental and TD-DFT investigation of three disperse azo dyes having the nitroterephthalate skeleton. *Dyes and Pigments*. 2014 Apr;103:25-33.
- Athira LS, Lakshmi CSN, Balachandran S, Arul Dhas D, Hubert Joe I. Synthesis, characterization, crystal structure and theoretical studies of 4-[(E)-(3-chloro-4-hydroxyphenyl) diazenyl]-1, 5-dimethyl-2-phenyl-1, 2-dihydro-3 H -pyrazol-3-one. *Journal of Molecular Structure*. 2017 Nov;1148:185-95.
- Biradar S, Kasugai R, Kanoh H, Nagao H, Kubota Y, Funabiki K, et al. Liquid azo dyes. *Dyes and Pigments*. 2016 Feb;125:249-58.
- Mahmut Gür, Hasan Kocaokutgen, Fatma Kandemirli, Sevil Özkinali and Zekeriya Yerlikaya. Synthesis, Spectral and Thermal Characterization of Some Azo-Polymers Containing Acrylate Derivatives. *Research & Reviews: Journal of Chemistry*. 2016 July; Volume 5, Issue 2: Pages 1-9
- Ghasemian M, Kakanejadifard A, Karami T. Synthesis, structural characterization, antimicrobial activities and theoretical investigations of some 4-(4-aminophenylsulfonyl) phenylimino) methyl)-4-(aryldiazenyl) phenol. *Spectrochimica Acta Part A: Molecular and Biomolecular Spectroscopy*. 2016 Nov; 168:190-8.
- Harisha S, Keshavayya J, Kumara Swamy BE, Viswanath CC. Synthesis, characterization and electrochemical studies of azo dyes derived from barbituric acid. *Dyes and Pigments*. 2017 Jan;136:742-53.
- Hasan Kocaokutgen, Mahmut Gür, M. Serkan Soylu and Peter Lönnecke. 2,6-Dimethyl-4-(4-chlorophenyldiazenyl)-phenol. *Acta Crystallographica Section E*. 2003 September;E59: Pages o1613-o1615.
- Shahab S, Sheikhi M, Filippovich L, Kumar R, Dikuser E, Yahyaei H, et al. Synthesis, geometry optimization, spectroscopic investigations (UV/Vis, excited states, FT-IR) and application of new azomethine dyes. *Journal of Molecular Structure*. 2017 Nov;1148:134-49.
- Sarigul M, Erkan Kariper S, Deveci P, Atabey H, Karakas D, Kurtoglu M. Multi-properties of a new azo-Schiff base and its binuclear copper(II) chelate: Preparation, spectral characterization, electrochemical, potentiometric and modeling studies. *Journal of Molecular Structure*. 2017 Dec;1149:520-9.
- Georgiev A, Bubev E, Dimov D, Yancheva D, Zhivkov I, Krajčovič J, et al. Synthesis, structure, spectral properties and DFT quantum chemical calculations of 4-aminoazobenzene dyes. Effect of intramolecular hydrogen bonding on photoisomerization. *Spectrochimica Acta Part A: Molecular and Biomolecular Spectroscopy*. 2017 Mar;175:76-91.
- Shahab S, Sheikhi M, Filippovich L, Anatol'evich DE, Yahyaei H. Quantum chemical modeling of new derivatives of (E,E)-azomethines: Synthesis, spectroscopic (FT-IR, UV/Vis, polarization) and thermophysical investigations. *Journal of Molecular Structure*. 2017 June;1137:335-48.
- Purtas F, Sayin K, Ceyhan G, Kose M, Kurtoglu M. New fluorescent azo-Schiff base Cu(II) and Zn(II) metal chelates; spectral, structural, electrochemical, photoluminescence and computational studies. *Journal of Molecular Structure*. 2017 June;1137:461-75.
- Mondal AS, Pramanik AK, Patra L, Manna CK, Mondal TK. Synthesis and characterization of a new zinc(II) complex with tetradentate azo-thioether ligand: X-ray structure, DNA binding study and DFT calculation. *Journal of Molecular Structure*. 2017 Oct;1146:146-52.
- Rocha M, Di Santo A, Echeverría GA, Piro OE, Cukiernik FD, Ulic SE, et al. Supramolecular self-assembly of a new multi-conformational Schiff base through hydrogen bonds: Crystal structure, spectroscopic and theoretical investigation. *Journal of Molecular Structure*. 2017 Apr;1133:24-36.
- Qian H-F, Tao T, Feng Y-N, Wang Y-G, Huang W. Crystal structures, solvatochromisms and DFT computations of three disperse azo dyes having the same azobenzene skeleton. *Journal of Molecular Structure*. 2016 Nov;1123:305-10.
- Sheikhi M, Shahab S, Filippovich L, Yahyaei H, Dikuser E, Khaleghian M. New derivatives of (E,E)-azomethines: Design, quantum chemical modeling, spectroscopic (FT-IR, UV/Vis, polarization) studies, synthesis and their applications: Experimental and theoretical investigations. *Journal of Molecular Structure*. 2018 Jan;1152:368-85.
- P. Hohenberg, W. Kohn, Inhomogeneous electron gas, *Phys. Rev.*, 136 (1964), pp. B864-B871.
- W. Kohn, L. Sham, Self-consistent equations including exchange and correlation effects *Phys. Rev.*, 140 (1965), pp. A1133-A1138

19. Gaussian 09, Revision B.01, Frisch M. J.; Trucks G. W.; Schlegel H. B.; Scuseria G.E.; Robb M. A.; Cheeseman J. R.; Scalmani G.; Barone V.; Mennucci B.; Petersson G. A.; Nakatsuji H.; Caricato M.; Li X.; Hratchian H. P.; Izmaylov A. F.; Bloino J.; Zheng G.; Sonnenberg J. L.; Hada M.; Ehara M.; Toyota K.; Fukuda R.; Hasegawa J.; Ishida M.; Nakajima T.; Honda Y.; Kitao O.; Nakai H.; Vreven T.; Montgomery J. A.; Jr.; Peralta J. E.; Ogliaro F.; Bearpark M.; Heyd J. J.; Brothers E.; Kudin K. N.; Staroverov V. N.; Keith T.; Kobayashi R.; Normand J.; Raghavachari K.; Rendell A.; Burant J. C.; Iyengar S. S.; Tomasi J.; Cossi M.; Rega N.; Millam J. M.; Klene M.; Knox J. E.; Cross J. B.; Bakken V.; Adamo C.; Jaramillo J.; Gomperts R.; Stratmann R. E.; Yazyev O.; Austin A. J.; Cammi R.; Pomelli C.; Ochterski J. W.; Martin R. L.; Morokuma K.; Zakrzewski V. G.; Voth G. A.; Salvador P.; Dannenberg J. J.; Dapprich S.; Daniels A. D.; Farkas O.; Foresman J. B.; Ortiz J. V.; Cioslowski J.; Fox D. J., Gaussian, Inc., Wallingford CT, 2010.
20. Yang J, Shi R, Zhou P, Qiu Q, Li H. Asymmetric Schiff bases derived from diaminomaleonitrile and their metal complexes. *Journal of Molecular Structure*. 2016 Feb;1106:242-58.
21. Geng J, Xu D, Chang F-F, Tao T, Huang W. From heterocyclic hydrazone to hydrazone-azomethine dyes: Solvent and pH induced hydrazone and azo-keto transformation for a family of pyrazolone-based heterocyclic dyes. *Dyes and Pigments*. 2017 Feb;137:101-10.
22. İspir E. The synthesis, characterization, electrochemical character, catalytic and antimicrobial activity of novel, azo-containing Schiff bases and their metal complexes. *Dyes and Pigments*. 2009 July;82(1):13-9.
23. Silku P, Özkınalı S, Öztürk Z, Asan A, Köse DA. Synthesis of novel Schiff Bases containing acryloyl moiety and the investigation of spectroscopic and electrochemical properties. *Journal of Molecular Structure*. 2016 July;1116:72-83.
24. Özkınalı S, Çavuş MS, Ceylan A, Gür M. Structural, absorption, and molecular properties of o,o'-dihydroxyazo resorcinol dyes bearing an acryloyloxy group. *Journal of Molecular Structure*. 2017 Dec;1149:206-15.
25. Temel E, Alaşalvar C, Gökçe H, Güder A, Albayrak Ç, Alpaslan YB, et al. DFT calculations, spectroscopy and antioxidant activity studies on (E)-2-nitro-4-[(phenylimino)methyl] phenol. *Spectrochimica Acta Part A: Molecular and Biomolecular Spectroscopy*. 2015 Feb;136:534-46.
26. Sevil Özkınalı, Muhammet Serdar Çavuş, Büşra Sakin. Synthesis, Characterisation and DFT Calculations of Azo-Imine Dyes. *Journal of the Turkish Chemical Society, Section A: Chemistry*. 2017 Nov;5(1):159-76
27. Tao Y, Han L, Han Y, Liu Z. Experimental and theoretical studies on the vibrational spectra of trans-3-phenylacryloyl chloride. *Spectrochimica Acta Part A: Molecular and Biomolecular Spectroscopy*. 2015 Feb;137:892-8.

Review of Chromatography Methods for Purification of Paraoxonase Enzyme

Başak Gökçe 

Suleyman Demirel University, Department of Biochemistry, Isparta, Turkey

ABSTRACT

Human serum paraoxonase1 (hPON1) is a calcium dependent enzyme, which has an important physiological role in organism with detoxification, antioxidant and also antiatherogenic properties. PON1 is mostly synthesized from the liver than secreted in serum with located on HDL.

In order to better understand the molecular mechanism of paraoxonase 1, researchers have been increasingly interested in the development of various methods for obtaining the enzyme in pure form over the last decades. In this paper, several different purification and characterization methods of multi functional enzyme paraoxonase 1 (EC 3.3.8.1) was reviewed.

Keywords:

Paraoxonase1, Chromatography Methods, Enzyme Purification and Characterization

INTRODUCTION

Paraoxonase Enzyme

In humans, the paraoxonase (PON) gene family has three members, PON1, PON2 and PON3 are aligned side-by-side in the long arm. chromosome 7q21.3-22.1. Although PON3 identified as a lactonase in rabbit HDL, PON2 has not yet been found in serum, though expresses in many biological tissues. PON1, considered as a component of HDL in mammalian, metabolizes lipid peroxides and prevents against accumulation on LDL [1-3].

PON1 is a glycoprotein consist of 354 amino acids that approximate molecular mass of 43 kDa and its active site involves two calcium ions, one essential for stability and the other one is essential for activity. Paraaxon substrate is widely used to measure paraoxonase enzyme activity. Furthermore, it has aryl esterase, organophosphates and lactonase activities, but the physiological substrate is still unknown [4-5]. PON1 is linked to HDL in circulation which has a protection against atherosclerosis, especially by protecting the oxidation of LDL lipids. The paraoxonase enzyme has an N-terminal hydrophobic region on it [6-7]. For this reason, generally hydrophobic interaction chromatography (HEK) was chosen for the purification of the enzyme.

PON1 is not only a nerve agent and toxic

pesticide hydrolyzer but also associated with several many diseases (aging, coronary artery diseases, cancer, diabetes mellitus Type 2, obesity, neurological disorders, connective tissue disorders, gynecology, liver disorders, adrenal diseases) [8-11].

The Importance of Purifying Enzymes

With the recent developments in biotechnology, the purification of the enzyme has gained importance by increasing the usage areas and new application fields of enzymes.

A purification technique is to achieve the target protein at the lowest cost, high purity and efficiency. The purified protein has a certain purpose. For this purpose method and protein should be chosen before the separation. The protein obtained in pure form is not a finish, but a beginning for academic or industrial usage. While the degree of purity of the enzyme is important for academic research, yield is important for industrial use. These studies suggest that protein activity, structure or function relationships [12]. With the purification, we can examine the amino acid sequences, biochemical and physiological functions properties and interaction with other metabolites, which of proteins. The target enzyme or receptor can be purified by chromatography method, which is a chromatographic purification technique by directing it on a substrate, ligand or a substrate analog.

Article History:

Received: 2017/11/23

Accepted: 2017/12/25

Online: 2018/01/31

Correspondence to: Başak Gökçe,
Suleyman Demirel University,
Department of Biochemistry, Isparta,
Turkey
E-Mail: basak1984@gmail.com

Purification of Paraoxonase Enzyme

The purification procedures of paraoxonase 1 have been described mostly at the beginning of the 90's.

Besides ApoA-I, the primary established apoprotein constituent, a number of proteins can bind paraoxonase-bearing HDL as well. To get rid of plate contamination HDL-related proteins such as apoproteins B, C, D, E, and ghrelin have been identified as susceptible to contamination of paraoxonase1 samples [13]. In literature there are different protocols and different sources have been used for purification and characterization of paraoxonase enzyme [14-27].

Furlong and colleagues have shown that PON enzyme purified 62.1 fold of human serum by four step purification protocols consisting of Agarose Blue, Sephadex G-200, DEAE-Tris acryl M and Sephadex G-75 [14]. Gan et al. have founded that the enzyme isoelectric point is 5.1 and the molecular weight of the enzyme is 43 kDa by purifying the enzyme paraoxonase [15].

Rodrigo et al. purified paraoxonase for the first time from rat liver 415-fold and specific activity of 1370 units/mg with five steps protocols [16]. The enzyme was purified from sheep liver microcosm by three step procedures including % 20- % 70 ammonium sulfate precipitation, DEAE-Sephadex A50 anion EC and Sephadex G-100 gel FC with nearly 141-fold but very low yield % 3,5 [17]. Beydemir et al. showed that PON1 was purified 225 times by ion exchange then gel filtration chromatography [18].

On account of reducing the number of purification steps and increase yield of the paraoxonase enzyme, researchers have focused to develop novel purification method, especially HIC by taking advantage of the hydrophobic character of the enzyme.

Purification of Paraoxonase Enzyme by HIC

Hydrophobic interaction chromatography separates proteins by their hydrophobicity differences. The separation method is based on a protein between a reversible interaction with the hydrophobic surface of a chromatographic medium. Hydrophobic interactions are one of the greatest forces that provide the stability of three-dimensional structures of protein molecules and most biomolecules exhibit a certain degree of hydrophobic character. Hydrophobic interactions play a role in antigen-antibody, enzyme-substrate reactions, formation of the lipid bilayer and binding of the protein molecules to the membrane. For the purification of protein molecules according to HIC; the tertiary and quaternary structure of proteins which are the source of surface hydrophobicity are utilized. It is necessary

to distinguish this from the hydrophobicity difference arising from the primer structure of the protein. In HIC, the separation by which the hydrophobic regions on the surface of the protein molecules are utilized is carried out under conditions in which the integrity of the protein molecules is preserved.

Sinan et al. [19] purified human paraoxonase including two-step procedures, first ammonium sulfate precipitation and then novel synthesized hydrophobic interaction chromatography called Sepharose-4B-L-tyrosine-1-naphthylamine. Overall purification rate was found 227-fold and 72,54 % yield. Before loading in the column; the precipitate was saturated with 1 M $(\text{NH}_4)_2\text{SO}_4$ to enhance the coupling efficiency of the hydrophobic interaction chromatography column. Above-mentioned hydrophobic gel was synthesized by diazotization of 1-naphthylamine and its binding to Sepharose-4B and L-tyrosine respectively [19].

This straightforward hydrophobic interaction chromatographic protocol including two step procedure has been used by many investigators for the purification and characterizing of the paraoxonase enzyme from different sources shown in **Table 1** [20-22].

Sayın et al. (20) purified Paraoxonase firstly was shark *Scyliorhinus canicula* serum by using the same method. The overall purification rates were 37-fold with a yield of 127%. This work has disproved the thesis that the enzyme paraoxonase is not found in fish. [20]. It was reported that paraoxonase 1 was purified and characterization of Swiss Black, Holstein, and Montofon Bovine's serums via first (%60-80) ammonium sulfate precipitation then Sepharose-4B-L-tyrosine-1-naphthylamine with 262.47-, 2,476.90-, and 538.06-fold for Swiss Black, Holstein, and Montofon bovines, respectively [21]. In a different study as enzyme sources were choosed from Kivircik and Merinosheep's serums for purification characterization of PON enzyme with Sinan's method [19]. Km values were found 0.482 mM and 0.153 mM, Vmax values were found 41.348 U/mL.min and 70.289 U/mL.min for MerinoPON, and KivircikPON respectively [22].

Various modified hydrophobic interaction chromatography methods are available in the literature, using different extension arms and different pre-purification processes shown in **Table 1** [23-24]. Ekinci et al. applied three-step procedures. After ammonium sulfate precipitation, diethylaminoethyl-Sephadex AEC and newly synthesized Sepharose 4B-4-phenylazo-2-naphthaleneamine hydro-phobic interaction chromatography were applied to purify the enzyme with 302-fold and yield of 32% [23]. In another study, firstly serum was treated with Triton X-100 then the enzyme was purified with Sepharose-4B-aniline-2-naphthylamine gel with 356 purification fold times by researchers [24].

Table 1: Isolation of paraoxonase (E.C. 4.2.1.1) enzyme by using hydrophobic gels.

Enzyme source	pre-purification processes	Ligand	Spacer arms	Overall purification rate
Human Serum	Ammonium sulfate precipitation (ASP)	1-naphthylamine	L-tyrosine	227-fold 72,54 % yield (19).
Scyliorhinus canicula serum	ASP	1-naphthylamine	L-tyrosine	37-fold 127 % yield (20).
Swiss Black, Holstein, and Montafon Bovine's serums	ASP	1-naphthylamine	L-tyrosine	262.47, 2,476.90, and 538.06 fold respectively (21).
Merino Sheep's Serum and Kıvrıkcık Sheep's Serum	ASP	1-naphthylamine	L-tyrosine	462.7 fold with % 6.5 yield and 461.7 fold with % 6.4 yield (22).
Human Serum	Triton X-100-treated serum ASP IEC	2-naphthaleneamine	4-phenylazo-	302 fold % 32 yield (23).
Human Serum	Triton X-100-treated serum ASP IEC	2-naphthaleneamine	aniline	356 fold (24).
Human Serum	ASP	9-aminophenanthrene	L-tyrosine	526 fold and % 39,8 yield (25).
Human Serum	ASP	3-aminophenanthrene	L-tyrosine	219 fold and % 10 yield (26).
Human Serum	ASP	1-aminophenanthrene	L-tyrosine	674 fold and % 16 yield (27).

In the last decades, researchers have focused on the effects of new ligands possess different hydrophobic characteristics on the purification of paraoxonase 1 enzyme shown in **Table 1** [25-27]. For this purpose, alternative novel HIC gels were synthesized. Amino anthracene and amino phenanthrene have three cyclic aromatic ring and more hydrophobic from naphthylamine. Gencer et al. [27] were used various ligands where amine was attached to different numbered carbons on [25-27]. In one study as ligand 9-aminophenanthrene was conducted. Since this ligand has more hydrophobic character than 2-naphthylamine, PON1 enzyme was attached HIC column tightly. According to this method purification fold was obtain 526 times, but yield 39,8 % [25], and the yield value is lower than the of Sinan et al.'s method. The large hydrophobic character for ligand selection in HIC can be disadvantageous. Because the hydrophobic interactions will be stronger, the elution of the enzyme may be difficult. Demir et al, conducted an alternative hydrophobic interaction chromatography gel namely, Sepharose-4B-L-tyrosine-3-aminophenanthrene. In this study researchers show that hPON1 was purified 219-fold and very low yield with of 10%. Also the effects of some anabolic steroid compounds on pure enzyme were investigated as a drug target study [26]. Gençer et al. [27] developed a novel HIC method include ammonium sulfate precipitation and Sepharose-4B-L-tyrosine-1-aminoanthracene. Enzym purity was controlled by SDS-electrophoresis with a single band on 43kDa molecular weight. As well, both purification factor and yield of hPON1 were calculated 674-fold and 16 % respectively (27). The biggest problem came

across is that the proteins can be absorbed very efficiently; the elution is usually a distressing condition due to the strong bonding in hydrophobic interaction chromatography. Even though a like difficulty could be experienced in affinity chromatography, hydrophobic interaction chromatography should be take into account in any general optimization procedure.

CONCLUSION

In the last few decades, studies have been increasingly focused on the physiological and biological properties of the paraoxonase enzyme. Paraoxonase act as an ideal drug target molecule for many diseases that both being connected to the HDL and possessing strong antioxidant properties. But studies in which the enzyme paraoxonase is used as a drug target are still very limited. Structural and functional researches require high purity enzyme, but for PON1, purity is a challenge work. The particular HDL environment of multiple interacting lipids and proteins may explain why study of paraoxonase in solution is so hard. The three-dimensional (3D) structure of human PON1, the catalytic mechanism and the physiological substrate of PON1 are still uncertain. In addition the drawbacks of this multifunctional enzyme are both not commercially available and still not an affinity chromatography method. These are reasons why purification method of paraoxonase must be well carried out. Here, the purification procedures of multifunctional molecule paraoxonase enzyme are thoroughly reviewed from the past to the present.

References

1. Humbert R, et al. The molecular basis of the human paraoxonase activity polymorphism. *Nat Genet* 1993;3:73-6
2. Aldridge WN, (1953) Serum esterase's 2-an enzyme hydrolyzing diethyl p-nitro phenyl phosphate (E600) and its identity with the A-esterase of mammalian sera. *Biochem. Journal*. 53, 117-124.
3. Aviram M, Rosenblat M, 2004. Paraoxonases 1, 2, and 3, oxidative stress, and macrophage foam cell formation during atherosclerosis development. *Free Radic. Biol. Med.* 37, 1304-1316
4. Mazur, A., 1946. An enzyme in the animal organism capable of hydrolysing the phosphorus-fluorine bond of alkyl fluorophosphates. *Journal of Biol. Chem.* 164, 271-289
5. Deakin, S.P., Bioletto, S., Bochaton-Piallat, M.L., James, R.W., 2011. HDL-associated paraoxonase-1 can redistribute to cell membranes and influence sensitivity to oxidative stress. *Free Radic. Biol. Med.* 50, 102-109
6. Mackness B, Durrington PN, Mackness MI, 1998 Human serum paraoxonase. *Gen. Pharmacol.* 31, 329-336.
7. Primo Parma S.L., Sorenson R.C., Teiber J., La Du BN. The human serum paraoxonase-arylesterase gene (PON1) is one member of a multigene family. *Genomics.* 1996;33:498-509.
8. La Du BN, Aviram M, Billecke S, Navab M, Primo-Parmo S, Sorenson RC, et al. On the physiological role(s) of the paraoxonases. *Chem Biol Interact* 1999;119-120: 379-88.
9. Sentí M, Tomás M, Fitó M, Weinbrenner T, Covas MI, Sala J, et al. Antioxidant paraoxonase 1 activity in the metabolic syndrome. *J Clin Endocrinol Metab* 2003;88:5422-6.
10. Van Himbergen TM, Van Tits L JH, Roest M, Stalenhoef AFH. The story of PON1: how an organophosphate hydrolyzing enzyme is becoming a player in cardiovascular medicine. *Neth J Med* 2006;64(2):34-8.
11. Hegele RA. Paraoxonase genes and disease. *Ann Med.* 1999;31: 217-224
12. Protein Purification. Principles, high resolution methods and applications. Third edition. Edited by J-C Jansson, 2011. Publ. John Wiley & Sons. ISBN 978-0-471-74661-4.
13. Renault F., Chabriere E., Andrieu JP , Dublet B., Masson P., Rochu D. Tandem purification of two HDL-associated partner proteins in human plasma, paraoxonase (PON1) and phosphate binding protein (HPBP) using hydroxyapatite chromatography *Journal of Chromatography B*, 836 (2006) 15-21
14. C.E. Furlong, R.J. Richter, C. Chapline, J.W. Crabb, *Biochemistry* 30 (1991) 10133.
15. K N Gan, A Smolen, H W Eckerson and B N La Du Purification of human serum paraoxonase/arylesterase. Evidence for one esterase catalyzing both activities. *Drug Metabolism and Disposition* January 1991, 19 (1) 100-106;
16. Rodrigo L, Gil F, Hernandez AF, et al. Purification and characterization of paraoxon hydrolase from rat liver. *Biochem J* 1997;321: 595-601
17. Cebeci BK, Alim Z, Beydemir Ş. In vitro effects of pesticide exposure on the activity of the paraoxonase-1 enzyme from sheep liver microsomes *Turk Journal of Chem* (2014) 38: 512-520
18. Beydemir S, Ekinci D, Ates O. (2009). In vitro effects of dexamethasone on human serum Paraoxonase-I (PON1) Activity. *Hacettepe J Biol Chem*, 37:197-205
19. Sinan S, Kockar F, Arslan O. Novel purification strategy for humanPON1 and inhibition of the activity by cephalosporin andaminoglikozide derived antibiotics. *Biochimie* 2006;88:565-74
20. Sayin D, Cakir DT, Gencer N, Arslan O. Effects of some metals onparaoxonase activity from shark *Scyliorhinus canicula*. *J Enzymelnhib Med Chem* 2012;27:595-8.
21. Erzenin M, Demir D, Arslan M, Sinan S. Purification and Characterization of Paraoxonase 1 (PON1) from Swiss Black, Holstein, and Montofon Bovines *Appl Biochem Biotechnol* (2014) 173:1597-1606
22. Erol K, Gencer N, Arslan M, Arslan O. Purification, characterization, and investigation of in vitro inhibition by metals of paraoxonase from different sheep breeds. *Artif Cells Nanomed Biotechnol* 2013;41:125-30.
23. Ekinci D, Senturk M, Beydemir S, et al. (2010). An alternativepurification of human serum paraoxonase 1 and interactions withsulfonamides. *Chem Biol Drug Des*, 76:552-8
24. Ekinci D., Beydemir Ş. Purification of PON1 from "Human Serum and Assessment of Enzyme Kinetics Against Metal Toxicity" *Biol Trace Elem Res* (2010) 135:112-120
25. Colak U, Gencer N. "Immobilization of paraoxonase onto chitosanan its characterization". *Artif Cells Blood Substit Immobil Biotechnol* 2012;40:290-5
26. Demir D, Gencer N, Arslan O. "An alternative purification method for human serum paraoxonase 1 and its interactions with anabolic compounds". *J Enzyme Inhib Med Chem.* 2016;31(2):247-52.
27. Gencer N, Yavuz E. "An alternative purification method for human serum paraoxonase 1 and its interaction with methidathion" *Arch Physiol Biochem*, 2017; 123(3): 159-164



Series Expansions and Polynomial Approximations of Monomolecular Growth Model for Some Populations of *Eucalyptus camaldulensis* Dehn. From Eastern Mediterranean Forest Research Manager

Mehmet Korkmaz[✉] and Erdal Unluyol[✉]

Ordu University, Department of Mathematics, Ordu, TURKEY

ABSTRACT

In this study, firstly the series expansions of monomolecular growth model from first degree polynomial to (n-1)th degree polynomial, were given with respect to (t-r) where t is time, n is the number of data, r is integer number: $t_0 \leq r \leq t_{n-1}$, t_0 and t_{n-1} are initial and final values of time, respectively. Secondly, monomolecular growth model's series expansions having m-th degree polynomials, studied on the data taken for *Eucalyptus camaldulensis* Dehn. from Eastern Mediterranean Forest Research Manager were given with R^2 with respect to (t-k), respectively where t is time; n is the number of data points; m, k are integer numbers $1 < m \leq n - 1$, $0 \leq k \leq 9$. Finally, for each data set, polynomial approximations having m-th degree were given with R^2 . For each purpose, the tables and the graphs were used for analyzing the differences.

Keywords:

Series expansions; polynomial approximation; monomolecular growth model; growth models; *Eucalyptus camaldulensis* Dehn.

INTRODUCTION

In mathematics, a series expansion is a method for calculating a function that cannot be expressed by only elementary operations such as addition, subtraction, multiplication and division. The resulting so called series often can be limited to a finite number of terms, thus yielding an approximation of the function. The fewer terms of the sequence are used, the simpler this approximation will be. Actually, there are some kinds of series such as divergent series, Taylor series and power series. A Taylor series is a representation of a function as an infinite sum of terms that are calculated from the values of the function's derivatives at a single point. If the Taylor series is centered at zero, then that series is also called a Maclaurin series [1]. The general idea behind Taylor series is that if a function satisfies certain criteria, then the function can be expressed as an infinite series of polynomials. In its most general terms, the value of a function, $f(x)$, in the vicinity of the point x_0 , is given by:

$$f(x) = \sum_{r=0}^{\infty} a_r (x - x_0)^r \quad (1)$$

where x_0 is the initial point of the series, a_r are the coefficient of the series.

A polynomial function is a function such as quadratic, cubic, and so on, involving only non-negative integer powers of x. The degree of a polynomial is the highest power of x in its expression. Actually polynomial is the special condition of a Maclaurin series when n is finite. In its most general terms, the value of a polynomial, $p(x)$ is given by:

$$p(x) = \sum_{r=0}^n a_r x^r \quad (2)$$

where a_r are the coefficient of the polynomial, n is the degree of the polynomial. A central problem of mathematical analysis is the approximation to more general functions by polynomials and the estimation of how small the discrepancy can be made.

Growth models have generally had sigmoidal shape. These models have one inflection point. For these growth models, growth rate increased continually until

Article History:

Received: 2017/11/15

Accepted: 2017/12/06

Online: 2018/04/06

Correspondence to: Mehmet Korkmaz,
Ordu University, Faculty of Arts and
Sciences, Department of Mathematics,
52100, Ordu, TURKEY
E-Mail: mkorkmaz52@yahoo.com

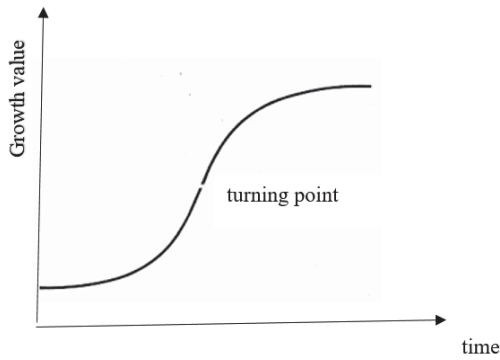


Figure 1. Sigmoidal function

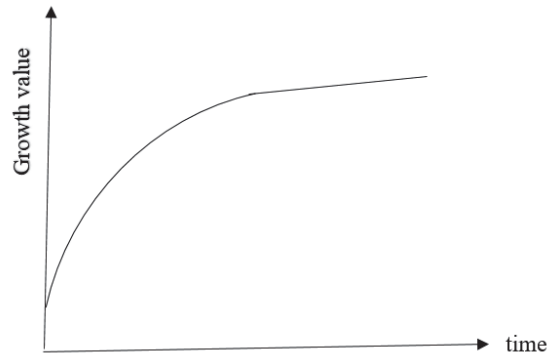


Figure 2. Increasing function by decreasing rate

the inflection point and the highest growth rate occurs at inflection point. After that point the growth rate decreased continually (Table 1).

The monomolecular or Brody function [2] is of decaying exponential type with no inflection point. Fabens [3] described a similar function based on the work of Bertalanffy. For these functions the highest growth rate occurs at birth and decreased continually (Table 2) [4].

In this study the series expansions of only one of the growth models were presented to investigate the series ex-

pansions. For that reason, series expansions of Monomolecular growth model w.r.t. (t-r) were given below where t is time, r is integer number $t_0 \leq r \leq t_{n-1}$, t_0 and t_{n-1} is initial and final values of time, respectively and n is the number of data points.

Monomolecular Growth Model (M.G.M.):

Series expansions of Monomolecular growth model, $y = a(1 - b \exp(-ct))$, with respect to (w.r.t.) (t-0), (t-1) and (t-2) are given in Tables 1-3, respectively.

Table 1. Series expansions of Monomolecular growth model w.r.t. (t-0)

Degrees of series expansion of M.G.M. w.r.t. (t-0)	$y = a(1 - b \exp(-ct))$
1	$a(1 - b) + abct$
2	$a(1 - b) + abct - \frac{abc^2t^2}{2}$
3	$a(1 - b) + abct - \frac{abc^2t^2}{2} + \frac{abc^3t^3}{6}$
4	$a(1 - b) + abct - \frac{abc^2t^2}{2} + \frac{abc^3t^3}{6} - \frac{abc^4t^4}{24}$
5	$a(1 - b) + abct - \frac{abc^2t^2}{2} + \frac{abc^3t^3}{6} - \frac{abc^4t^4}{24} + \frac{abc^5t^5}{120}$
6	$a(1 - b) + abct - \frac{abc^2t^2}{2} + \frac{abc^3t^3}{6} - \frac{abc^4t^4}{24} + \frac{abc^5t^5}{120} - \frac{abc^6t^6}{720}$
7	$a(1 - b) + abct - \frac{abc^2t^2}{2} + \frac{abc^3t^3}{6} - \frac{abc^4t^4}{24} + \frac{abc^5t^5}{120} - \frac{abc^6t^6}{720} + \frac{abc^7t^7}{5040}$
8	$a(1 - b) + abct - \frac{abc^2t^2}{2} + \frac{abc^3t^3}{6} - \frac{abc^4t^4}{24} + \frac{abc^5t^5}{120} - \frac{abc^6t^6}{720} + \frac{abc^7t^7}{5040} - \frac{abc^8t^8}{40320}$
9	$a(1 - b) + abct - \frac{abc^2t^2}{2} + \frac{abc^3t^3}{6} - \frac{abc^4t^4}{24} + \frac{abc^5t^5}{120} - \frac{abc^6t^6}{720} + \frac{abc^7t^7}{5040} - \frac{abc^8t^8}{40320} + \frac{abc^9t^9}{362880}$

Table 2. Series expansions of Monomolecular growth model w.r.t. (t-1)

Degrees of series expansion of M.G.M. w.r.t. (t-1)	$y = a(1 - b \exp(-ct))$
1	$a(1 - be^{(-c)}) + abe^{(-c)}c(t-1)$

Table 2. Series expansions of Monomolecular growth model w.r.t. (t-1)(continued)

Degrees of series expansion of M.G.M. w.r.t. (t-1)	$y = a(1 - b \exp(-ct))$
2	$a(1 - be^{(-c)}) + abe^{(-c)}c(t-1) - \frac{1}{2}abe^{(-c)}c^2(t-1)^2$
3	$a(1 - be^{(-c)}) + abe^{(-c)}c(t-1) - \frac{1}{2}abe^{(-c)}c^2(t-1)^2 + \frac{1}{6}abe^{(-c)}c^3(t-1)^3$
4	$a(1 - be^{(-c)}) + abe^{(-c)}c(t-1) - \frac{1}{2}abe^{(-c)}c^2(t-1)^2 + \frac{1}{6}abe^{(-c)}c^3(t-1)^3 - \frac{1}{24}abe^{(-c)}c^4(t-1)^4$
5	$a(1 - be^{(-c)}) + abe^{(-c)}c(t-1) - \frac{1}{2}abe^{(-c)}c^2(t-1)^2 + \frac{1}{6}abe^{(-c)}c^3(t-1)^3 - \frac{1}{24}abe^{(-c)}c^4(t-1)^4 + \frac{1}{120}abe^{(-c)}c^5(t-1)^5$
6	$a(1 - be^{(-c)}) + abe^{(-c)}c(t-1) - \frac{1}{2}abe^{(-c)}c^2(t-1)^2 + \frac{1}{6}abe^{(-c)}c^3(t-1)^3 - \frac{1}{24}abe^{(-c)}c^4(t-1)^4 + \frac{1}{120}abe^{(-c)}c^5(t-1)^5 - \frac{1}{720}abe^{(-c)}c^6(t-1)^6$
7	$a(1 - be^{(-c)}) + abe^{(-c)}c(t-1) - \frac{1}{2}abe^{(-c)}c^2(t-1)^2 + \frac{1}{6}abe^{(-c)}c^3(t-1)^3 - \frac{1}{24}abe^{(-c)}c^4(t-1)^4 + \frac{1}{120}abe^{(-c)}c^5(t-1)^5 - \frac{1}{720}abe^{(-c)}c^6(t-1)^6 + \frac{1}{5040}abe^{(-c)}c^7(t-1)^7$
8	$a(1 - be^{(-c)}) + abe^{(-c)}c(t-1) - \frac{1}{2}abe^{(-c)}c^2(t-1)^2 + \frac{1}{6}abe^{(-c)}c^3(t-1)^3 - \frac{1}{24}abe^{(-c)}c^4(t-1)^4 + \frac{1}{120}abe^{(-c)}c^5(t-1)^5 - \frac{1}{720}abe^{(-c)}c^6(t-1)^6 + \frac{1}{5040}abe^{(-c)}c^7(t-1)^7 - \frac{1}{40320}abe^{(-c)}c^8(t-1)^8$
9	$a(1 - be^{(-c)}) + abe^{(-c)}c(t-1) - \frac{1}{2}abe^{(-c)}c^2(t-1)^2 + \frac{1}{6}abe^{(-c)}c^3(t-1)^3 - \frac{1}{24}abe^{(-c)}c^4(t-1)^4 + \frac{1}{120}abe^{(-c)}c^5(t-1)^5 - \frac{1}{720}abe^{(-c)}c^6(t-1)^6 + \frac{1}{5040}abe^{(-c)}c^7(t-1)^7 - \frac{1}{40320}abe^{(-c)}c^8(t-1)^8 + \frac{1}{362880}abe^{(-c)}c^9(t-1)^9$

Table 3. Series expansions of Monomolecular growth model w.r.t. (t-2)

Degrees of series expansion of M.G.M.	$y = a(1 - b \exp(-ct))$
1	$a(1 - be^{(-2c)}) + abe^{(-2c)}c(t-2)$
2	$a(1 - be^{(-2c)}) + abe^{(-2c)}c(t-2) - \frac{1}{2}abe^{(-2c)}c^2(t-2)^2$
3	$a(1 - be^{(-2c)}) + abe^{(-2c)}c(t-2) - \frac{1}{2}abe^{(-2c)}c^2(t-2)^2 + \frac{1}{6}abe^{(-2c)}c^3(t-2)^3$
4	$a(1 - be^{(-2c)}) + abe^{(-2c)}c(t-2) - \frac{1}{2}abe^{(-2c)}c^2(t-2)^2 + \frac{1}{6}abe^{(-2c)}c^3(t-2)^3 - \frac{1}{24}abe^{(-2c)}c^4(t-2)^4$
5	$a(1 - be^{(-2c)}) + abe^{(-2c)}c(t-2) - \frac{1}{2}abe^{(-2c)}c^2(t-2)^2 + \frac{1}{6}abe^{(-2c)}c^3(t-2)^3 - \frac{1}{24}abe^{(-2c)}c^4(t-2)^4 + \frac{1}{120}abe^{(-2c)}c^5(t-2)^5$
6	$a(1 - be^{(-2c)}) + abe^{(-2c)}c(t-2) - \frac{1}{2}abe^{(-2c)}c^2(t-2)^2 + \frac{1}{6}abe^{(-2c)}c^3(t-2)^3 - \frac{1}{24}abe^{(-2c)}c^4(t-2)^4 + \frac{1}{120}abe^{(-2c)}c^5(t-2)^5 - \frac{1}{720}abe^{(-2c)}c^6(t-2)^6$
7	$a(1 - be^{(-2c)}) + abe^{(-2c)}c(t-2) - \frac{1}{2}abe^{(-2c)}c^2(t-2)^2 + \frac{1}{6}abe^{(-2c)}c^3(t-2)^3 - \frac{1}{24}abe^{(-2c)}c^4(t-2)^4 + \frac{1}{120}abe^{(-2c)}c^5(t-2)^5 - \frac{1}{720}abe^{(-2c)}c^6(t-2)^6 + \frac{1}{5040}abe^{(-2c)}c^7(t-2)^7$
8	$a(1 - be^{(-2c)}) + abe^{(-2c)}c(t-2) - \frac{1}{2}abe^{(-2c)}c^2(t-2)^2 + \frac{1}{6}abe^{(-2c)}c^3(t-2)^3 - \frac{1}{24}abe^{(-2c)}c^4(t-2)^4 + \frac{1}{120}abe^{(-2c)}c^5(t-2)^5 - \frac{1}{720}abe^{(-2c)}c^6(t-2)^6 + \frac{1}{5040}abe^{(-2c)}c^7(t-2)^7 - \frac{1}{40320}abe^{(-2c)}c^8(t-2)^8$

Table 3. Series expansions of Monomolecular growth model w.r.t. (t-2)(continued)

Degrees of series expansion of M.G.M.	$y = a(1 - b \exp(-ct))$
9	$a(1 - be^{(-2c)}) + abe^{(-2c)}c(t-2) - \frac{1}{2}abe^{(-2c)}c^2(t-2)^2 + \frac{1}{6}abe^{(-2c)}c^3(t-2)^3 - \frac{1}{24}abe^{(-2c)}c^4(t-2)^4 + \frac{1}{120}abe^{(-2c)}c^5(t-2)^5$ $- \frac{1}{720}abe^{(-2c)}c^6(t-2)^6 + \frac{1}{5040}abe^{(-2c)}c^7(t-2)^7 - \frac{1}{40320}abe^{(-2c)}c^8(t-2)^8 + \frac{1}{362880}abe^{(-2c)}c^9(t-2)^9$

Similarly, the remainder series expansions of Monomolecular growth model w.r.t. (t-r) could easily be shown in a similar manner where t is time, r is integer number $3 \leq r \leq t_{n-1}$, and n is the number of data points.

MATERIAL AND METHODS

In this study, monomolecular growth model was studied on the data taken for Eucalyptus camaldulensis Dehn. in Table 3.1. [5]. For the presentation of the models, the measurements of the mean tree lengths (m) in the age-structured of Eucalyptus camaldulensis Dehn. from Eastern Mediterranean Forest Research Manager were used [6] in this study in Table 4.

kept on the same value while k is increasing where t is time, m and k are integer numbers $1 < m \leq n-1, 0 \leq k \leq 9$.

RESULTS AND DISCUSSIONS

By using Table 4, the series expansions of Monomolecular growth model were given in the following tables. Since this monomolecular growth model is a nonlinear model, we have started to fit the monomolecular growth model by using second degree polynomial and then for fitting the model we have found third, fourth, fifth, sixth seventh, eighth and ninth degree polynomials respectively.

For each degree polynomial, we got the series expansion

Table 4. Average heights of samples of trees, Eucalyptus camaldulensis Dehn. according to each age class

Ages (year)	Planting Age (0)	1	2	3	4	5	6	7	8	9
Average heights of the trees (m)	0.41	3.23	7.45	11.41	14.83	18.11	18.95	19.69	21.50	23.40

While the degrees of Taylor series expansions in the neighborhood of (t-k) were increasing, these expansions did not show uniform convergence and also continuous decrease of Sum of Squared Errors (SSE) and continuous increase of coefficient of determination (R^2) were not found. However, R^2 of the series expansion having m-th degree polynomial with respect to (t-k) generally increased uniformly or

sions w.r.t. (t-k) where k is an integer, $0 \leq k \leq 9$, respectively. While k was increasing, R^2 of the series expansions generally increased uniformly or kept on the same value (Table 5-12).

Since we got the same Sum of Squared Errors (SSE) and R^2 of all series expansions for 10 and higher degrees, we did not make a table for them.

Table 5. Second degree series expansions of Monomolecular growth model with respect to (t-k) where t is time and k is integer number: $0 \leq k \leq 9$ and their the values of R^2

Series expansion of M.G.M. w.r.t. (t-k)	$y = a(1 - b \exp(-ct))$	R^2
t-0	$-0.229272729041378 + 4.52265151414627 t - 0.218409090681348 t^2$	0.992
t-1	$-0.0108636352328890 + 4.08583332987219 t - 0.218409090163881 (t-1)^2$	0.992
t-2	$0.644363620911388 + 3.64901516282561 t - 0.218409093453883 (t-2)^2$	0.992
t-3	$1.73640908901081 + 3.21219697132384 t - 0.218409089883235 (t-3)^2$	0.992
t-4	$3.26527273991154 + 2.77537878811066 t - 0.218409092757985 (t-4)^2$	0.992
t-5	$5.23095453353882 + 2.33856060811264 t - 0.218409090505056 (t-5)^2$	0.992
t-6	$7.63345457478377 + 1.90174242086438 t - 0.218409092246574 (t-6)^2$	0.992
t-7	$10.472727007942 + 1.46492424543531 t - 0.218409090291847 (t-7)^2$	0.992
t-8	$13.7489090224325 + 1.02810607045345 t - 0.218409089669624 (t-8)^2$	0.992
t-9	$17.4618636837107 + 0.591287872286244 t - 0.218409091611633 (t-9)^2$	0.992

Table 6. Third degree series expansions of Monomolecular growth model with respect to (t-k) where t is time and k is integer number: $0 \leq k \leq 9$ and their the values of R^2

Series expansion of M.G.M. w.r.t.(t-k)	$y = a(1 - b \exp(-ct))$	R^2
t-0	$0.680675653955140 + 4.03930304476615 t - 0.243612355615930 t^2 + 0.00979492074928451 t^3$	0.981
t-1	$0.584963946591832 + 3.84007601577501 t - 0.278675898534364 (t-1)^2 + 0.0134824165120530 (t-1)^3$	0.985
t-2	$1.16594322063417 + 3.49770679765588 t - 0.297738072649563 (t-2)^2 + 0.0168963962263288 (t-2)^3$	0.988
t-3	$2.44639528844028 + 3.03058995617843 t - 0.220092625499482 (t-3)^2 + 0.0160474863319337 (t-3)^3$	0.990
t-4	$4.05447741988629 + 2.58111809971917 t - 0.228191132177259 (t-4)^2 + 0.0134492600474202 (t-4)^3$	0.991
t-5	$5.85739358168628 + 2.18639715508841 t - 0.194574411773702 (t-5)^2 + 0.0115438623548554 (t-5)^3$	0.991
t-6	$7.81113723933999 + 1.83610476659678 t - 0.16778046315177 (t-6)^2 + 0.0102207213653038 (t-6)^3$	0.991
t-7	$9.87660717922102 + 1.52160347167066 t - 0.145386300126691 (t-7)^2 + 0.00926092185340971 (t-7)^3$	0.992
t-8	$12.0145428710101 + 1.23768798475280 t - 0.125887808125803 (t-8)^2 + 0.00853620644833953 (t-8)^3$	0.992
t-9	$14.1839446628479 + 0.981364682263551 t - 0.108335472603878 (t-9)^2 + 0.00797296175854134 (t-9)^3$	0.992

Table 7. Fourth degree series expansions of Monomolecular growth model with respect to (t-k) where t is time and k is integer number: $0 \leq k \leq 9$ and their the values of R^2

Series expansion of M.G.M. w.r.t.(t-k)	$y = a(1 - b \exp(-ct))$	R^2
t-0	$-0.360744304989450 + 4.87762730457168 t - 0.360902568792858 t^2 + 0.0178024622804074 t^3 - 0.000658614728703753 t^4$	0.991
t-1	$-0.0438660693301349 + 4.23718011942472 t - 0.329511408421765 (t-1)^2 + 0.0170833376946988 (t-1)^3 - 0.000664257183512074 (t-1)^4$	0.991
t-2	$0.890733909398483 + 3.62671056678083 t - 0.291729601195510 (t-2)^2 + 0.0156443253735637 (t-2)^3 - 0.000629208302973788 (t-2)^4$	0.991
t-3	$2.26927816549750 + 3.07908820492831 t - 0.252588727915214 (t-3)^2 + 0.0138138438445744 (t-3)^3 - 0.000566599754878032 (t-3)^4$	0.991
t-4	$3.92458563383874 + 2.60640074179350 t - 0.216329159127621 (t-4)^2 + 0.0119700971377770 (t-4)^3 - 0.000496754203405687 (t-4)^4$	0.991
t-5	$5.73867075761085 + 2.20328073831089 t - 0.184587731331811 (t-5)^2 + 0.0103096653294535 (t-5)^3 - 0.000431864560167892 (t-5)^4$	0.991
t-6	$7.63416937574968 + 1.85894948599934 t - 0.157378864957577 (t-6)^2 + 0.00888247450934917 (t-6)^3 - 0.000375995627321871 (t-6)^4$	0.991
t-7	$9.55867222085055 + 1.56310018181112 t - 0.134151138918962 (t-7)^2 + 0.00767557033245839 (t-7)^3 - 0.000329373163004440 (t-7)^4$	0.991
t-8	$11.4745852571453 + 1.30732060953373 t - 0.114255413382824 (t-8)^2 + 0.00665702526326516 (t-8)^3 - 0.000290900781264948 (t-8)^4$	0.991
t-9	$13.3530729890336 + 1.08508386831010 t - 0.0971025039789758 (t-9)^2 + 0.00579303686677019 (t-9)^3 - 0.000259205026373660 (t-9)^4$	0.991

Table 8. Fifth degree series expansions of Monomolecular growth model with respect to (t-k) where t is time and k is integer number: $0 \leq k \leq 9$ and their the values of R^2

Series expansion of M.G.M. w.r.t.(t-k)	$y = a(1 - b \exp(-ct))$	R^2
t-0	$-0.398733365062543 + 5.06605109275128 t - 0.431023810813641 t^2 + 0.0244479078591920 t^3 - 0.00104002409558871 t^4 + 0.0000353944435862534 t^5$	0.990
t-1	$-0.0519088215751733 + 4.29129401652697 t - 0.362192522099715 (t-1)^2 + 0.0203797770648711 (t-1)^3 - 0.000860043943217098 (t-1)^4 + 0.0000290356693072724 (t-1)^5$	0.991
t-2	$0.924442518467425 + 3.62833242423506 t - 0.303655112677479 (t-2)^2 + 0.0169419293629748 (t-2)^3 - 0.000708934969040578 (t-2)^4 + 0.0000237323048425372 (t-2)^5$	0.991
t-3	$2.30476251761820 + 3.07162584755017 t - 0.256007762241889 (t-3)^2 + 0.0142248172099415 (t-3)^3 - 0.000592790887132543 (t-3)^4 + 0.0000197627023634046 (t-3)^5$	0.991

Table 8. Fifth degree series expansions of Monomolecular growth model with respect to (t-k) where t is time and k is integer number: $0 \leq k \leq 9$ and their the values of R^2 (continued)

Series expansion of M.G.M. w.r.t.(t-k)	$y = a(1 - b \exp(-ct))$	R^2
t-4	$3.94333421828184 + 2.60142194209407 t - 0.216525639783785 (t-4)^2 + 0.0120148015783598 (t-4)^3$ $- 0.000500017424419706 (t-4)^4 + 0.0000166472944620995 (t-4)^5$	0.991
t-5	$5.73254173978960 + 2.20283829673356 t - 0.183425184277512 (t-5)^2 + 0.0101822569173987 (t-5)^3$ $- 0.000423926339533021 (t-5)^4 + 0.0000141197412564034 (t-5)^5$	0.991
t-6	$7.59228787448331 + 1.86419135505680 t - 0.155514792387977 (t-6)^2 + 0.00864891564050795 (t-6)^3$ $- 0.000360755433332042 (t-6)^4 + 0.0000120379930236846 (t-6)^5$	0.991
t-7	$9.46427391817074 + 1.57581977438594 t - 0.131901861644774 (t-7)^2 + 0.00736044455004877 (t-7)^3$ $- 0.000308048025055050 (t-7)^4 + 0.0000103138972212963 (t-7)^5$	0.991
t-8	$11.3069711424540 + 1.32963294973438 t - 0.111868341452826 (t-8)^2 + 0.00627467694344072 (t-8)^3$ $- 0.000263959201280032 (t-8)^4 + 0.888325701143577 10^{-5} (t-8)^5$	0.991
t-9	$13.0912078624012 + 1.11889304425699 t - 0.0948209241970095 (t-9)^2 + 0.00535708496996129 (t-9)^3$ $- 0.000226993880452155 (t-9)^4 + 0.769466559543478 10^{-5} (t-9)^5$	0.991

Table 9. Sixth degree series expansions of Monomolecular growth model with respect to (t-k) where t is time and k is integer number: $0 \leq k \leq 9$ and their the values of R^2

Series expansion of M.G.M. w.r.t.(t-k)	$y = a(1 - b \exp(-ct))$	R^2
t-0	$-0.429522115482260 + 5.04575821101274 t - 0.415950307240173 t^2 + 0.0228594198476887 t^3$ $- 0.000942215452201562 t^4 + 0.0000310688535153583 t^5 - 0.853726940852854 10^{-6} t^6$	0.991
t-1	$-0.0564049542016347 + 4.28180099690690 t - 0.354716647774369 (t-1)^2 + 0.0195904947940020 (t-1)^3$ $- 0.000811466325337110 (t-1)^4 + 0.0000268896770226637 (t-1)^5 - 0.742539264833108 10^{-6} (t-1)^6$	0.991
t-2	$0.917252604051328 + 3.62802249505953 t - 0.301198922338968 (t-2)^2 + 0.0166703837405814 (t-2)^3$ $- 0.000691988765246638 (t-2)^4 + 0.0000229796006863249 (t-2)^5 - 0.635923194332095 10^{-6} (t-2)^6$	0.991
t-3	$2.29893582306801 + 3.07263401789004 t - 0.255309485257502 (t-3)^2 + 0.0141426829842476 (t-3)^3$ $- 0.000587567717444554 (t-3)^4 + 0.0000195287314559782 (t-3)^5 - 0.540889927743661 10^{-6} (t-3)^6$	0.991
t-4	$3.94000249171290 + 2.60198312158441 t - 0.216276386757099 (t-4)^2 + 0.0119845705584294 (t-4)^3$ $- 0.000498077715364870 (t-4)^4 + 0.0000165600534006362 (t-4)^5 - 0.458822924238559 10^{-6} (t-4)^6$	0.991
t-5	$5.72855228163803 + 2.20335108905297 t - 0.183185744072797 (t-5)^2 + 0.0101533272048586 (t-5)^3$ $- 0.000422071817804583 (t-5)^4 + 0.0000140363540573868 (t-5)^5 - 0.388992320961550 10^{-6} (t-5)^6$	0.991
t-6	$7.58181706814705 + 1.86560662707831 t - 0.155166918568407 (t-6)^2 + 0.00860373323741911 (t-6)^3$ $- 0.000357796428051299 (t-6)^4 + 0.0000119035102919737 (t-6)^5 - 0.330014374474623 10^{-6} (t-6)^6$	0.991
t-7	$9.43970404519211 + 1.57921656112010 t - 0.131446193031418 (t-7)^2 + 0.00729395494273774 (t-7)^3$ $- 0.000303556406692425 (t-7)^4 + 0.0000101066148905417 (t-7)^5 - 0.280408248938763 10^{-6} (t-7)^6$	0.991
t-8	$11.2595567001189 + 1.33609057445753 t - 0.111354547940796 (t-8)^2 + 0.00618712313079704 (t-8)^3$ $- 0.000257828440846414 (t-8)^4 + 0.859533628201506 10^{-5} (t-8)^5 - 0.238788648110308 10^{-6} (t-8)^6$	0.991
t-9	$13.0119301184415 + 1.12940133849068 t - 0.094320770723575 (t-9)^2 + 0.00525140100590662 (t-9)^3$ $- 0.000219282644138534 (t-9)^4 + 0.732526470041843 10^{-5} (t-9)^5 - 0.203920618607707 10^{-6} (t-9)^6$	0.991

Table 10. Seventh degree series expansions of Monomolecular growth model with respect to (t-k) where t is time and k is integer number: $0 \leq k \leq 9$ and their the values of R^2

Series expansion of M.G.M. w.r.t.(t-k)	$y = a(1 - b \exp(-ct))$	R^2
t-0	$-0.434828123120450 + 5.06217611621347 t - 0.421486259768881 t^2 + 0.0233958233370519 t^3$ $- 0.000973990023871748 t^4 + 0.0000324384930740797 t^5 - 0.900296552605892 10^{-6} t^6 + 10^{-7} t^7$	0.991
t-1	$-0.0573655320578679 + 4.28498718704676 t - 0.356403272656266 (t-1)^2 + 0.0197625317129037 (t-1)^3$ $- 0.000821873050139327 (t-1)^4 + 0.0000273436752075354 (t-1)^5 - 0.758102253675752 10^{-6} (t-1)^6$ $+ 0.180157314312161 10^{-7} (t-1)^7$	0.991
t-2	$0.918211722789252 + 3.62827592183363 t - 0.301656184232409 (t-2)^2 + 0.0167198701616699 (t-2)^3$ $- 0.000695048053468011 (t-2)^4 + 0.0000231146195255585 (t-2)^5 - 0.64058596756221 10^{-6} (t-2)^6$ $+ 0.152167288907535 10^{-7} (t-2)^7$	0.991

Table 10. Seventh degree series expansions of Monomolecular growth model with respect to (t-k) where t is time and k is integer number: $0 \leq k \leq 9$ and their the values of R^2 (continued)

Series expansion of M.G.M. w.r.t.(t-k)	$y = a(1 - b \exp(-ct))$	R^2
t-3	$2.29978449123599 + 3.07250276125247 t - 0.255412094951390 (t-3)^3 + 0.0141546579051981 (t-3)^3$ $- 0.000588326701358795 (t-3)^4 + 0.0000195626519467975 (t-3)^5 - 0.542070347291260 10^{-6} (t-3)^6$ $+ 0.128746900929205 10^7 (t-3)^7$	0.991
t-4	$3.94030372900206 + 2.60191113903930 t - 0.216284326063926 (t-4)^2 + 0.0119857820402478 (t-4)^3$ $- 0.000498160131610271 (t-4)^4 + 0.0000165638598060696 (t-4)^5 - 0.458957930502304 10^{-6} (t-4)^6$ $+ 0.109002741650714 10^7 (t-4)^7$	0.991
t-5	$5.72815540513387 + 2.20338912024644 t - 0.183158896998366 (t-5)^2 + 0.0101501761510335 (t-5)^3$ $- 0.000421871709150150 (t-5)^4 + 0.0000140274010092443 (t-5)^5 - 0.388680521444407 10^{-6} (t-5)^6$ $+ 0.923127207450638 10^{-8} (t-5)^7$	0.991
t-6	$7.57989286794269 + 1.86587022056233 t - 0.155111243519455 (t-6)^2 + 0.00859634559110287 (t-6)^3$ $- 0.000357310449479465 (t-6)^4 + 0.0000118813982945828 (t-6)^5 - 0.329236628913246 10^{-6} (t-6)^6$ $+ 0.781991348136531 10^{-8} (t-6)^7$	0.991
t-7	$9.43437496048621 + 1.57996492941454 t - 0.131362230938031 (t-7)^2 + 0.00728118934615032 (t-7)^3$ $- 0.000302688135219226 (t-7)^4 + 0.0000100664990673188 (t-7)^5 - 0.278984626093062 10^{-6} (t-7)^6$ $+ 0.662727963110582 10^{-8} (t-7)^7$	0.991
t-8	$11.2479524265758 + 1.33769725429912 t - 0.111251118362609 (t-8)^2 + 0.00616821745834955 (t-8)^3$ $- 0.000256493421190692 (t-8)^4 + 0.853262720497008 10^{-5} (t-8)^5 - 0.236541892189077 10^{-6} (t-8)^6$ $+ 0.562065038281674 10^{-8} (t-8)^7$	0.991
t-9	$12.9905117588151 + 1.13229795488828 t - 0.0942165079072939 (t-9)^2 + 0.00522639253147285 (t-9)^3$ $- 0.000217439434179989 (t-9)^4 + 0.723710012239584 10^{-5} (t-9)^5 - 0.200728762237868 10^{-6} (t-9)^6$ $+ 0.477208139504774 10^{-8} (t-9)^7$	0.991

Table 11. Eighth degree series expansions of Monomolecular growth model with respect to (t-k) where t is time and k is integer number: $0 \leq k \leq 9$ and their the values of R^2

Series expansion of M.G.M. w.r.t.(t-k)	$y = a(1 - b \exp(-ct))$	R^2
t-0	$-0.433608228852283 + 5.05878273346574 t - 0.420376461012291 t^2 + 0.0232883914680598 t^3 - 0.000967613367070306 t^4$ $+ 0.0000321628268544778 t^5 - 0.890892535589199 10^{-6} t^6 + 0.211519123408160 10^7 t^7 - 0.439422214886404 10^9 t^8$	0.991
t-1	$-0.0570835327271100 + 4.28434713167022 t - 0.356095349204152 (t-1)^2 + 0.0197313451077891 (t-1)^3$ $- 0.000819989605240820 (t-1)^4 + 0.0000272615150778572 (t-1)^5 - 0.755284172293431 10^{-6} (t-1)^6$ $+ 0.179359336817422 10^7 (t-1)^7 - 0.372688204959517 10^9 (t-1)^8$	0.991
t-2	$0.918092664360992 + 3.62821699634121 t - 0.301582499855520 (t-2)^2 + 0.0167119743776485 (t-2)^3$ $- 0.000694561407905749 (t-2)^4 + 0.0000230931684527820 (t-2)^5 - 0.639845547514368 10^{-6} (t-2)^6$ $+ 0.151956748165362 10^7 (t-2)^7 - 0.315771465900738 10^9 (t-2)^8$	0.991
t-3	$2.29967652480385 + 3.07251590966884 t - 0.255397423275344 (t-3)^2 + 0.0141529712095596 (t-3)^3$ $- 0.000588220286709800 (t-3)^4 + 0.0000195579062840601 (t-3)^5 - 0.541905397884822 10^{-6} (t-3)^6$ $+ 0.128699779731700 10^7 (t-3)^7 - 0.267448510324584 10^9 (t-3)^8$	0.991
t-4	$3.94025714066446 + 2.60191851167342 t - 0.216281109727798 (t-4)^2 + 0.0119853916037267 (t-4)^3$ $- 0.000498135084735814 (t-4)^4 + 0.0000165627337578257 (t-4)^5 - 0.458918604508833 10^{-6} (t-4)^6$ $+ 0.108991472048245 10^7 (t-4)^7 - 0.2264943737319102 10^9 (t-4)^8$	0.991
t-5	$5.72808264413668 + 2.20339840980785 t - 0.183155223840188 (t-5)^2 + 0.0101497262503318 (t-5)^3$ $- 0.000421842771380205 (t-5)^4 + 0.0000140260983893956 (t-5)^5 - 0.388634995026958 10^{-6} (t-5)^6$ $+ 0.922996678863383 10^{-8} (t-5)^7 - 0.191807871159936 10^9 (t-5)^8$	0.991
t-6	$7.57958865400335 + 1.86591267002906 t - 0.155103330790887 (t-6)^2 + 0.00859527301173300 (t-6)^3$ $- 0.000357239514632815 (t-6)^4 + 0.0000118781633245046 (t-6)^5 - 0.329122708492054 10^{-6} (t-6)^6$ $+ 0.781663106991428 10^{-8} (t-6)^7 - 0.162438673307304 10^9 (t-6)^8$	0.991
t-7	$9.43340041614564 + 1.58010329740721 t - 0.131348514134999 (t-7)^2 + 0.00727903135353300 (t-7)^3$ $- 0.000302540332077490 (t-7)^4 + 0.0000100596519606013 (t-7)^5 - 0.278741341343180 10^{-6} (t-7)^6$ $+ 0.662022920969791 10^7 (t-7)^7 - 0.137579180955098 10^9 (t-7)^8$	0.991
t-8	$11.2455245506238 + 1.33803742398329 t - 0.111232356224621 (t-8)^2 + 0.00616456951527712 (t-8)^3$ $- 0.000256233338471745 (t-8)^4 + 0.852037094647629 10^{-5} (t-8)^5 - 0.236102249283624 10^{-6} (t-8)^6$ $+ 0.560783151011653 10^{-8} (t-8)^7 - 0.116546125878152 10^9 (t-8)^8$	0.991
t-9	$12.9854825929341 + 1.13298835527921 t - 0.0941966567280208 (t-9)^2 + 0.00522100696351228 (t-9)^3$ $- 0.000217037270694356 (t-9)^4 + 0.721779184738210 10^{-5} (t-9)^5 - 0.200029081738918 10^{-6} (t-9)^6$ $+ 0.475154820445459 10^{-8} (t-9)^7 - 0.987609345356764 10^{10} (t-9)^8$	0.991

Table 12. Ninth degree series expansions of Monomolecular growth model with respect to (t-k) where t is time and k is integer number: $0 \leq k \leq 9$ and their the values of R^2

Series expansion of M.G.M. w.r.t.(t-k)	$y = a(1 - b \exp(-ct))$	R^2
t-0	$-0.433914558778196 + 5.05945588447531 t - 0.420582327983030 t^2 + 0.0233081051468270 t^3$ $- 0.000968777804111872 t^4 + 0.0000322130152692428 t^5 - 0.892600921432618 10^{-6} t^6$ $+ 0.212000308823644 10^7 t^7 - 0.440578915273099 10^8 t^8 + 0.813876301136041 10^{11} t^9$	0.991
t-1	$-0.0571499574470016 + 4.28446268530283 t - 0.356145918363578 (t-1)^2 + 0.0197364172956297 (t-1)^3$ $- 0.000820294746301659 (t-1)^4 + 0.0000272747970710612 (t-1)^5 - 0.755739078972881 10^{-6} (t-1)^6$ $+ 0.179488009911674 10^7 (t-1)^7 - 0.372998476241402 10^8 (t-1)^8 + 0.689010992232219 10^{11} (t-1)^9$	0.991
t-2	$0.918105241106358 + 3.62822766715208 t - 0.301593044792331 (t-2)^2 + 0.0167130939238083 (t-2)^3$ $- 0.000694630181288771 (t-2)^4 + 0.0000230961946821788 (t-2)^5 - 0.639949888883564 10^{-6} (t-2)^6$ $+ 0.151986395254758 10^7 (t-2)^7 - 0.315843187893670 10^8 (t-2)^8 + 0.583426016792124 10^{11} (t-2)^9$	0.991
t-3	$2.29968888992291 + 3.07251464656294 t - 0.255399178727401 (t-3)^2 + 0.0141531715870146 (t-3)^3$ $- 0.000588232899679598 (t-3)^4 + 0.0000195584681292460 (t-3)^5 - 0.541924912976777 10^{-6} (t-3)^6$ $+ 0.128705352016109 10^7 (t-3)^7 - 0.267462038297415 10^8 (t-3)^8 + 0.494054854300104 10^{11} (t-3)^9$	0.991
t-4	$3.94026043483711 + 2.60191783595405 t - 0.216281244612934 (t-4)^2 + 0.0119854096658842 (t-4)^3$ $- 0.000498136275464446 (t-4)^4 + 0.0000165627879797823 (t-4)^5 - 0.458920512275896 10^{-6} (t-4)^6$ $+ 0.108992021414677 10^7 (t-4)^7 - 0.226495719029905 10^8 (t-4)^8 + 0.418381782633787 10^{11} (t-4)^9$	0.991
t-5	$5.72807619305896 + 2.20339915670248 t - 0.183154886929434 (t-5)^2 + 0.0101496854694080 (t-5)^3$ $- 0.000421840157482132 (t-5)^4 + 0.0000140259809233224 (t-5)^5 - 0.388630893661299 10^{-6} (t-5)^6$ $+ 0.922984927554837 10^7 (t-5)^7 - 0.191805011281830 10^8 (t-5)^8 + 0.354301318154633 10^{11} (t-5)^9$	0.991
t-6	$7.57954821613993 + 1.86591836038502 t - 0.155102348424211 (t-6)^2 + 0.00859513792151890 (t-6)^3$ $- 0.000357230547959905 (t-6)^4 + 0.000011877537310939 (t-6)^5 - 0.329108271260228 10^{-6} (t-6)^6$ $+ 0.781621484504528 10^7 (t-6)^7 - 0.162428499551898 10^8 (t-6)^8 + 0.300037441989715 10^{11} (t-6)^9$	0.991
t-7	$9.43324763988232 + 1.58012515736214 t - 0.131346529575979 (t-7)^2 + 0.00727871069844188 (t-7)^3$ $- 0.000302518248498711 (t-7)^4 + 0.0000100586265305825 (t-7)^5 - 0.278704861012072 10^{-6} (t-7)^6$ $+ 0.661917120015674 10^7 (t-7)^7 - 0.137553212440026 10^8 (t-7)^8 + 0.254088692515500 10^{11} (t-7)^9$	0.991
t-8	$11.2450867730620 + 1.33809928927531 t - 0.111229311596016 (t-8)^2 + 0.00616394705399585 (t-8)^3$ $- 0.000256188607611311 (t-8)^4 + 0.851825651257341 10^{-5} (t-8)^5 - 0.236026283820578 10^{-6} (t-8)^6$ $+ 0.560561457335014 10^7 (t-8)^7 - 0.116491476952360 10^8 (t-8)^8 + 0.215185273819447 10^{11} (t-8)^9$	0.991
t-9	$12.9844573832616 + 1.13313065903825 t - 0.0941932390184142 (t-9)^2 + 0.00521997247537813 (t-9)^3$ $- 0.000216959143732002 (t-9)^4 + 0.721402578591395 10^{-5} (t-9)^5 - 0.199892351253455 10^{-6} (t-9)^6$ $+ 0.474753169633848 10^7 (t-9)^7 - 0.986614792067005 10^8 (t-9)^8 + 0.182253068693670 10^{11} (t-9)^9$	0.991

The highest value of R^2 (0.992) was found at the second degree expansions of monomolecular growth model. The values of R^2 of third, fourth, ... and ninth degree expansions of monomolecular growth model were generally found as 0.991. Furthermore, the values of R^2 of tenth and higher degree expansions in the neighborhood of (t-k), where t is time and k is integer number, $0 \leq k \leq 9$ are the same with those of third, fourth,... and ninth degree expansions of monomolecular growth model: $R^2=0.991$.

For all degree series expansions, the values of R^2 are generally increasing or keeping the same level w.r.t. (t-k) while k is increasing where t is time and k is the value of age. Even so the best approaches according to R^2 were found at the second degree expansions of Monomolecular growth model.

The research for the second degree series expansions of monomolecular growth model in the neighborhood of (t-k), where t is time and k is integer number, $0 \leq k \leq 9$ was done and for each one the same R^2 was found (0.992). Moreover, the research for the third, fourth, ... and ninth degree series expansions of monomolecular growth model in the neighborhood of (t-k) was done and for each one the same R^2 was

generally found (0.991).

Since the number of data points is 10 and the only ninth degree polynomial for monomolecular model is unique, for all series expansions of ninth degree polynomial are actually the same function. For that reason, R^2 is the same for all series expansions of ninth degree polynomial.

Here the following question comes to mind. I wonder if it can be directly fitted (n-1)th degree polynomial instead of using the series expansions of Monomolecular growth model. I wonder how it results. After this, this investigation will be done.

For each degree of polynomial approximations, we got the approach equations. While the degree of polynomial was increasing, R^2 of the polynomial approximations generally increased uniformly (Table 13).

For ninth degree polynomial, SSE was found as zero, but actually since the degree of freedom is zero, values for the items of ninth degree polynomial are not available. We can see that in the plot in Fig. 3.

Table 13. Polynomial approximations and their values of R²

Polynomial Degree	Polynomial Approximations	R ²
1	$2.39163636363637 + 2.55696969696970 t$	0.9475
2	$-0.229272727272729 + 4.52265151515151 t - 0.218409090909091 t^2$	0.9918
3	$-0.269902097902094 + 4.59697746697747 t - 0.240174825174825 t^2 + 0.00161227661227660 t^3$	0.9918
4	$0.404405594405547 + 1.78736208236217 t + 1.33633158508155 t^2 - 0.279349261849256 t^3 + 0.0156089743589741 t^4$	0.9988
5	$0.427328671328617 + 1.55532960372979 t + 1.55123543123531 t^2 - 0.346844988344958 t^3 + 0.0242051282051249 t^4 - 0.000382051282051152 t^5$	0.9989
6	$0.379328671328654 + 2.97852960372992 t - 0.399697902098311 t^2 + 0.586155011655198 t^3 - 0.176128205128243 t^4 + 0.0194179487179522 t^5 - 0.000733333333333456 t^6$	0.9992
7	$0.410025915261181 - 0.709987883685088 t + 6.36290493624040 t^2 - 3.86973469708383 t^3 + 1.22379402337848 t^4 - 0.207414787581678 t^5 + 0.0175571078431354 t^6 - 0.000580648926237101 t^7$	0.9998
8	$0.411627313865612 - 1.98339717437018 t + 9.21625186286223 t^2 - 6.26102315856714 t^3 + 2.22612775732909 t^4 - 0.439277287576093 t^5 + 0.0476133578424037 t^6 - 0.00262529178332981 t^7 + 0.0000567956349192339 t^8$	0.9998
9	$0.409999999958488 + 16.8924801581856 t - 39.2281795615017 t^2 + 42.2230666864486 t^3 - 23.0818489570843 t^4 + 7.22164814776001 t^5 - 1.34619791659509 t^6 + 0.147586970891698 t^7 - 0.00877356150747743 t^8 + 0.000218033509688805 t^9$	1

As it was seen in Table 13, as the degree of the polynomial approximation increases, a better approach is provided. Even significantly better results than series expansions of monomolecular growth model were found.

Since degree of freedom of SSE is n-2 where n is the number of data points, (n-2)th degree polynomial has better approximation especially when n is large. It shows that it can be directly used (n-2)th degree polynomial approximation instead of using series expansions of any model. For example, in the following figure (Fig. 4), it can be seen that how ninth degree polynomial deviates from the data points while eighth degree polynomial is perfect fitting the data set.

Fig. 5 showing Monomolecular growth model and its

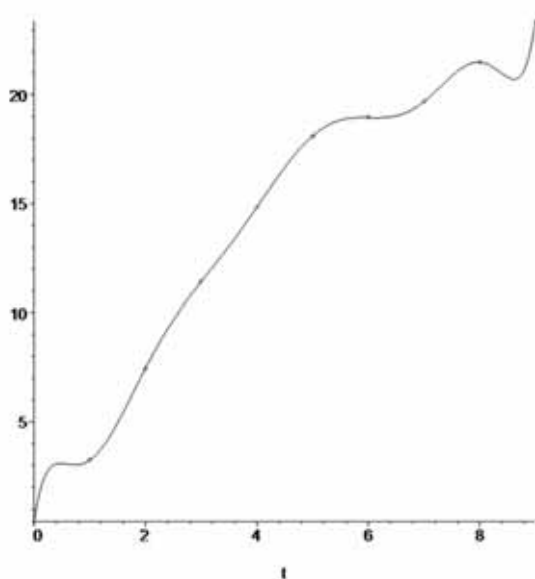


Figure 3. Ninth degree polynomial approximation

ninth degree series expansion w.r.t. (t-0) with eighth and ninth degree polynomial approximations is presented below. In this Fig. 5, the graphics of monomolecular growth model and its ninth degree series expansion overlap. It also seems that eighth degree polynomial shows better approach.

But as the number of data points increases, it can be met with some approach problems. For example, if we add the points (10,25) and (11,27), it can be seen that the graphics of tenth and eleventh degree polynomial approximations exclusively deviate from the data endpoints. This situation is presented in the following figure (Fig. 6).

In addition to the points (10,25) and (11,27) if we also add the points (12,28), (13,31), (14,34), (15,36), (16,39), (17,42),

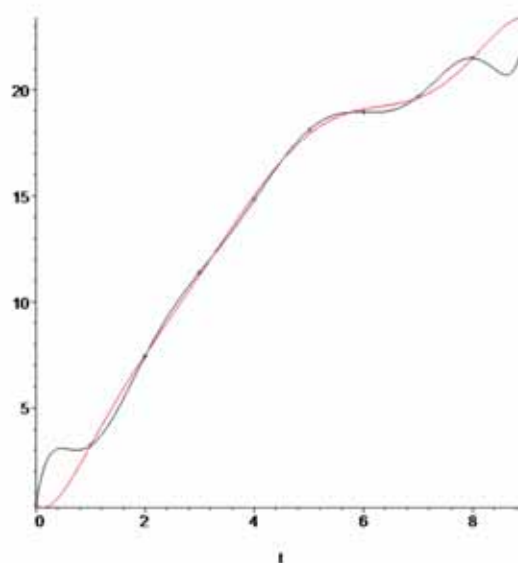


Figure 4. Eighth degree (red) and ninth degree (black) polynomial approximation

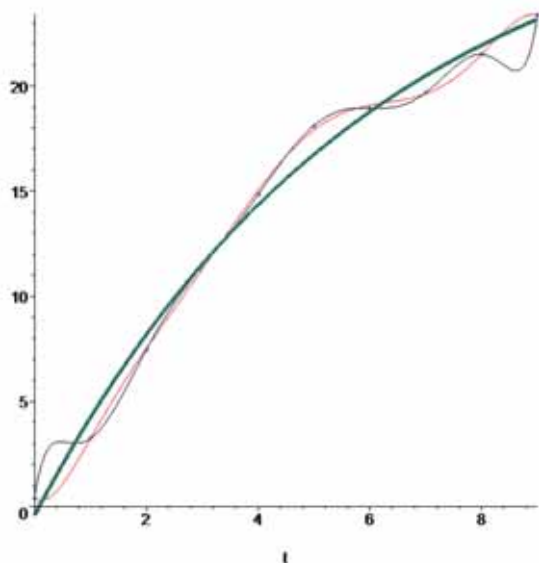


Figure 5. Monomolecular growth model (blue) and its ninth degree series expansion w.r.t. (t-0) (green) with eighth degree (red) and ninth degree (black) polynomial approximations

(18,46) and (19,52), it can be seen that although the graphic of tenth degree polynomial approximation exclusively deviates from the data endpoints, the graphics of eighteenth and nineteenth degree polynomial approximations have huge irreparable deviations from the data points. This situation is also presented in the following figure (Fig. 7).

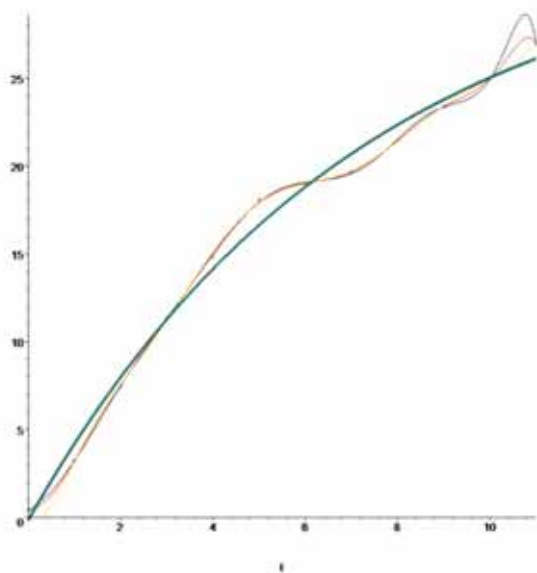


Figure 6. Monomolecular growth model (blue) and its eleventh degree series expansion w.r.t.(t-0) (green) with ninth degree (yellow), tenth degree (red) and eleventh degree (black) polynomial approximations

CONCLUSION

It can be said that if there are too many data points especially much more than 10, polynomial approximation

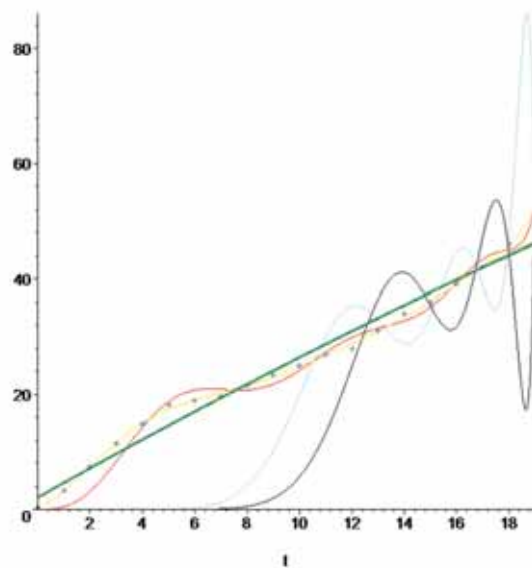


Figure 7. Monomolecular growth model (blue) and its nineteenth degree series expansion w.r.t. (t-0) (green) with ninth degree (yellow), tenth degree (red), eighteenth degree (light blue) and nineteenth degree (black) polynomial approximations

can be much more problematic. However, high degree series expansions of Monomolecular growth model have not any problem. For that reason, polynomial approximation should be used especially when the number of data points is 10 or fewer. Nevertheless, if researcher decides to do polynomial approximation of any model, he can do (n-1)th degree polynomial approximation where n is the number of data points. Although R^2 of (n-1)th degree polynomial is closer or equal to one, in order to see whether there is any deviation particularly at endpoints or not he must draw the graph of the polynomial function. If there is any deviation for (n-1)th degree polynomial approximation, (n-2)th degree series expansion and its R^2 should be used.

References

1. Fitzpatrick P. Advanced Calculus (Just the facts 101), Cram 101 Publishing, 2014.
2. Brody B. Bioenergetics and Growth, Reinhold Publishing Corporation, New York 1945.
3. Fabens AJ. Properties and fitting of the Von Bertalanffy growth curve. Growth Development and Aging, 29 (1965):265-289.
4. Bethard GL. A micro-computer Simulation to Evaluate Management Strategies For Rearing Dairy Replacements, Faculty of the Virginia Polytechnic Institute and State University (Ph.D. Thesis), 1997.
5. Yıldızbakan A. Analysis on Mathematical Models of Tree Growth and Comparison of These Models, University of Çukurova, Institute of Natural and Applied Sciences, Master of Science Thesis, Adana, 50p (in Turkish), 2005.
6. Gülbaba AG. Okalıptüste (Eucalyptus camaldulensis Dehn.) Genetic Improvement Works: Six-month results of Clone Trial, DOA Journal (in Turkish), Tarsus, 8(2002), 17-32.

Combinations of Interleukin-10 Gene Promoter Polymorphisms with -1082A, -819T, -592A Minor Allele are Associated with Sinonasal Polyposis.

Sibel Ozdas

Adana Science and Technology University, Department of Bioengineering, Adana, TURKEY

ABSTRACT

Sinonasal polyposis (SP) is an inflammatory disease involving multiple etiologies and pathogenesis. The disarray of Interleukin (IL)-10 is associated with a raised immunopathological response during the progression of many autoimmune diseases as well as the response to infection. We studied the possible role of the single nucleotide polymorphisms (SNPs) in IL-10 gene and their genotypic combinations in the SP pathogenesis. The IL-10's promoter was genotyped in 200 participants (100 patients and 100 controls). The sites that were encompassed -1082, -819, and -592 SNP regions of extracted DNAs were analyzed by sequencing for polymorphisms. The IL-10 gene promoter polymorphisms with -1082A, -819T, -592A minor alleles, their heterozygotes and homozygotes mutant genotypes had significantly higher risks for SP ($P < 0.05$). Also, haplotype analysis demonstrated that the GTC, ACC, and GCA haplotypes in IL-10 were high-risk of SP but ATA was only in controls ($P = 0.007$). Also, the multifactor dimensionality reduction (MDR) analysis indicated that the IL-10-1082_-819 and -1082_-819_-592 were the best predictive models for SP with 66.6% and 69% accuracy, respectively. IL-10 genotypic variations and their combinations are linked with a high-risk for the SP development in the Turkish population. The IL-10 genetic polymorphisms may lead to SP by altering the arrangement of the gene expression, affecting the severity of the inflammatory response.

Keywords:

Sinonasal polyposis; IL-10 gene; Single nucleotide polymorphisms; Interaction; Multifactor dimensionality reduction.

INTRODUCTION

Sinonasal polyposis (SP) is a chronic inflammation of the sinonasal mucosa. Chronic sinusitis, odor loss headache and nasal obstruction are among the clinical symptoms of SP with low life quality among the patients. Sinonasal polyposis is often accompanied by allergic rhinitis, allergy, aspirin susceptibility and asthma [1]. SP has been implicated in many immunological pathways and is a localized manifestation of systemic disorders [2,3]. SP cases frequently accompanied by T helper (Th) type 1-, Th2-, or Th17-biased inflammatory processes regulated by increased expression levels of a number of cytokines with pro- and anti-inflammatory activities [4]. However, the underlying etiology of SP is multifactorial. Also the pathogenesis of SP is still unexplained.

Interleukin (IL)-10 is a crucial Th2 group anti-inf-

lammatory cytokine. IL-10 plays an important role in defense against host pathogens, protection against excessive tissue damage, and development of immune response [5,6]. Since the increased IL-10 gene expression triggers local inflammatory response that result in increased tissue damage, it has been associated with many chronic inflammatory diseases. Various studies have demonstrated that the levels of IL-10 in serum [7], blood [8], nasal secretion [9] and tissue samples significantly increased [10]. In addition, Xu et al [11] had shown an increase in IL-10 mRNA level and had claimed that it could have played a role in SP pathogenesis.

The IL-10 gene has single nucleotide polymorphisms (SNPs), and the vast majority of these are found in the promoter region. The SNPs at sites -1082, -819 and -592 in the IL-10 gene show strong linkage disequilibrium.

Article History:

Received: 2018/02/13

Accepted: 2018/04/04

Online: 2018/04/27

Correspondence to: Sibel Özdas,
Adana Science and Technology University,
Department of Bioengineering, 01250,
Adana, TURKEY

E-Mail: sozdas@adanabtu.edu.tr

Phone: +90 505 511 89 47

Fax: +90 322 455 00 09

Table 1. The primer's designs

SNP position	Direction	Primers	Fragment size
-1082	Forward	5'-ACACACACACAAATCCAAG-3'	277 bp
	Reverse	5'-TAGGAGGTCCCTTACTTTCTC-3'	
-819	Forward	5'-CTCTAAGGCCAATTTAATCCAAGGTTT-3'	215 bp
	Reverse	5'-GAAGTCGTTACGTCATGATGAGAAGG-3'	
-1082	Forward	5'-AAATCGGGGTAAGGAGC-3'	270 bp
	Reverse	5'-AGCAGCCCTCCATTTACT-3'	

SNP: Single-nucleotide polymorphism; bp: base pairs

ilibrium leading to variations in expression level and are associated with various disease pathogenesis [12,13].

We studied the IL-10 -1082, -819, and -592 SNPs and their genotypic combinations in SP patients and controls to investigate the role of IL-10 in pathogenesis of SP in this study.

METHODS

Subjects

The samples used in this study were obtained from the individuals who were admitted to otorhinolaryngology clinic. One hundred (mean age 45.5945 ± 10.031 ; range: 22-64 years) patients with SP were included. Patients were received to the clinic with complaints of nasal obstruction/congestion, loss or reduction of smell, facial pressure and poor quality of life. The patients were diagnosed with nasal endoscopic examination as SP [3]. In the last four weeks, The patients that had an acute upper respiratory tract infection, cystic fibrosis, inverted papillomas, fungal sinusitis, and antrochoanal polyps were not included in the study.

According to the Lund-Mackay system, computed tomography scanning of paranasal sinus were acquired and evaluated [14]. The size of the polyp was classified according

to the Lidtholdt scale [15]. The presence of asthma and aspirin susceptibility were assessed in the clinical history and the allergy presence was assessed by prick skin test.

A 100 (mean age 44.62 ± 11.615 ; range 18-63 years) healthy volunteer subjects with no history of sinonasal disorder, inflammatory-related disorder or any other disease was included in the control group. In addition, absence of rhinosinusitis and SP were confirmed with the nasal endoscopic examination. The study has ethics committee approval.

Genotyping

The genomic DNA was extracted from blood sample with kit (Qiagen Inc.). The polymerase chain reaction (PCR) for direct sequencing was used to amplify specific regions of the IL-10 gene's promotor and primer's designs were summarized in Table 1.

The PCR reaction mixture (25 μ L) constituted of 0.5 μ L dNTP (10 μ M concentration), 1 μ L forward and reverse primer (5 μ M), 0.2 μ L SuperHot Taq DNA polymerase (Bioron Inc.), 5 μ L 10x PCR buffer (Bioron Inc.) and 2.5 μ L template DNA (20-50 ng/ μ L). Thermal conditions of the PCR was followed by initial-denaturation at 95°C for 10 min, denaturation at 95°C for 45 sec, annealing at 60°C for 45 sec, extension at 72°C for 45 sec. Also the final extension was at 72°C for 10 min. The amplified products were verified by 2% agarose gel

Table 2. Clinical characteristics of subjects

Clinical characteristics	Patients with SP (n: 100)	Controls (n: 100)	P value
Age, years	45.59 \pm 10.031	44.62 \pm 11.615	> 0.05
Gender, Male/Female	49/51	44/46	> 0.05
Computed tomography score	8,58 \pm 3,994 (4-19)	-	-
Asthma presence, n (%)	34 (34)	0 (0)	< 0.001
Aspirin intolerance presence, n (%)	19 (19)	0 (0)	< 0.001
Allergy presence, n (%)	35 (35)	0 (0)	< 0.001
	1	40 (40)	< 0.001
Polyp size, n (%)	2	33 (33)	< 0.001
	3	27 (27)	< 0.001

SP: Sinonasal polyposis

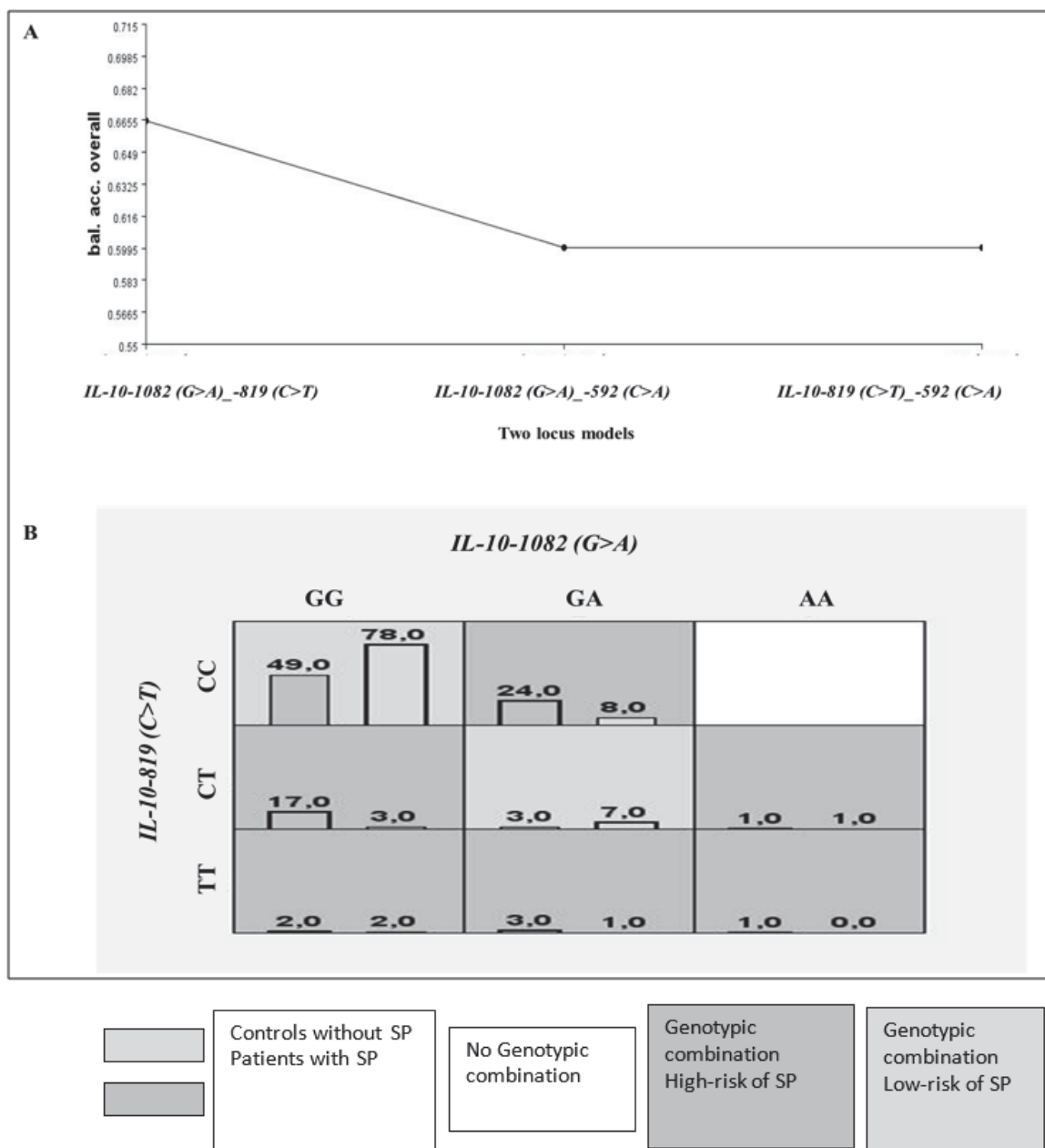


Figure 1. The best predictive models in application of MDR
 A. The graphic shows the character of the interactions between the three SNPs in the IL-10. The strongest interacting pair is the IL-10-1082_{-819} SNPs.
 B. The IL-10-1082_{-819} genotypic combinations which are able to accurately predict SP presence. The IL-10 AA+TT, GG+CT, GA+CC, and GA+TT diplotypes had a ∞ -, 5-, 3-, and 3-fold elevated risk for developing SP. However but only patients with SP but also controls had the AA+CC diplotype (TBA 0.66, CVC 10/10, OR 5.18, 95% CI 2.60-10.20, P= 0.001)

electrophoresis ethidium bromide was used to stain DNA fragments in the gel for visualization.

PCR products were purified and sequenced. The sequencing reaction mixture (20 μ L) constituted of 2 μ L purified PCR product, 1.2 μ L forward and reverse primer (5 μ M), 2 μ L BigDye 3.1 reaction mix (Applied Biosystems Inc.), 4 μ L of 5x reaction buffer (Applied Biosystems Inc.). PCR product thermal conditions comprised of an at 95°C for 20 seconds

(50 cycles/minute), followed by 25 seconds at 50°C (50 cycles/minute), and 2 minutes at 72°C.

Capillary electrophoresis was performed using ABI 3130 (Applied Biosystems Inc.) capillary electrophoresis device and in accordance with the manufacturer's protocol. Electroforegrams were analyzed by using SeqScape 2.5.0 (Applied Biosystems Inc.) software and sequence variations were determined.

Statistical analysis

SPSS version 16.0 was used for statistical analysis. The genotypic distributions were checked consistency with Hardy-Weinberg-Equilibrium (HWE) [16]. The genotypic and haplotypic frequencies were evaluated using a software (<http://bioinfo.iconologia.net/SNPstats>) [17]. P-value<0.05 was considered significant. The Multifactor Dimensionality Reduction (MDR) package software was performed all potential recognition of SNP-SNP interactions and that are fine identified as playing a significant role in insight complicated properties. MDR has the testing balance accuracy (TBA) and cross-validation consistency (CVC) [18].

RESULTS

SP and control groups were similar in age distribution and gender ($P > 0.05$). The demographic data of the subjects shown in Table 2.

The genotypic distributions in the controls found consistent with the HWE (for -1082 $P = 0.47$; for -819 $P = 0.07$; for -592 $P = 1$). In patients with SP, DNA sequence analysis of the IL-10 gene revealed that in all genetic models carrying the A allele for -1082 (G>A), the dominant and log-addictive genetic model carrying the T allele for -819 (C>T), the genotype frequencies in all other genetic models except the overdominant model bearing the A allele for -592 (C>A) were statistically significant ($P < 0.05$ for all). We also found that the minor allele frequencies for three SNPs were significantly elevated in patients with SP, and summarized in Table 3.

The IL-10 ACC, GTC, GCA haplotype frequencies were higher in patients with SP. Moreover the ATA haplotype was only in patients, but the GTA only in the controls (-1082, -819, -592, respectively) ($P < 0.05$) (Table 4).

MDR analysis was evaluated all potential combinations, and two models for SP's prediction were found. Binary SNP interplay between the best two-locus predictive model IL-10-1082_-819 was detected with a CVC 10/10 and a TBA 66.6% (Fig. 1A). According to this model, individuals with GG+CT and GA+CC, GA+TT diplotypes have 5-, 3- and 3-fold higher SP risks when compared to control group, respectively. On the contrary, GG+CC and GA+CT diplotypes were 1.5 and 2.5-fold higher in controls, respectively [Odds ratio (OR)= 5.18, 95% Confidence interval (CI)= 2.60-10.20, $P = 0.001$]. In Fig. 1, high-risk diplotypes for SP are shown as dark, and protective diplotypes are shown as light gray boxes (Fig. 1B).

The triple SNP interaction between the best tree-locus predictive model IL-10-1082_-819_-592 was detected

with a CVC 10/10 and a TBA 69%. Individuals carrying triplotypes of GG+CT+CA, GG+CT+CC, GA+CC+CC, and GA+CT+CA according to this model have 4-, 6-, 2.3- and 1.5-fold higher SP risks when compared to control group, respectively. In contrast, triplotypes GG+TT+AA, GA+TT+CA and AA+CT+CA were observed only in the controls (OR= 5.9, 95% CI = 3.10-11.40, $P = 0.001$).

DISCUSSION

SP is a complex mucosal inflammatory disorder involving pathogenesis and multiple etiologies. Despite many efforts, the sinonasal polyposis's pathogenesis is still unexplained. Most of the studies indicate cytokine balance leading to inflammation [5]. IL-10, which was previously reported to be up-regulated in inflammatory diseases, has recently been demonstrated to have increased expression levels in nasal fluid and SP mucosa compared to control groups [9-10]. The up-regulated activity of the immune response regulatory IL-10 gene in the inflammatory sinus mucosa has been considered as one of the key mechanisms in polypogenesis. However, there might be a relationship between the polymorphisms that may lead to regulatory defects in the level of IL-10 gene expression and polyp formation that may affect SP susceptibility.

The IL-10 has remarkable genetic polymorphisms, environmental factors together with variations in the promoter region may cause the emergence of a variety of disease phenotypes [12]. IL-10 gene promoter SNPs affect the affinity of a nuclear protein to binding site on promoter, and cause change in the level of gene expression. IL-10 gene -1082, -819, and -592 positions of the proximal promoter are the most studied polymorphisms. The presence of common allelic combinations in these three SNPs, their linkage disequilibrium and varying IL-10 serum levels that depend on their combinations has been confirmed in several studies [12,13].

Malagutti and colleagues found that the IL-10 serum levels in sinonasal polyposis patients were significantly higher, and examined the exonic and intronic regions of the IL-10 by DNA sequencing. In that study, it was reported that some intronic genotypes of the IL-10 were found to be highly frequent in the patients (30%) and that these genotypes might cause high serum levels of IL-10. In advanced studies, it has been reported that the genetic polymorphisms of promoter and regulatory region in the IL-10 may be critical in the polyp genesis of sinonasal polyposis patients [19,20]. However, far as we know, there is no study investigating the relationship between the IL-10 gene SNPs -1082, -819, -592 and SNP-SNP interactions SP pathogenesis in the literature. In this study, the IL-10 gene SNPs -1082, -819, -592 and their genotypic combinations in 100 SP patients and 100 volunteer-healthy controls in the Turkish population were

Table 3. The genotyping distributions for promotor SNPs in IL-10 gene

SNPs	Genotype_ Allele	Patients with SP (n: 100) n (%)	Controls (n: 100) n (%)	Genetic Models	Odds ratio (%95 CI)	Minor allele frequencies	P value	P value for HWE
-1082 (G>A)	GG	68 (68)	83 (83)	Codominant	1.00 (Reference)	0.33-0.97	0.037	0.47
	GA	30 (30)	16 (16)		0.43 (0.19-0.87)			
	AA	2 (2)	1 (1)		0.50 (0.15-6.57)			
	GG	68 (68)	83 (83)	Dominant	1.00 (Reference)	0.017		
		GA+AA	32 (32)		17 (17)		0.43 (0.21-0.89)	
	GG+GA	98 (98)	99 (99)	Recessive	1.00 (Reference)	0.72		
		AA	2 (2)		1 (1)		0.56 (0.16-6.99)	
	GG+AA	70 (70)	85 (85)	Overdominant	1.00 (Reference)	0.019		
		GA	30 (30)		15 (15)		0.41 (0.21-0.89)	
	---	---	---	Log-addictive	0.44 (0.21-0.99)	0.022		
A‡	0.17	0.09	1.256 (1.189-1.331)		0.028			
-819 (C>T)	CC	73 (73)	86 (86)	Codominant	1.00 (Reference)	0.16-0.70	0.19	> 0.05
	CT	21 (21)	11 (11)		0.41 (0.19-1.00)			
	TT	6 (6)	3 (3)		0.35 (0.03-1.90)			
	CC	73 (73)	86 (86)	Dominant	1.00 (Reference)	0.031		
		CT+TT	27 (27)		14 (14)		0.41 (0.19-0.94)	
	CC+CT	94 (94)	97 (97)	Recessive	1.00 (Reference)	0.27		
		TT	6 (6)		3 (3)		0.41 (0.07-2.09)	
	CC+TT	98 (98)	88 (88)	Overdominant	1.00 (Reference)	0.081		
		CT	21 (21)		12 (12)		0.49 (0.21-1.13)	
	---	---	---	Log-addictive	0.51 (0.27-1.00)	0.036		
T‡	0.16	0.08	1.257 (1.175-1.334)		0.023			
-592 (C>A)	CC	81 (81)	92 (92)	Codominant	1.00 (Reference)	0.26-1	0.016	> 0.05
	CA	14 (14)	8 (8)		0.45 (0.15-1.26)			
	AA	5 (5)	0 (0)		0.00 (0.00-NA)			
	CC	81 (81)	92 (92)	Dominant	1.00 (Reference)	0.022		
		CA+AA	19 (19)		8 (8)		0.33 (0.15-0.93)	
	CC+CA	95 (95)	100 (100)	Recessive	1.00 (Reference)	0.016		
		AA	5 (5)		0 (0)		0.00 (0.00-NA)	
	CC+AA	86 (86)	92 (92)	Overdominant	1.00 (Reference)	0.15		
		CA	14 (14)		8 (8)		0.49 (0.18-1.34)	
	---	---	---	Log-addictive	0.34 (0.16-0.86)	0.0082		
A‡	0.12	0.04	1.159 (1.101-1.216)		0.048			

SNP: Single-nucleotide polymorphism; n (%): Frequency; CI: Confidence interval; HWE: Hardy-Weinberg Equilibrium
‡ Minor risk allele

investigated.

In this study, DNA sequence analysis of the IL-10 gene's promoter in patients with SP revealed 32% of position -1082

guanine into adenine (c.-1082 G>A), 27% of position -819 cytosine into thymine (c.-819 C>T) and 19% of position -592 cytosine into adenine conversions (c.-592 C> A). The allele frequencies of -1082A, -819T, -592A in patients with SP

Table 4. The haplotypes distributions for promotor SNPs in IL-10 gene

Haplotype IL-10 (-1082_-819_-592)	Haplotype frequencies		Odds ratio (95% CI)	P value*
	Patients with SP	Controls		
GCC	0.6125	0.7902	1.00 (Reference)	0.20
ACC	0.1142	0.0907	0.62 (0.29 - 1.30)	0.18
GTC	0.0988	0.0724	0.59 (0.27 - 1.25)	0.010
GCA	0.1184	0.0277	0.24 (0.08 - 0.71)	<0.0001
GTA	0	0.0127	-	<0.0001
ATA	0.0619	0	-	---

SP: Sinonasal polyposis; CI: Confidence interval;

*P-value= 0.0071

were 0.17, 0.16, 0.12, while the allele frequencies in control were 0.09, 0.08 and 0.04, respectively. Minor allele frequencies are high and significant in the patients according to databases (www.ncbi.nlm.nih.gov/snp; www.hapmap.org). Wide variation has been also recorded in the frequencies of IL-10 gene's promoter SNPs among distinct populations. Despite the fact that the global prevalence notified of the allele frequencies of -1082, -819, and -592 SNPs in IL-10 gene in control groups vary, and they are same to last studies in Turkish society [13, 21, 22].

In addition, the current study, the effect of IL-10 gene promoter SNPs on clinical heterogeneity of the disease was investigated by separating the patient group into subgroups according to clinical characteristics such as CT score, asthma presence, aspirin susceptibility, allergy presence and polyp phase, and no connection was observed.

The frequencies of IL10-1082GA, AA, GA-AA and AA genotypes containing the minor allele were found to be higher and statistically significant compared to IL-10-1082GG, GG-GA and GG-AA genotypes in SP patients. Furthermore, the frequency of IL10-819CT, TT genotypes containing the minor allele was found to be higher and statistically significant compared to IL-10-819CC, CC-CT and CC-TT genotypes in patients with SP. The IL-10-592CA, AA, CA-AA genotypes's frequency containing the minor allele were higher and statistically significant compared to IL-10-592CC, CC-CA genotypes in SP patients. MDR showed that the individual with the IL-10-1082_-819 GG+CT, GA+CC, GA+TT diplotypes had 5-, 3- and 3-fold risk of developing SP, respectively.

The estimated frequency of haplotypes formed by the investigated SNPs was calculated in the control and patient groups. The haplotypes GCC, ACC and GCA were commonly observed whereas ATA and GTA haplotypes were less frequent (< 0.01). The distribution of haplotypes was significantly different between patients and controls. Based on the most common haplotype (GCC) in the control group,

the probability rate of other haplotypes was assessed. When compared, a significant difference was observed between the patient and the control group for ACC, GTC and GCA haplotypes. This data show that those carrying the ACC, GTC and GCA haplotypes are at a greater risk of developing SP than those carrying the GCC haplotype. The disease is not associated with a single mutation or allelic variation, but may occur with the common effect of multiple SNPs or mutations. When rare alleles come together, they can prepare the ground for disease. These rare alleles with the contribution of environmental factors may also be critical in the pathogenesis of the disorder [23]. However, considering these haplotypes and their frequencies, further research is needed to reach a definite conclusion. According to the tree-locus model MDR analysis, GG+CT+CC, GG+CT+CA, GA+CC+CC and GA+CT+CA triplotype had 6-, 4-, 2.3- and 1.5-fold risk of developing SP.

The haplotypes of the IL-10 gene SNPs also show ethnic differences. These polymorphisms may constitute a variety of haplotypes, but generally only three haplotypes (ATA, ACC, GCC) with GCC (50-52%) as the most common have been identified [24,25]. In the previous studies, haplotypes were shown to be the combinations carrying GCC, ACC, or ATA alleles at IL-10-1082, -592 junctions [7, 8, 12]. The haplotypes and their frequencies found in our study are consistent with the literature.

We have analyzed the best dual IL-10-(-1082_-819) and triple IL-10-(-1082_-819_-592) locus models in MDR analysis and p value was found to be 0.001 in both. Among the dual locus models, the IL-10-1082_-819 model showed a high (66%) predictive value in SP diagnosis compared to other SNP-SNP interactions. In addition, in dual and triple locus models, for individuals carrying diplotypes and/or triplotypes involving the minor allele of SNPs, the SP risk was found to be significantly higher than control group. MDR data is consistent with genotype and haplotype analysis results. However, the observation of higher frequency GG+CC and GA+CT diplotypes in SP in the dual locus

model, and the presence of GG+TT+AA triplotype only in the control group in the triple locus model emphasize the protective effect of the -1082G allele. Previous studies have reported a significant decrease in the amount of serum IL-10 in individuals carrying the IL-10-1082A allele compared to those carrying IL-10-1082G alleles and that the -1082 allele has a predictive value in determining IL-10 secretion levels [7, 8, 12].

In studies related to SP pathogenesis it was reported that there was an unbalance between Th1 and 2 cytokines including IL-10 (Th1/Th2) ratio, and IL-10's levels in serum were especially high in eosinophilic sinonasal polyposis and allergic or asthmatic sinonasal polyposis [7,19]. In our study, although the level of IL-10 serum was not investigated, 34% of patients with SP were asthmatic, 19% were aspirin sensitive and 35% were allergic.

Understanding the clinical characteristics of SP patients with IL-10 gene promoter SNPs may provide important clinical data for follow-up of the patient's disease progression and treatment. Although the literature on the IL-10 gene is quite extensive, there has been no published study investigating the sinonasal polyp-linkage of promoter genotypic variations and their interactions with each other yet. Although our study was the first community-based study of the IL-10 gene promoter SP patients, our results were limited due to the low sample number and financial problems. The number of samples in community-based studies is an important constraint, and further studies involving more subjects may increase the reliability of the data or the results may change. For this reason, our results carry preliminary meaning for future studies.

CONCLUSION

In conclusion, the IL-10's genotypic variations in SP patients were examined. The genotypes and haplotypes including the -1082A, -819T and -592A minor alleles that were associated with SP susceptibility, affecting the level of genetic expression, altering the severity of inflammation and contributing to SP development were identified in our study. Further work including functional studies evaluating the effect of hereby reported IL-10 gene promoter nucleotide variations on the amount of protein and including higher number of subjects to investigate the relationship between this variation and the pathogenesis of inflammatory diseases are required.

ACKNOWLEDGMENT

This work was supported by The Turkey Ministry of Health through a research Grant No16103018 (2015/SA-GEM/0005)

References

1. Cingi C, Demirbas D, Ural A. Nasal polyposis: an overview of differential diagnosis and treatment. *Recent Patents Inflammation Allergy Drug Discovery* 5 (2011) 241-252.
2. Hulse KE, Stevens WW, Tan BK, Schleimer RP. Pathogenesis of nasal polyposis. *Clinical and Experimental Allergy* 45 (2015) 328-346.
3. Riechelmann H, Europäischen Akademie für Allergie und Klinische Immunologie (EAACI) und der European Rhinologic Society (ERS). [Chronic Rhinosinusitis - EPOS 2012 Part I]. *Laryngorhinootologie* 92 (2013) 193-201; quiz 202-3.
4. Kato A. Immunopathology of chronic rhinosinusitis. *Allergology International* 64 (2015) 121-130.
5. Iyer SS, Cheng G. Role of interleukin 10 transcriptional regulation in inflammation and autoimmune disease. *Critical Reviews In Immunology* 32 (2012) 23-63.
6. Ouyang W, Rutz S, Crellin NK, Valdez PA, Hymowitz SG. Regulation and functions of the IL-10 family of cytokines in inflammation and disease. *Annual Review of Immunology* 29 (2011) 71-109.
7. Ozkara S, Keles E, Ilhan N, Gungor H, Kaygusuz I, Alpaz HC. The relationship between Th1/Th2 balance and 1alpha,25-dihydroxyvitamin D(3) in patients with nasal polyposis. *European Archives of Otorhinolaryngology* 269 (2012) 2519-2524.
8. Shen Y, Hu GH, Kang HY, Tang XY, Hong SL. Allergen induced Treg response in the peripheral blood mononuclear cells (PBMCs) of patients with nasal polyposis. *Asian Pacific Journal of Allergy and Immunology* 32 (2014) 300-307.
9. Kim DW, Eun KM, Jin HR, Cho SH, Kim DK. Prolonged allergen exposure is associated with increased thymic stromal lymphopoietin expression and Th2-skewing in mouse models of chronic rhinosinusitis. *Laryngoscope* 126 (2016) E265-72.
10. Okano M, Fujiwara T, Kariya S, Higaki T, Haruna T, Matsushita O, Noda Y, Makihara S, Kanai K, Noyama Y, Taniguchi M, Nishizaki K. Cellular responses to Staphylococcus aureus alpha-toxin in chronic rhinosinusitis with nasal polyps. *Allergology International* 63 (2014) 563-573.
11. Xu J, Han R, Kim DW, Mo JH, Jin Y, Rha KS, Kim YM. Correction: Role of Interleukin-10 on Nasal Polypogenesis in Patients with Chronic Rhinosinusitis with Nasal Polyps. *PLoS One* 11 (2016) e0161013.
12. Trifunović J, Miller L, Debeljak Ž, Horvat V. Pathologic patterns of interleukin 10 expression- a review. *Zagre: Croatian Society for Medical Biochemistry and Laboratory Medicine* 25 (2015) 36-48.
13. Özdaş S, Özdaş T, Acar M, Erbek SS, Köseoğlu S, Göktürk G, Izbirak A. Association of Interleukin-10 gene promoter polymorphisms with obstructive sleep apnea. *Sleep Breath* 20 (2016) 855-866.
14. Lund VJ, Mackay IS. Staging in rhinosinusitis. *Rhinology* 31 (1993) 183-184.
15. Lildholdt T, Rundcrantz H, Lindqvist N. Efficacy of topical corticosteroid powder for nasal polyps: a double-blind, placebo-controlled study of budesonide. *Clinical Otolaryngology and Allied Sciences* 20 (1995) 26-30.
16. Lee WC. Testing for Sufficient-Cause Gene-Environment Interactions Under the Assumptions of Independence and Hardy-Weinberg Equilibrium. *American Journal of Epidemiology* 182 (2015) 9-16.
17. Moradi MT, Khazaei M, Khazaei M. The effect of catalase C262T gene polymorphism in susceptibility to ovarian cancer in Kermanshah province, Western Iran. *Journal of Cases in Obstetrics & Gynecology* 8 (2018) 1-5.

18. Moore JH, Andrews PC. Epistasis analysis using multifactor dimensionality reduction. *Methods in Molecular Biology* 1253 (2015) 301-314.
19. Malagutti N, Stomeo F, Pelucchi S, Ronchin R, Ceccon M, Malacrida G, Ciorba A, Pastore A, Borin M, Rizzo R. Analysis of IL-10 gene sequence in patients with sinonasal polyposis. *International Journal of Immunopathology and Pharmacology* 28 (2015) 434-439.
20. Zhang ML, Ni PH, Cai CP, Chen NJ, Wang SL. Association of susceptibility to chronic rhinosinusitis with genetic polymorphisms of IL-4 and IL-10. *Zhonghua Er Bi Yan Hou Tou Jing Wai Ke Za Zhi* 47 (2012) 212-217.
21. Fidancı ID, Zülfikar B, Kavaklı K, Ar MC, Kılınc Y, Başlar Z, Çağlayan SH A polymorphism in the IL-5 gene is associated with inhibitor development in severe hemophilia A patients. *Turkish Journal of Hematology* 31 (2014) 17-24.
22. Nursal AF, Pehlivan M, Sahin HH, Pehlivan S. The Associations of IL-6, IFN- γ , TNF- α , IL-10, and TGF- β 1 Functional Variants with Acute Myeloid Leukemia in Turkish Patients. *Genetic Testing and Molecular Biomarkers* 20 (2016) 544-551.
23. DiStefano JK, Kingsley CB. Identification of Disease Susceptibility Alleles in the Next Generation Sequencing Era. *Methods in Molecular Biology* 1706 (2018) 3-16.
24. Reynard MP, Turner D, Navarrete CV. Allele frequencies of polymorphisms of the tumour necrosis factor-alpha, interleukin-10, interferon-gamma and interleukin-2 genes in a North European Caucasoid group from the UK. *European Journal of Immunogenetics* 27 (2000) 241-249.
25. Kalish RB, Vardhana S, Gupta M, Perni SC, Witkin SS. Interleukin-4 and -10 gene polymorphisms and spontaneous preterm birth in multifetal gestations. *American Journal of Obstetrics and Gynecology* 190 (2004) 702-706.



Development of Bismuth Telluride Nanostructure Pellet for Thermoelectric Applications

Hayati Mamur¹ M.R.A. Bhuiyan²

¹Department of Electrical and Electronics Engineering, Manisa Celal Bayar University, Manisa, Turkey

²Department of Electrical and Electronic Engineering, Islamic University, Kushtia, Bangladesh

ABSTRACT

The bismuth telluride (Bi_2Te_3) nanostructure powders and pellet was successfully developed for thermoelectric applications by using a simple chemical process. Several characterization tools such as X-ray diffraction (XRD), scanning electron microscopy (SEM), energy dispersive X-ray (EDX), atomic force microscopy (AFM) and Fourier transform infrared (FT-IR) spectrometry were carried out. The XRD, SEM, EDX, and FTIR analyses showed that the chemical structure of pellet is Bi_2Te_3 . The average crystalline size of the Bi_2Te_3 pellet is found to be 3.93 nm, as determined by the SEM. The AFM studies confirmed that the pellet is of nanostructure form and average surface roughness value is 68.06 nm. This is within the roughness range which can lead to an enhancement in thermoelectric properties of Bi_2Te_3 nanostructure. This could be evidenced by thermal conductivity which should be higher than the electrical conductivity.

Keywords:

Bismuth telluride (Bi_2Te_3); Nanostructure pellet; Chemical process; Microstructural properties; Thermoelectric

Article History:

Received: 2017/10/19

Accepted: 2018/05/01

Online: 2018/05/24

Correspondence to: Hayati Mamur,
Department of Electrical and Electronics
Engineering, Manisa Celal Bayar
University, Manisa, Turkey
E-Mail: hayati.mamur@cbu.edu.tr

INTRODUCTION

The bismuth telluride (Bi_2Te_3) is an efficient thermoelectric (TE) semiconductor type material. When the post transition metal elements of bismuth (Bi) is alloyed with a metalloid non-metal elements of tellurium (Te) then it makes a compound semiconductor material, Bi_2Te_3 . An acceptable TE material is indicated by large density and mobility of charge carriers, at the coinciding by the low thermal conductivity and high electrical conductivity. Another attractive aspect is that the efficient energy conversion adaptability of a TE material is performed by the extensive dimensionless figure of merit: $ZT = (S^2\sigma T)/K$, where S is the Seebeck coefficient, σ is the electrical conductivity, K is the thermal conductivity and T is the temperature.

Nowadays, Bi_2Te_3 nanostructure has a great deal of interest in thermoelectric applications such as thermoelectric heating and cooling, thermoelectric generators and portable power supply [1-10]. Recent studies suggest that Bi_2Te_3 material usage in nanostructure form generates the higher ZT (from 0.62 to 1.13) values [11-17].

However, there are few studies about this [18,19]. For this reason it is a challenging task to develop the single crystal Bi_2Te_3 nanostructure materials. Development of the nanostructured thermoelectric material is firmly connected to the capability to find out the microstructural and optical characterization.

In this paper, a simple chemical method was tried to develop the Bi_2Te_3 nanostructure pellet for thermoelectric applications. In the studies presented previously [20-23], this method was compared with other electrochemical synthesis methods. Ultimately, the recommended method was suitable for the producing nanostructure material. Furthermore, the superiority of this method was demonstrated via comparing with other methods in two reviewed papers [24, 25]. In this paper handling a development of Bi_2Te_3 nanostructure pellet for TE applications, after the first introduction, experimental methods was presented in the second section. In the third section, the results and discussion section was given. Finally, the conclusion and future research section were clarified.

EXPERIMENTAL METHODS

Developed Bi₂Te₃ nanostructure pellet

The reagents of Bi(NO₃)₃·5H₂O (≥98%, Sigma Aldrich) and TeO₂ (≥97%, Sigma Aldrich) were purchased from Sigma Aldrich and used as starting materials for the co-precipitation of a simple chemical solution method. The solvents of HNO₃ (65%, Sigma Aldrich), NaOH (98-100%, Sigma Aldrich), NaBH₄ (98-100%, mark) and Ethanol (Analytical grade, Mark) were also supplied and used without any further purification. In advance of the synthesis of Bi₂Te₃ nanostructure, Bi(NO₃)₃·5H₂O and TeO₂ were employed as the starting materials in this method. The starting materials were taken with stoichiometric ratio of Bi:Te (2:3) for the co-precipitation. NaOH was utilized to precipitates of BiONO₃ and TeO₂ and regulated the pH value of the solution.

The NaBH₄ was used as a reducing agent to remove the oxidation. The chemicals were weighed according to their stoichiometry (Bi₂Te₃=2:3) and were prepared separate metal ion solutions by using 2 mmol (0.97 gm) Bi(NO₃)₃·5H₂O and 3 mmol (0.47 gm) TeO₂. Dissolving these materials was handled in concentrated (2 M = 31.86 ml) HNO₃. A stock solution of (3 M = 30 gm) NaOH was employed for pH value regulated. The two metallic solutions were reserved in one flux (sol. 1) and other flux has been fulfilled with NaOH solution (sol. 2). These two solutions were mixed together at room temperature with adjusted the hydro dynamic atmosphere and complete co-precipitation was developed by magnetic stirring for half an hour. After magnetic stirring, white precipitates were grown in a flux. 150 ml white precipitates were collected and reserved in a borosilicate flux (sol. 3) at 80°C by using the magnetic stirrer for several minutes.

The Bi and Te oxides were eliminated by using NaBH₄. Other flux was fulfilled with 15 mmol (1.134 gm) NaBH₄ solution of 100 ml distilled water at 80°C soluble by magnetic stirrer for 15 minute (sol. 4). The sol. 3 and sol. 4 was blended together at the 80°C temperature with adjusted the same conditions and black colour precipitate was developed by magnetic stirring for four hours to remove the oxidation. The developed black precipitates were collected, washed and separated by centrifuged in several times using ethanol and deionized water to remove the byproducts thereafter dried in an oven at 80°C for 18 hours. In the end, the product powder was put in a 1 cm diameter pellet base and was pressed 5 MPa pressure. Then the formed pellet was heated in a vacuum furnace at 180°C for two hours. Finally, the Bi₂Te₃ nanostructure pellet having 1 cm diameter and 1 mm thickness was made. The manufactured pellets are sequentially shown in Fig. 1.

Experimental techniques

The XRD patterns were recorded by using a X'Pert high score PANalytical diffractometer with Cu-K α radiation, operated at 45 kV and 40 mA, with angular range 05° ≤ 2θ ≤ 85°. The morphology and elemental atomic composition of the pellet was accomplished with a scanning electron microscopy (SEM) and energy dispersive X-ray spectroscopy (EDX) of LEO 1430 VP system. 3D topographic surface were recorded in 0.01 nm discrimination using 10 MP CCD cameras by an atomic force microscopy. BRUKER TENSOR II spectrometry was used for FTIR measurements.

RESULTS AND DISCUSSION

The improvement of the TE materials into next generation devices crucially depends on the improvement of new characterization techniques and theoretical models for the initial understanding of the relationship between the structure and characteristics.

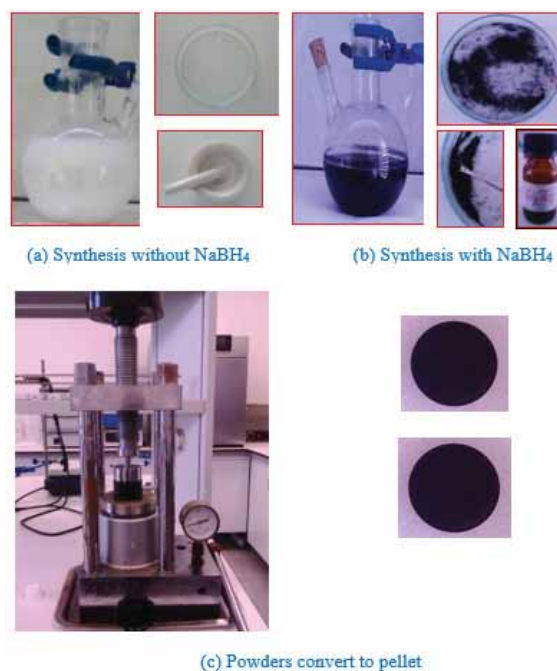
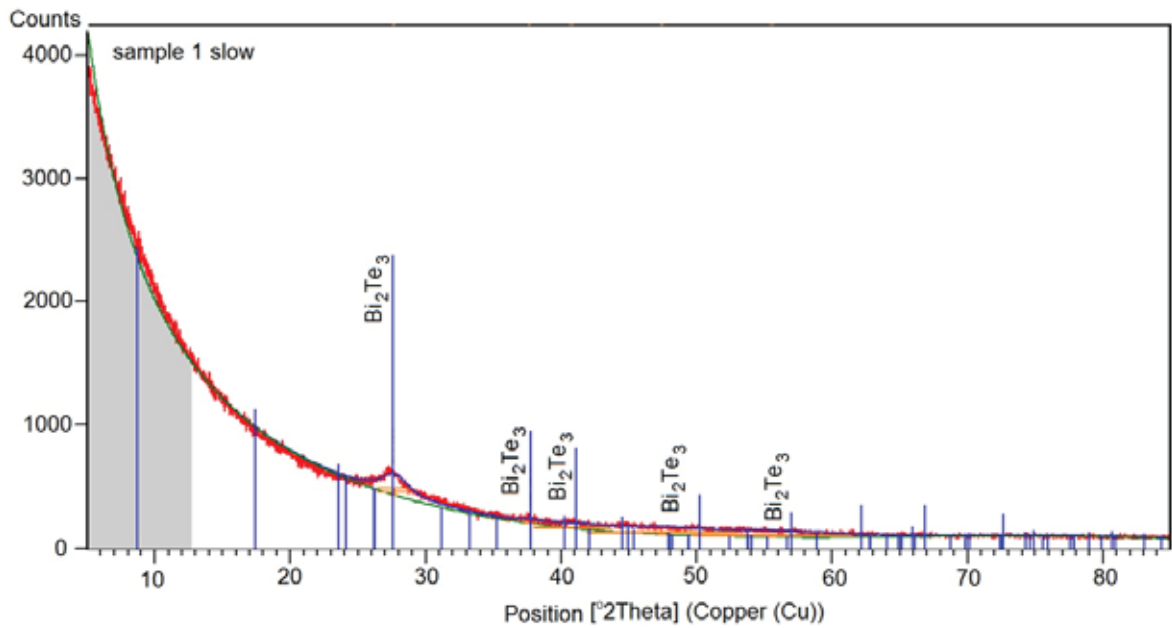
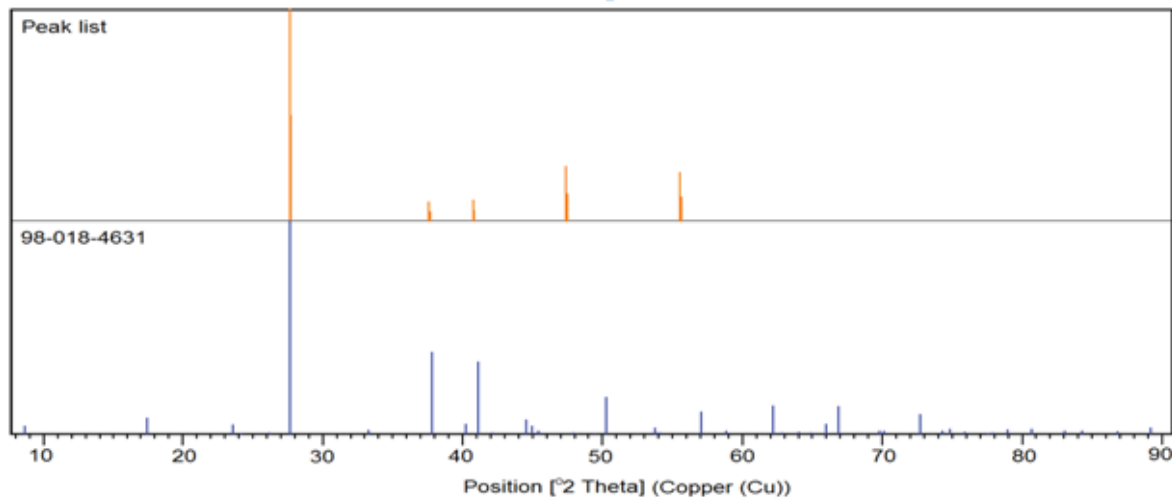


Figure 1. The manufacture of pellets is shown sequentially

The XRD provides complimentary information about the nanostructure materials by showing the average coherence length as a function of direction. Their results are averaged over a large volume giving an overall view of the nanostructure. A typical XRD spectrum of Bi₂Te₃ nanostructure pellet is shown in Fig. 2a. Fig. 2b shows the compare study of the spectrum with a standard reference code 98-018-4631 for Bi₂Te₃.



(a) XRD spectrum



(b) Spectrum is compared with a standard reference code 98-018-4631

Figure 2. XRD spectrum of Bi_2Te_3 nanostructure pellet.

The XRD revealed that the structure was nanocrystalline with a (015) preferred orientation. By using the Scherrer equation [26], simplified by other researcher

$$B_{\text{crystalline}} = \frac{0.94\lambda}{B \cos \theta} \quad (1)$$

where, λ is the wavelength of Cu-K α radiation, and B is the full-width half-maximum (FWHM) of high intensity peak. The unit of B should be converted into radian. Therefore the above equation takes the form:

$$B_{\text{crystalline}} = \frac{50.97\lambda}{B \cos \theta} \quad (2)$$

The calculated value shows the crystalline size. The average crystalline size of the pellet was calculated to be 3.93 nm, which conformed reasonably well to the literature value [27]. The smallest crystallites materials have the lowest thermal conductivity but their high resistivity dominates and has a detrimental effect on the thermoelectric figure of merit, ZT. Recently, due to its capability of converting waste heat into electricity, thermoelectric applications have attracted increasing interest. In this overview, a thermoelectric material with size effect, specifically low dimensional materials is suitable for thermoelectric applications. In order to compare the spectrum with the Bi_2Te_3 nanostructure standard reference code, three peaks (015), (1010) and (110)

were similar. Other two peaks (205) and (2011) were slightly shifted to the reference code. The peaks did not match the Bi_2Te_3 nanostructure. The peaks matched with other oxides form of Bi_2Te_3 materials.

According to the XRD result, the pellets may be some oxidization form. When an atom is oxidized, its characteristics may be change. Every researcher wants to produce oxide free materials that the materials are pure form. In the literature [28], one report was issued that the pure H_2 gas was passed to synthesize Bi_2Te_3 nanostructure throughout the sample at 400°C for 2 hours. In order to overcome or minimize the oxidization and obtain pure Bi_2Te_3 nanostructure pellets, before construct the pellets, it has been recommended that the produced powder should be passed in 99% pure hydrogen (H_2) or nitrogen (N_2) gas at 250°C for 2 hours in a quartz crystal chamber atmosphere.

SEM provides the detailed high resolution images of the specimen by restoring a focused electron beam across the surface and detecting secondary or backscattered electron signals. The signals reveal the information about the specimen including external morphology, chemical composition, crystalline structure and orientation of materials. Fig. 3 shows the SEM image for the morphological and microstructural information about the prepared pellets. The homogeneity of the sample was arranged sequentially. A preliminary electron diffraction study indicated that the samples were quasi spherical granule shapes in agglomerated clusters with crystalline in nature. The results were quite in agreement with the previous report [29].

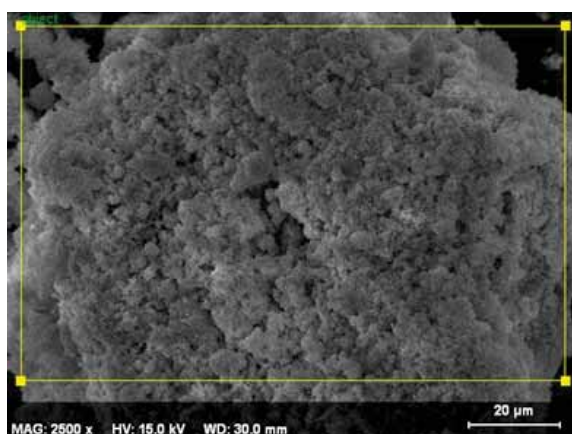


Figure 3. SEM image of Bi_2Te_3 nanostructure pellet

EDX is an x-ray technique used to identify the elemental composition of materials. The systems are attachments to SEM instruments where the image capability of the microscope identifies the specimen of interest. Table 1 shows the elemental atomic composition of the Bi_2Te_3 nanostructure. The materials of Bi and Te were arranged with their atomic stoichiometric ratio (34.62:51.52). From this table, it

was confirmed that ultra-fine device quality Bi_2Te_3 nanostructure pellet has been developed. It is also clear that the pellet contains stoichiometric form of Bi and Te.

Table 1. The atomic composition of the Bi_2Te_3 nanostructure.

Element	Series	Atom.[at.%]
Carbon	K series	3.73
Oxygen	K series	10.13
Bismuth	M series	34.62
Tellurium	L series	51.52
Total: 100.00 %		

Fig. 4 shows the EDX spectrum of the Bi_2Te_3 nanostructure. The materials of Bi and Te were arranged with their stoichiometric (2:3) form. From these curve it was cleared that Bi_2Te_3 nanostructure were developed which was in good agreement with other researchers' report [30]. The spectrum shows the other peck that is carbon and oxygen which indicates the little amount of contamination of the pellet. H_2 gas passing throughout the pellet at $\sim 250^\circ\text{C}$ that the effects of post-depositional contamination. Contamination may be artificially caused, it occurs in the post-depositional environment. It is concerned with removing post-depositional contaminants by isolating the pellet fractions that containing a very small amount of carbon and oxygen.

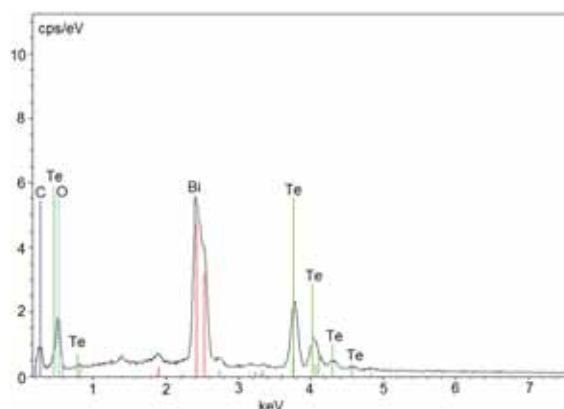


Figure 4. EDX spectrum of Bi_2Te_3 nanostructure pellet

It was also expressed that Bi_2Te_3 nanostructures consisted of Bi and Te. Moreover, same results were also found in the other researcher reports [31]. In this investigation, some other impurities such as carbon and oxygen were observed in this sample. In order to reduce the impurities and the obtained pure Bi_2Te_3 nanostructure pellet, while it is being mixed with the metal solution, the accurate hydro thermal condition was recommended. In here, the previous recommendation indicated the XRD investigation section was followed.

AFM demonstrates a 3D image of the produced pellet surface on a nano scale size by measuring forces between a sharp probe (<10 nm) and surface at very little distance

between 0.2-10 nm probe sample separation. The probe is supported on a flexible cantilever. The AFM tip gently touches the pellet surface and records the small force between the probe and the pellet surface. The sample in the study was prepared the topological surface and measurement the roughness value of the pellet surface. As shown Fig. 5, the AFM measurements were another confirmation that the technology set the standard for the lowest position noise. The surface roughness increases the efficiency of the heat to electricity conversion factor in nanostructure materials. The electronic parts of these conductivities are linearly connected. Therefore, only the phonon part of the thermal conductivity can be manipulated almost independently without effecting very much on the electrical counterpart. In nanostructure materials, the phonon scattering cross section of the rough surfaces dominates all other bulk scattering agents (point defects, dislocation, grain boundaries etc) due to the fact that it has higher weight factor in the sum of surface and bulk contributions. Therefore, ZT may show enhancement if one has rough surfaces in nano size materials. The surface roughness is important in evaluating the performance of a membrane as it may influence the transmembrane transport and fouling potential of nanostructure materials. Therefore, the surface roughness may also correlate with crystalline size.

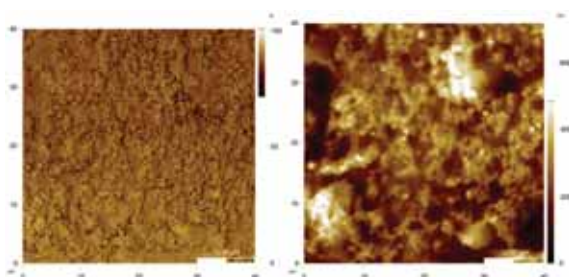


Figure 5. AFM images of Bi_2Te_3 nanostructure pellet

In addition, according to Fig. 5, the AFM studies revealed that the atom arrangement of the pellet was in homogeneous. Furthermore, in Fig. 5, it conformed to the structure in nano crystalline in form [32].



Figure 6. 3D AFM image and roughness parameters of Bi_2Te_3 nanostructure pellet

Fig. 6 gives the 3D view of the pellet. The roughness parameter was observed through Fig. 6. AFM image was not ideally sharp identification. As a consequence, an AFM ima-

ge does not reflect the accurate sample topography, but rather represents the interaction of the probe with the sample upper surface roughness value. The surface roughness at the nano scale plays an important role in determining of the functional performance of the TE devices.

Understanding and characterizing of nano scale roughness was a crucial data to continue the ability exploring and building TE devices at ever smaller length scales. In this observation, the average roughness value was about ~ 68 nm. The results of this investigation were significant because large position noise in a nano positioner could obscure an AFM surface roughness measurement. The nano meter size surface roughness value has been strongly influences the thermoelectric behaviour of nanostructure materials. AFM is especially recommended for the analyses of such nanostructure surfaces with nano meter size irregularities. It was found that variation in surface roughness influences the thermoelectric characteristics of the nanostructure materials even at low surface roughness values (~ 68 nm).

The FTIR spectroscopy is an analytical process used to clarification the organic, polymeric, and in some cases, inorganic materials. The FTIR analysis process uses infrared light to scan the test specimen and investigate the chemical behaviour of the materials. Fig. 7 illustrates the FT-IR spectrum of Bi_2Te_3 nanostructure pellet. Expected peak for the FTIR spectrum of the Bi_2Te_3 nanostructure were absorbed in the bands between 400 and 2366 cm^{-1} which correspond to C-S, C-H, C-O and O-H stretching vibrations. In this observation, the Bi_2Te_3 nanostructure pellet was adjusted the same stretching with the similar bands. In the developed pellet were conformed the nanostructure form according to other researcher reports [33].

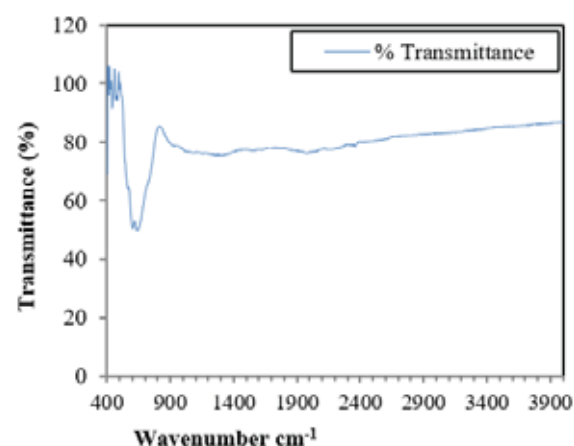


Figure 7. FT-IR spectrum of Bi_2Te_3 nanostructure pellet

On the other hand, the oxygen containing functional groups were almost reduced in the technique of reduction with NaBH_4 and thus the metal ions were transformed into Bi_2Te_3 nanostructure form. Eventually, nanostructure

of material was enhanced the thermoelectric power due to quantum confinement. Size effect was led to carrier confinement. Selective scattering and interface scattering was reduced. The thermal conductivity was improved more than the electrical conductivity; thus the figure of merit was increased.

CONCLUSION AND FUTURE RESEARCH

Current research activities on Bi₂Te₃ nanostructure are developed by using the several processes such as the thermal evaporation, sputtering, lithographic, pulsed laser ablation, simple chemical, electrochemical, grinding, solvothermal and hydrothermal. In this paper, the simple chemical process was employed in terms of financial aspect and potential for very large quantity of productions. The pellet was excited by some oxidization and impurity. In order to minimize the oxidization, a computer controlled pure H₂ or N₂ gas was passed throughout the pellet. It was concluded that by using this method, pure pellets would be produced. Further research recommended that the pellet to measure the electrical and thermal conductivity, Seebeck coefficient and figure of merit for proper utilization in thermoelectric applications.

ACKNOWLEDGEMENT




This work was supported by the Scientific & Technological Research Council of Turkey under grant of TUBİTAK 2221 Fellowship Program, Ref No: 21514107–115.02–E.69236 and Manisa Celal Bayar University Scientific Research Projects Coordination Unit, No: 2016–147.

References

1. Akshay VR, Suneesh MV, Vasundhara M. Tailoring thermoelectric properties through structure and morphology in chemically synthesized n-type bismuth telluride nanostructures. *Inorganic Chemistry* 56 (2017) 6264-6274.
2. Dharmiaiah P, Hong SJ. Thermoelectric properties of Bi₂Te₃ nanocrystals with diverse morphologies obtained via modified hydrothermal method. *Journal of Electronic Materials* 6 (2017) 3012-3019.
3. Dharmiaiah P, Lee C, Madavali B, Hong SJ. Effect of surfactant addition on Bi₂Te₃ nanostructures synthesized by hydrothermal method. *Archives of Metallurgy and Materials* 62 (2017) 1005-1010.
4. Sharma YC, Purohit A. Tellurium based thermoelectric materials: New directions and prospects. *Journal of Integrated Science and Technology* 4 (2016) 29-32.
5. Hong M, Chen ZG, Yang L, Zou J. Enhancing thermoelectric performance of Bi₂Te₃-based nanostructures through rational structure design. *Nanoscale* 8 (2016) 8681-8686.
6. Smith CJW, Cahill JS, Nuhoglu A. Macro to nano: Scaling effects of Bi₂Te₃ thermoelectric generators for applications in space. *PAM Review: Energy Science & Technology* 3 (2016) 86-99.
7. Ng IK, Kok KY, Rahman CCA, Choo TF, Saidin NU. Bismuth telluride based nanowires for thermoelectric power generation. *Materials Today: Proceedings* 3 (2016) 533-537.
8. Razak, ANA, Nor NM, Ibrahim T. Heat energy harvesting for portable power supply. Paper presented at 5th International Conference on Power Engineering and Optimization, Shah Alam, Selangor, Malaysia, 6-7 June. pp 436-439, 2011.
9. Rashad MM, El-Dissouky A, Soliman HM, Elseman AM, Refaat HM, Ebrahim A. Structure evaluation of bismuth telluride (Bi₂Te₃) nanoparticles with enhanced Seebeck coefficient and low thermal conductivity. *Materials Research Innovations* 22 (2017) 1-9.
10. Pradhan S, Das R, Bhar R, Bandyopadhyay R, Pramanik P. A simple fast microwave-assisted synthesis of thermoelectric bismuth telluride nanoparticles from homogeneous reaction-mixture. *Journal of Nanoparticle Research* 19 (2017) 69.
11. Sherchenkov AA, Shtern YI, Shtern MY, Rogachev MS. Prospects of creating efficient thermoelectric materials based on the achievements of nanotechnology. *Nanotechnologies in Russia* 11 (2016) 387-400.
12. Cornett J, Chen B, Haidar S, Berney H, McGuinness P, Lane B, Gao Y, He Y, Sun N, Dunham M, Asheghi M. Fabrication and Characterization of Bi₂Te₃-based chip-scale thermoelectric energy harvesting devices. *Journal of Electronic Materials* 46 (2017) 2844-2846.
13. Ge ZH, Ji YH, Qiu Y, Chong X, Feng J, He J. Enhanced thermoelectric properties of bismuth telluride bulk achieved by telluride-spilling during the spark plasma sintering process. *Scripta Materialia* 143 (2018) 90-93.
14. Gaul A, Peng Q, Singh DJ, Ramanath G, Borca-Tasciuc T. Pressure-induced insulator-to-metal transitions for enhancing thermoelectric power factor in bismuth telluride-based alloys. *Physical Chemistry Chemical Physics* 19 (2017) 12784-12793.
15. Yamashita O, Tomiyoshi S, Makita K. Bismuth telluride compounds with high thermoelectric figures of merit. *Journal of Applied Physics* 93 (2003) 368-374.
16. Fu J, Shen J, Shi H, Liang Y, Qu Z, Wang W. Preparation and characterization of single crystalline structure Sb/Bi₂Te₃ superlattice nanowires. *Micro and Nano Letters* 11 (2016) 738-740.
17. Son JS, Choi MK, Han MK, Park K, Kim JY, Lim SJ, Ho M, Kok Y, Park C, Kim SJ, Hyeon T. n-type nanostructured thermoelectric materials prepared from chemically synthesized ultrathin Bi₂Te₃ nanoplates. *Nano Letters* 12 (2012) 640-647.
18. Ganguly S, Zhou C, Morelli D, Sakamoto J, Brock SL. Synthesis and characterization of telluride aerogels: effect of gelation on thermoelectric performance of Bi₂Te₃ and Bi₂-xSbxTe₃ nanostructures. *The Journal of Physical Chemistry C* 116 (2012) 17431-17439.
19. Sharma S, Schwingenschlöggl U. Thermoelectric response in single quintuple layer Bi₂Te₃. *ACS Energy Letters* 1 (2016) 875-879.
20. Barman SC, Saha DK, Mamur H, Bhuiyan MRA. Growth and description of Cu nanostructure via a chemical reducing process. *Journal of Nanoscience, NanoEngineering & Applications* 6 (2016) 27-31.
21. Bhuiyan MRA, Alam MM, Momin MA, Rahman MK, Saha DK. Growth and characterization of CuInSe₂ nanoparticles for

- solar cell applications. *Journal of Alternate Energy Sources and Technologies* 5 (2014) 13-17.
22. Bhuiyan MRA, Alam MM, Momin MA, Mamur H. Characterization of Al doped ZnO nanostructures via an electrochemical route. *International Journal of Energy Applications and Technologies* 4 (2017) 28-33.
 23. Bhuiyan MRA, Rahman MK. Synthesis and characterization of Ni doped ZnO nanoparticles. *International Journal of Engineering and Manufacturing* 3 (2014) 67-73.
 24. Bhuiyan MRA, Mamur H. Review of the bismuth telluride (Bi₂Te₃) nanoparticle: growth and characterization. *International Journal of Energy Applications and Technologies* 3 (2016) 74-78.
 25. Bhuiyan MRA, Mamur H, Korkmaz F, Nil M. A review on bismuth telluride (Bi₂Te₃) nanostructure for thermoelectric applications. *Renewable & Sustainable Energy Reviews* 82 (2018) 4159-4169.
 26. Burton AW, Ong K, Rea T, Chan IY. On the estimation of average crystallite size of zeolites from the Scherrer equation: A critical evaluation of its application to zeolites with one-dimensional pore systems. *Microporous and Mesoporous Materials* 117 (2009) 75-90.
 27. Scheele M, Oeschler N, Meier K, Kornowski A, Klinke C, Weller H. Synthesis and thermoelectric characterization of Bi₂Te₃ nanoparticles. *Advanced Functional Materials* 19 (2009) 3476-3483.
 28. Saleemi M, Toprak MS, Li S, Johnsson M, Muhammed M. Synthesis, processing, and thermoelectric properties of bulk nanostructured bismuth telluride (Bi₂Te₃). *Journal of Materials Chemistry* 22 (2012) 725-730.
 29. Kim DH, Kim C, Ha DW, Kim H. Fabrication and thermoelectric properties of crystal-aligned nano-structured Bi₂Te₃. *Journal of Alloys and Compounds* 509 (2011) 5211-5215.
 30. Zhao XB, Ji XH, Zhang YH, Cao GS, Tu JP. Hydrothermal synthesis and microstructure investigation of nanostructured bismuth telluride powder. *Applied Physics A* 80 (2005) 1567-1571.
 31. Tezuka K, Kase S, Shan YJ. Syntheses of Bi₂X₃ (X= S, Se, Te) from elements under hydrothermal conditions. *Journal of Asian Ceramic Societies* 2 (2014) 366-370.
 32. Macedo RJ, Harrison SE, Dorofeeva TS, Harris JS, Kiehl RA. Nanoscale probing of local electrical characteristics on MBE-grown Bi₂Te₃ surfaces under ambient conditions. *Nano Letters* 15 (2015) 4241-4247.
 33. Du Y, Cai KF, Shen SZ, An B, Qin Z, Casey PS. Influence of sintering temperature on thermoelectric properties of Bi₂Te₃/Polythiophene composite materials. *Journal of Material Science: Materials in Electronics* 23 (2012) 870-876.

Strain Hardening Behavior Characterization of Dual Phase Steels

Kemal Davut^{1,2}  Caner Şimşir^{2,3}  Barış Çetin⁴ 

¹ Atılım University, Department of Metallurgical and Materials Engineering, Ankara, Turkey

² Atılım University, Metal Forming Center of Excellence, Ankara, Turkey

³ Atılım University, Department of Manufacturing Engineering, Ankara, Turkey

⁴ FNSS Defense Systems Co. Inc., Department of Engineering and Research, Ankara Turkey

ABSTRACT

The requirements for higher passenger safety, improved fuel economy and weight reduction in automobile industry necessitates the usage of advanced high strength steel (AHSS) grades. Dual phase (DP) steels are the most widely used one among AHSS. DP steels become increasingly popular, since they provide a combination of sufficient formability at room temperature and tensile strength over 1000 MPa. The current standards for DP steels only specifies yield and tensile strength. Steels from various producers have considerably different composition and microstructure; however they still have the same grade name. Combined with the inherited heterogeneous microstructure, those steels exhibit different strain hardening behavior. The aim of this study is to evaluate the strain hardening behavior of DP800 steels, obtained from different vendors and thus having different compositions and microstructures. The strain hardening behavior was characterized with tensile tests performed along rolling and transverse directions. The microstructure has been characterized with optical and scanning electron microscopes. The martensite fraction, grain size of ferrite and chemical composition has been correlated to the strain hardening behavior. The results show that the steel with more micro-alloying addition has finer ferritic grain size, which cause higher initial strain hardening rate. The steel with higher Mn and Cr has higher martensite fraction, which cause strain hardening rate to be higher at higher strain levels.

Keywords:

Dual phase steels, hardening behavior, alloying design

INTRODUCTION

Dual phase (DP) steels have been continuously used in automotive industry for decades. Due to the necessity of light-weighting, DP steels have been served as a good solution for the automotive industry and more specifically for the body design engineering. The production of A-pillar, B-pillar, and bumper like automotive components are generally made up of DP steels. DP steels typically have high ultimate tensile strength (590-1400 MPa) due to the presence of martensite; combined with low initial yield strength (enabled by ferritic matrix), high early-stage strain hardening, and macroscopically homogeneous plastic flow (due to the absence of Luder's bands). These features render DP steels ideal alloy systems for automotive-related sheet forming operations [1, 2].

DP steels are basically composed of a ferritic-martensitic microstructure as seen in Fig. 1, usually involving some alloying elements as well. Although the term dual phase refers to the predominance of

two phases, ferrite and martensite, small amounts of other phases, such as bainite, pearlite, or retained austenite, may also be present [3]. Thus, the parameters such as the fraction of two basic phases, alloying design, average grain size, distribution of the phases and etc. directly influence the overall mechanical behavior. In other words, different grades of DP steels can be obtained by altering these parameters with a high precision control. The mechanical properties of DP steels can be enhanced by changing the amount of martensite in the structure, by carrying out inter-critical annealing followed by water quenching. The amount of martensite in DP-steel depends on the inter-critical annealing temperature in the ferrite plus austenite region. Different amounts of martensite in a dual phase steel, which determines the mechanical properties, can be produced by inter-critically annealing in the range of 760°C - 840°C for different holding times of 2 to 6 minutes, followed by water quenching [4].

Article History:

Received: 2017/03/23

Accepted: 2018/05/01

Online: 2018/07/09

Correspondence to: Kemal Davut
Atılım University, Department of
Metallurgical and Materials Engineering,
Ankara, Turkey
E-Mail:
kemal.davut@materialforming.org

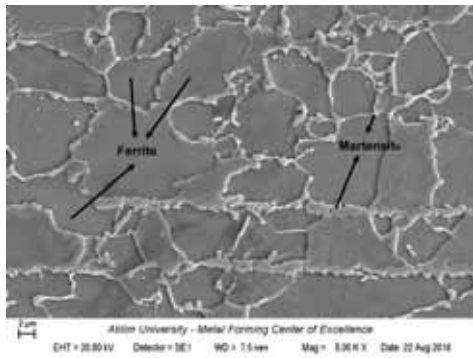


Figure 1. A representative microstructure of a DP steel, obtained by scanning electron microscope (SEM)

As a result of this remarkably sophisticated thermo-metallurgical process including specific rolling constraints, steelmakers have various individual solutions. Furthermore, steelmaker could employ different production strategies and methods to obtain dual phase microstructure either. In general, there exists three commercial production methods of dual-phase steels. These are (a) the hot-rolled approach, where the dual phase microstructure is developed during the conventional hot-rolling cycle by careful control of chemistry and processing conditions., (b) the continuous annealing approach, where hot or cold rolled strip is uncoiled and annealed intercritically to produce the desired microstructure and (c) the batch annealing where the hot or cold rolled material is annealed in the coiled condition [5]. It is the fact that this variety of production methods in general combined with the lack of a detailed standard for DP steels. The consequence is the existence of different microstructure and strain hardening behavior under the same grade name. Even some steelmakers have some DP grades with “Low Yield Strength” and “High Yield Strength” options [6]. Therefore, in this contribution the different hardening behaviors of two specific DP steel is investigated aiming to correlate this behavior with both specific micro-structures. Such correlations between macro-mechanical properties with microstructural characteristics like phase composition, texture and etc. would definitely contribute to define a reference volume element (RVE) for any finite element modeling. For instance, Darabi et al showed the effects of martensite phase distributions on the mechanical propert-

ies of DP800 and DP980 steels by 2D and 3D micro-mechanical modeling. The micro-mechanical models resulted in successful predictions of the flow curve and even the initial yielding of the ferrite phase compared to experimental studies [7]. Huang et al, also studied on the RVE modeling of DP 800 steel by means of point interpolation method. The proposed model is capable of predicting the effects of grain sizes of ferrite and martensite phases on the hardening behavior [8]. As aforementioned, the authors would like to discuss the fundamental correlations between the hardening and the microstructural properties in this study. The detailed RVE modeling of DP steels with mesoscopic micro-mechanical modeling approach is intended to be treated as a future work.

EXPERIMENTAL STUDIES

Within the scope of this project two commercially available hot rolled DP steels of 2 mm thickness (DP-800) were compared regarding their strain hardening behavior. It should be noted that those DP steels have identical strength levels. The efforts focused on mechanical comparison performed by means of tensile testing which is being assisted by the detailed microstructural analysis. In order to determine the representative volume element (phase composition, average grain size and etc.) SEM and quantitative metallographic techniques were employed. As an another comparison criteria the chemical compositions of two different DP800 steels were determined by optical emission spectroscopy. Since the alloying solutions for DP steels may alter among steelmakers, the strain hardening behavior may also be influenced by the weight fraction of the specific alloying elements.

CHEMICAL COMPOSITION

Chemical compositions of the samples were determined via Bruker Tasman Q4 optical emission spectrometer (OES). The RD-TD surfaces of the samples were carefully ground with 120 grit (ANSI) emery papers using a belt grinder, before the OES measurements. The chemical compositions of the samples are given in Tables 1 and 2.

The chemical composition of the Sample-2 is relatively richer in C, Mn, Cr compared to Sample-1. Those ele-

Table 1. Chemical composition of sample-1 (in weight percent)

C	Si	Mn	Cr	Mo	Al	Nb	V	Co	P	S	Ca
0.12	0.194	1.549	0.035	0.0091	0.032	0.016	0.015	0.013	0.0073	0.0026	0.0034

Table 2. Chemical Composition of Sample-2 (in weight percent)

C	Si	Mn	Cr	Mo	Al	Nb	V	Co	P	S	Ca
0.145	0.208	1.986	0.258	0.015	<0.001	0.006	0.0051	0.0052	0.018	<0.0003	0.00013

ments retard diffusional transformations, and hence make martensite transformation easier. On the other hand, the amounts of Nb and V (i.e. micro-alloying), as well as Co are higher in Sample-1.

TENSILE TESTS

Tensile tests were performed on Zwick/Roell Z300 Machine (load cell capacity 300 kN) using standard tensile test specimens conformed to ISO 6892-1. The elongations were recorded by extensometer which was attached to the Zwick machine. The extensometer used was class 0.5 type. By means of the extensometer the elongations of the specimens could have been recorded with a 100 Hz frequency. After performing the tensile tests, data processing studies have been completed, for this purpose specific MatLab scripts were created. The flow curves were obtained by plotting true plastic strain versus true stress curves, as seen in Figs. 2 and 3. Furthermore, in order to observe the strain hardening behavior, (which can be totally linear or not) logarithm of true stress versus logarithm of true strain values were also plotted, as seen in Figs. 4 and 5. Due to the fact that martensite and ferrite have to yield at different stress states, normally there should exist a non-linearity in the strain hardening exponent “n”. The data observed within this study correspond with the data in the literature. A small amount of non-linearity could be more easily seen in Figs. 4 and 5.

As it could be observed in Figs. 4 and 5, the here investigated two DP800 steels have different strain hardening behavior. Sample 1 shows non-linearity at higher strain levels, whereas sample 2 at lower strain levels. This trend is same among the tests performed among the transverse di-

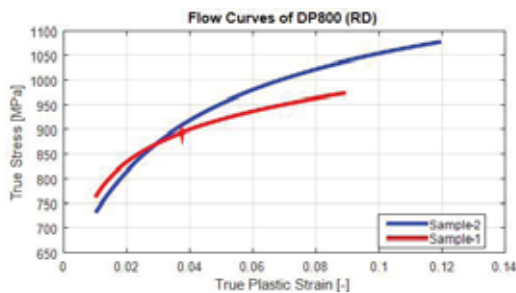


Figure 2. Flow curves in rolling directions

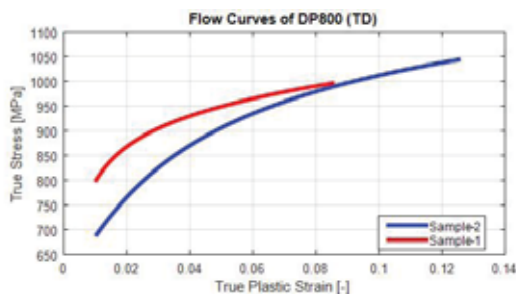


Figure 3. Flow curves in transverse directions

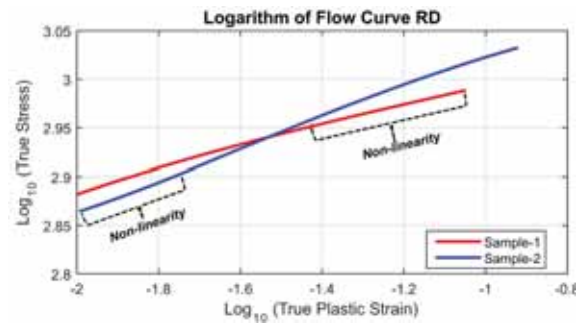


Figure 4. Logarithm of flow curves in rolling direction

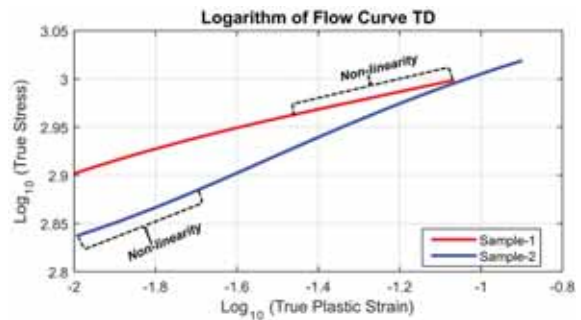


Figure 5. Logarithm of flow curves in transverse direction

rection. The non-linearity in Figs. 4 and 5 indicate that the flow curve is deviating from the Hollomon Law (power law). Discontinuous yielding, changes in stress and strain partitioning can cause this non-linearity. In other words, “n” (strain hardening exponent) exhibits specific variation with increasing strains for two DP steels. For further investigation of the strain hardening behavior, Kocks-Mecking plots are created. Kocks and Mecking presented a novel way of depicting the stress-strain curves namely, by plotting the work hardening rate (θ) against stress (σ); where the work hardening coefficient is given as

$$\theta = \left. \frac{\partial \sigma}{\partial \varepsilon} \right|_{\varepsilon, T} \quad (A1)$$

This plot is very commonly referred to as the “Kocks-Mecking” plot [9].

In order to plot Kocks-Mecking curves, differentiation on the flow curve is necessary. This task is accomplished by taking the numerical derivative via “diff” command of MatLab software. As it is a well-known fact that numerical derivative approach is fairly sensitive to the noise level in experimental data. To overcome this problem before taking numerical derivative, data filtering is engaged. The possible data filtering algorithms were all performed to make a meaningful comparison among them. By means of this comparison, “moving average filtering” is found to be the most proper one as can be seen in Fig. 6. After applying the moving average filtering of the raw data, the Kocks-Mecking curves of the present DP800 steels were determined for tests

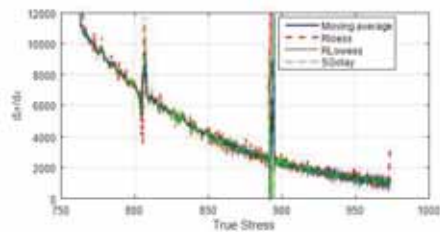


Figure 6. Comparison for different filtering algorithms

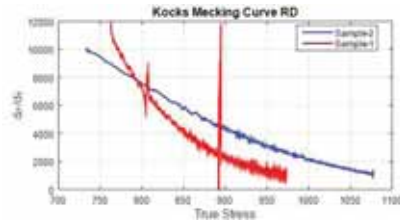


Figure 7. Kocks Mecking curves for tests along rolling direction

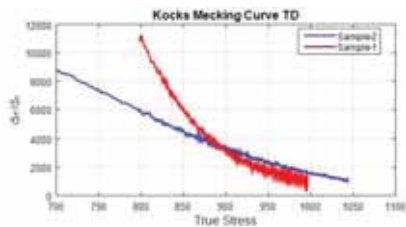


Figure 8. Kocks Mecking curves for tests along transverse direction

among rolling and transverse directions, and shown in Figs. 7 and 8. The Kocks-Mecking curves of both directions exhibit the same trend; sample 1 shows higher initial strain hardening but it decays faster. It should also be noted that the strain hardening rates along rolling and transverse directions are almost the same, the differences in those values are less than 10%.

MICROSTRUCTURAL ANALYSIS

The microstructural analysis of the samples were performed along the RD-ND section, using optical and scanning electron microscopes. In order to obtain relief-free,

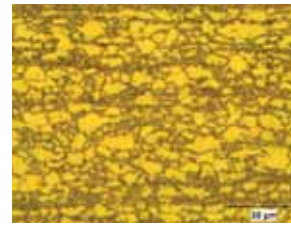


Figure 9. Optical micrograph of Sample-1

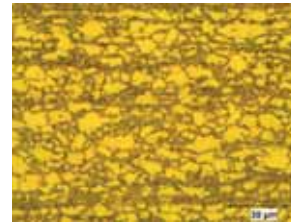


Figure 10. Optical micrograph of Sample-2

artifact-free surfaces samples were ground mechanically by 320 and 500 grit (ANSI) SiC grinding papers and then polished mechanically by conventional 9 μm, 3 μm, 1 μm diamond pastes and finally with 0.05 μm-diameter colloidal silica particles. Afterwards, the samples were etched with 2% Nital solution as well as with the method of LaPera [10]. The optical micrographs of Sample-1 and 2, taken under bright field illumination, are shown in Figs. 9 and 10, respectively. In both samples the martensite islands decorate the grain boundaries of ferrite; moreover, martensite is present in the form of bands, elongated along the rolling direction (RD). This second morphological form is more predominant in Sample-2. Using the optical micrographs, the volume fraction of martensite as well as the average grain size of ferrite were determined, and shown in Fig. 11. For each sample, the quantitative metallographic analysis were performed on randomly selected 3 different fields. For grain size determination, at each field 5 horizontal (RD) and 5 vertical (ND) lines were used to determine the grain size values. In both samples, since ferrite grains are elongated along rolling direction (RD),

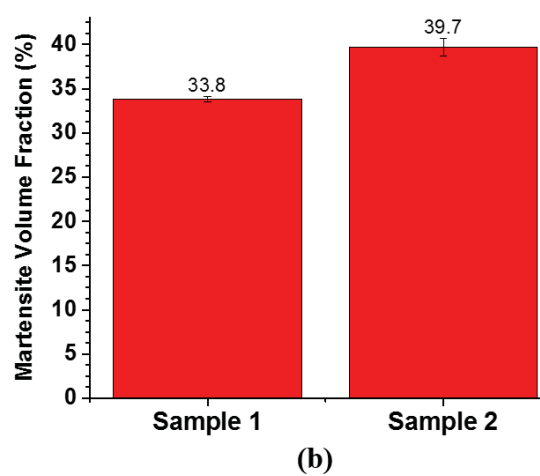
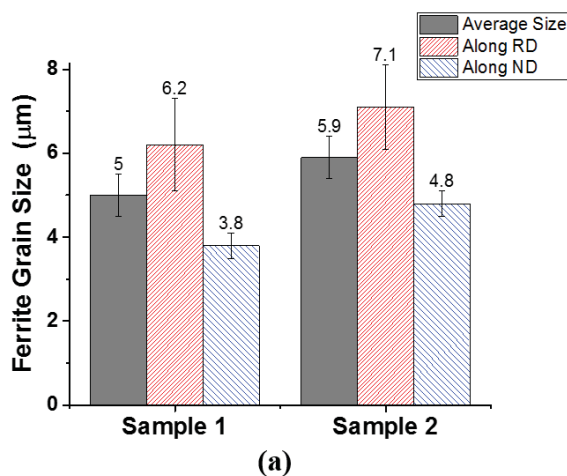


Figure 11. Results of quantitative metallographic analysis showing (a) average grain size of ferrite, and (b) volume fraction of martensite

their intercept lengths are higher along this direction. The standard deviations in both phase fraction and average grain size values are quite low, indicating the selection of correct magnification and representative field-size for the quantitative metallographic analysis.

RESULTS AND DISCUSSION

Conducted tests clearly reveal that DP-800 steels from different manufacturers have significant differences in microstructure and mechanical properties; as well as in alloying concepts. This clearly indicates the importance of processing route in production of DP steels.

The most obvious observations that can be made from the flow curves is that those steels have significantly different yield stresses and ductility, especially in the transverse direction. Because of that, significant differences are also expected in planar and normal anisotropy values.

Control of strain hardening is probably the key for development of high strength steels for metal forming application. Large strain hardening rates have an impeding effect on localization and associated damage processes. Most of the metals have a decaying hardening rate which limits the failure strain due to saturation of hardening. A strong and formable steel must have a high strain hardening together with a large saturation strain. Although both samples have approximately the same saturation strain according to Kocks-Mecking plot, the evolution of strain hardening is quite different. Sample-1 has a larger initial hardening rate which decays exponentially in a shorter strain range. In contrast, Sample-2 has a relatively smaller initial hardening rate with a smaller decay rate. Significantly higher uniform elongation in Sample-2 is probably associated with this contrast.

Aside from investigation of strain hardening behavior, Kocks-Mecking plots are also useful for selection of most appropriate hardening law for the simulation of metal forming processes. In this study, they indicate a power law hardening for Sample-1, while an exponential-saturation type hardening law seems to be more appropriate for Sample-2.

The microstructural differences of the samples correlate well with the mechanical properties. Both the martensite content and the UTS of Sample-2 is higher. This sample contains more C, Mn, Cr and Mo all of which retards bainite transformation and hence making the formation of martensite easier. On the other hand, the ferritic matrix of Sample-1 contains smaller grains. Moreover, this sample contains more micro-alloying elements than Sample-2. Due to those characteristics, the initial hardening rate of Sample-1 is higher; since the strain is predominantly partitioned into ferrite at earlier stages of deformation [11]. At

later stages, localized strain fields in ferrite appear, and the fraction and strength of martensite, which is directly related to carbon content, influence the strain hardening behavior. Therefore, at second stage of deformation Sample-2 shows higher strain hardening.

CONCLUSION

The following conclusions can be derived from the presented results:

- DP-800 steels from different steel producers have significantly different mechanical and microstructural properties based on chemical composition. Additionally, it is thought that possibly different manufacturing routes have an effect on the aforementioned properties.
- Kocks-Mecking plots indicate the differences in the strain hardening behavior of the DP steel. The sample with a smaller hardening decay rate has a significantly large uniform elongation as suggested by the theory.
- The fraction of martensite, grain size of ferrite as well as the micro-alloying elements correlate well to the differences in the strain hardening behavior of the DP steels investigated.
- The sample with high initial-strain hardening has smaller ferrite grains as well as more micro-alloying elements. Moreover, this sample has slightly less martensite fraction, which may cause more strain to be partitioned into ferrite.

The here presented results agree well with the previous studies on identical steel grades. Further investigations are necessarily to clarify underlying microscopic mechanisms. More detailed mechanical characterization including determination of damage parameters, yield surface and its evolution is ongoing together with detailed microstructural characterization. This information will be coupled with mesoscopic computer simulations in the future.

ACKNOWLEDGEMENTS

Authors would like to thank to managerial board of FNSS Defense Systems for their financial support. Thanks are also extended to Atılım University Metal Forming Center of Excellence for the use of their facilities.

REFERENCES

1. Taşan, CC. et al. An Overview of Dual-Phase Steels: Advances in Microstructure-Oriented Processing and Micromechanically Guided Design. Annual Review on Material Research 45, pp. 19-40, 2005.
2. Billur E, et al. New Generation Advanced High Strength Steels: Developments, Trends and Constraints. International Journal of Scientific and Technological Research 2, pp.50-62, 2016.
3. Speich GR. Dual Phase Steels, ASM International, ABD,

- 1990.
4. Singh RR, et al. Comparison of Mechanical Properties of Medium Carbon Steel with Dual Phase Steel. *International Journal of Mechanical Engineering* 4, pp. 1–8, 2008.
 5. Tsipouridis P. Mechanical Properties of Dual Phase Steels. Ph.D. Thesis, Technische Universität München, Germany, 2006.
 6. http://automotive.arcelormittal.com/repository2/About/Automotive/201404_datasheet-dualphase.pdf
Date:01.03.2017
 7. Darabi A Ch, et al. Micromechanical Analysis of Two Heat-Treated Dual Phase Steels: DP 800 and DP 980, *Mechanics of Materials* 110, pp. 68–83, 2017.
 8. Huang TT, et al. Strain-hardening Behaviors of Dual Phase Steels with Microstructure Features, *Material Science and Engineering A*. 672, pp. 88–97 2016.
 9. Parasad GVSS. An Improved Dislocation Density Based Work Hardening Model for Al-Alloys. Master Thesis, RWTH Germany, 2007.
 10. LePera F. Improved Etching Technique for the Determination of Percent Martensite in High-Strength Dual-phase Steels, *Metallography* 12, pp. 263–268, 1979.
 11. Taşan CC, et al. Integrated Experimental-simulation Analysis of Stress and Strain Partitioning in Multiphase Alloys. *Acta Materiala* 81, pp. 386–400, 2014.

Kinetic and Equilibrium Studies of Adsorption of Reactive Red 120 on Chitin

Murat Torun¹  Y. Doruk Aracagök², Mahmut Kabalak²

¹Hacettepe University, Department of Chemistry, Ankara, TURKEY

²Hacettepe University, Department of Biology, Ankara, TURKEY

ABSTRACT

Chitin is a natural compound that can be extracted from various organisms that is used in various applications from medicine to environmental applications. In this study, effect of chitin is followed for adsorption of reactive red 120 textile dye from water at different conditions such as pH, initial concentration of dye, ionic strength, initial concentration of chitin, effect of temperature, effect of contact time. Characterization of the adsorption were recorded by Fourier Transform Infrared (FT-IR) spectroscopy.

Keywords:

Chitin; Textile Dye Removal; Adsorption.

Article History:

Received: 2018/01/29

Accepted: 2018/08/12

Online: 2018/12/31

Correspondence to: Murat Torun,
Hacettepe University, Department of
Chemistry, 06800, Beytepe, Ankara, TURKEY
E-mail: mtorun@hacettepe.edu.tr

INTRODUCTION

The increase in population brings contamination of water with time. Textile dyes are great environmental problem for the environment since they change the quality of water as well as color of water. Their complicated structure with multiple aromatic compounds makes these contaminants resistance for degradation in water and under sunlight, their photolytic conversion to more toxic compounds is possible. Dyes have been widely used in different industries. As a result of dyeing process in textile industry, high amount of pollutant formed in liquid form [1]. Due to their highly brilliant colors, azo dyes the most important groups of dyes used in the textile dyeing processes [2]. Azo dyes, contains one or more azo ($-N=N-$) bonds in their structure [3]. Azo dyes are widely used in various industries such as textile, cosmetics, food, paper printing etc.. Because of complex structure of azo dyes, they are resistant to ozone, light, biodegradation and other environmental conditions. Thus treated of these dyes with conventional treatment methods remains ineffective [4].

Untreated dye contained effluents cause several adverse effects such as decrease photosynthetic activity by means of reduce penetration of light, reduce dissolved oxygen, reduce water quality, dyes and breakdown products have toxic effects on aquatic flora and fauna [1]. Azo dyes are large group of carcinogenic and mutagenic pollutants [5]. Various kind of physico-chemical

methods have been used for treat dye contained waste water, including activated carbon adsorption, membrane filtration, oxidation, ozonation, and coagulation/flocculation. These physico-chemical methods have disadvantages, they have high operation costs and applicability are limited [1,6]. The use of biomass as a sorbent for treatment of wastewater is an effective alternative processes [7].

Chitin, poly (b-(1-4)-N-acetyl-D-glucosamine) is the most abundant biopolymer after cellulose. Chitin is found in the exoskeleton of arthropods and cell wall of fungi [8]. Chitin is a good biosorbent for environmental pollutants. Cadmium ions were removed from aqueous solution by chitin particles [9]. Another study showed that chitin adsorb zinc and arsenate ions effectively [10]. Chitin can adsorb reactive black 5 and reactive yellow 2 dyes [11]. Previous study reported that chitin adsorbed anionic dyes orange G, orange IV and xylenol orange [12].

The main objective of this study is to investigate biosorption of the dye reactive red 120 by the biopolymer chitin. The effect of initial pH, dye concentration, salt concentration, chitin dosage, and temperature and contact time was evaluated. Kinetic and thermodynamic parameters will be detected as well as with adsorption isotherms.

MATERIALS AND METHODS

Dye and Chitin

Reactive red 120 (CAS Number 61951-82-4) and chitin (CAS Number 1398-61-4) were obtained from Sigma-Aldrich.

Removal of Dye

The removal of dye was determined spectrophotometrically at 553 nm wave length with Shimadzu Shimadzu UV-1700 spectrophotometer. The adsorption of dye capacity was calculated by following equation:

$$q = (C_i - C_e) \frac{V}{m} \quad (1)$$

in which q is adsorption capacity, C_f and C_i are initial dye concentrations, respectively. V is the volume of dye solution and m is the mass of the adsorbent that is chitin here.

Biosorption Experiments

Biosorption of dye reactive red 120 experiments were carried out in 250 ml Erlenmeyer flasks containing 100 ml dye solution. In order to reveal effect of initial pH on dye biosorption by chitin, 50 mg L⁻¹ dye contained mediums were adjusted to pH 2-9 using 1M HCl and 1M NaOH. Then 0.1 g chitin added into flasks and flasks were shaken on an orbital shaker at 150 rpm and 30°C for 24 h. The effect of initial dye concentration was also evaluated, different dye concentration was studied in the concentration range of 10-150 mg L⁻¹ dye. The influence of chitin dosage was studied in the range of 0.025-0.2 g. In order to determine effect of contact time on removal of dye, samples were taken different time intervals (0-1440 min). The influence of temperature on dye removal was studied in different temperatures (20-60° C). To determine effect of salt on removal of dye, different NaCl so-

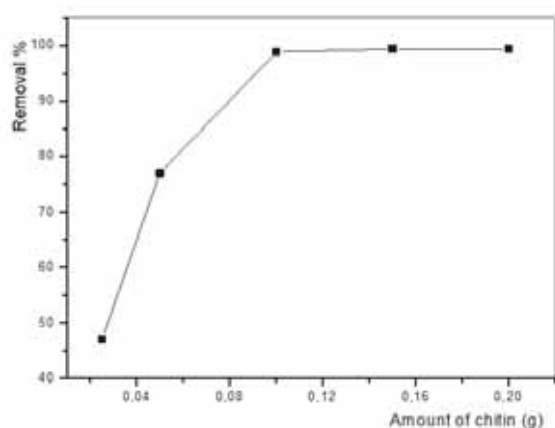


Figure 1. Effect of chitin amount on percent removal of reactive red 120.

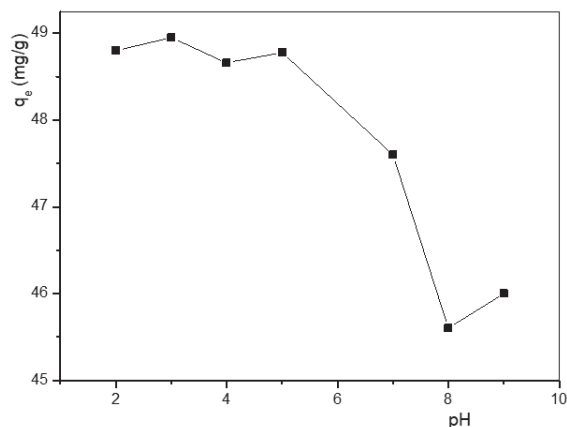


Figure 2. Effect of pH on adsorption capacity of chitin at equilibrium.

lutions (1-5 % m/v) were used. Unless otherwise stated, all experiments were carried out same conditions, (0,1 g chitin, pH 3, 50 mg l⁻¹ dye conc., 30°C, 150 rpm, 24 h).

Spectroscopic Analyses

Characterization of the adsorption were recorded Fourier Transform Infrared (FT-IR) spectroscopy in ATR mode by Thermo instruments.

RESULTS AND DISCUSSION

Effect of Chitin Amount

The effect of adsorbent amount was followed in 50 ppm dye solution at pH 3 and 30°C. The amounts of chitin ranges from 0.025 g to 0.2 g (Fig. 1). It is clear that 0.1 g chitin is enough to remove nearly 99% of the dye from solution which is used for further experiments.

Effect of pH

The effect of initial pH on adsorption capacity at equilibrium is shown in Fig. 2. There is no strong effect on adsorption capacity of chitin since its change is narrow with wide pH change at 30°C for 50 ppm dye, 0.1 g chitin and 24 hours contact time. This is attributed to the rigid structure of chitin.

Effect of Salt

The adsorption of reactive red 120 by chitin is followed for 50 ppm dye solution at pH 3 and 30°C for different concentrations of salt from 1% to 5% by mass. Sodium chloride was used to observe the effect of ionic strength. The change in the ionic strength is not effective for the equilibrium adsorption capacity since the change adsorption capacity is minor (Fig. 3).

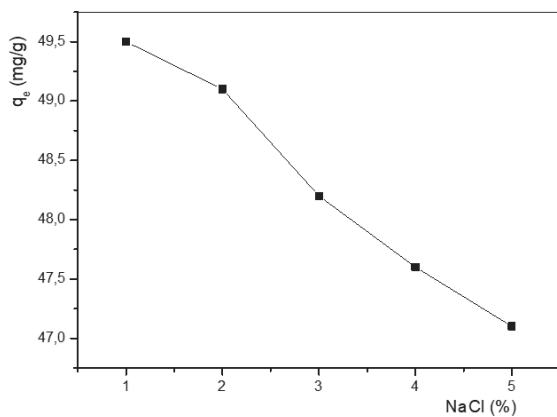


Figure 3. Effect of ionic strength on adsorption capacity of chitin at equilibrium.

Effect of Contact Time

The change in the adsorption capacity with different contact times for 50 ppm dye solution at pH 3 and 30°C is shown in Fig. 4. Dye adsorption is high up to 180 minutes and reaches equilibrium for further contact times finally all dye is adsorbed.

Effect of Temperature

The effect of temperature on adsorption of dye is given in Fig. 5 at pH 3 for 50 ppm dye and various temperatures at 20°C, 30°C, 40°C and 60°C. The adsorption capacity increased only 5% with temperature since the polymeric chains in chitin becomes more flexible with temperature and the diffusion of dye is more possible through the chains.

Effect of Initial Dye Concentration

Fig. 6 shows the effect of initial dye concentration on adsorption capacity on 0.1 gram of chitin. There is an increase in adsorption capacity with increase in chitin concentration upto 100 ppm initial chitin concentration and

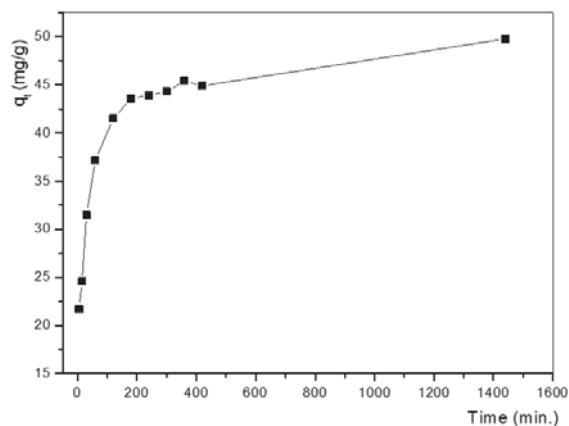


Figure 4. Effect of contact time on adsorption capacity of chitin at equilibrium.

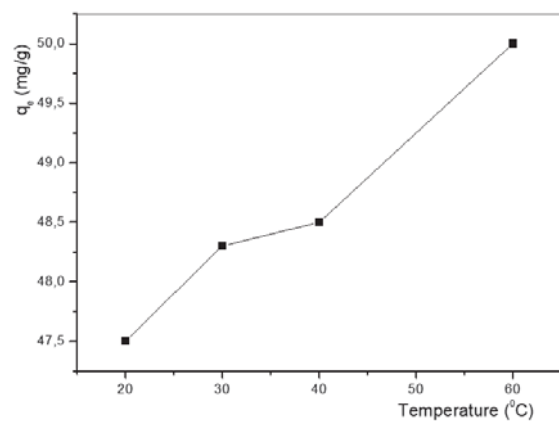


Figure 5. Effect of temperature on adsorption capacity of chitin at equilibrium.

it seems to be constant above this value. The active sites of the chitin may be filled with textile dyes upto 100 ppm initial textile dye for 0.1 g chitin sample.

Equilibrium Isotherms

There are several isotherm equations that are used to analyze the experimental adsorption parameters in which well known are Langmuir and Freundlich models. Langmuir isotherm model depends on the homogeneous finite number of active sites on the adsorbent that corresponds monolayer adsorption with no interaction between adsorbed species [13].

The linear form of the Langmuir equation follows the expressed equation:

$$C_e / q_e = C_e / q_m + 1 / (q_m K_a) \quad (2)$$

q_e is the amount of dye adsorbed per gram of adsorbent (mg/g), C_e is the equilibrium concentration of dye (mg/L), q_m is the maximum adsorption capacity (mg/g) and K_a is adsorption equilibrium constant (L/mg). Langmuir isotherm that is fitted linear is given in Fig. 7 with some analytical parameters and from the isotherm q_m is 5.92

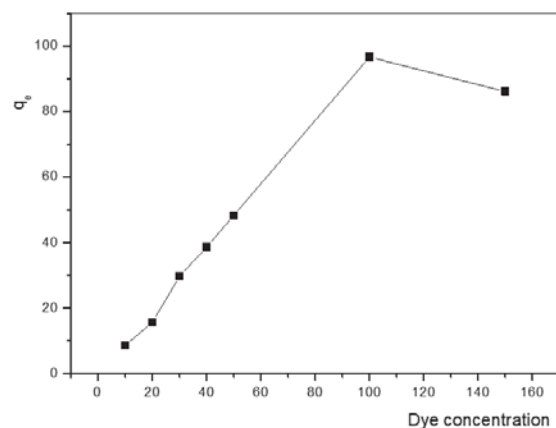


Figure 6. Effect of initial dye concentration on adsorption capacity of chitin at equilibrium.

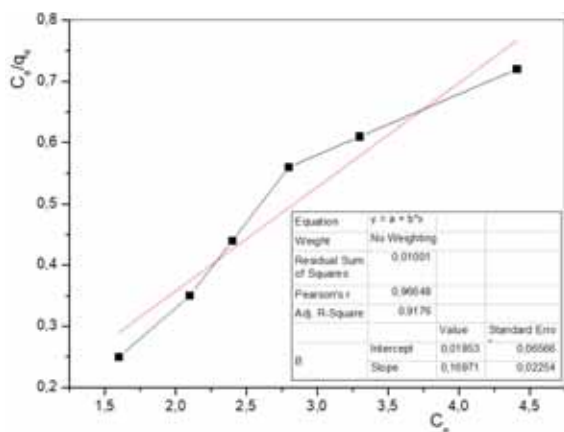


Figure 7. Langmuir isotherms for the adsorption of Reactive Red 120 on chitin.

mg/g as well as K_a is 9.12 L/mg. Dimensionless separation factor (K_R) is one of the essential parameter of the Langmuir isotherm that indicates the characteristic of isotherm [14].

$$K_R = 1 / (1 + K_a C_o) \tag{3}$$

where C_o is the initial concentration of the dye. K_R values are between 0 and 1 ($0 < K_R < 1$) that indicates favorable adsorption (Table 1) at pH 3 and 30°C.

The Freundlich isotherm is one of the widely used model for adsorption studies. It generally applies on heterogeneous surfaces that is in contact with adsorbed molecules. Freundlich isotherm differs from Langmuir isotherm that is not restricted with monolayer coverage. The widely used expression for Freundlich isotherm model is [15].

$$\log(q_e) = \log K_f + (1/n) \log C_e \tag{4}$$

where K_f is Freundlich constant, n is relates the deviation of the adsorption from linearity. The Freundlich isotherm was also evaluated for adsorption of reactive red 120 on chitin but this model fails for our data especially for higher concentrations as in literature. The data for dilute dye was used to evaluate the parameters of Freundlich isotherm (Fig. 8) which are 4.12 and 2.29 for K_f and n , respectively at pH 3 and 30°C. Adsorption is favorable if Freundlich isotherm is assumed since n value is greater

Table 1. K_f values of the Langmuir isotherm at different initial concentrations.

Initial concentration (C_o)	Dimensionless separation factor (K_R)
10	0.0108
20	0.00545
30	0.00364
40	0.00273
50	0.00218
100	0.00109

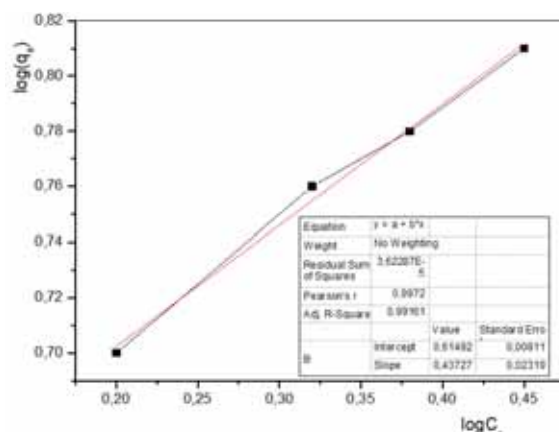


Figure 8. Freundlich isotherms for the adsorption of Reactive Red 120 on chitin.

than one [16], same was assumed as in the case of Langmuir. Correlation coefficient, r^2 is higher for Freundlich isotherm that means in dilute solutions, the adsorption of reactive red 120 on chitin is expressed as Freundlich model rather than Langmuir model.

Kinetic Studies

The kinetics of adsorption of reactive red 120 on chitin was also followed at pH 3 and 30°C for 50 ppm dye and 0.1 gram of chitin. The pseudo-first order and pseudo-second order diffusion models were applied for linear region of the plots. The first order rate equation is followed for pseudo-first order formula derived by Lagergren [17].

$$\ln(q_e - q_t) = \ln q_e - kt \tag{5}$$

where q_t is the amount of dye adsorbed at any time t (mg/g) and k is the rate constant for pseudo-first order assumption. The adsorption data of reactive red on chitin is not a linear line for pseudo-first order assumption. A pseudo-second order model for adsorption of solute on adsorbent is proposed by Ho [18] (Fig. 9) and adsorption of dye on chitin in this study follows this model.

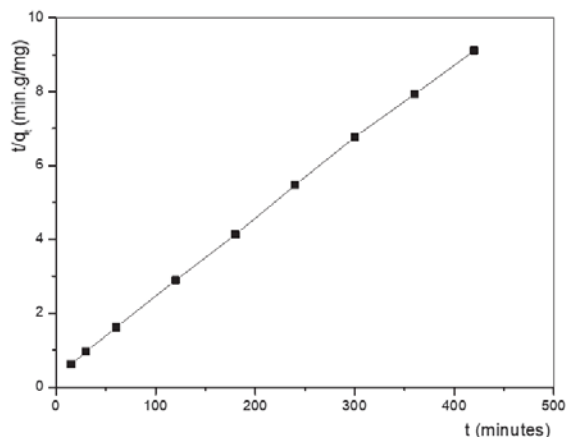


Figure 9. Pseudo-second order kinetic evaluation of adsorption of reactive red 120 on chitin.

$$t/q_t = 1/(kq_e^2) + t/q_e \quad (6)$$

where t is time elapsed for adsorption (min.), q_t is the amount of dye adsorbed at any time t (mg/g) and k is the adsorption rate constant. From expressed graph, equilibrium amount of adsorbed dye (q_e) was found as 47.6 mg/g where this value is found as 46.1 experimentally. The close value of experimental q_e and its value expressed from the graph proves that the adsorption of reactive red 120 on chitin obeys the pseudo-second order model suggested by Ho. The adsorption rate constant (k) was found as 0.0013 g/(mg.min.).

SPECTROSCOPIC CHARACTERIZATION (FTIR-ATR)

The FTIR-ATR spectrum of the chitin after absorption of reactive red 120 is given in Fig. 10. The characteristic peaks of chitin are O-H stretching at 3433 cm^{-1} , N-H stretching at 3255 cm^{-1} and 3099 cm^{-1} , C=O amide stretching at 1650 cm^{-1} and 1620 cm^{-1} , C-O-C stretching for bridge oxygen at 1152 cm^{-1} and N-acetylglucosamine in ring stretching mode at 1115 cm^{-1} were observed in the spectra. The peaks from reactive red 120 are N-H stretching of secondary aromatic amine that overlaps with chitin O-H stretching at 3436 cm^{-1} , C=O stretching frequency of hydrazone at 1735 cm^{-1} , 1020 cm^{-1} and 1045 cm^{-1} is O-H from phenol, the peaks at 1205 cm^{-1} is due to aromatic C-O and 1670 cm^{-1} is from N=N.

CONCLUSION

Chitin is one of the most produced natural polymer with variety of applications. In this study, chitin from crab shells was used to remove reactive red 120 dye from water that is more than 95%. There is no significant change in adsorption of reactive red 120 by chitin when pH, ionic strength and temperature changes since the rigid

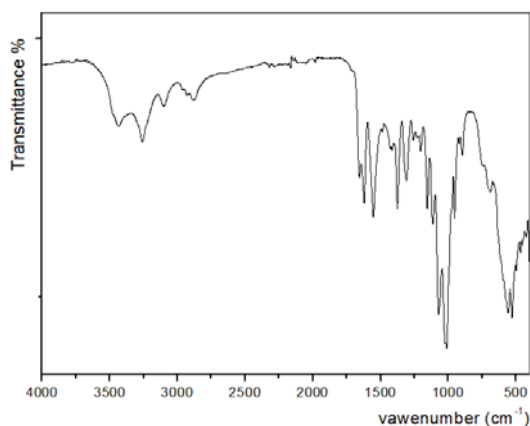


Figure 10. FTIR-ATR spectrum of the chitin after absorption of reactive red 120.

structure of chitin. The increase in chitin amount increases the adsorption as well as the same is for contact time up to a special time that equilibrium is established. The adsorption models were evaluated for Langmuir and Freundlich models, although adsorption process obeys both of the models, the linearity was observed for Freundlich model rather well. The adsorption kinetics were observed as pseudo-second order diffusion. FTIR-ATR spectra were evaluated for spectroscopic characterization.

References

1. Saratale GD, Chang J. Bacterial Decolorization and Degradation of Azo Dyes : A Review. *J Taiwan Inst Chem Eng* 42 (2011) 138–157.
2. Akar ST, Akar T, Çabuk A Decolorization Of A Textile Dye , Reactive Red 198 (RR198), BY *Aspergillus parasiticus*. *Fungal Biosorbent* 26 (2009) 399–405.
3. Wang X, Cheng X, Sun D. Interaction in anaerobic biodecolorization of mixed azo dyes of Acid Red 1 and Reactive Black 5 under batch and continuous conditions. *Colloids Surfaces A Physicochem Eng Asp* 379 (2011) 127–135.
4. Kaushik P, Malik A (2009) Fungal dye decolourization : Recent advances and future potential. *Environ Int* 35:127–141.
5. Oturkar CC, Nemade HN, Mulik PM, et al. Bioresource Technology Mechanistic investigation of decolorization and degradation of Reactive Red 120 by *Bacillus lentus* BI377. *Bioresour Technol* 102 (2011)758–764.
6. Murugesan K, Dhamija A, Nam I (2007) Decolourization of reactive black 5 by laccase : Optimization by response surface methodology. *75 (2007) 176–184.*
7. Kumar KV, Ramamurthi V, Sivanesan S (2006) Biosorption of malachite green , a cationic dye onto *Pithophora* sp ., a fresh water algae. *69 (2006) 102–107.*
8. Rinaudo M Chitin and chitosan: Properties and applications. *Prog Polym Sci* 31 (2006) 603–632.
9. Benguella B, Benaissa H Cadmium removal from aqueous solutions by chitin: Kinetic and equilibrium studies. *Water Res* 36 (2002) 2463–2474.
10. Jaafarzadeh N, Mengelizadeh N, Takdastan A, et al. Biosorption of heavy metals from aqueous solutions onto chitin. *Int J Environ Health Eng* 4 (2015) 7.
11. G. Akkaya, İ. Uzun GF. Kinetics of the adsorption of reactive dyes by chitin. *Dye Pigment* 73 (2007) 168–177.
12. Longhinotti E, Pozza F, Furlan L, et al. Adsorption of Anionic Dyes on the Biopolymer Chitin. *9 (1998) 435–440.*
13. Langmuir, I. The adsorption of gases on plane surfaces of glass, mica and platinum, *40(9) (1918) 1361-1403.*
14. Hall K.R., Eagleton L.C., Acrivos A., Vermeulen T. Pore-and solid-diffusion kinetics in fixed-bed adsorption under constant-pattern conditions. *Ind. Eng. Chem. Fund.*, 5, (1966), 212-223.
15. Freundlich HMF, Über die Adsorption in Lösungen, *Z. Phys. Chem-Leipzig* 57A, (1906), 385-470.
16. Roulia M., Vassiliadis AA., Sorption characterization of a cationic dye retained by clays and perlite. *Microporous Mesoporous Materials*, 116, (2008), 732-740.
17. Lagergren S., About the Theory of so Called Adsorption of Soluble Substances, *Kungliga Svenska Vetenskapsakademiens Handlingar*, 24, (1898), 1-39.
18. Ho YS, PhD Thesis, University of Birmingham, Birmingham, U.K. (1995).

The Effects of Olive Pomace Ash on The Color Change of The Composite Material and Its Mechanical Properties

Soner Celen¹  Sencer Süreyya Karabeyoglu²  Türkan Aktas³  and Aylin Akyıldız⁴ 

¹Namık Kemal University, Department of Mechanical Engineering, 59830, Tekirdağ, TURKEY

²Kırklareli University, Department of Mechanical Engineering, 39000, Kırklareli, TURKEY

³Namık Kemal University, Department of Biosystem Engineering, 59000, Tekirdağ, TURKEY

⁴Namık Kemal University, Department of Civil Engineering, 59830, Tekirdağ, TURKEY

ABSTRACT

The purpose of this study is to apply olive pomace ash (Prina ash), which is the remaining pulp after the pressing of olives, to a plastic material. Prina particles transformed into the ash were mixed in Polypropylene (PP) polymer with a weight ratio of 0%, 1% and 3% and then molded in the injection machine. Tensile-Stress Test, impact test, SEM images and color change measurements were carried out with produced samples. The effects of prina ash ratio on the color change and mechanical properties were investigated for the availability of Prina. As a result, it was determined that an increase in prina ash ratio caused an increase in both color change and mechanical properties of the material.

Keywords:

Polypropylene Polymer; Prina Ash; Impact Test; Color Change; SEM.

Article History:

Received: 2017/10/23

Accepted: 2017/10/25

Online: 2018/12/31

Correspondence to: Soner Çelen,

Namık Kemal University, Department of Mechanical Engineering, 59830, Tekirdağ, TURKEY

E-Mail: scelen@nku.edu.tr

Phone: +90 282 250 23 66

INTRODUCTION

The wastes of the factories, which manufacture olive oil, one of the important product materials of our country, pollute the environment. Recycling of the wastes, which pollute the environment, is recently the goal of the environment friendly technologies. The pollutions consisting of various industrial wastes have increased nowadays and caused pretty important environmental problems. The wastes occurred in the olive oil factories generally in Mediterranean countries are one of the important pollutants of the agricultural industry. The olive oil factory waste includes organic substances such as nitrogenous compounds, toxic substances, sugars, organic acids and waste oil, which have commercial importance [1]. Olive pomace is a product consisting of the remaining seed, rind and pomace after the oil is extracted from the olive. The oil and moisture content of the obtained olive pomace changes depending on the applied procedure after the oil extraction process [2].

Olive pomace oil output obtained after getting the olive oil is directly linked to the olive oil production since it is a secondary oil. Even though the olive pomace and olive pomace oil depends on the olive growing technique, climate, soil, variety features and the technology

used for the olive handling, the olive pomace obtained weigh around one and a half or two times more than the output of the olive oil produced at the olive oil factories. The olive pomace production in Turkey depends on the olive production and it is known that this value is 200000-250000 ton per year [3]. Even though the handling style of the olive oil factories changes the content of the olive pomace, oily olive pomace contains approximately 6-8% oil and 20-30% moisture [4].

The olive pomace can be used as fertilizer, as the feed for the bovine animals and even as the admixture material for the road construction when mixed with bitumen and it is used most commonly as the fuel due to its high-energy content [5].

There are many scientific studies on the use of prina. In these investigations, feeding of Lambs [6], obtaining Biosurfactant [1], drying [7], cement production [8] were studied.

In this study, the application of the olive pomace ash to the plastic material is intended. The olive pomace particles which were converted to the ash is mixed with Polypropylene (PP) polymer over the range of 0%, 1%

and 3% and Tensile-Strain Test, Hit-Test, SEM images and Color Change measurements are applied. The effects of the olive pomace rate change on the change at the resulting color values and the mechanical features are examined.

MATERIAL AND METHOD

The olive pomace used for the tests is obtained from a factory in Balıkesir city. The olive pomace material is shown in Fig. 1. The first moisture of the procured Olive Pomace material according to the wet base is determined as 50%.



Figure 1. Olive pomace example

The olive pomace is converted to the ash according to ASTM E1755-01 standards by using Nüve MF 106 (max. 1100 °C temperature, max. 2 kW power and 6.3 l internal volume, Turkey) model ash furnace. The olive pomace, which is an olive waste, reached up to 250 °C with 10 °C/min in the ash furnace and it was kept here for 30 minutes. After this process, it is kept at 575 °C by 10 °C/min step for 3 hours. As a result, the ash process is carried out by cooling to 100 °C. Petoplen MH 418 product belonging to PETKİM A.Ş. is used as the homopolymer material. The features of the product are as shown in the Table 1.

Olive pomace and PP materials were mixed at 40 rpm for 60 minutes by means of a mixer bunker before they are formed in the injection machine. Mixed test materials were produced by the help of the injection machine in the mold with 220-235 °C screw temperatures and in 38 sec.

Tensile features of the prepared samples were performed

Table 1. Petoplen MH 418 tensile values

Test Name	Unit	Value	Method
Tensile Strength at Yield Point	kg/cm ²	350	ASTM – 638
Tensile Strength at Breaking Point	kg/cm ²	430	ASTM – 638
Color B 10 D 65	-	1.8	Hunter Lab. CO

med by applying the tensile tests by using the jaws of the equipment at a constant speed. Accepted plastic standard was given in [9] for the tests which the equipment force measurement range is between 500 N and 10 kN. Izod-Charpy testing setup was used for impact tests of the composite materials formed by using the ash additives. The plastic standard impact tests were performed according to [10]. The images of the prepared plastic samples were taken by using FEI brand Quanta FEG 256 model scanning electron microscope. In order to define the color changes of the samples, ASTM 6290-05e1 [10] standard is used.

Color Measurement

In this study, D25LT Hunter Lab (USA) model color measuring instrument is used. L*, a*, b* color scale numerical values are given at each reading of the colorimeter. The measurements are repeated for 10 times and the arithmetic mean of the results is taken. L* value represents the blackness and the whiteness which show the brightness. 0 value represents the blackness and 100 value represents the whiteness. A* color scale is known as the redness value. While the positiveness of the a* values represents the redness, the negativeness of the a* values represents the green color. B* color scale is known as the yellowness/blueness value. While the positiveness of the b* values represent the yellowness, the negativeness of the b* values represents the blueness. C value defines the color density (Eq.1) and H defines hue angle (Eq.2) [12]:

$$C = \sqrt{a^{*2} + b^{*2}} \quad (1)$$

$$H = \arctan \frac{b^*}{a^*} \quad (2)$$

RESULTS AND DISCUSSION

The test specimens with mass of 1% and 3% ash as additive were produced in the temperature range of 220-235 °C by means of plastic injection machine. The composite materials produced using pomace ash were removed by ejector pin and allowed to cool to room temperature and then made suitable for the tests. Test samples produced by means of plastic injection are listed according to their contribution rates and are given in Fig. 2.

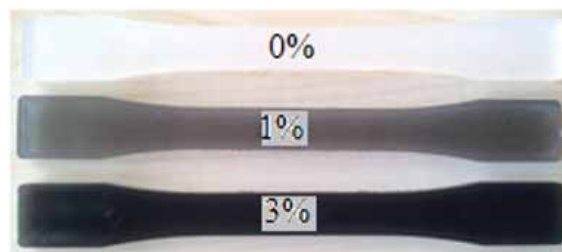


Figure 2. With and without ash added plastic material samples

Table 2. The color values of the plastic material sample

Ash content rate, %	L*	a*	b*	C	H
0	33.31±0.3	1.86±0.4	-0.20±0.2	1.87	353.74
1	5.75±0.4	-3.47±0.3	-9.89±0.4	10.48	250.67
3	0±0.1	-5.21±0.3	-10.39±0.3	11.62	243.34

±: standard deviation

The results obtained by the additive-free produced plastic sample (0%) and the results obtained by 1% and 3% added samples are compared. The color parameters of the resultant plastic samples are given in Table 2. It shows that the micro mixture in the material has an important effect by the increase in the ash rate. It is observed that the brightness value (L*) decreases and the sample turns to black color by the increase in the ash rate. It shows how good the brightness value (L*) is distributed as the micro dispersion for painting the polymer material with olive pomace.

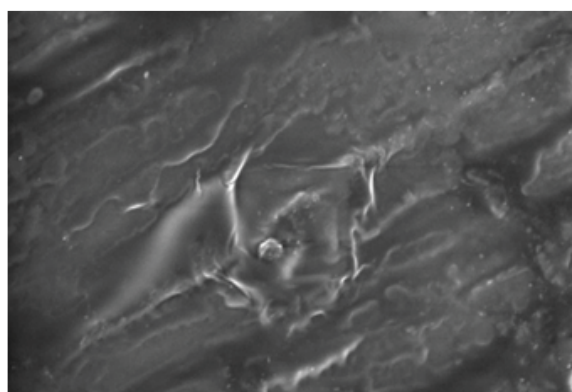


Figure 3. SEM images of the additive-free produced plastic material, 100000x

Interface band images of the polymer materials are shown in Fig. 3-5, which are taken by using Scanning Electron Microscope (SEM) at 100000x magnification rate. The color change results and SEM images give the effects of the distribution of the ash rate in the material and the interface connection. When SEM images taken from the experimental samples were examined, it was seen that the interfacial bonds formed high interaction with the additive material

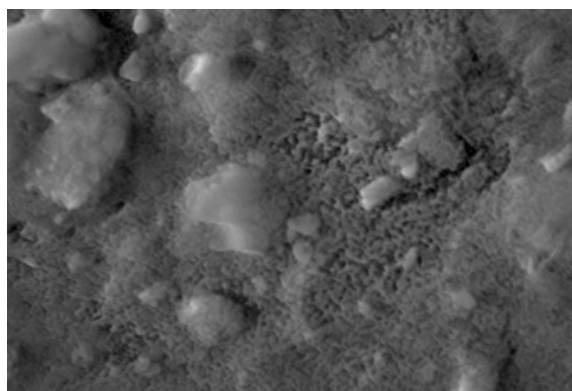


Figure 4. SEM images of the plastic material produced by adding 1% ash, 100000x

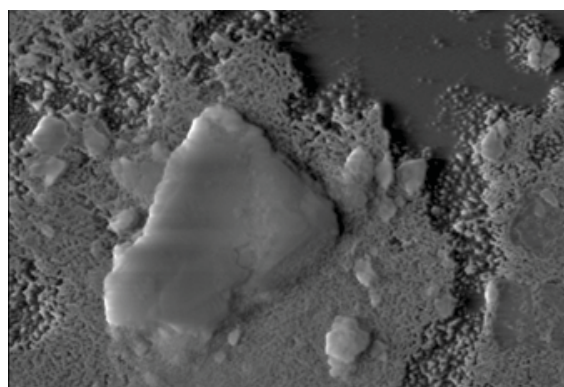


Figure 5. SEM images of the plastic material produced by adding 3% ash, 100000x

and produced a homogeneous distribution throughout the material. As the additive ratio increased, it was determined that the distribution and clusters within the matrix were more frequent and the surface area within the unit was larger. This situation caused the color intensity of the material to increase.

Table 3. Tensile test results

Content rates %	L*	a*	b*
0	1479.50±0.2	56.01±0.1	9.71±0.2
1	1490.58±0.3	60.53±0.1	9.39±0.1
3	1542.17±0.3	69.69±0.3	9.39±0.2

The tensile tests for three different samples with 50 mm/min tensile speed are carried out according to ISO 527-1 standard. The obtained results are given in Table 3 and tensile-force graphic is given in Fig. 6.

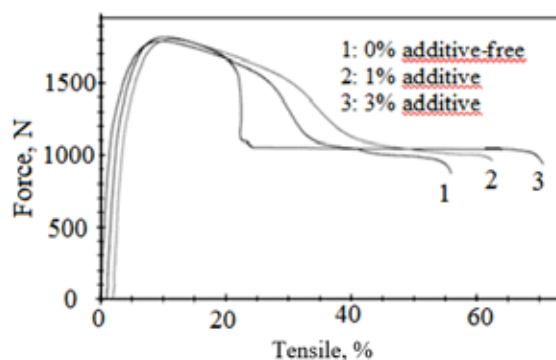


Figure 6. Tensile-Force Diagram applied on three different sample

As a result of the tensile test on the material, it is seen in Table 3 that there is an increase in E-module and the breaking elongation along with the increase in the olive pomace ash. It is thought that the reason for this increase is functioning of the olive pomace in the composite material as the reinforcement element. However, when the received results are examined, it is determined that the differences of the results of the tensile tests between the samples are at minimum level. The increase in the breaking elongation shows

that the interface connection between the polymer, which functions as the matrix material and the ash olive pomace is strong.

The results of the experiments obtained from the tensile specimens, the density of the additive material in the composite and the effect of the interfacial bond formed by the additive on the modulus of elasticity of the material increased.

The results of the impact tests performed at different temperatures are given in Table 4. It is determined that the breaking difference between the test temperatures decreases as the content rate increases. This situation shows that the olive pomace additive partially ensures the interface connection between the plastic material and the heating insulation. Besides, it is obvious that the used olive pomace additive decreases the toughness of the plastic material.

Table 4. The results of the impact test applied to three different samples at different temperatures

Test temperature, °C	The results of the impact test, J		
	0%	1% additive	3% additive
-10	1.34 ± 0.01	1.28 ± 0.01	1.04 ± 0.01
20	6.56 ± 0.01	4.71 ± 0.01	3.07 ± 0.01

It is an original study since it has not been worked before. Therefore, no comparison was made with other studies.

CONCLUSION

The following results are obtained at the study:

(1) It has seen that the E module and the breaking elongation increase as the olive pomace ash increases. The reason for this is the increase of the distribution density of the additive material in the matrix and the increase of the surface area of the interfacial bond with the plastic matrix.

(2) The energy value increases as the temperature increases. This situation shows that the heat insulation can be obtained by using the olive pomace ash.

(3) When the color changes of the composite materials and the findings obtained from the SEM images are compared, it is observed that the olive pomace waste increases in PP content along with the color rate of the interface connection formations. In return for this, it is determined that the breaking surfaces of the material increase.

(4) The existence of the olive pomace particles, which increase the color change rate and the smooth distribution of the material, are found out from the image of the material and the results of the received color measurements. As a result of this, it has seen that the usage as the colorant in the material can be achieved easily.

(5) It has been determined that the dye properties of olive pomach reinforced materials can be reduced by decreasing the used masterbatch ratio and reducing the ratio of waste material transferred to nature. The composite material produced can be used in the construction of simple household appliances.

ACKNOWLEDGEMENT

The authors acknowledge the support received from the Namık Kemal University Research Fund (NKUBAP.00.17.AR.12.04).

References

- Sidal, U., Kolankaya, N. and Kurtonur, C. Pseudomonas sp. İle Zeytinyağı Fabrikası Atığından Biyosülfektan Eldesi, Turk J Biol, 24 (2000) 611-625.
- Keser, O. and Bilal, T. The Use of Olive-by products in Animal Nutrition, Hayvansal Üretim 51(1) (2010) 64-72.
- Kurtuluş, E. Pirinanin Bir Yakıt Olarak Kullanımı Ve Eldesi, Yeni ve Yenilenebilir Enerji Kaynakları Sempozyumu ve Sergisi, 3-4 Ekim 2003, Kayseri, Turkey (in Turkish).
- Tunalıoğlu, R. and Armağan, G. An Evaluation Of Oliveoil Byproducts Produced In Aydın Province In Terms Of Agriculture-Industry And Environment, 8th Congress Of Agricultural Economics Of Turkey, 135-143, Bursa, 2008.
- Başkan A. E. Zeytinyağı İşletmelerinin atıkları ve değerlendirme yolları. T.C. Güney Ege Kalkınma Ajansı, Denizli, 2010 (in Turkish).
- Beken, Y and Şahin, A. The Effect of Prina (Olive Cake) Feeding Methods on Growth Performance and Behaviour of Awassi Lambs, International Journal Of Agriculture & Biology, 13(3), 423-426.
- Jumah, R., Al-Kteimat, E., Al-Hamad, A. and Telfah, E. Constant and Intermittent Drying Characteristics of Olive Cake, Drying Technology, 25, 1421-1426, 2007.
- Altinkoru, N. Industrial Waste And Pomace Of Boron Waste As An Additive In Cement Production Evaluation, Msc. Thesis, Dumlupınar University, 2010.
- ISO 527 -1: Plastics - Determination of tensile properties -- Part 1: General principles, 2012
- ISO 179 -1, Plastics - Determination of Charpy impact properties -- Part 1: Non-instrumented impact test, 2010.
- ASTM 6290-05e1, Standard Test Method for Color Determination of Plastic Pellets, 2013.
- Çelen S and Kahveci K. Microwave drying behaviour of apple slices, Proceedings of the Institution of Mechanical Engineers, Part E, Journal of Process Mechanical Engineering, 227(4) (2013) 264-272.

Low-cost IoT Design and Implementation of a Remote Food and Water Control System for Pet Owners

Ugur Baran Asaner  Armagan Elibol 

Yildiz Technical University, Department of Mathematical Engineering, 34220, Istanbul, Turkey

ABSTRACT

The Internet of things (IoT) concept basically aims to connect any device, vehicle or other items to transfer data between these subsystems. IoT applications make people's lives easier and more efficient in many ways. One of the areas where IoT can be useful is that monitoring food and water supply for pets that are left unattended for either a short or a long time. The main purpose of this paper is to state and detail an instance of low-cost IoT by designing a remote food and water control system for pet owners. The whole system consists of three subsystems; the performing unit, server, and mobile application. Each subsystem has developed by using different open-source programming languages and frameworks.

Keywords:

Internet of things, remote monitoring, open-source development

INTRODUCTION

The Internet of things (IoT) is commonly used to name a set of objects that are directly connected to the Internet. One prediction is that the number of connected things in the world will have a thirty-fold increase between 2009 and 2020, thus by 2020, there will be 26 billion things that are connected to the Internet [1, 2]. Typical application areas for the IoT are home automation [3], personal health monitoring [4, 5], building automation [6], industrial automation [7] and smart cities [8]. The purpose of this paper is to implement a design of low-cost IoT concept, which is a food and water control system for pet owners. There are previous studies on the context of pet feeding: Some of them state an automated system without the remote control [9], while some of them require additional components to be bonded to pets [10]. These studies introduce remote scheduled or automated systems. However, most of these studies do not provide instant access to food or water amounts, which may be important for some pet owners. There are also commercial products aiming to provide automated [11] or remote-controlled [12] pet feeding systems with higher costs. Our proposal is easy to use, low-cost and does not require precise calibration and installation work. Our project consists of three subsystems; performing unit, server, and mobile application. The subsystems and the communication between them have detailed in Section Design and Implementation.

Article History:

Received: 2017/11/30

Accepted: 2018/08/03

Online: 2018/12/31

Correspondence to: Ugur Baran Asaner

Netaş, Kurtkoy, Istanbul

E-Mail: ugurasaner@gmail.com

DESIGN AND IMPLEMENTATION

Our IoT system is designed to provide food and water control for pets and it is controlled by a mobile application interface. The user can observe and monitor the amounts of food and water remotely by using the interface. The user can also refill the food or water if needed. Our system is composed of three main components: Performing unit, server and mobile application respectively. The server has a connecting role between other components as it manages the requests and responses between the performing unit and mobile applications. It also provides authentication to use the system. The information coming from the sensors is stored in the database component, which only accessed by the server. The performing unit has sensors to measure the amounts and motors to refill and the mobile application provides a Graphical User Interface (GUI) for the user to access the server functions. Thus, the system does not allow the mobile application to contact with neither the performing unit nor the database directly. The overview of the system components can be seen in Fig. 1.

Performing Unit

Performing Unit is the major part of our IoT system. It is responsible for core processes such as measuring current food and water amounts and performing refill operation separately for both food and water. The main component of the unit is a single-board computer (SBC) whose role is to control the sensors and motors using some specific drivers. This SBC is



Figure 1. Component relation diagram of the designed IoT.

connected to the internet so that it can receive requests remotely and transmit sensor data to the server at a pre-defined time interval (i.e., hourly). The overview of the unit is given in Fig. 2.



Figure 2. Performing Unit components and flow diagram of the designed IoT.

The unit has a food dispenser and a water tank as storage. There is a motor to refill the food container and water pump to refill water container. Both containers are attached to suitable sensors to measure the amounts. The design sketch of the performing unit is illustrated in Fig. 3.

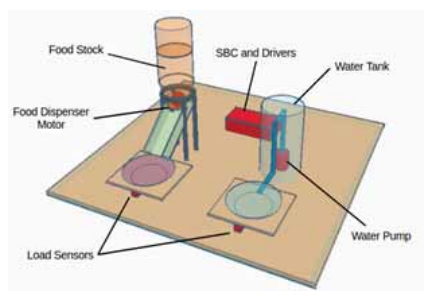


Figure 3. Design sketch of the Performing Unit.

The technical details of the performing unit are detailed in two parts, hardware and software respectively. Each of them will be detailed separately.

Performing Unit Hardware

Performing unit hardware is composed of an SBC, a DC and a Stepper motor, and two load sensors. We used Raspberry Pi B+ model as an SBC and it has General Purpose Input / Output (GPIO) pins, which allow the computer to send and receive signals. There are forty pins available on the SBC and seventeen of them are used by three diffe-

Used For	Function	Pin No	Pin No	Function	Used For
	3.3 V	1	2	5 V	Load Sensors 1-2
	GPIO 2	3	4	5 V	DC Motor
	GPIO 3	5	6	GND	DC Motor
	GPIO 4	7	8	GPIO 14	DC Motor
Load Sensor 1	GND	9	10	GPIO 15	DC Motor
Load Sensor 1	GPIO 17	11	12	GPIO 18	DC Motor
Load Sensor 1	GPIO 27	13	14	GND	
	GPIO 22	15	16	GPIO 23	
	3.3 V	17	18	GPIO 24	
	GPIO 10	19	20	GND	
	GPIO 9	21	22	GPIO 25	
	GPIO 11	23	24	GPIO 8	
	GND	25	26	GPIO 7	
	DNC	27	28	DNC	
	GPIO 5	29	30	GND	
	GPIO 6	31	32	GPIO 12	Stepper Motor
	GPIO 13	33	34	GND	Stepper Motor
Load Sensor 2	GPIO 19	35	36	GPIO 16	Stepper Motor
Load Sensor 2	GPIO 26	37	38	GPIO20	Stepper Motor
Load Sensor 2	GND	39	40	GPIO 21	Stepper Motor

Figure 4. SBC Pins usage diagram

rent components as illustrated in Fig. 4.

The DC motor is used for designing a water pump to refill water container from the water tank. This motor is controlled by an H-bridge driver named 'l293b'. The stepper motor is responsible for refilling the food container from the food tank. The working principle of the motor is based on a vector-based position declaration. This allows defining the rotation with a specific angle. Two load sensors provide weight data and the data is read by SBC using 'hx711' driver. The range of the sensor is from 1gr. to 5kg. The sensor does not require an external power supply to work.

Performing Unit Software

The software side of the performing unit accomplishes two main tasks: The first task is to control electronic components and the second one is to make the performing unit accessible over the internet to handle the remote requests. Python programming language is preferred for the first task as there are many sources available and there are also included libraries to control the pins on the SBC. For a second task, open-source web framework Django is used to develop a web server. The performing unit includes a database to store some basic configurations, which makes the development easier and adjustable to different implementations. This database stores API paths, GPIO pin numbers, server IP address, the current amount of food and water in the containers, tare and threshold values for scaling, and the step size of the stepper motor.

The SBC has the operating system called 'raspi-an', which is an optimized version of Debian for low-performance architecture. The performing unit sends the current amount of data to the server hourly, 'cron' is preferred to use on this task, which is a time-based job scheduling software utility in Unix-like operating systems. Cron is used by defining a cronjob, which could be any task on command line interface. On the other hand, Django has an external package to manage cronjobs in the project, which is called Django-cron [18]. The package works on the operating

system's conjob utility and allows defining classes in Python language, which is suitable for our project. The cronjob checks the defined classes every five minutes and the classes send the data of current amounts to the server, if necessary.

A current control class in the GPIO library is used to control the DC motor. This class allows running the motor for five seconds, which pumps approximately 50ml. of water from the tank to the container. The motor starts running when the appropriate pin set as high current and stops when the pin set as low current.

The stepper motor is also controlled by a class in GPIO library. Besides the pin numbers, the number of steps is obtained from the internal database of the performing unit and provided for the class.

The load sensors require an additional library with the same name as the driver chip 'hx711'. Load sensors used are prone to return inconsistent sensor readings sometimes. These outliers should be filtered out. To do this, several readings from the sensor are made and extreme readings (as minimum and maximum) are removed. The arithmetic mean of the remaining readings is computed and returned as data. The library called the same name with the driver chip, hx711 is used.

Server

The server is running on a Virtual Private Server (VPS) that has an Ubuntu Server operating system. Laravel web framework is preferred to develop the software on the server as it provides easy configuration and management. The server has an API role between the performing unit and the mobile application. There are two main tasks handled by the server; tracking the amount of food and water and the authentication of the mobile application. The amount track is composed of communicating with the performing unit and receiving/requesting the current amount of food and water in the containers. The server maintains a web server software that keeps track of the requests coming from the mobile application and authentication related data between performing unit and the mobile application.

Mobile Application

The main purpose of the mobile application is to provide a GUI for the IoT. The mobile application is developed for the Android platform. The main functions are showing the amount of food and water for the last ten hours and refilling the food and water. There are two line graphs showing the food and water amounts on the y-axis and time on the x-axis. The previously specified minimum amount of food and water are also shown in these graphs as flat lines. The function of refilling food and water is



Figure 5. Mobile Application main screens. The graphs are for monitoring the current amounts of food and water over a pre-defined time period

accessed through two buttons. Once the user wishes to perform refill operation, the application asks for the confirmation. The user needs to swipe down the screen while running the application to obtain the current amounts. The screens of the mobile applications are given in Fig. 5. The demonstration video of our IoT prototype can be seen at <https://goo.gl/4z59Aq>

CONCLUSION

The Internet has been continuously changing our daily life over two decades. Recently, not only computers but also mobile platforms (e.g., phones, tablets etc.) make internet access possible. Lately, the concept of the Internet of Things (IoT) has been developing rapidly. It aims to create smart tools by connecting everything to the internet. As they make life easier for humans, the need for them has been increasing and the new application areas have been expanding day and day. One of these emerging areas is home automation and/or monitoring in the context of smart homes.

Pets are usually left unattended during a day-time of working days. They are also left unattended when their owners are in travel. Therefore, it would be useful to have a system to feed them remotely. In this study, from top to toe, a low-cost IoT system is presented for pet owners to monitor food and water supply and feed their pets remotely. The system is composed of performing unit, server, and mobile application. The performing unit is mainly for controlling the amounts of food and water and refilling. The server plays a bridge role between performing unit and mobile application with suitably arranged security measures. The mobile application is a GUI of the whole system. It provides the current amounts of food and water and allows the user to perform a refill operation. All software parts of the subsystems are developed by using open-source programming environments with relevant security measures and its sensor suite was designed in a minimalistic way.

REFERENCES

1. http://www.faz.net/aktuell/wirtschaft/diginomics/grosse-internationale-allianz-gegen-cyber-attacken-15451953-p2.html?printPagedArticle=true#pageIndex_1, Retrieved on May 21, 2018
2. Nordrum, Amy (18 August 2016). "Popular Internet of Things Forecast of 50 Billion Devices by 2020 Is Outdated". IEEE.
3. Pavithra, D., & Balakrishnan, R. (2015, April). IoT based monitoring and control system for home automation. In Communication Technologies (GCCT), 2015 Global Conference on (pp. 169–173). IEEE.
4. Hassanali, M., Page, A., Soyata, T., Sharma, G., Aktas, M., Mateos, G., ... & Andreescu, S. (2015, June). Health monitoring and management using Internet-of-Things (IoT) sensing with cloud-based processing: Opportunities and challenges. In Services Computing (SCC), 2015 IEEE International Conference on (pp. 285–292). IEEE.
5. Kirci, P. and Kurt, G., Long Term and Remote Health Monitoring with Smartphone, International Journal of Intelligent Systems and Applications in Engineering, Vol.4, No. 4, 2016
6. Kastner, W., Kofler, M., Jung, M., Gridling, G., & Weidinger, J. (2014, September). Building Automation Systems Integration into the Internet of Things The IoT6 approach, its realization and validation. In Emerging Technology and Factory Automation (ETF), 2014 IEEE (pp. 1–9). IEEE.
7. Da Xu, L., He, W., & Li, S. (2014). Internet of things in industries: A survey. IEEE Transactions on industrial informatics, 10(4), 2233–2243.
8. Zanella, A., Bui, N., Castellani, A., Vangelista, L., & Zorzi, M. (2014). Internet of things for smart cities. IEEE Internet of Things journal, 1(1), 22–32.
9. Manoj M, "Automatic Pet Feeder", International Journal of Advances in Science Engineering and Technology, ISSN: 2321-9009, Volume-3, Issue-3, Special Issue Sept.-2015 http://www.ijar.in/journal/journal_file/journal_pdf/6-185-14414356149-11.pdf
10. Own, C. M., Shin, H. Y., & Teng, C. Y. (2013). The study and application of the IOT in pet systems. Advances in Internet of Things, 3(01),
11. Healthy Pet Simply Feed Programmable Digital Pet Feeder, Petsafe, <https://store.intl.petsafe.net/en-gb/healthy-pet-simply-feed-programmable-digital-pet-feeder>, Retrieved on May 26, 2018
12. Smart Pet Feeder, Petnet, <https://petnet.io/smartfeeder>, Retrieved on May 26, 2018
13. Overview of the Internet of things.. International Telecommunications Union. <http://handle.itu.int/11.1002/1000/11559>, Retrieved on May 26, 2018.
14. Whitmore, A., Agarwal, A., & Da Xu, L. (2015). The Internet of Things—A survey of topics and trends. Information Systems Frontiers, 17(2), 261–274.
15. Gubbi, J., Buyya, R., Marusic, S., & Palaniswami, M. (2013). Internet of Things (IoT): A vision, architectural elements, and future directions. Future generation computer systems, 29(7), 1645–1660.
16. Govindraj, V., Sathiyarayanan, M., & Abubakar, B. (2017, August). Customary homes to smart homes using Internet of Things (IoT) and mobile application. In Smart Technologies For Smart Nation (SmartTechCon), 2017 International Conference On (pp. 1059–1063). IEEE.
17. Wunderlich, S., Cabrera, J. A., Fitzek, F. H., & Reisslein, M. (2017). Network coding in heterogeneous multicore IoT nodes with DAG scheduling of parallel matrix block operations. IEEE Internet of Things Journal, 4(4), 917–933.
18. https://djangopackages.org/packages/p/django_cron/, Retrieved on August 21, 2017

Energetic And Exergetic Investigations of an Integrated Heat Pump System for Drying Applications

Canan Acar 

Bahcesehir University, Faculty of Engineering and Natural Sciences, 34353, Istanbul, TURKEY

ABSTRACT

The main aim of this study is to conduct energetic and exergetic investigations of a dual stage heat pump for drying applications in order to evaluate the performance of the overall system. The integrated system consists of two processes, namely a drying unit and a dual stage heat pump. In the heat pump process, R-134A is used as the thermodynamic fluid and the drying unit is used to reduce the moisture content of the air. There are two evaporators used in the dual stage heat pump process: the first evaporator works at high pressures and the second evaporator works at lower pressures. The second evaporator provides supplementary cooling and drying effect for the air used in the drying unit. In the integrated system, there are two sub-coolers which provide additional heating to R-134A after the condenser. In this study, the energy and exergy efficiencies and exergy destruction rates of the overall integrated system, and each component and subprocess are calculated and discussed in detail. Exergetic performance of each component and subprocess are further investigated to identify where the highest exergy destructions occur in order to minimize irreversibilities within the integrated system and hence enhance the overall exergetic efficiency of the integrated system. The impact of environmental conditions on exergetic efficiency and exergy destruction is investigated via parametric studies. In addition, the coefficient of performance (COP) of the whole system and the effect of operating conditions are examined. The highest energy and exergy efficiencies occur when the drying unit's inlet air mass flow rate is 0.5 kg/s and the environmental pressure and temperature are at 101 kPa and 298K which are 62% and 35%, respectively. The overall integrated system has a COP of around 3.8.

Keywords:

Energy; exergy; efficiency; heat pump, drying, sustainability.

INTRODUCTION

As the world faces unprecedented energy challenges, many countries are looking to include smart solutions to energy consuming processes as an effort to reach a sustainable future. Drying is a major energy-intensive process used in a wide variety of industrial applications. The main reason for the wide use of drying as a popular industrial application is drying reduces overall product weight and size for easier transportation which also decreases the space requirements and fuel consumption. Drying also increases the storage time of foods and industrial products. However, drying is the main reason of high energy consumption of many industries, for instance, the energy consumption during the drying process is equal to almost 50% and 70% of the overall energy consumption in the textile and forestry industries,

respectively [1]. The most commonly utilized primary energy resources in air conductive industrial dryers are fossil fuels, electricity, and biomass. Reducing the high energy consumption of drying processes can be done by increasing system efficiencies which essentially decreases the harmful greenhouse gas emissions during drying. In heat pump integrated drying processes, significant amounts of energy can be recovered, energy loss and harmful wastes can be minimized, and, as a result, up to 50% of the primary energy sources can be saved [2, 3].

The core aim of a drying system is to provide its output at a preferred moisture content and quality at a lowest possible cost and environmental impact and highest possible efficiency by optimizing the system para-

Article History:

Received: 2018/02/11

Accepted: 2018/09/13

Online: 2018/12/31

Correspondence to: Canan Acar,
Bahcesehir University, Faculty of
Engineering and Natural Sciences, Çırağan
Caddesi No: 4 – 6, 34353, Beşiktaş,
Istanbul, TURKEY
E-Mail: Canan.Acar@eng.bau.edu.tr

Table 1. Technical comparison of heat pump dryers with selected drying technologies

Parameter	Freeze drying	Hot air drying	Vacuum drying	Heat pump drying
SMER, kg water/kWh	< 0.4	0.1–1.3	0.7–1.2	1.0–4.0
Operating temperature range, °C	-35–50	40–90	30–60	-10–80
Operating relative humidity range, %	Low	Variable	Low	10–80
Drying efficiency, %	Very low	35–40	< 70	<95
Drying rate	Very low	Average	Very low	Faster
Capital cost	Very high	Low	High	Moderate
Running cost		High	Very high	Low
Control	Good	Moderate	Good	Very good

Source: Erbay and Hepbasli [8].

meters. Drying has very high energy demand. For example, 15% of the entire industrial energy use is caused by drying applications. What is more important is the fact that a significant amount of energy is wasted in industrial dryers. More specifically, here are some examples of the contribution of drying in different industrial operations:

- 70% of the energy use in forestry
- 50% of the energy use in the textile industry
- More than 60% of the energy use in farms

In developed countries, 9–25% of the energy demand is caused by the drying processes. As a consequence, to decrease the energy demand of the drying processes, it is essential to inspect alternative and innovative technologies to enhance the performance of dryers. For example, compared to traditional dryers, heat pump drying processes can reduce energy consumption significantly. In addition, heat pump dryers can lower CO₂, NO_x, and other GHG emissions considerably. In addition, the literature shows that heat pump dryers enhance the quality of the final product.

Heat pump assisted drying processes to have significant advantages such as reduced greenhouse gas emissions, less energy loss, and better control of drying gas temperature and moisture content [4, 5]. In some industrial applications, the moisture content and temperature of the product and the overall product quality are especially important, therefore, this critical requirement makes heat pump assisted drying processes very promising options when it comes to better control and monitoring of all key drying process parameters [6, 7]. Furthermore, regardless of their primary energy source requirement, any conventional dryer can be integrated into any type of heat pump, and this is another major advantage. In heat pump integrated drying processes, latent heat can be converted to sensible heat, and therefore these systems are considered as outstanding alternatives when recovering heat in a drying unit is a critical require-

ment [8, 9]. Table 1 summarizes some of the technical characteristics of three drying options: (i) freeze drying, (ii) hot air drying, (iii) vacuum drying, and (iv) heat pump drying. Table 1 shows some of the most important benefits of using heat pump dryers, which are namely enhanced SMER (Specific Moisture Extraction Ratio), better drying quality and rate at lower operating temperatures, applicability in a wide range of drying operating conditions, enhanced operation control when delivering high quality and critical end-use products, and less energy consumption and waste. Potential benefits of heat pump drying systems are illustrated in Fig. 1.

The idea of heat pump integrated drying systems is becoming more popular in the literature. First, Perry [10] have suggested an integrated system which utilizes a heat pump with two evaporators. In their system, the first evaporator has operated at higher pressures and the second one has operated at lower pressures. This dual stage heat pump has been integrated with a drying unit. In Perry's design, the high-pressure evaporator has delivered cooling via sensible heat transfer and the second evaporator has been utilized to deliver cooling via latent heat transfer. In the beginning, Perry's proposal has not been acknowledged widely because

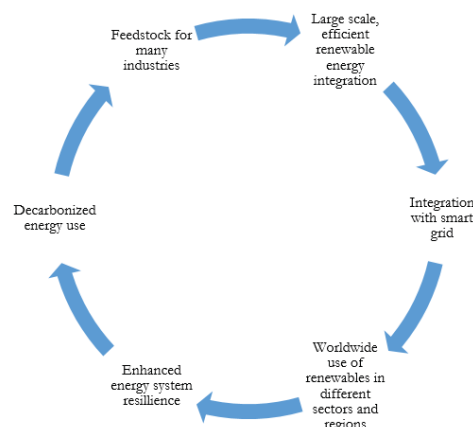


Figure 1. Potential benefits of heat pump drying systems as a smart energy solution.

controlling a system with one evaporator had been considered a lot easier. Therefore, Perry's proposed integrated system has been assumed to be a complex idea. Following Perry's work, Chua and Chou have designed, constructed, and verified Perry's proposed system, primarily for agricultural product drying purposes [2, 11, 12]. Then, a refrigeration process with two evaporators has shown higher efficiencies compared to the ones with one evaporator only [13]. These aforementioned previous studies on double evaporator processes show that from the thermodynamic perspective, a dual evaporator process can offer enhanced surface areas for better heat transfer rates, as a result, these systems can minimize the compressor load of the entire system.

Heat pump drying systems have the potential to become a part of a clean, reliable, affordable, safe, and sustainable portfolio of smart energy solutions. Heat pump dryers can be used to provide high-quality products cleanly and efficiently in a wide range of operating conditions and for different applications. Widespread deployment of heat pump drying systems offers a broad range of benefits for the environment, for our energy security, for our domestic economy, and for end-users. Heat pump dryers are smart solutions for the sustainability of future energy systems. They offer many sustainable end use options for small scale, large scale, and mobile and stationary applications. Many different industries such as pharmaceutical, forestry, textile, agriculture, food, etc. highly benefit from heat pump dryers. Globally, heat pump drying systems have been getting more popular among end users. Heat pump dryers work with a wide range of locally available, abundant, clean, and efficient resources. They can smartly link these resources to end users via a diverse set of industrial and residential applications.

We live in an era where everything we use and everything we interact with in our daily lives has to be smart. Therefore, it is safe to say that future energy solutions, including heat pump dryers, have to be smart as well. In regards to future heat pump drying systems, we need to make it in line with these under smart energy solutions. With the developed cutting-edge technologies and artificial intelligence applications, we need to change the course of action in dealing with energy matters, covering the entire energy spectrum under five categories, as energy fundamentals and concepts, energy materials, energy production, energy conversion, and energy management.

With the global energy crisis and climate change concerns, it is becoming more and more obvious that we need to change the course of action and switch from conventional methods, approaches, systems, solutions to a smart energy portfolio where the smart solutions are targeted. Switching to smart energy solutions does not mean that we can ignore the concepts and fundamentals which should be treated like

a building cannot stand without pillars. Energy solutions cannot survive without concepts and fundamentals.

The primary aim of the present research is to perform a complete investigation of the energetic and exergetic performance of a dual-step integrated heat pump drying system formerly designed by Chua and Chou [2]. In this study, R134A is selected instead of R22 used by [2] due to the environmental benefits of R134A. In addition, the literature including [2] lacks the comprehensive exergetic investigation of the proposed heat pump-drying system, and a better understanding of any energy system can be accomplished only with a thorough exergy analysis [14], which is the main motivation behind this study. The performance investigation of the overall integrated system is conducted according to comprehensive energy and exergy assessments of each and every constituent, unit, and subprocess of the entire integrated system. Overall system performance and the component based efficiency analysis are conducted by changing a variety of key parameters such as environmental temperature via parametric studies. In the last part of this study, suggestions for enhanced system performance are presented for less environmental impact and better sustainability in the future directions section.

HEAT PUMP DRYING PERFORMANCE CHARACTERISTICS

The performance characteristics of a heat pump drying system can be classified in four groups as follows: (i) thermodynamic performance, (ii) economic performance, (iii) environmental impact, and (iii) final product quality. Compared to other drying alternatives, heat pump drying systems are environmentally benign since they do not emit harmful gases and at the drying site [15]. In heat pump dryers, the condensate can be recovered and disposed of properly and the valuable volatiles can be recovered from the condensate [16]. In this section, the quality aspects of heat pump dried products are discussed in detail.

Quality of the Final Product

The key expectations from effective heat pump drying systems with high-quality final products are the ability to [17]:

- operate at an absolute humidity less than that of the environment
- select the operating temperature to be less than or above the environmental temperature
- provide drying in a non-vented chamber using a

modified drying atmosphere

The quality of dried products is enhanced by heat pump drying is comprised of a number of physical, chemical and sensory characteristics are discussed in this section.

Microbial safety

Quality deterioration caused by microorganisms is undesirable commercially because they limit the shelf life and lower the quality of the final product. Drying helps in reducing or overcoming potential microbial damages. With heat pump drying, microbial safety is minimized by ensuring that all raw materials conform to recognized standards of preparation [18]. Heat pump dryers are able to enhance microbial safety in the final product by maintaining the relative humidity at reasonably low levels. Also, the operating temperature of heat pump dryers is not limited by the environmental humidity.

Color

Color degradation is a major cause of loss in the quality of the final product. Especially in the food industry, the color of food is an important indicator of the final product quality. Although sulfating agents prevent the browning reactions in the final product, their use is restricted due to several health and safety concerns. On the other hand, enzymatic browning in food drying can be reduced without the use of sulfates by increasing the air velocity at low relative humidity (<20%) and high moisture content (~2kg/kg dry matter) [19]. This strategy is applicable in heat pump dryers because the humidity can be controlled independently by the environmental conditions. Also, drying under nitrogen has been found to be effective in inhibiting browning during the critical initial drying period when the moisture content is high [20]. This shows that there is the possibility of using heat pump drying processes to produce high-quality final products. Another way constrain browning in dried products is utilizing heat pump dryers to produce specific temperature-humidity conditions [21].

Ascorbic acid (AA) and volatile compound content and preservation of active ingredients

The impact of constant temperature drying on product quality is well recorded in the literature [22]. As the drying temperature increases, the browning of the final product accelerates and the AA content of the final product decreases. With proper selection of the drying temperature, the AA content of the final product can be kept at desired levels without significant enhancement in drying time. In addition, using reduced air temperatures

at the onset of drying as in the case of heat pump drying followed by temperature elevation as drying proceeds yield a better quality product [23]. The volatile component concentration usually increases, especially in low-temperature heat pump drying systems. Therefore, heat pump dryers are seen as the best systems for the preservation of volatile compounds in the final product. Also, the preservation of total chlorophyll and ascorbic acid content in fried fruits can be accomplished in heat pump dryers with higher rehydration ratios and sensory scores than hot air dryers [24].

Aroma and flavor loss

Drying methods that employ lower temperatures provide a higher concentration of key aroma compounds [25]. Therefore, heat pump dryers can effectively retain the aroma content of the final products and minimize the degradation of the aromatic compounds by keeping the drying operation at low temperatures. Furthermore, since heat pump drying occurs in a closed chamber, any compound that volatilizes remain inside the drying unit. As the partial pressure of the volatile compound gradually builds up within the chamber, further volatilization from the product slows down [26]. Therefore, it can be said that the color and aroma of the final products can be better preserved with heat pump dryers.

Viability

When drying oxygen-sensitive materials such as flavor compounds and fatty acids, the product can undergo oxidation, causing poor flavor, color, and rehydration properties of the final product. Heat pump dryers have the advantage of drying without unacceptable deterioration of viability and activity. This could be accomplished by freeze-drying too, however, heat pump dryers are cheaper, which makes them more favorable [27].

Rehydration

During drying, important changes in structural properties can be observed as water is removed from the moist material. Rehydration is a process of moistening the dried product. For example, in most cases, dried foods are soaked in water before cooking or consumption, therefore rehydration is a very important quality criterion. Factors affecting the rehydration process include:

- porosity, capillarity, and a cavity near the product surface
- temperature, trapped air bubbles, amorphous crystalline state, soluble solids, and pH of soaking water

Using heat pump dryers can accelerate the rehydration times and enhance the rehydration ratios of the final product [28].

Shrinkage

Heating produces major changes in the structure of the dried products. Shrinkage occurs because the dried product's structure cannot support their weight and, therefore, collapse under gravitational force in the absence of moisture. Shrinkage occurs first at the surface and gradually moves to the bottom with increasing drying times. When the drying process occurs at higher temperatures, cracks are formed in the final product. With their lower drying times and temperatures, heat pump dryers minimize shrinkage problems and offer products which have less structural damage and deformation [29].

Drying Efficiency

The performance of a drying system is characterized by various indices, including energy efficiency, thermal efficiency, volumetric evaporation rate, specific heat consumption, surface heat losses, unit steam consumption, and others which have been defined to reflect the requirements of various drying technologies [30]. Energy efficiency is critical because energy consumption strongly affects the drying costs [31]. Efficiency calculations are useful when assessing the system performance, identifying potential improvements, and selecting the optimum drying system and conditions [32]. Energy efficiencies are meant for providing an objective comparison between different dryers and drying processes. There are three groups of factors affecting drying efficiency [33]:

- Environmental conditions
- Current and desired moisture content of the product
- Operating conditions

For heat pump drying systems, drying efficiency is a measure of the quantity of energy used to remove one unit mass of water from the product, normally measured in kJ/kg water or kWh/kg water. In general, drying efficiency, η can be defined by:

$$\eta = \frac{T_{in} - T_{out}}{T_1 - T_0} \quad (1)$$

where T_{in} is the inlet temperature of the dryer, T_{out} is the outlet temperature of the dryer, and T_0 is the environmental temperature. The numerator of Equation 1 is a

major factor in determining the efficiency of a dryer [34]. Energy efficiency is also the ratio of the latent heat of evaporation of the moisture removed to the drying air heat input.

Coefficient of Performance (COP)

COP can be used to evaluate the amount of work converted into heat for two different system operations: for cooling and for heating. For a heat pump, the heat transfer Q_{out} from the system to the hot body is desired, and the coefficient of performance is expressed in Equation 2, where W_{comp} is the electrical power input of the compressor.

$$COP = \frac{\text{Desired output}}{\text{Required input}} = \frac{\text{Heat added}}{\text{Work required}} = \frac{Q_{out}}{W_{comp}} \quad (2)$$

Specific Moisture Extraction Ratio (SMER)

An alternative indicator of the energy efficiency for heat pump dryers is the specific moisture extraction ratio which is calculated as

$$SMER = \frac{\text{Amount of water evaporated (kg)}}{\text{Energy use (kWh)}} \quad (3)$$

The SMER can be calculated either as an instantaneous value or as an average value during drying [35]. During the drying process, the SMER value decreases as the removal of moisture become more difficult due to smaller water vapor deficits at the surface of the product. For heat pump dryers, the SMER value can be above the theoretical maximum value. The energy efficiency of heat pump dryers can be reflected by their higher SMER values and drying efficiency when compared to other drying systems as shown in Table 1. Consequently, higher SMER would then be translated to lower operating cost, making the payback period for initial capital considerably shorter. The following are some suggestions for maximizing the capacity and efficiency of a heat pump dryer:

- use of continuous operation instead of batch drying so that the system can be operated at stable optimal conditions
- air flow should be counter current instead of cross-flow or co-current relative to the product movement to maximize the relative humidity at the dryer outlet and to match the drying characteristics of the product
- the inlet temperature of the dryer should be maximized in accordance with the product requirement,
- the refrigeration capacity should not be oversized so as not to reduce the relative humidity and a consequent

reduced SMER

- if possible, evaporating and condensing temperatures should be selected to optimize the COP and the thermal efficiency

Exergy

Exergy analysis is a useful tool that can be successfully used in the design of an energy system and provides the information necessary to choose the appropriate component design and operating procedure [36]. Exergy efficiency has been used rather than the energy efficiency in the performance analysis of heat pump dryers, particularly to indicate the possibilities for thermodynamic improvement [37]. It is defined as the maximum amount of work that can be produced by a stream of matter, heat, or work as it comes to equilibrium with its reference environment [38]. Information on exergy is effective in determining the processing plant and operating cost as well as energy conservation, fuel versatility, and pollution associated with the process [39]. Using an exergy analysis method, the magnitudes and locations of exergy destructions (i.e., irreversibilities) in the whole system can be identified [40].

Due to the definition of the first law of thermodyna-

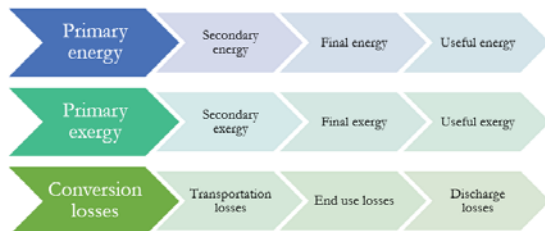


Figure 2. 3S (system-source-service) approach from energy and exergy perspectives, including losses.

mics, energy is already conserved, therefore, instead of energy conservation, exergy conservation must be accomplished via exergization. Exergization should be applied to every component of heat pump drying systems from source, to the system, to service. With this approach, both energy and exergy losses in each step of a heat pump drying process such as conversion transportation, end use, and discharge losses as shown in Fig. 2 can be identified and addressed. Exergization is a useful smart energy solution to properly evaluate and point out which step in a process requires the highest attention to modifying for the better management of the “quality of energy”.

DETAILED INFORMATION ON THE SYSTEM

The integrated heat pump drying process examined in

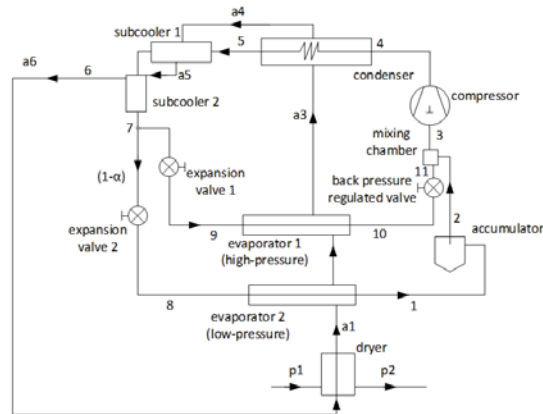


Figure 3. Graphic illustration of the dual stage integrated heat pump drying process (modified from [2]).

the present research is given in Fig. 3. The system is developed according to Chua and Chou’s proposal [2]. Overall, the integrated system is different than most of the heat pumps since it has two evaporators instead of one. Other components are schematically presented in Fig. 3.

The review of every stream, together with their matching stream numbers, constituents, stream flow rates (kg/s), temperatures (°C), pressures (kPa), and states are shown in detail in Table 2. The comprehensive energetic and exergetic performance investigation of the integrated dual stage heat pump drying system is carried out by using the data presented in Table 2. In this study, R-134A is carefully chosen for the heat pump and the air is used in the drying unit. More detailed information on mass, energy, entropy, and exergy balance equations, in addition to energy and exergy efficiency, COP, relative irreversibility, and sustainability index equations, are presented in the following segment entitled “System Analysis”. And the thermodynamic evaluation results are presented in the upcoming section, along with detailed discussion and suggestions for better system performance.

SYSTEM ANALYSIS

Quantitative and comprehensive approach to the first and second laws of thermodynamics is conducted in this research in order to comprehensively investigate the thermodynamic performance of the integrated dual stage heat pump integrated dryer. The thermodynamic evaluation criteria used in this study are energetic and exergetic efficiencies, exergy destruction rates, relative irreversibilities, and sustainability indexes. For the performance analysis part, the EES software is utilized in order to find the thermodynamic properties of each stream and solve the mass, energy, entropy, and exergy balance equations.

The integrated dual stage heat pump drying system

Table 2. Thermodynamic properties of each stream of the selected system.

Stream Number	Component	State	Temperature (°C)	Pressure (kPa)	Mass flow rate, \dot{m} (kg/s)
1	R-134A	Gas	7.45	500	0.0429
2	R-134A	Gas	7.45	500	0.0429
3	R-134A	Gas	7.45	500	0.066
4	R-134A	Liquid	83.48	2500	0.066
5	R-134A	Liquid	61.35	2500	0.066
6	R-134A	Liquid	56.35	2500	0.066
7	R-134A	Liquid	51.35	2500	0.066
8	R-134A	VLE*	0.1148	500	0.0429
9	R-134A	VLE*	23.4	1000	0.0231
10	R-134A	Gas	23.4	1000	0.0231
11	R-134A	Gas	7.45	500	0.0231
a1	air	Gas	28.05	101.3	0.5
a2	air	Gas	25.27	101.3	0.5
a3	air	Gas	23.6	101.3	0.5
a4	air	Gas	44.21	101.3	0.5
a5	air	Gas	45.17	101.3	0.5
a6	air	Gas	46.08	101.3	0.5

* VLE: Vapor-liquid equilibrium

operates at steady state steady flow and the changes in kinetic and potential energy in all streams and components are neglected. There are no chemical reactions in any components and streams within the entire system, therefore, chemical exergies are not taken into account. All auxiliary components such as tubing, pipes, valves, etc. are assumed to be very well insulated and there are no heat losses or pressure drops within these components. The compressor's isentropic efficiency is presumed to be 95%. The energy efficiency of the condenser and expansion valve are taken as 100%. Specific heat capacity and density of air, water, and R-134A are assumed to be constant within the selected operating temperature interval. All equipment is assumed to be adiabatic except the evaporators, sub-coolers, condenser, and drying unit. The general mass balance equation within a given control volume (cv) can be written as in the following form:

$$\frac{dm_{cv}}{dt} = \sum \dot{m}_{in} - \sum \dot{m}_{out} \quad (4)$$

Here, m and \dot{m} specify the mass and mass flow rate, and the subscripts "cv", "in" and "out" mean the control volume and the inlet and outlet streams to/from the control volume, respectively. When a system operates in steady state steady flow conditions, the general mass balance equation (Equation 1) becomes:

$$\sum \dot{m}_{in} = \sum \dot{m}_{out} \quad (5)$$

The steady state steady flow energy, entropy, and exergy balance equations are developed in a similar fashion to Equation 2 such as

Energy Balance Equation (EBE):

$$\sum \dot{E}_{in} = \sum \dot{E}_{out} \quad (6)$$

Entropy Balance Equation (EnBE):

$$\sum \dot{S}_{in} + \dot{S}_{gen} = \sum \dot{S}_{out} \quad (7)$$

Exergy Balance Equation (ExBE):

$$\sum \dot{E}x_{in} = \sum \dot{E}x_{out} + \dot{E}x_{dest} \quad (8)$$

where \dot{E}_i shows the energy input/output rate and "in" and "out" point out the inlet and outlet streams to/from the selected control volume, respectively. The energy flow rate (\dot{E}) is either in heat form (\dot{Q}), or work form (\dot{W}), as the inlet or outlet stream. The energy flow rate is calculated by using the following equation:

$$\dot{E}_i = \dot{m}_i h_i \quad (9)$$

The subscript i signifies the "stream i " and h_i denotes the specific enthalpy (kJ/kg) of that stream. In the same way, \dot{S} in Equation 4 implies the entropy input rate (\dot{S}_{in}), entropy output rate (\dot{S}_{out}), or entropy generation rate (\dot{S}_{gen}). The entropy flow rate within a stream is calculated by using

its specific entropy content s_i according to:

$$\dot{S}_i = \dot{m}_i s_i \quad (10)$$

The term ($\dot{E}x$) in Equation 5 represents the exergy flow rate and the subscript *dest* denotes the exergy destruction rate. The exergy destruction rate is an important indicator of potential system irreversibilities. The main goal is to enhance exergetic system performance by lowering exergy destruction rates. The mode specific steady state exergy balance equation is given in the following equation as

$$\begin{aligned} & \sum \dot{m}_m ex_{in} + \sum \dot{E}x_{\dot{Q}_m} + \sum \dot{E}x_{\dot{W}_m} \\ & = \sum \dot{m}_{out} ex_{out} + \sum \dot{E}x_{\dot{Q}_{out}} + \sum \dot{E}x_{\dot{W}_{out}} + \dot{E}x_{dest} \end{aligned} \quad (11)$$

The exergy content of work ($\dot{E}x_w$) is equal to its energy content (\dot{W}). For the energy content of heat input or output (\dot{Q}), the maximum amount of useful work which could be obtained from the heat source is called thermal exergy flow. And the thermal exergy flow rate ($\dot{E}x_Q$) can be calculated by using the following equation

$$\dot{E}x_Q = \dot{Q} \left(1 - \frac{T_0}{T} \right) \quad (12)$$

In equation (9), $(1-T_0/T)$ is the Carnot efficiency, which is also called as the dimensionless exergetic temperature. The Carnot efficiency of a system is calculated based on its operating temperature (T) and the environmental temperature (T_0). Exergy content of an energy or matter flow is the maximum amount of useful work which could be obtained from that particular energy or matter flow. When a matter or system is in complete equilibrium with its environment, its exergy content reaches zero. Therefore, the environment's state is also referred to as "dead state". When calculating the specific exergy content of matter, the physical (ex^{ph}), chemical (ex^{ch}), kinetic (ex^{ke}) and potential (ex^{pe}) exergy components are all taken into account. Here, the chemical, kinetic, and potential exergies are not taken into account because the kinetic and potential energy changes are neglected and no chemical reactions occur within the system. Hence, the exergy amount stored in the matter can be calculated based on its specific enthalpy and entropy at the environmental temperature (T_0) and pressure (P_0), which is given in the following equation as

$$ex = (h - h_0) - T_0 (s - s_0) \quad (13)$$

Here, h and h_0 are specific enthalpies at system temperature and pressure (T, P) and environmental (T_0, P_0), respectively. Similarly, s and s_0 are specific enthalpies at system temperature and pressure (T, P) and environmental (T_0, P_0), respectively.

The total exergy output rate of a process is always less than the total exergy input rate due to exergy destruction. The exergy destruction rate is shown as $\dot{E}x_{dest}$ in this study and it can be calculated from the entropy generation rate by

using the following equation:

$$\dot{E}x_{dest} = T_0 \dot{S}_{gen} \quad (14)$$

Energy analysis alone is not enough to understand system irreversibilities and identify points for improvement. Energy conservation is misleading because due to the first law of thermodynamics, energy is conserved. However, the second law of energy states that the quality of energy (exergy) decreases. Therefore, our aim must be conserving exergy as much as possible by eliminating or minimizing exergy destructions (i.e., irreversibilities) [14]. The energy and exergy efficiency equations of each component are presented in detail in Table 3.

The following equations are used to calculate the relative irreversibility (RI) and sustainability index (SI) of each system component:

$$RI_i = \frac{\dot{E}x_{dest,i}}{\dot{E}x_{dest}} \quad (15)$$

$$SI_i = \frac{1}{1 - \psi_i} \quad (16)$$

The COP and energy and exergy efficiency equations of the overall system are estimated via the subsequent equ-

Table 3. Efficiency equations of the main components of the integrated design.

	Units	Energetic Efficiency	Exergetic Efficiency
1	Compressor	$\eta_1 = \frac{\dot{E}_4 - \dot{E}_3}{\dot{W}_1}$	$\psi_1 = \frac{\dot{E}x_4 - \dot{E}x_3}{\dot{W}_1}$
2	Condenser	$\eta_2 = \frac{\dot{E}_{a4} - \dot{E}_{a3}}{\dot{E}_4 - \dot{E}_5}$	$\psi_2 = \frac{\dot{E}x_{a4} - \dot{E}x_{a3}}{\dot{E}x_4 - \dot{E}x_5}$
3	Sub-cooler 1	$\eta_3 = \frac{\dot{E}_{a5} - \dot{E}_{a4}}{\dot{E}_5 - \dot{E}_6}$	$\psi_3 = \frac{\dot{E}x_{a5} - \dot{E}x_{a6}}{\dot{E}x_5 - \dot{E}x_6}$
4	Sub-cooler 2	$\eta_4 = \frac{\dot{E}_{a6} - \dot{E}_{a5}}{\dot{E}_6 - \dot{E}_7}$	$\psi_4 = \frac{\dot{E}x_{a6} - \dot{E}x_{a5}}{\dot{E}x_6 - \dot{E}x_7}$
5	Expansion Valve 1	$\eta_5 = \frac{\dot{E}_9}{\dot{E}_{a7}\alpha}$	$\psi_5 = \frac{\dot{E}x_9}{\dot{E}x_7\alpha}$
6	Expansion Valve 2	$\eta_6 = \frac{\dot{E}_8}{\dot{E}_7(1-\alpha)}$	$\psi_6 = \frac{\dot{E}x_8}{\dot{E}x_7(1-\alpha)}$
7	Low-Pressure Evaporator	$\eta_7 = \frac{\dot{E}_1 - \dot{E}_8}{\dot{E}_{a1} - \dot{E}_{a2}}$	$\psi_7 = \frac{\dot{E}x_1 - \dot{E}x_8}{\dot{E}x_{a1} - \dot{E}x_{a2}}$
8	High-Pressure Evaporator	$\eta_8 = \frac{\dot{E}_{10} - \dot{E}_9}{\dot{E}_{a2} - \dot{E}_{a3}}$	$\psi_8 = \frac{\dot{E}x_{10} - \dot{E}x_9}{\dot{E}x_{a2} - \dot{E}x_{a3}}$
9	Back Pressure Regulated Valve	$\eta_9 = \frac{\dot{E}_{11}}{\dot{E}_{10}}$	$\psi_9 = \frac{\dot{E}x_{11}}{\dot{E}x_{10}}$
10	Accumulator	$\eta_{10} = \frac{\dot{E}_2}{\dot{E}_1}$	$\psi_{10} = \frac{\dot{E}x_2}{\dot{E}x_1}$
11	Mixing Chamber	$\eta_{11} = \frac{\dot{E}_3}{\dot{E}_2 + \dot{E}_{11}}$	$\psi_{11} = \frac{\dot{E}x_3}{\dot{E}x_2 + \dot{E}x_{11}}$

Table 4. Input data of the integrated dual stage heat pump drying system.

\dot{m}_r	Mass flow rate of the refrigerant (kg/s)	0.066
\dot{m}_a	Mass flow rate of the air used in the dryer (kg/s)	0.5
α	Mass ratio of the refrigerant used in the HP evaporator	0.35
T_3	Compressor inlet stream's refrigerant temperature (K)	280.6
P_3	Compressor inlet stream's refrigerant pressure (kPa)	500
ΔT_{sc1}	Sub-cooling degree in Sub-cooler 1 (K)	5
ΔT_{sc2}	Sub-cooling degree in Sub-cooler 2 (K)	5
T_0	Environmental temperature (K)	278.15
P_0	Environmental pressure (kPa)	101.33

ations:

$$COP = \frac{\text{Condenser Load} (\dot{E}_3 - \dot{E}_4)}{\text{Compressor} (\dot{W}_1)} \quad (17)$$

$$\eta = \frac{\dot{Q}_2}{\dot{W}_1} \quad (18)$$

$$\psi = \frac{\dot{Q}_2 \left(1 - \frac{T_0}{T}\right)}{\dot{W}_1} \quad (19)$$

RESULTS AND DISCUSSION

When conducting the comprehensive energetic and exergetic investigations of the integrated dual stage heat pump drying system, the very first step is to define each and every stream along with their state, composition, temperature, and pressure. In the next step, after all, streams are clearly identified, the specific enthalpy, entropy, and exergy flow rates and the total energy and exergy flow

rates of all streams are computed. This calculation is conducted by using the input data listed in Table 4 together with balance equations (shown in the equations provided in Section 4) and the Engineering Equation Solver (EES) software package.

The inlet conditions of the system are selected by taking the model previously introduced by [2] into account. The environmental temperature and pressure are considered to be 20°C and 101.3 kPa, respectively. The thermodynamic properties of each stream are obtained via the EES software package. In this section, the results of the exergetic and exergetic performance analyses, including RI, and SI, COP, and efficiencies of all components and the entire system are given and these results are discussed in detail.

Table 5 sums up the major findings of this study such as the energy inputs and outputs, exergy efficiencies, exergy destruction rates, RI and SI of all components of the integrated dual stage heat pump system.

From Table 5, it can be understood that the high-pressure evaporator has the lowest exergy efficiency within the entire system (37%), followed by the low-pressure evaporator (41%), and the condenser (59%). By the same token, the largest rate of exergy destruction occurs in the low-pressure evaporator (0.9 kW), followed by the condenser (0.8 kW), and the high-pressure evaporator (0.7 kW). The electrical energy input to the compressor is around 2.8 kW. Taken as a whole, the overall energy and the exergy efficiencies are 62% and 35%, respectively. The overall exergy destruction rate in the entire system is almost 4 kW and the overall sustainability index is around 1.5.

In Fig. 4, the relative irreversibilities of the process components (compressor, condenser, sub-coolers, expan-

Table 5. Thermodynamic performance results of the main system units.

Unit	Exergy efficiency	Heat (kW)	Work (kW)	Exergy destruction rate (kW)	Relative irreversibility	Sustainability index
1 Compressor	84%		2.808	0.37	10%	6.2
2 Condenser	59%	10.73*		0.83	22%	2.42
3 Sub-cooler 1	79%	0.5*		0.02	0%	4.78
4 Sub-cooler 2	87%	0.48*		0.01	0%	7.49
5 Expansion Valve 1	94%			0.06	2%	17.51
6 Expansion Valve 2	85%			0.07	2%	6.61
7 Low-Pressure Evaporator	41%	6.24**		0.9	24%	1.68
8 High-Pressure Evaporator	37%	3.42**		0.7	19%	1.58
9 Back Pressure Regulated Valve	72%			0.17	5%	3.51
10 Dryer (D)	66%	8.52**		0.42	11%	2.9

* Heat rejected

** Heat input

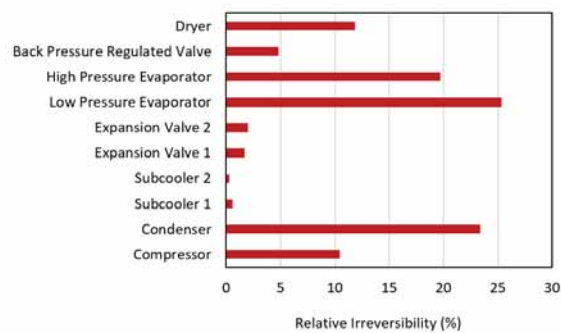


Figure 4. RI of the selected components of the system

sion valves, evaporators, regulation valve, and the dryer) are shown. The low-pressure evaporator (Unit 7) has the greatest irreversibility (24%) because of the elevated exergy destruction rate within this unit, which is mentioned earlier in this section. Following the low-pressure evaporator, the condenser (Unit 2) has the second highest irreversibility (22%). Third highest irreversibility occurs in the high-pressure evaporator (Unit 8) which is also quite high (19%). Combined together, the low-pressure evaporator, condenser, and the high-pressure evaporator account for more than half of the irreversibilities within the entire system, which is 64%.

The primary reasons of the in the evaporator and the condenser irreversibilities can be listed as the (i) temperature difference between the two heat exchanging fluids within these components; (ii) changes in stream pressures; (iii) flow imbalances; and (iv) heat transfer between the system and the environment. In view of the fact that compressor energy requirements depend firmly on the pressures of inlet and outlet streams, any improvements in heat exchanger operation which could lower the temperature difference can potentially significantly lower the compressor energy requirements by bringing the condensation and evaporation temperatures closer to each other.

From an innovative system development point of view, compressor irreversibilities could potentially be lowered independently from the other system components. For instance, modern improvements in the heat pump system design have pointed out the importance of scroll compressors in such systems. The overall system cooling efficiencies can be significantly enhanced by substituting the reciprocating compressor with novel scroll compressors. There is only one technique to minimize or completely get rid of the throttling losses which is to substitute the expansion devices with isentropic expanders. This way, some of the shaft work can be recovered from the pressure drop within the tubes and expanders. Another possible reason for compressor irreversibilities is because of the significant amounts of superheat emissions as a result of the compression process. This excess superheat leads to big temperature differences between the

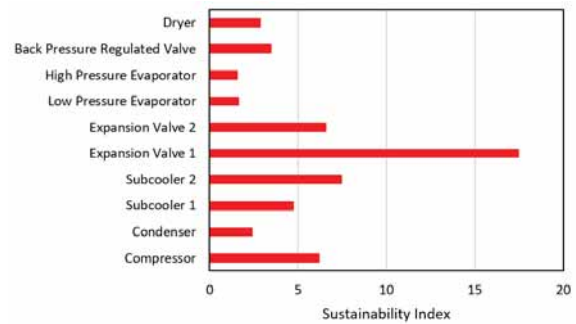


Figure 5. SI of the selected components of the system

inlet and outlet streams of the compressors, causing high exergy destruction rates and irreversibilities. The main reasons for mechanical and electrical losses within this process can be the imperfect electrical and mechanical conditions and low isentropic efficiencies. Therefore, there is a significant need for careful material selection for this equipment, since components with low-quality materials could potentially lower overall system efficiencies significantly.

In Fig. 5, the sustainability indexes of the key components of the integrated dual stage heat pump drying system (compressor, condenser, sub-coolers, expansion valves, evaporators, regulation valve, and the dryer) are presented. The average sustainability index values of the sub-coolers (Units 3 and 4) and expansion valves (Units 5 and 6) are considered as the base values while preparing the data shown in Fig. 5. Here, it is important to note that the accumulator (Unit 10) and the mixing chamber (Unit 11) are considered to have hundred percent energy efficiencies. For that reason, these components' sustainability indexes are not calculated and presented here. Because the auxiliary system components (such as the regulators, tubing, etc.) are presumed to be completely reversible and all the exergetic losses within these components are ignored, that is why the expansion valves have very high sustainability indexes (which means these components have high exergetic efficiencies) with respect to other system components. The high exergy destruction and losses within the condenser (Unit 2), the low-pressure evaporator (Unit 7) and high-pressure evaporator (Unit 8) cause their poor sustainability indexes. Sustainability index of the overall integrated dual stage heat pump system is 1.54.

The exergetic performance of the integrated dual stage heat pump system is evaluated when the environmental temperature is 5°C first. In the next step, in order to investigate the impact of the environmental temperature on the exergetic performance of the integrated system, several parametric investigations are performed. In this part, the impact of the environmental temperature on the exergy destruction rates and exergy efficiencies of the individual system components and the overall system is studied and the results are presented in Fig. 4–6.

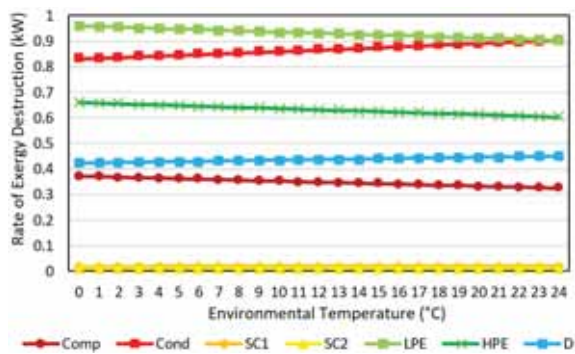


Figure 6. Impact of the environmental temperature on the exergy destruction rates of the main components

Fig. 6 shows that when the environmental temperature is varied between 0°C and 25°C, the exergy destruction rate of the compressor (Unit 1) decreases by around 0.05 kW as the environmental temperature increases. Within the same environmental temperature interval, the rate of exergy destruction within low-pressure evaporator (Unit 7) and high-pressure evaporator (Unit 8) decrease by about 0.06 kW as the environmental temperature is increased. As a result, it can be said that the environmental temperature has a similar impact on the exergy destruction rates of the compressor and the evaporators. Contrariwise, when the environmental temperature is raised from 0°C to 25°C, the condenser (Unit 2)'s exergy destruction rate increases by about 0.07 kW, the exergy destruction rate of the drying unit (Unit 12) increases by around 0.03 kW. This reason behind this tendency could be rationalized by the change in temperatures and pressures within the corresponding components. When the stream's exergy flow rate decreases, it means the stream is getting closer to the environmental conditions. Therefore, higher environmental temperatures affect each stream in different ways; several streams' exergy flow rates increase with increasing environmental temperatures and in contrast, other streams' exergy content could decrease by increasing environmental temperatures.

Fig. 7 shows the change in exergy efficiencies of the major components of the integrated dual stage heat pump drying system with respect to increasing environmental temperatures from 0 to 25°C. The effect of environmental temperature on exergy efficiencies of the components is similar to the effect of the environmental temperature on exergy destruction rates. When the environmental temperature is raised within the selected environmental temperature interval from 0°C to 25°C, the exergetic effectiveness of the compressor (Unit 1) increases by around 1.6%, and the exergetic effectiveness of the low-pressure evaporator (Unit 7) and the high-pressure evaporator (Unit 8) increase by about 1.7%. Oppositely, within the when the environmental temperature is raised within the same selected interval, the exergetic effectiveness of the condenser (Unit 2) and the drying unit (Unit 12) decrease by around 10%. As discussed

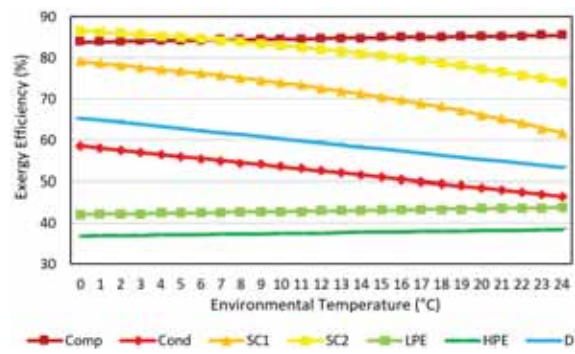


Figure 7. Impact of the environmental temperature on exergy efficiencies of the selected system components

sed before, higher environmental temperatures affect each stream in a different way; several streams' exergy flow rates increase with increasing environmental temperatures and in contrast, other streams' exergy content could decrease by increasing environmental temperatures.

Fig. 8 represents the impact of the environmental temperature on the exergetic effectiveness of the overall system. As the environmental temperature increases within the selected interval from 0°C to 25°C, the overall system's exergy destruction rate increases from about 3.7 kW to around 6.8 kW. In contrast, the exergetic effectiveness of the system decreases from about 35% to around 10%. The change in the exergetic effectiveness based on the variation in the environmental temperature is parallel to the change in the exergetic performance of the condenser and the drying unit.

This study is the comprehensive energy and exergy performance analysis of the system proposed in [2]. The study is strengthened with parametric studies to have a comprehensive understanding of the impact of some key parameters on the system performance. The mass flow rate, temperature, and pressure of each stream within the integrated dual stage heat pump system are given in Table 2. Here, the reason for selecting 0.5 kg/s as the dryer's inlet air mass flow rate is because this amount is selected in [2]. The COP of the system and all initial energy and exergy investigations are conducted based on the input values provided in Table 4. Under

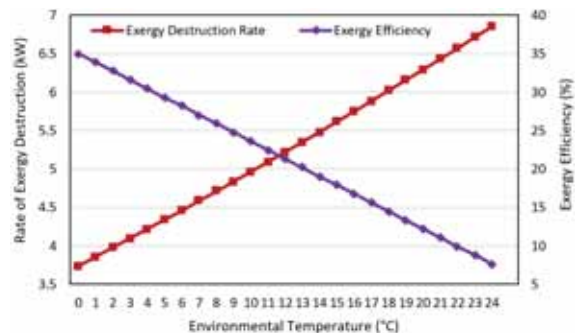


Figure 8. Impact of the environmental temperature on the overall system's exergy efficiency and destruction rate

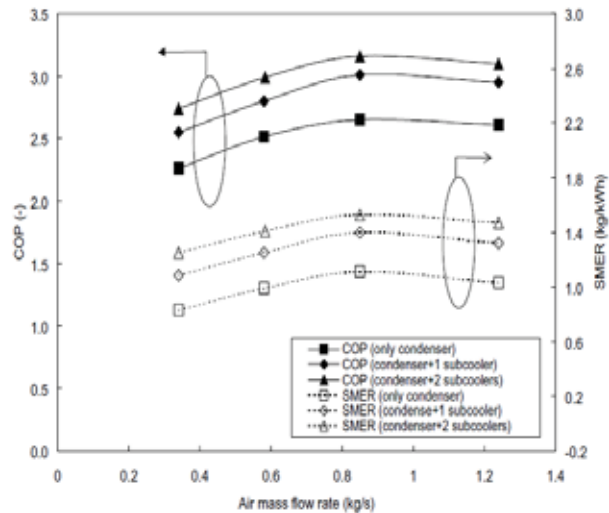
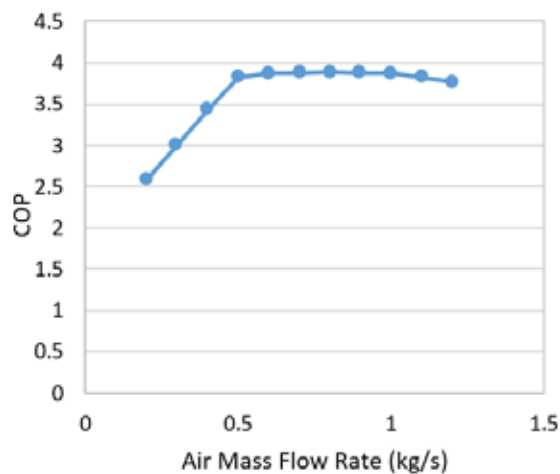


Figure 9. Overall COP with respect to the air mass flow rate (left) and the results from the literature [2] (right)

these conditions, the COP of the integrated dual stage heat pump drying system is estimated to be about 3.82. In the next step, the impact of the dryer's inlet air mass flow rate on the overall COP of the system is examined and the parametric study findings are given in comparison with the data published in the literature [2] in Fig. 9. From Fig. 9, it can be seen that the results of this study show significant similarities to the originally published work, in terms of COP calculations. The small differences can be justified by the assumptions taken into account when conducting the comprehensive energetic and exergetic investigations of the integrated dual stage heat pump drying system. One major reason is ignoring the heat losses within the system components which increase the overall system's energy efficiency quite significantly. Furthermore, the supplementary units are assumed to perfectly insulated with zero mechanical and heat energy losses. As a result, any losses within these components are ignored and most of the auxiliary components are assumed to be isenthalpic. In addition, all heat losses and pressure drops within the pipes, tubes, connecting components, and valves are ignored. When these assumptions are taken into consideration, and when these assumptions are eliminated, the COP and energetic and exergetic efficiencies of the overall system could further decrease.

In this study, an existing model of an integrated dual stage heat pump based drying process is modified and thoroughly investigated from energy and exergy perspectives, which has not been done before. Below, there is a list of results presented in this study which makes it unique and different than the previously published studies in the literature, including [2] based on which the design parameters of the integrated heat pump-drying system is selected:

- Technical comparison of heat pump dryers with other drying technologies

- Potential benefits of heat pump drying systems as a smart energy solution
- 3S (system-source-service) approach from energy and exergy perspectives, including losses
- Energy and exergy efficiency equations of each component of the heat pump-drying system
- Results are presented for each component of the heat pump-drying system including:
 - o Exergy destruction rates
 - o Relative irreversibilities
 - o Energy and exergy efficiencies
 - o Sustainability indexes
- Parametric studies are conducted to understand the effect of environmental temperature on:
 - o Exergy destruction rates of each component and the overall system
 - o Exergy efficiencies of each component and the overall system

The comprehensive energy and exergy analyses performed in this study have not been conducted and presented in the literature before, including the basis study [2]. By taking exergy into account and by conducting parametric studies on key factors, a better insight into system performance is obtained and solid future directions are provided for enhanced performance of heat pump-drying systems. The results

of this study could further be utilized to design optimum operating parameters for integrated dual stage heat pump drying systems.

FUTURE DIRECTIONS

Heat pump dryers are recognized as smart solutions for sustainable drying since they have many advantages as presented in Table 1. However, in order to be considered as 100% sustainable, the smart energy solutions criteria should be followed when developing heat pump dryers [41]. And a crucial challenge is to use renewable resources in a cost competitive, emission-free, and efficient manner in heat pump dryers. This section aims to present the future directions of heat pump drying processes to guide students, researchers, policy makers, and industry members.

To reduce overall system cost, research is focused on improving the efficiency of heat pump drying technologies as well as reducing the cost of capital equipment, operations, and maintenance while minimizing the overall environmental impact of the process.

In the literature, there are many conventional and novel heat pump dryer process designs. Each one of these processes is at different stages of research and development. Among these alternatives, the ones that are already commercially available such as fossil fuel powered systems can be used as near-term solutions as the renewable based and sustainable technologies are being developed and commercialized. Another research focus is on minimizing and/or eliminating the emissions of these technologies. Future directions of heat pump drying systems in light of smart energy solutions is shown in Fig. 10.

The first step in Fig. 10 is “exergization”, meaning including the concept of exergy and exergy analysis when evaluating the performance of heat pump dryers. Efficient use of exergy, or minimization of exergy losses, is the key smart energy solution for a sustainable future [42]. The se-

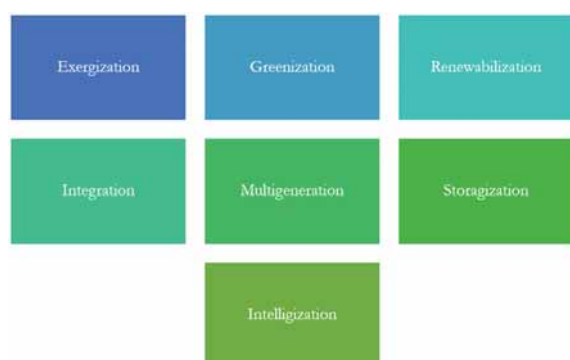


Figure 10. Future directions of heat pump drying systems in light of smart energy solutions

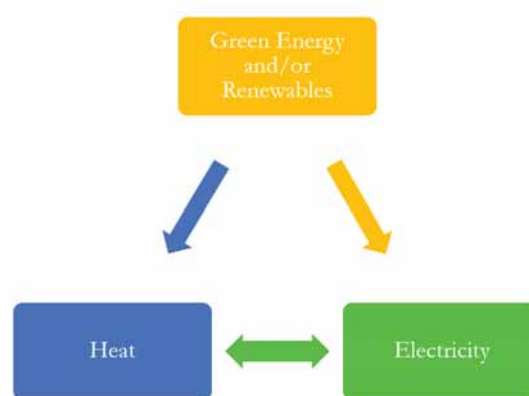


Figure 11. Green and renewable energy integration options with heat pump drying systems

cond step is “greenization” which means using green energy and material resources in heat pump drying systems which include carbon capture and storage technologies, taking advantage of waste and loss of energy, etc. From the source, system, and service approach; all components of heat pump drying systems must be greenized [43]. One example of greenization is the growing interest in green electricity as a means of utilizing renewable electrical energy based heat pump drying systems. This relationship is illustrated in Fig. 11. The third step is “renewabilization”, which goes one step beyond “greenization” and suggests all steps in heat pump drying systems must use renewable energy and material resources. Since sustainability is widely defined as “providing for today without harming tomorrow”, using renewable resources certainly is a smart solution for a sustainable future. The fourth step is “integration”, which includes a variety of future directions from the integration of different methods for a more efficient and comprehensive energy system. “Integration” also means integrating heat pump drying systems with different sustainable energy systems such as hydrogen production, desalination, heating, cooling, water purification, etc. The fifth step is “multigeneration” which is essential in smart energy systems. Heat pump drying systems must operate in a multigeneration mode in order to minimize system losses and enhance desirable process outputs, which increases system efficiencies and as a result, costs and negative environmental impacts decrease. This is certainly a key step toward sustainability. The sixth step is “storagization” as effective heat storage is still one of the most challenging aspects of energy systems. And lastly, the seventh step is “intelligization” which means making every step of heat pump drying systems intelligent, with smart control devices, better forecasting, and effective information, material, and energy flow.

Reducing the cost of heat pump drying systems is the key challenge of the emerging technologies. Cost reduction especially becomes more challenging when renewable resources and novel technologies come into the picture. The



Figure 12. Challenges, strategies, and R&D focus of heat pump drying systems for a sustainable future

challenges, strategies, and research and development suggestions for future heat pump drying systems are shown in Fig. 12.

Another important future direction for understanding and therefore enhancing heat pump drying systems' performance is proper and comprehensive life cycle analysis (LCA). With the cradle-to-grave type of LCA approach, the cost, emissions, and efficiency of a heat pump dryer can be calculated in the most accurate manner. This also allows consumers, policymakers, scientists, industry, academia, and governments choose the smart energy option among different alternatives. As a result, heat pump drying systems can get truly exergetized, greenized, renewabilized, integrated, and intelligent with multigeneration options. And heat pump dryers could become the most sustainable drying option for end users of all types.

CONCLUSION

Heat pumps are very well known technologies in terms of delivering efficient heating and cooling with the lowest possible electrical energy consumption. Here, it is shown that heat pump dryers have significant advantages compared to other available drying technologies. Heat pump drying systems can become more sustainable when green, clean, and eventually 100% renewable energy and material resources are used instead of fossil fuels. Enhancing the COP of heat pump dryers is essential. However, in the next steps, SMER must also be taken into account. When developing a sustainable energy system; capital, operating, and maintenance cost and other financial factors, energetic and exergetic performance, and environmental impact must all be taken into account together simultaneously. Hybrid technologies could potentially enhance energetic and exergetic efficiencies. On the other, further research is required to lower their capital, operating, and maintenance cost and environmental impact.

The main aim of this study is to conduct energetic and exergetic investigations of an integrated heat pump drying process in order to evaluate the performance of the overall system. For that reason, exergy efficiencies and exergy destruction rates of each system component along with the overall system are carefully calculated. Here, this analysis is done in order to take all process irreversibilities into account to tackle the end results the loss of the quality of energy. By calculating the overall exergetic performance of the entire process along with all of its components, it is aimed to identify where there is a loss in the quality of energy. In addition, the location of these quality losses within major components is investigated at different environmental temperatures. In order to provide a straight advantage to the society and industry, it is essential to take advantage of the possible profits of exergy. Also, it should be noted that, unlike the assumptions in this study, it is not possible in reality to perfectly insulate the components of the heat pump system, not with the current material science and engineering technologies. On the other hand, appropriate insulating materials and technologies for the overall system including all components, auxiliary units, and monitoring devices could potentially enhance the system COP and energetic and exergetic efficiencies significantly. Imperfections because of the component and material inefficiencies can be increased to further increase system COP and energy and exergy efficiencies. The careful material, equipment, and technology selection could further enhance the system COP and energy and exergy efficiencies. The following items are the summary of some of the major particular results of this study:

- At the selected environmental temperature and pressure, the integrated heat pump drying system has overall energetic and exergetic efficiencies around 62% and 35%, respectively.
- At the selected environmental temperature and pressure, the integrated heat pump drying system's exergy

destruction rate is 3.96 kW.

- The components where the highest exergy destruction occurs are the low-pressure evaporator (0.9 kW), the condenser (0.83 kW), and the high-pressure evaporator (0.7 kW).

- As the environmental temperature increases, the overall exergy destruction rate increases and the exergy efficiency decreases.

In this study, the primary aim is to improve the exergy efficiency of the proposed integrated dual stage heat pump based drying process by identification of where the irreversibilities occur and developing strategies to minimize these irreversibilities. There are several reasons behind high irreversibilities (exergy destruction) in a process, some of these reasons can be listed as: (i) temperature difference between the inlet and outlet streams of a system component, (ii) pressure difference between the inlet and outlet streams of a system component, (iii) any other flow imbalances between the inlet and outlet streams of a system component, and (iv) not being able to recover the latent heat in heat exchangers which is caused by high temperature differences. Lowering the inlet and outlet streams' temperature variance also lowers the difference between the condensing and evaporating temperatures. And as a result, enhances the amount of heat recovery per unit of energy input to a system or component.

TERMINOLOGY

E	Energy (kJ)
\dot{E}	Energy flow rate (kW)
ex	Specific exergy (kJ/kg)
Ex	Exergy (kJ)
$\dot{E}x$	Exergy (kJ)
h	Specific enthalpy (kJ/kg)
m	Mass (kg)
\dot{m}	Mass flow rate (kg/s)
P	Pressure (kPa)
Q	Heat (kJ)
\dot{Q}	Heat transfer rate (kW)

s	Specific entropy (kJ/kg-K)
S	Entropy (kJ/K)
\dot{S}	Entropy flow rate (kW/K)
t	Time (s)
T	Temperature (K)
W	Work (kJ)
\dot{W}	Work transfer rate (kW)

Greek Letters

α	Mass ratio of the refrigerant sent to HPE
Δ	Change
η	Energy efficiency
ψ	Exergy efficiency

Subscript and Superscripts

a	Air
ch	Chemical
$comp$	Compressor
$cond$	Condenser
cv	Control volume
$dest$	Destruction
en	Energy
ex	Exergy
gen	Generation
in	Inlet stream
ke	Kinetic energy
out	Outlet stream
pe	Potential energy
ph	Physical

r	Refrigerant
$^{\circ}$	Standard state
0	Environmental state

Abbreviations

AA	Ascorbic Acid
BPRV	Back Pressure Regulated Valve
COP	Coefficient of Performance
D	Dryer
EES	Engineering Equation Solver
EV	Expansion Valve
GHG	Greenhouse Gas
HPE	High-Pressure Evaporator
LCA	Life Cycle Analysis
LPE	Low-Pressure Evaporator
RH	Relative Humidity
RI	Relative Irreversibility
SC	Sub-cooler
SI	Sustainability Index
SMER	Specific Moisture Extraction Ratio
VLE	Vapor-liquid Equilibrium

References

- Mujumdar, A. S. (Ed.). (2014). Handbook of Industrial Drying. CRC press.
- Chua, K. J., Chou, S. K. (2005). A modular approach to study the performance of a two-stage heat pump system for drying. Applied Thermal Engineering, 25(8), 1363-1379.
- Liu, X., Lee, D. J. (2015). Some recent research and development in drying technologies: Product perspective. Drying Technology, 33(11), 1339-1349.
- Sivasakthivel, T., Murugesan, K., Thomas, H. R. (2014). Optimization of operating parameters of ground source heat pump system for space heating and cooling by Taguchi method and utility concept. Applied Energy, 116, 76-85.
- Zamfirescu, C., Dincer, I., Naterer, G. (2009). Performance evaluation of organic and titanium based working fluids for high-temperature heat pumps. Thermochimica Acta, 496(1), 18-25.
- Tian, Y., Zhao, Y., Huang, J., Zeng, H., Zheng, B. (2016). Effects of different drying methods on the product quality and volatile compounds of whole shiitake mushrooms. Food Chemistry, 197, 714-722.
- Kucuk, H., Midilli, A., Kilic, A., Dincer, I. (2014). A review on thin-layer drying-curve equations. Drying Technology, 32(7), 757-773.
- Erbay, Z., Hepbasli, A. (2014). Application of conventional and advanced exergy analyses to evaluate the performance of a ground-source heat pump (GSHP) dryer used in food drying. Energy Conversion and Management, 78, 499-507.
- Barzegaravval, H., Dincer, I. (2014). Investigation of Organic Rankine Cycle Performance with Variable Mixture Composition. In Progress in Sustainable Energy Technologies: Generating Renewable Energy (pp. 47-64). Springer International Publishing.
- Perry, E. J. (1981). Drying by cascade heat pumps. Institute of Refrigeration Management, 18, 1-8.
- Chua, E. K. J. (2001). Dynamic modelling, experimentation, and optimization of heat pump drying for agricultural products. Drying Technology, 19(3-4), 717-721.
- Chua, K. J., Chou, S. K., Ho, J. C., Hawlader, M. N. A. (2002). Heat pump drying: Recent developments and future trends. Drying Technology, 20(8), 1579-1610.
- Li, C. J., Su, C. C. (2003). Experimental study of a series-connected two-evaporator refrigerating system with propane (R-290) as the refrigerant. Applied Thermal Engineering, 23(12), 1503-1514.
- Dincer, I., Rosen, M. A. (2013). Exergy: Energy, Environment and Sustainable Development. Newnes. Oxford: Elsevier.
- Gungor, A., Tsatsaronis, G., Gunerhan, H., Hepbasli, A. (2015). Advanced exergoeconomic analysis of a gas engine heat pump (GEHP) for food drying processes. Energy Conversion and Management, 91, 132-139.
- Erbay, Z., Hepbasli, A. (2014). Application of conventional and advanced exergy analyses to evaluate the performance of a ground-source heat pump (GSHP) dryer used in food drying. Energy Conversion and Management, 78, 499-507.
- Aktaş, M., Şevik, S., Özdemir, M. B., Gönen, E. (2015). Performance analysis and modeling of a closed-loop heat pump dryer for bay leaves using artificial neural network. Applied Thermal Engineering, 87, 714-723.
- Chong, C. H., Figiel, A., Law, C. L., Wojdyło, A. (2014). Combined drying of apple cubes by using of heat pump, vacuum-microwave, and intermittent techniques. Food and Bioprocess Technology, 7(4), 975-989.
- Aktaş, M., Şevik, S., Aktekel, B. (2016). Development of heat pump and infrared-convective dryer and performance analysis for stale bread drying. Energy Conversion and Management, 113, 82-94.
- Yang, Z., Zhu, Z., Zhao, F. (2016). Simultaneous control of drying temperature and superheat for a closed-loop heat pump dryer. Applied Thermal Engineering, 93, 571-579.
- Şevik, S. (2014). Experimental investigation of a new design solar-heat pump dryer under the different climatic conditions and drying behavior of selected products. Solar Energy, 105, 190-205.
- Gao, R., Yuan, L., Yu, M., Liu, W. (2016). Effects of Heat Pump Drying Parameters on the Volatile Flavor Compounds in Silver Carp. Journal of Aquatic Food Product Technology, 25(5), 735-744.
- Chapchaimoh, K., Poomsa-ad, N., Wiset, L., Morris, J. (2016). Thermal characteristics of heat pump dryer for ginger drying. Applied Thermal Engineering, 95, 491-498.
- Zhang, R., Gao, Y., Feng, J., Xie, H., Deng, H., Zhuang, G., Dou, Z. (2016). Technologic parameter optimization in pilot-scale process of heat pump drying of Areca catechu L. Transactions of the

- Chinese Society of Agricultural Engineering, 32(9), 241-247.
25. Ceylan, İ., & Gürel, A. E. (2016). Solar-assisted fluidized bed dryer integrated with a heat pump for mint leaves. *Applied Thermal Engineering*, 106, 899-905.
 26. Buker, M. S., Riffat, S. B. (2016). Solar assisted heat pump systems for low temperature water heating applications: A systematic review. *Renewable and Sustainable Energy Reviews*, 55, 399-413.
 27. Erbay, Z., Hepbasli, A. (2014). Advanced exergoeconomic evaluation of a heat pump food dryer. *Biosystems Engineering*, 124, 29-39.
 28. Mohanraj, M. (2014). Performance of a solar-ambient hybrid source heat pump drier for copra drying under hot-humid weather conditions. *Energy for Sustainable Development*, 23, 165-169.
 29. Minea, V. (2015). Overview of heat-pump-assisted drying systems, part I: Integration, control complexity, and applicability of new innovative concepts. *Drying Technology*, 33(5), 515-526.
 30. Bansal, P., Mohabir, A., Miller, W. (2016). A novel method to determine air leakage in heat pump clothes dryers. *Energy*, 96, 1-7.
 31. Mehrpooya, M., Hemmatabady, H., Ahmadi, M. H. (2015). Optimization of performance of combined solar collector-geothermal heat pump systems to supply thermal load needed for heating greenhouses. *Energy Conversion and Management*, 97, 382-392.
 32. Ahn, J. H., Kang, H., Lee, H. S., Kim, Y. (2015). Performance characteristics of a dual-evaporator heat pump system for effective dehumidifying and heating of a cabin in electric vehicles. *Applied Energy*, 146, 29-37.
 33. Yahya, M. (2016). Design and performance evaluation of a solar assisted heat pump dryer integrated with biomass furnace for red chilli. *International Journal of Photoenergy*, 2016.
 34. Minea, V. (2015). Overview of Heat-Pump-Assisted Drying Systems, Part II: Data Provided vs. Results Reported. *Drying Technology*, 33(5), 527-540.
 35. Trirattanapikul, W., Phoungchandang, S. (2014). Microwave blanching and drying characteristics of *Centella asiatica* (L.) urban leaves using tray and heat pump-assisted dehumidified drying. *Journal of Food Science and Technology*, 51(12), 3623-3634.
 36. Syahrul, S., Hamdullahpur, F., Dincer, I. (2002). Exergy analysis of fluidized bed drying of moist particles. *Exergy, an International Journal*, 2(2), 87-98.
 37. Dincer, I. (2002). On energetic, exergetic and environmental aspects of drying systems. *International Journal of Energy Research*, 26(8), 717-727.
 38. Dincer, I., Sahin, A. Z. (2004). A new model for thermodynamic analysis of a drying process. *International Journal of Heat and Mass Transfer*, 47(4), 645-652.
 39. Rosen, M. A., Dincer, I. (1997). On exergy and environmental impact. *International Journal of Energy Research*, 21(7), 643-654.
 40. Dincer, I. (2011). Exergy as a potential tool for sustainable drying systems. *Sustainable Cities and Society*, 1(2), 91-96.
 41. Dincer, I. (2016). Smart energy solutions. *International Journal of Energy Research*, 40(13), 1741-1742.
 42. Dincer, I. (2016). Exergization. *International Journal of Energy Research*, 40(14), 1887-1889.
 43. Dincer, I. (2016). Greenization. *International Journal of Energy Research*, 40(15), 2035-2037.

Exergy Destruction Analysis of a Gas Turbine Power Plant

Ali Kilicarslan¹, Mehmet Kiris²

¹Hittit University, Department of Mechanical Engineering, 19030 Corum-TURKEY

²Republic of Turkey-Revenue Administration, Ankara-TURKEY

ABSTRACT

According to the data released by “Republic of Turkey-the Ministry of Energy and Natural Resources”, by the end of July 2017, 34% of the electricity of Turkey was produced from natural gas. As it is compared to the other resources such as coal (31%), hydraulic power (24%), wind (6%), geothermal energy (2%) and from other sources (3%), natural gas still occupies the highest place in electricity production.

The efficiency of the natural gas-fired power plants should be raised while the harmful effects of the exhaust gas emissions should be decreased. In this study, a natural gas-fired gas turbine power plant that produces electricity in a private factory in the city of Corum-Turkey was analysed at increasing environment temperatures of $-2.7\text{ }^{\circ}\text{C}$ to $7.5\text{ }^{\circ}\text{C}$ based on the exergy destruction.

The gas turbine data related to the operating conditions was provided by the private company. A computer code was improved with EES (Engineering Equation Solver) software to perform the exergy destruction analyses of the elements of the gas turbine cycle such as compressor, combustion chamber, turbine, boiler and economizer. At increasing environment temperatures of between $-2.7\text{ }^{\circ}\text{C}$ and $7.5\text{ }^{\circ}\text{C}$, it was found that the exergy destructions of the compressor, turbine, combustion chamber, boiler and economizer decreased. The maximum exergy destruction happened in the boiler and the minimum one happened in the combustion chamber.

Keywords:

Gas turbine; Second law; Exergy destruction; Exergetic efficiency

INTRODUCTION

Nowadays, the importance of electricity generating systems by means of renewable energy such as wind and sun has been increasing because of decreasing the life of fossil fuels, but a large part of the need for electricity from fossil-based fuels is provided by power plants. In power generating plants, the emissions of power plants are considered as important parameters that must be taken into consideration. Interest in gas-fired gas turbine power plants has been increasing day by day because of low investment cost, efficient operation and minimal environmental impacts. It is not enough to analyse the thermal systems only in terms of the conservation of energy. Because the conservation of energy analyses systems only quantitatively in terms of energy balance. However, the second law of thermodynamics performs

analysis of the thermal systems in terms of quality and enables the irreversibilities in the systems and elements of the systems to be found.

In a study, energy and exergy analyses of natural gas fired gas turbine power plants were carried and the losses in the natural gas fired gas turbine power plants were determined (Rahim and Gündüz, 2013). Sürer (2003) examined the thermodynamic and economic analysis of a cogeneration system consisting of combined gas and steam turbines and the efficiencies of this are compared. Sevilgen (2004) investigated cogeneration systems using exergy-economic analysis methods.

In the other studies carried out in the literature, gas turbine cycles have been investigated in terms

Article History:

Received: 2018/09/14

Accepted: 2018/12/11

Online: 2018/12/31

Correspondence to: Ali KILICARSLAN
Hittit University, Mechanical Engineering
Department, 19030 Corum-TURKEY
Telephone: +90(364) 2274533/1236
Fax: +90 (364) 2274535
e-mail: alikilicarslan@hitit.edu.tr

of the first and second laws of thermodynamics. Arpacı (2002) examined exergy analysis of natural gas cogeneration systems with different data. Gürer (1997), has prepared a master of science thesis that is based on the first and second laws of analyses of the gas turbine systems used in the industrial sector in Turkey.

Sue and Chuang (2004), carried out the engineering design and exergy analysis of gas turbine systems for power generation. They found that the raise in the gas temperature in the preheated gas turbine from 22.5 °C to 118 °C caused the exergetic efficiency by 0.06%. They also resulted that the efficiency decreased by 1 % as the inlet air temperature of the compressor was reduced from 10 °C to 5 °C.

Ozcan et al. (2014) performed the exergy and energy analysis of the elements of the chemical cycle-based trigeneration system and derived the equations for the exergy and energy efficiencies for these elements. The highest energy consuming devices are the air separation unit and the compression air unit while the gas turbine and fuel cell are the most power producing elements.

Turan and Aydın (2014) conducted an exergy analysis of the elements of the LM6000 gas turbine engine (high and low pressure compressors and turbines, combustion unit) and analysed these elements from an exergy-economic perspective. Exergy destruction, exergetic efficiency and exergy-economic equations are written for each component. As a result of exergy analysis, it was determined that the largest exergy destruction occurred in the combustion unit (25,91 MW) and the highest exergetic efficiency (97,4%) was obtained in the high pressure turbine. As a result of the study, the total exergetic efficiency and the exergy destruction of the system were 39 and 39.3 MW respectively. In addition, they determined that the gas turbine cycle element with the highest exergy-economic factor is the high-pressure turbine. The effect of different gas turbine cycle operating parameters such as on the energy performance of two different gas turbine cycles including “basic gas turbine cycle” and “inter-cooled gas turbine cycle” was investigated by (Kumari and Sanjay, 2015). It was resulted that the total exergy destruction of “intercooled gas turbine cycle” was less than that of basic gas turbine cycle by 4.42%.

Ersayin and Ozgener (2015) performed a case study in order to investigate the energy and exergy analyses of a combined cycle power plant operated by a private company in Turkey and determined the energy and exergetic efficiencies of the power plant as 56 % and 50.04 %, respectively. In a similar study performed by (Ibrahim et al., 2017), it was observed that the largest exergy destruction occurred in the combustion chamber, followed by the turbine and air compressor. The exergetic efficiencies of the compressor,

turbine and combustion chamber are 94.9%, 92% and 67.5%, respectively.

As the studies mentioned above in the literature are examined, it has been found that there is no a detailed case study focusing to observe the effect of the environment air temperature on the exergy destruction of the main and auxiliary elements of a gas turbine cycle. In this study, the effect of the environment air temperature on the exergy destructions and exergetic efficiencies of the elements of the gas turbine cycle such as the compressor, combustion chamber, turbine, boiler and economizer were carried out with respect to the actual data obtained from the gas turbine power plant operating in the city of Corum, Turkey. A computer program was improved with of EES (Klein, 2017) software and the actual table values are used for specific values of enthalpy, entropy and exergy.

GAS TURBINE MODEL

The gas turbine model to be used in this study is based on the natural gas-fired gas turbine power plant operating in the city of Çorum, Turkey and producing electricity and heat. The schematic of this cycle is depicted in Fig. 1.

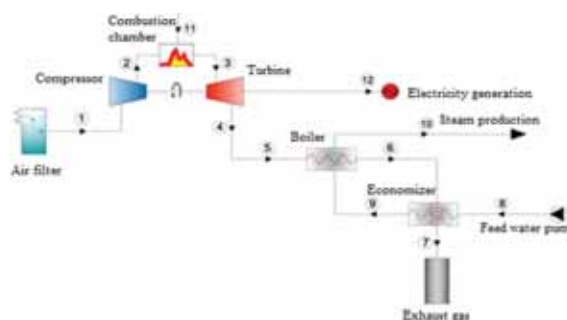


Figure 1. Gas turbine power plant

The environment air that is separated from foreign materials is sucked and compressed by the compressor from state 1 to state 2 and brought to the desired temperature and pressure conditions required for the combustion chamber. Natural gas is reacted with the environment air compressed by the compressor, and combustion products at high temperature flows to the gas turbine at state 3. The mechanical energy produced in the turbine is used to drive to the generator to produce electricity at state 12 and the exhaust gases simultaneously exhausted from the turbine at state 4. The exhaust gases enter the boiler at state 5 and leaves state 6, during this process, the steam is produced by the heat transfer between the exhaust gases and the feed water flowing throughout states 9 and 10. In the economizer, the heat is recovered from the exhaust gases flowing from state 6 to state 7 and the temperature of the feed water passing throughout state 8 and 9. At state 7, the exhaust gases exhausted

to the atmosphere.

Energy equation can be written as (Van Wylen and Sonntag, 1985),

$$\dot{Q}_{cv} + \sum \dot{m}_i \left(h_i + \frac{V_i^2}{2} + gZ_i \right) = \frac{dE_{cv}}{dt} + \sum \dot{m}_e \left(h_e + \frac{V_e^2}{2} + gZ_e \right) + \dot{W}_{cv} \quad (1)$$

The variation of the exergy with time for a control volume is expressed as (Moran and Shapiro, 2006),

$$\frac{dE_{x,cv}}{dt} = \sum \dot{m}_i e_{xi} - \sum \dot{m}_e e_{xe} + \sum \left(1 - \frac{T_o}{T_s} \right) \dot{Q}_{cv} - \left(\dot{W}_{cv} - P_o \frac{dV_{cv}}{dt} \right) - \dot{E}_D \quad (2)$$

Where \dot{E}_x is the exergy rate, $\frac{dE_{x,cv}}{dt}$ is the variation rate for a control volume, $\frac{dE_{cv}}{dt}$ is the variation of volume of a control volume with time, \dot{W}_{cv} is the power, \dot{E}_D is the exergy destruction,

$\left(1 - \frac{T_o}{T_s} \right) \dot{Q}_{cv}$ is exergy transfer related to the heat transfer, T_s is the boundary temperature, e_{xi} , and e_{xo} are specific exergies at the inlet and outlet, respectively.

The assumptions regarding to the gas turbine power plant are given below,

- Air standard assumptions are valid in the combustion chamber, that is, combustion process is replaced by the heat transfer from any source.
- It is assumed that the flow through the elements of gas turbine power plant such as compressor, combustion chamber, turbine, boiler and economizer is in accordance with the "Steady-State Steady Flow (SSSF)" model.
- Pressure losses in ducts and piping connecting combustion chamber, boiler, economizer and elements are neglected.
- Adiabatic compression of the air in the compressor and adiabatic expansion of the air in the turbine are assumed.
- It is also assumed that there was no heat loss from the pipes and ducts.
- The combustion chamber, boiler and economizer are considered to be insulated from the environment.
- It is assumed that the flow through the elements of the elements only includes the air.
- The variations in kinetic and potential energies are neglected in the gas turbine elements.

Compressor

In the compressor, air is adiabatically compressed and SSSF model is valid. In this case, the energy and exergy destruction equation for the compressor become

$$\dot{W}_c = \dot{m}_c (h_1 + h_2) \quad (3)$$

$$\dot{E}_{D,c} = \dot{m}_c (e_{x1} - e_{x2}) - \dot{W}_c \quad (4)$$

where \dot{m}_c is the mass flow rate of air flowing throughout the compressor, \dot{W}_c is the power delivered to the compressor and $\dot{E}_{D,c}$ is the compressor exergy destruction.

The exergetic efficiency of the compressor is expressed as

$$\varepsilon_c = \frac{\dot{E}_{x1} - \dot{E}_{x2}}{\dot{W}_c} = \frac{\dot{m}_c ((h_1 - h_2) - T_o (s_1 - s_2))}{\dot{W}_c} \quad (5)$$

where ε_c is the exergetic efficiency of the compressor.

Combustion Chamber

In the real case, the natural gas coming from the natural gas pipe line in the combustion chamber and the compressed air in the compressor chemically react and the gases which are formed as a result of the combustion leave the combustion chamber. In the gas turbine model, combustion chamber will be regarded as a heat exchanger through which air flows. The basic equations are written as,

$$\dot{Q}_{cc} = \dot{m}_{cc} (h_3 - h_2) \quad (6)$$

$$\dot{E}_{D,cc} = \dot{m}_{cc} (e_{x2} - e_{x3}) + \left(1 - \frac{T_o}{T_s} \right) \dot{Q}_{cc} \quad (7)$$

where \dot{m}_{cc} is the mass flow rate of air flowing throughout the combustion chamber, \dot{Q}_{cc} is the heat transfer rate to the combustion chamber and $\dot{E}_{D,cc}$ is the exergy destruction in the combustion chamber.

The exergetic efficiency of the combustion chamber, ε_{cc} can be expressed as

$$\varepsilon_{cc} = \frac{\left(1 - \frac{T_o}{T_s} \right) \dot{Q}_{cc}}{\dot{m}_{cc} (e_{x3} - e_{x2})} = \frac{\left(1 - \frac{T_o}{T_s} \right) \dot{Q}_{cc}}{\dot{m}_{cc} ((h_3 - h_2) - T_o (s_3 - s_2))} \quad (8)$$

Turbine

The mass flow of the fluid circulating in the turbine consists of the mass flow of the gases burning in the combustion chamber. It is assumed that the air expands instead of combustion gases in the expansion process in the tur-

bine and the flow is in accordance with the SSSF model. The energy and exergy destruction equation for the turbine are expressed as follows,

$$\dot{W}_t = \dot{m}_{cc}(h_3 - h_4) \quad (9)$$

$$\dot{E}_{D,t} = \dot{m}_{cc}(e_{x3} - e_{x4}) - \dot{W}_t \quad (10)$$

where \dot{W}_t is the turbine power and $\dot{E}_{D,t}$ is the turbine exergy destruction.

The exergetic efficiency of the turbine is expressed as

$$\varepsilon_t = \frac{\dot{W}_t}{\dot{E}_{x3} - \dot{E}_{x4}} = \frac{\dot{W}_t}{\dot{m}_{cc}((h_3 - h_4) - T_o(s_3 - s_4))} \quad (11)$$

where ε_t is the exergetic efficiency of the turbine.

Boiler

As can be seen in Fig. 2.1, the boiler is a heat exchanger in which the exhaust gases from the turbine cause the water that is preheated in the economizer to become vapor. It is assumed that the boiler is completely insulated against the environment. The energy balance and exergy destruction equations for the boiler are expressed as follows.

$$\dot{m}_{cc}(h_5 - h_6) = \dot{m}_w(h_{10} - h_9) \quad (12)$$

$$\dot{E}_{D,b} = \dot{m}_{cc}(e_{x5} - e_{x6}) = \dot{m}_w(e_{x9} - e_{x10}) \quad (13)$$

where \dot{m}_w is the mass flow rate of water flowing throughout the boiler and $\dot{E}_{D,b}$ is the exergy destruction in the boiler. As the irreversibilities that are caused by the entropy flow and friction are taken into consideration, the exergetic efficiency of the boiler ε_b is expressed as

$$\varepsilon_b = \frac{\dot{m}_w(e_{x10} - e_{x9})}{\dot{m}_{cc}(e_{x5} - e_{x6})} = \frac{\dot{m}_w((h_{10} - h_9) - T_o(s_{10} - s_9))}{\dot{m}_{cc}((h_5 - h_6) - T_o(s_5 - s_6))} \quad (14)$$

Economizer

The economizer is a heat exchanger in which exhaust gases from the turbine preheat the water before the water is passed to the boiler. It is assumed that the economizer is completely insulated from the environment like the boiler. The equation of energy balance and exergy for the economizer can be written as,

$$\dot{m}_t(h_6 - h_7) = \dot{m}_w(h_9 - h_8) \quad (15)$$

$$\dot{E}_{D,e} = \dot{m}_{cc}(e_{x6} - e_{x7}) = \dot{m}_w(e_{x8} - e_{x9}) \quad (16)$$

where $\dot{E}_{D,e}$ is the exergy destruction in the boiler. Same types of irreversibilities exist in the economizer. The exergetic efficiency of the economizer ε_e is expressed as

$$\varepsilon_e = \frac{\dot{m}_w(e_{x9} - e_{x8})}{\dot{m}_{cc}(e_{x6} - e_{x7})} = \frac{\dot{m}_w((h_9 - h_8) - T_o(s_9 - s_8))}{\dot{m}_{cc}((h_6 - h_7) - T_o(s_6 - s_7))} \quad (17)$$

Auxiliary Equations

The isentropic efficiencies of the compressor and turbine, the back work ratio and the net power can be expressed as,

$$\eta_c = \frac{h_{2s} - h_1}{h_2 - h_1} \quad (18)$$

$$\eta_t = \frac{h_3 - h_4}{h_3 - h_{4s}} \quad (19)$$

$$BWR = \frac{\dot{W}_c}{\dot{W}_t} \quad (20)$$

$$\dot{W}_{net} = \dot{W}_t - |\dot{W}_c| \quad (21)$$

where $\eta_c, \eta_t, \dot{W}_{net}$ and BWR are the isentropic efficiencies of the compressor and turbine, net power produced by the gas turbine power plant and the back work ratio, respectively.

In terms of giving an idea about the type of data used in the analysis, the data that was obtained at an environment temperature of -1 °C in the actual operating conditions are depicted in Table 1. Table 2 shows the constant parameters used in the developed computer code.

Table 1. Operating conditions of the gas turbine power plant at -1 °C

$T_1(^{\circ}C)$	$T_3(^{\circ}C)$	$T_4(^{\circ}C)$	$T_5(^{\circ}C)$	$T_6(^{\circ}C)$	$T_7(^{\circ}C)$	$T_8(^{\circ}C)$
-1	759.5	483.1	460	213	148	95
$T_9(^{\circ}C)$	$T_{10}(^{\circ}C)$	$\dot{W}_{net}(kW)$	$P_1(Bar)$	$P_2(Bar)$	$P_3(Bar)$	$\dot{m}_w(kg/s)$
184	192	7240	0.922	17.1	12	3.30

Table 2. Constant parameters in the computer code

η_c	η_t	BWR	$P_{10}(kPa)$	$T_o(^{\circ}C)$
0,8	0,8	0,45	1200	25

UNCERTAINTY ANALYSIS OF THE GAS TURBINE POWER PLANT

The uncertainties of the measurements that are obtained from (Kilicarslan, 2004) and (Tore, 2016) are ± 0.5 for temperature, $\pm 3\%$ for pressure, $\pm 3\%$ for mass flow rate, and $\pm 2\%$ for power. EES software was used to create the uncertainty propagation table of the exergy destructions and exergetic efficiencies of the main and auxiliary elements as a function environment air temperatures ranging from -2.7 °C and 7.5 °C. The maximum and minimum uncertainties related to the exergy destructions and exergetic efficiencies of the main and auxiliary elements are depicted in Table 3.

Table 3. Uncertainties of exergy destructions and exergetic efficiencies

$\dot{E}_{D,c}(\%)$	$\dot{E}_{D,cc}(\%)$	$\dot{E}_{D,t}(\%)$	$\dot{E}_{D,b}(\%)$	$\dot{E}_{D,e}(\%)$
± 2.27	± 9.92	± 2.00	± 4.42	± 3.30
η_c	η_{cc}	η_t	η_{eb}	η_{ec}
$\pm 0,0009783$	$\pm 0,001672$	$\pm 0,00009653$	$\pm 0,005504$	$\pm 0,01702$

RESULTS AND DISCUSSIONS

The analysis of the gas turbine power plant is based on the actual data collected from the gas turbine power plant located in the city of Çorum, Turkey. The exergy destructions and exergetic efficiencies of the main elements such as compressor, turbine, combustion chamber and those of auxiliary elements such as boiler, economizer are investigated by means of computer program developed using EES software. In order to show the validation of the model developed in this study, the present study is compared to the similar studies in the literature and Table 4 depicts the exergetic efficiencies of the compressor, combustion chamber and turbine of the present study and those obtained from (Ibrahim et al., 2017) and (Ersayin and Ozgener, 2015).

Table 4. Exergetic efficiency comparison of the main elements

	Ibrahim et al., 2017	Ersayin and Ozgener, 2015	Present Study	Difference (%)
η_{ec}	94.89	94.9	91	- 4.27
η_{ecc}	67.49	64	66.5	-1.48 / 3.75
η_{et}	91.96	81.7	89.5	-2.74 / 8.71

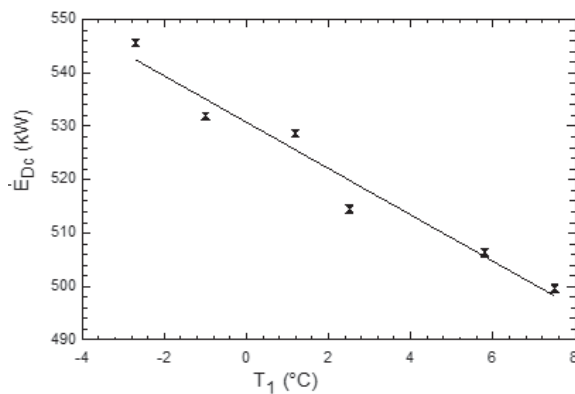


Figure 2. Compressor exergy destruction vs environment air temperature

Fig. 2 shows the compressor exergy destruction. As seen in Fig. 2, as the environment air temperature raises, the compressor exergy destruction decreases. The reason for the exergy destruction in the compressor is the entropy generation that occurs during compression of the fluid in the compressor. As mentioned earlier, at increasing environment air temperatures, entropy in the compressor decreases. As a result, the decrease in the entropy production causes the compressor exergy destruction to decrease. At increasing environment air temperatures of -2.7°C to 7.5°C , the compressor exergy destruction decreased from 545.6 kW to 499.6 kW

The variation of the exergy destruction of the combustion chamber with the environment air temperature is depicted in Fig. 3. As the environment air temperature raises,

the exergy destruction of the combustion chamber decreases as seen in Fig. 3. When the environment air temperature raises, the temperature difference between the combustion chamber and the environment air decreases. This causes the amount of heat given to the combustion chamber to decrease and thereby decreasing the amount of exergy destruction in the combustion chamber as seen in Fig. 3. Fig. 3 also depicts that the exergy destruction of the combustion chamber varies between 51 kW and 38 kW. It is reduced by 11%. In the actual operating conditions of a gas turbine power plant, the combustion chamber exergy destruction occupies the largest part of exergy destruction as it is compared to the other elements such as compressor, turbine, boiler and economizer because of higher values of chemical exergy. But, the chemical exergy is not taken into consideration in this study because the air standard assumptions are assumed.

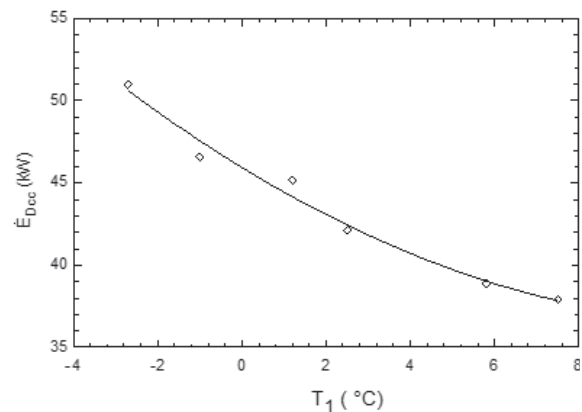


Figure 3. Combustion chamber exergy destruction vs environment air temperature

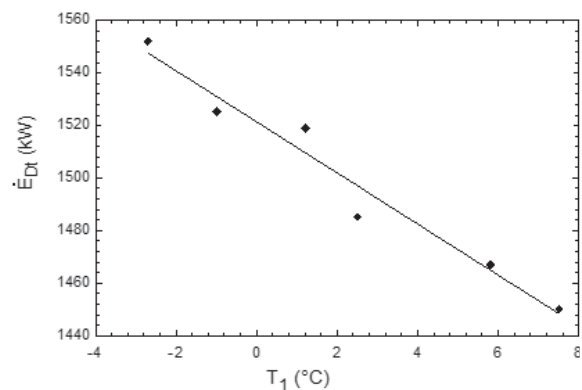


Figure 4. Turbine exergy destruction vs environment air temperature

The variation in exergy destruction of the turbine as a function of the environment air temperature is depicted in Fig. 4. As the environment air temperature raises, the exergy destruction of the turbine decreases. It was mentioned earlier that the main reasons of the entropy generation in the turbine are the sudden expansion of the fluid and friction. The production of entropy in the turbine decreases at inc-

raising environment temperatures. This causes the exergy destruction in the turbine to decrease as depicted in Fig. 4. The maximum exergy destruction is 1552 kW at -2.7°C while the minimum is 1450 kW at 7.5°C

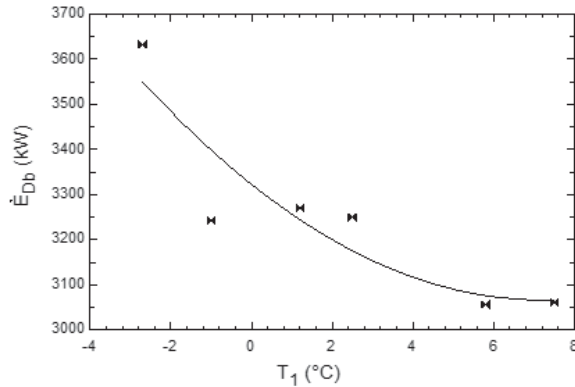


Figure 5. Boiler exergy destruction vs environment air temperature

Fig. 5 shows the variation in exergy destruction of the boiler according to the environment air temperature. As can be seen from Fig. 5, the exergy destruction in the boiler averagely decreases as the environment air temperature raises. The main reason for the exergy destruction in the boiler is the entropy flows of water and air. At -2.7°C , the maximum exergy destruction occurs as 3632 kW, and then the exergy destruction suddenly decreased to around 3254 kW at the environment temperatures between -1°C and 2.5°C . Finally, the average exergy destruction of the boiler is 3059 kW as minimum between the environment temperature of 5.8°C and 7.5°C is. At increasing environment air temperatures between -2.7°C and 7.5°C , the exergy destruction in the boiler decreases averagely % 15.7.

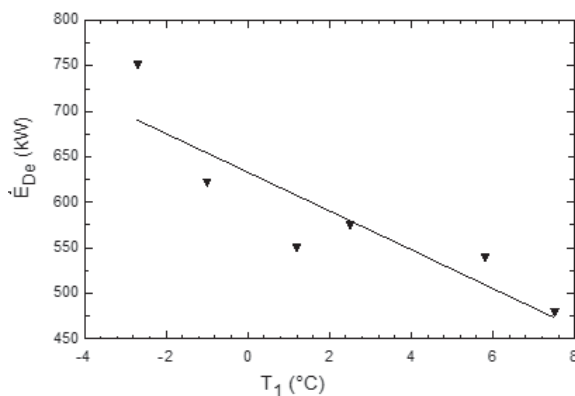


Figure 6. Economizer exergy destruction vs environment air temperature

The variation in the exergy destruction of the economizer as a function of the environment air temperature is depicted in Fig. 6. As the environment air temperature raises, the irreversibility of the economizer decreases. Entropy flows of water and air only cause the exergy destruction in the economizer because the economizer is insulated from

the environment like the boiler. The exergy destruction values in the economizer are lower than those in the boiler because the average temperatures the fluids during flow in the economizer are lower than those in the boiler. so the irreversibilities that occur are also smaller. As the environment air temperature raises from -2.7°C to 7.5°C , the exergy destruction of the economizer decreases between 750.9 kW and 478.9 kW. At the above-mentioned environment temperatures, the irreversibility of the economizer averagely decreased % 36.

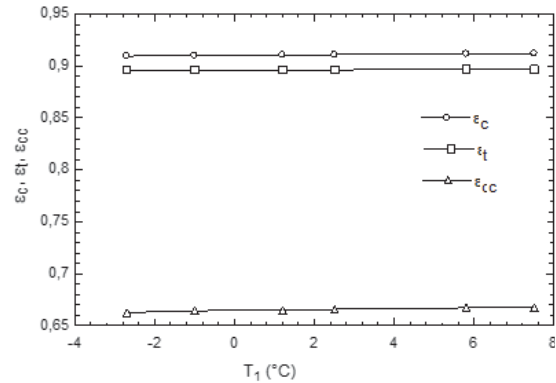


Figure 7. Exergetic efficiencies of the main elements vs environment air temperature

The variation in the exergetic efficiency of the main elements of the gas turbine power plant such as compressor, turbine and combustion chamber as a function of the environment air temperature is depicted in Fig. 7. The highest exergetic efficiency occurred in the compressor with 91%, followed by the turbine with 89% and the lowest exergetic efficiency occurred with 66% in the combustion chamber. The variation in the exergetic efficiencies of the compressor, turbine and combustion chamber are almost neglected at increasing environment temperatures of between -2.7°C and 7.5°C .

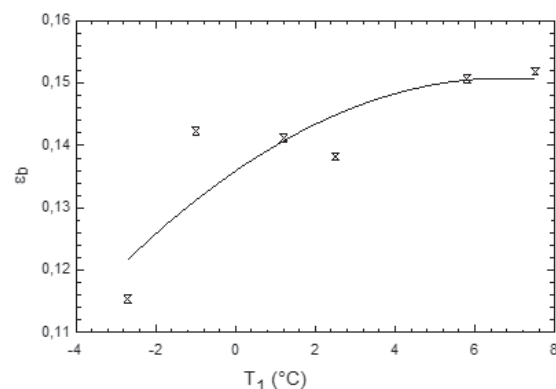


Figure 8. Boiler exergetic efficiency vs environment air temperature

Fig. 8 depicts the variation of the exergetic efficiency of the boiler as a function of the environment air temperature. As the environment air temperature raises, the exergetic efficiency of the boiler raises. At increasing environment air

temperatures between $-2.7\text{ }^{\circ}\text{C}$ and $7.5\text{ }^{\circ}\text{C}$, the decrease in the exergy destruction of the boiler causes the exergetic efficiency of the boiler to raise. The exergetic efficiency of the boiler is 11.5% at $-2.7\text{ }^{\circ}\text{C}$ and it is 15.2% at $7.5\text{ }^{\circ}\text{C}$.

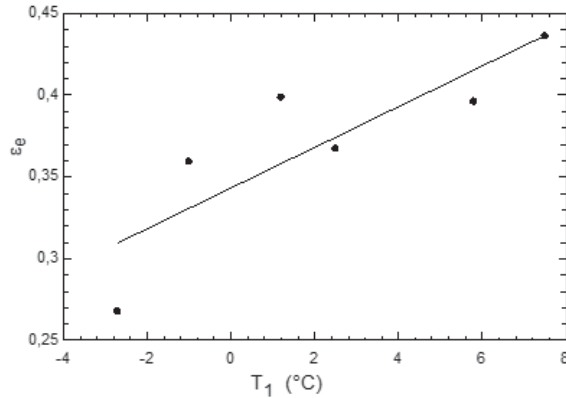


Figure 9. Economizer exergetic efficiency vs environment air temperature

Fig. 9 shows the variation in the exergetic efficiency of the economizer as a function of the environment air temperature. As the environment air temperature raises, the exergetic efficiency of the economizer averagely raises. At increasing environment air temperatures between $-2.7\text{ }^{\circ}\text{C}$ and $7.5\text{ }^{\circ}\text{C}$, the exergetic efficiency of the economizer variations between 26.7% and 43.61%. A decrease in the exergy destruction of the economizer causes the exergetic efficiency of the economizer to raise by 36%. As depicted in Figure 9. The exergetic efficiency of the economizer, which tends to raise smoothly at the environment air temperatures between $-2.7\text{ }^{\circ}\text{C}$ and $1.2\text{ }^{\circ}\text{C}$, decreases between $1.2\text{ }^{\circ}\text{C}$ and $5.8\text{ }^{\circ}\text{C}$ and then raises to its maximum at a temperature of $7.5\text{ }^{\circ}\text{C}$.

CONCLUSIONS

A real time data including temperature, pressure, flow rate and net power at the environment air temperatures between $-2.7\text{ }^{\circ}\text{C}$ and $7.5\text{ }^{\circ}\text{C}$ was collected from the gas turbine power plant generating electricity and waste heat, located in Çorum-Turkey. According to the real data, the exergy destructions and exergetic efficiencies of the main and auxiliary elements were carried out with respect to the environment air temperatures.

At increasing environment air temperatures between $-2.7\text{ }^{\circ}\text{C}$ and $7.5\text{ }^{\circ}\text{C}$, the exergy destruction values in the compressor, turbine and combustion chamber decreased. The exergy destruction decreased from 545.6 kW to 499.6 kW for the compressor; from 51 kW and 38 kW for the combustion chamber, from 1552 kW to 1450 kW for the turbine, from 3632 kW to 3254 kW for the boiler and from 750.9 kW to 478.9 kW for the economizer at the environment air temperatures studied in this experimental work. Maximum

exergy destruction occurred at $-2.7\text{ }^{\circ}\text{C}$ and minimum one occurred at $7.5\text{ }^{\circ}\text{C}$ occurred in each of the main elements of the gas turbine power plant. At increasing environment air temperatures between $-2.7\text{ }^{\circ}\text{C}$ and $7.5\text{ }^{\circ}\text{C}$, the maximum exergy destruction occurred in the boiler as 3652 kW while the minimum one occurred in the combustion chamber as 379 kW. As it was mentioned before, the maximum exergy destruction occurs in the combustion chamber in an actual gas turbine power plant where the chemical exergies of the reactants and exhaust products are taken into consideration, but the air standard assumptions are presumed in this work.

At increasing environment temperatures between $-2.7\text{ }^{\circ}\text{C}$ and $7.5\text{ }^{\circ}\text{C}$, the exergetic efficiencies of the main and auxiliary elements mainly raised because of decreasing the exergy destructions. The variation in the exergetic efficiency of the main elements such as the compressor, turbine and combustion chamber can be neglected. The maximum exergetic efficiency was observed as 91% in the compressor, followed by as 89% in the turbine and 66% in the combustion chamber. Exergetic efficiency of the economizer ranged from 26% to 43% while that of the boiler ranged from 11.5% and 15%.

ACKNOWLEDGMENTS

We thank to the Scientific Research Projects Unit of Hitit University for its support to the project numbered (MUH19004.14.009).

This paper was presented orally in 17th International Conference on Sustainable Energy Technologies – SET 2018, 21st - 23rd of August 2018, Wuhan, China and its abstract was published in Conference Abstract Book.

NOMENCLATURE

BWR	: Back work ratio
e_x	: specific exergy (kJ/kg)
\dot{E}_x	: Exergy rate (kW)
\dot{E}_D	: Exergy destruction rate (kW)
\dot{m}	: Mass flow rate (kg/s)
ϵ	: Exergetic efficiency
η_c	: Compressor isentropic efficiency
η_t	: Turbine isentropic efficiency
P_0	: Atmospheric pressure (kPa)
\dot{Q}	: Heat transfer (kW)
T_s	: Boundary temperature (K)
\dot{W}	: Power (kW)

Subscript

b	: Boiler
c	: Compressor
cc	: Combustion chamber
cv	: Control volume
e	: Economizer
i	: Inlet
o	: Outlet
t	: Turbine
w	: Water

References

1. Arpacı, İ, 2002. Exergy analysis of natural gas fired cogeneration systems, M.Sc. Thesis, Marmara University, Graduate School of Natural and Applied Sciences, İstanbul-Turkey.
2. Ersayın, E, Ozgener, L, 2015. Performance analysis of combined cycle power plants: A case study. *Renewable and Sustainable Energy Reviews*, 43, 832-842.
3. Gürer, A.,T, 1997. Energy and Exergy Utilization in Turkish Industrial Sector up to 2010. M.Sc. Thesis, Middle East Technical University, Graduate School of Natural and Applied Sciences, Mechanical Engineering Department, Ankara-Turkey.
4. Ibrahim, T.K, Basrawi, F, Awad, O.I, Abdullah, A.N, Najafi, G, Mamat, R, Hagos, F.Y, 2017. Thermal performance of gas turbine power plant based on exergy analysis. *Applied Thermal Engineering*, 115, 977-985.
5. Kilicarslan A. An experimental investigation of a different type vapor compression cascade refrigeration system. *Applied Thermal Engineering* 2004; 24:2611-2626.
6. Klein, S.A., 2017. Engineering Equation Solver (EES) Professional version V10.294-3D, F-Chart Software.
7. Kumari, A, Sanjay, 2015. Investigation of parameters affecting exergy and emission performance of basic and intercooled gas turbine cycles. *Energy*, 90, 525-536.
8. Moran, M.J., Shapiro, H.N., 2006. *Fundamentals of Engineering Thermodynamics*, 5th Edition, John Wiley&Sons.
9. Özcan, H, Dinçer, I, 2014. Thermodynamic analysis of a combined chemical looping-based trigeneration system. *Energy Conversion and Management*, 85, 477-487.
10. Rahim, M.A, Gündüz, D., 2013. Energy and exergy analyses of a gas turbine power plant with cogeneration: An application in Ankara. *Tübav Bilim Dergisi*, 6(2), 19-27.
11. Sevilgen, S.H, 2004. Exergoeconomic analysis of cogeneration system. *Journal of Engineering and Natural Sciences*, 4, 234- 248.
12. Sue, D.C, Chuang, C.C, 2004. Engineering design and exergy analyses for combustion gas turbine based power generation system. *Energy*, 29, 1183-1205.
13. Sürer, F, 2003. Thermodynamic and economical analysis of a combined gas/vapor cogeneration system. M.Sc. Thesis, Yildiz Technical University, Graduate School of Natural and Applied Sciences, İstanbul-Turkey.
14. Töre, H, 2015. An experimental investigation of a heat pump operating in the cooling mode for different refrigerants. M.Sc. Thesis, Hitit University, Graduate School of Natural and Applied Sciences, Çorum-Turkey.
15. Turan, O, Aydın, H, 2014. Exergetic and exergo-economic analyses of an aero-derivative gas turbine engine. *Energy*, 74, 638-650.
16. Van Wylen, G.J, Sonntag, R.E, 1985. *Fundamentals of Classical Thermodynamics*, 3rd Edition, John Wiley & Sons.

